

A BIOPHYSICAL MODEL OF ATRIAL FIBRILLATION AND ELECTROGRAMS: FORMULATION, VALIDATION AND APPLICATIONS

THÈSE N° 2996 (2004)

PRÉSENTÉE À LA FACULTÉ SCIENCES ET TECHNIQUES DE L'INGÉNIEUR

Institut de traitement des signaux

SECTION D'ÉLECTRICITÉ

ÉCOLE POLYTECHNIQUE FÉDÉRALE DE LAUSANNE

POUR L'OBTENTION DU GRADE DE DOCTEUR ÈS SCIENCES

PAR

Vincent JACQUEMET

ingénieur physicien diplômé EPF
de nationalité suisse et originaire de Conthey (VS)

acceptée sur proposition du jury:

Prof. M. Kunt, directeur de thèse
Prof. C. Henriquez, rapporteur
Prof. L. Kappenberger, rapporteur
Prof. J.-J. Meister, rapporteur
Dr J.-M. Vesin, rapporteur

Lausanne, EPFL
2004

*“Nature is FreeWare,
but unfortunately not Open Source.”*

— anonymous, from usenet (sci.math)

Abstract

Atrial arrhythmias are the most frequent rhythm disorders in humans and often lead to severe complications such as heart failure and stroke. While different mapping techniques have provided significant information on the electrophysiological processes associated with atrial fibrillation (AF), the mechanisms underlying AF initiation and maintenance remain unclear. Hence the treatment of atrial arrhythmias is still based on empirical considerations.

To assist the study of the complex spatio-temporal dynamics of AF, a realistic-size computer model of human atria was developed. The model geometry was derived from magnetic resonance images of the human heart. Mathematical models of cell electrophysiology describing the ionic currents through the cell membrane were used. By representing the domain as a three-dimensional monolayer, the computational load was sufficiently reduced to allow the simulation of more than 20 seconds of an arrhythmia.

With this model, simulated AF, *i.e.* multiple reentrant wavelets, were induced using different clinically relevant protocols. The model outputs both transmembrane potential maps and electrograms at any location in the atria, facilitating comparisons of simulation results to experimental or clinical data. It is also possible to study separately the conditions leading to the initiation and perpetuation of AF, and, more generally, to uncouple the phenomena by controlling separately the parameters affecting the simulation.

First, the mechanisms leading to AF initiation and perpetuation were investigated. In a model of normal conduction in the atria, electrically-induced AF was unsustainable and converted to sinus rhythm after a few seconds. After remodeling (applied as an abrupt alteration of tissue properties), however, episodes of sustained AF were obtained. Simulated AF was observed as several wavelets propagating randomly over the whole atrial surface and undergoing anatomical and functional reentries, collisions, and annihilation by mutual interaction. The simulation studies suggest that the restitution dynamics (describing the dependence of the action potential duration on the previous diastolic interval) and the wavelength (effective refractory period \times conduction velocity) play a crucial role in determining the duration of AF.

Electrograms were then computed during simulated AF and their morphology was characterized by their amplitude and asymmetry. These simulated electrograms were similar to those recorded in humans. By simulating wavefront propagation in carefully prepared conditions, it was possible to determine the effect of the different components of AF dynamics (wavefront shape, collisions, conduction blocks, wavelength) as well as the influence of the underlying substrate (tissue conductivity, anisotropy, heterogeneity) on waveform morphol-

ogy. Analysis of the amplitude and symmetry of unipolar atrial electrograms is believed to provide information about the electrophysiological substrate maintaining AF.

Version Abrégée

Les arythmies auriculaires sont l'un des plus fréquents troubles du rythme cardiaque et entraînent souvent de sérieuses complications telles que l'insuffisance cardiaque ou des embolies. Bien que différentes techniques expérimentales aient apporté de précieuses informations sur les processus électrophysiologiques associés à la fibrillation auriculaire (FA), certaines zones d'ombre concernant les mécanismes d'initiation et de perpétuation de la FA persistent. Le traitement des arythmies auriculaires reste donc essentiellement basé sur des considérations empiriques.

Dans le but d'assister l'étude de la dynamique spatiotemporelle complexe de la FA, un modèle numérique des oreillettes humaines a été développé. La géométrie du modèle a été construite sur la base d'imagerie par résonance magnétique. Des modèles d'électrophysiologie cellulaire décrivant les courants ioniques à travers la membrane cellulaire ont été utilisés. Grâce à une représentation tridimensionnelle formée d'une fine couche de tissu, le temps de calcul a été suffisamment réduit pour permettre la simulation d'arythmies de plus de 20 secondes.

A l'aide de ce modèle, des FA simulées, c'est-à-dire de multiples ondelettes réentrantes, ont pu être induites par des protocoles de stimulation réalistes. Le modèle est capable d'afficher des potentiels transmembranaires et des électrogrammes pour n'importe quel point des oreillettes, ce qui facilite la comparaison des résultats avec des données expérimentales ou cliniques. Il est également possible d'étudier séparément les conditions menant à l'initiation ou à la perpétuation de la FA, et, plus généralement, de découpler les phénomènes en contrôlant séparément les paramètres qui affectent la simulation.

En premier lieu, les mécanismes menant à l'initiation et à la perpétuation de la FA ont été étudiés. Dans un modèle reproduisant une propagation normale dans les oreillettes, les FA induites par stimulations électriques furent non-soutenues et le rythme normal reprit après quelques secondes. Cependant, après remodelage (appliqué comme une modification abrupte des propriétés du tissu), des épisodes de FA soutenues ont pu être obtenus. Durant la FA simulée, plusieurs ondelettes se propagent aléatoirement sur toute la surface des oreillettes, subissent des réentrées anatomiques et fonctionnelles, des collisions, ou s'annihilent par interaction mutuelle. Les simulations suggèrent que la dynamique de restitution (décrivant la dépendance de la durée du potentiel d'action par rapport à l'intervalle diastolique précédent) et la longueur d'onde (période réfractaire effective \times vitesse de conduction) jouent un rôle prépondérant dans la détermination de la durée de la FA.

Des électrogrammes ont ensuite été calculés durant la FA simulée et leur morphologie a

été caractérisée par leur amplitude et leur asymétrie. Ces électrogrammes simulés sont similaires à ceux enregistrés sur des patients. En simulant la propagation de fronts d'onde dans des conditions contrôlées, il a été possible de déterminer l'effet des différentes composantes de la dynamique de la FA (forme du front, collisions, blocs de conduction, longueur d'onde) sur la morphologie des électrogrammes ainsi que l'influence du substrat sous-jacent (conductivité du tissu, anisotropie, hétérogénéité). Une analyse de l'amplitude et de l'asymétrie des électrogrammes auriculaires unipolaires est donc susceptible d'apporter des informations sur le substrat électrophysiologique assurant la maintenance de la FA.

Remerciements

La recherche est un *travail d'équipe*. Je souhaite donc remercier sincèrement toutes les personnes qui ont participé à la réussite de ce projet:

- Je tiens tout d'abord à remercier mon directeur de thèse, Prof. Murat Kunt (Institut de Traitement des Signaux, EPFL), pour m'avoir accueilli dans son laboratoire qui fournit un environnement international et multiculturel propice à la recherche et à l'innovation.
- L'intérêt et l'enthousiasme du Prof. Lukas Kappenberger (Service de Cardiologie, CHUV) pour la modélisation des oreillettes sont aujourd'hui bien connus et participent à la revalorisation de notre travail. Il a toujours su créer des liens avec des partenaires académiques et industriels, encourager les collaborations entre ingénieurs et médecins, et œuvrer pour faire connaître ce projet. Je le remercie donc pour son engagement personnel dans le projet.
- Un grand merci également au Dr. Jean-Marc Vesin, mon superviseur à l'EPFL, pour son soutien moral et technique, et pour son enseignement du traitement des signaux, anecdotes à l'appui, ainsi qu'au Dr. Etienne Pruvot pour son ouverture d'esprit et sa disponibilité lors de ma première année de thèse. J'aimerais aussi exprimer ma gratitude envers Dr. Nathalie Virag (Medtronic Europe, Tolochenaz). Son sens de l'organisation et de la diplomatie s'est révélé d'une redoutable efficacité.
- I would like to thank Prof. Craig S. Henriquez (Duke Univ., Durham, NC) for his guidance, his encouragement and for his relevant comments and suggestions during our fruitful collaboration.
- Une mention spéciale pour Olivier Blanc avec qui j'ai partagé les bons moments et les périodes difficiles de ce projet. Il est par ailleurs le tout premier lecteur de cette thèse. Je le remercie pour ce minutieux et attentif travail de correction.
- Je voudrais mentionner les autres membres du groupe qui ont, de près ou de loin, contribué à ce travail: Max Boegli, Steeve Zozor, Mattia Bertschi, Zenichi Ihara, Lam Dang, Andrei Forclaz, et, plus récemment Mathieu Lemay, et Prof. Adriaan van Oosterom. I want to thank Kevin J. Sampson and Peter van Dam for interesting collaboration and discussion.
- I am grateful to Prof. Maurits Allestie, Dr. Fredric Lindemans and Richard Houben, who gave us the opportunity to present them our work several times. Their comments and criticism have been very helpful and have suggested new developments and analysis.
- We would like to thank Ryan Lahm, Drs. Josée Morissette and Arthur Stillman who kindly furnished the atrial geometry surface model.

- Merci à tous les membres de l'ITS, en particulier mes collègues du labo ELE-227, pour l'agréable ambiance de travail qui combine à la fois sérieux et fantaisie.
- Saluons également la bonne humeur de notre aimable assistance logistique et administrative: Marianne Marion, Fabienne Vionnet et Gilles Auric.
- Pour finir, j'adresse toutes mes pensées à ma famille, Benoît, Marie-Hélène, Claire et Lucien, qui m'ont soutenu pendant toutes ces années et qui m'ont changé les idées lors de mes week-ends en Valais.

Bonne lecture à ceux qui trouveront la persévérance pour parcourir tous les chapitres de cette thèse!

Vincent Jacquemet
le 12 mai 2004

Contents

Abstract / Version abrégée	i
Acknowledgments	v
1 Introduction	1
1.1 Motivations and Problem Statement	1
1.2 Organization of the Dissertation	3
1.3 Original Contributions	4
<hr/>	
Part I Modeling	5
2 Modeling Heart Electrophysiology	7
2.1 Cell Excitability	7
2.2 Shape of the Action Potential	9
2.3 Impulse Propagation	11
2.4 Restitution Properties	11
2.5 Atrial Geometry	13
2.6 Conclusion	14
3 From Ion Electrodiffusion to Cell Models	15
3.1 Molecular Level : Kinetics	17
3.1.1 Chemical Kinetics and Markov Models	17
3.1.2 Reaction Rates	18
3.2 Membrane Level : Channels, Pumps and Exchangers	19
3.2.1 Ionic Channels	20
3.2.2 Gating Kinetics	20
3.2.3 Pore Conductance	23
3.2.4 Active Transport	26
3.2.5 Ion Exchangers	27
3.3 Cellular Level : Cell Models	28
3.3.1 Membrane potential	29
3.3.2 Fluid Compartment Model	30
3.4 Conclusion	35
4 From Cell to Organ	37
4.1 Tissue Level : Propagation Equations	37
4.1.1 Cell-to-Cell Coupling	37
4.1.2 Spatial Homogenization	37
4.1.3 Bidomain Theory	38

4.1.4	Monodomain Approximation	40
4.2	Organ Level : Anatomy	41
4.2.1	Geometry	41
4.2.2	Conduction Properties and Fiber Orientation	42
4.2.3	Heterogeneities	44
4.3	Experimentalist's Level : Electrical Mapping	45
4.3.1	Optical and Electrical Mapping	45
4.3.2	Model of Electrode	46
4.3.3	Simulated High Density Mapping	46
4.4	Conclusion	47

Part II Numerical Methods **49**

5	Spatial Discretization	51
5.1	Discretization Strategies	51
5.2	Structured Mesh	53
5.2.1	Spatial Discretization	53
5.2.2	Finite Difference Operators	53
5.2.3	Approximation of Diffusion Operators	53
5.2.4	Stability and Resistor Interpretation	54
5.3	Triangular Mesh	55
5.3.1	Spatial Discretization	55
5.3.2	Semi-Discretized Equation	56
5.3.3	Structure of the Stiffness Matrix	58
5.3.4	Practical Formulation	61
5.3.5	Stability	61
5.3.6	Computing the Matrix A	61
5.3.7	The Isotropic Case	62
5.4	Multi-Layer Triangular Mesh	62
5.4.1	Spatial Discretization	63
5.4.2	Semi-discretized Equation	63
5.4.3	Stability	64
5.5	Conclusion	64
6	Time Integration	65
6.1	Operator Splitting	65
6.1.1	Principle	65
6.1.2	Flow Operators	66
6.1.3	Splitting Formulae	67
6.1.4	Application to Reaction–Diffusion Systems	67
6.1.5	Adaptive Time Steps	68
6.2	The Diffusion Step	68
6.2.1	Padé Approximants	69
6.2.2	Alternating Direction Implicit	69
6.2.3	Time Step Subdivision	71
6.3	The Reaction Step	71
6.3.1	Forward Euler Update	71
6.3.2	Time-Adaptive Stepping	72
6.3.3	Gating variables: Rush–Larsen Scheme	72
6.3.4	Slow Variables	73

6.4	Conclusion	73
7	Numerical Methods in Action	75
7.1	Running Simulations	75
7.2	Computing Electrograms	79
7.3	Numerical Accuracy	80
7.3.1	Mesh Quality	81
7.3.2	Convergence	83
7.4	Conclusion	84
<hr/> Part III Simulated Atrial Fibrillation <hr/>		85
8	Initiation of Atrial Fibrillation	87
8.1	Initiation Protocols	88
8.1.1	Single Cell Model	88
8.1.2	Conduction Properties	92
8.1.3	Stimulation Protocols	92
8.1.4	Output Data and Signal Analysis	93
8.2	Restitution-Based Simulated Atrial Fibrillation	94
8.2.1	S_1 - S_2 - S_3 protocols	94
8.2.2	Burst Pacing Protocols	96
8.2.3	Effect of Restitution	98
8.2.4	Ramp Protocols	100
8.3	Arrhythmogenic Effect of Heterogeneity	101
8.4	Conclusion	103
9	Perpetuation of Atrial Fibrillation	105
9.1	A Model of Multiple Reentrant Wavelets	105
9.1.1	Unsustained Atrial Fibrillation	106
9.1.2	Effect of Action Potential Duration Restitution	108
9.1.3	Remodeling and Sustained Atrial Fibrillation	109
9.1.4	Factors Promoting Atrial Fibrillation	112
9.2	A Model of Meandering Wavelets	112
9.3	A Model of Mother Rotor	115
9.4	Conclusion	118
10	Analysis of Simulated Atrial Fibrillation	119
10.1	Electrograms and Activation Patterns	119
10.1.1	Comparison of Different Simulated Atrial Fibrillation Dynamics	119
10.1.2	Effect of Anisotropy	122
10.2	Measures of Organization and Complexity	122
10.2.1	Overview of Existing Methods	122
10.2.2	Space Constant of Activation	124
10.2.3	Coherence Analysis	125
10.2.4	Linear Prediction Error	127
10.2.5	Principal Component Analysis	128
10.3	Estimation of Wavelength	129
10.3.1	Hypotheses of Botteron's Method	130
10.3.2	Evaluation of Botteron's Method	131
10.3.3	Critical Wavelength of Simulated Atrial Fibrillation	132

10.4 Conclusion	133
<hr/>	
Part IV Electrogram Morphology	135
11 Electrogram Morphology: Effect of Wavefront Dynamics	137
11.1 Characterization of Electrogram Waveforms	137
11.1.1 Waveform Detection	138
11.1.2 Waveform Morphology: Qualitative Description	138
11.1.3 Waveform Morphology: Quantitative Description	139
11.1.4 Amplitude-versus-Asymmetry Diagrams	140
11.2 Wavefront Curvature	140
11.2.1 Motivation	140
11.2.2 Theory of Oblique Dipole Layer	142
11.2.3 Working Hypothesis	143
11.2.4 Estimation of Local Curvature	143
11.2.5 Two-Dimensional Circular Wavefronts	145
11.2.6 Curved Wavefronts in the Atrial Model	146
11.2.7 Wavefront Classification during Simulated AF	148
11.3 Wavefront Collisions	148
11.3.1 Collision in a One-dimensional Fiber	149
11.3.2 Collision with a Boundary	150
11.3.3 Colliding Wavefronts in the Atrial Model	151
11.4 Refractoriness and Front-Tail Interactions	152
11.4.1 Waveform Amplitude and Peak Sodium Current	152
11.4.2 Conduction Blocks and Long Double Potentials	153
11.4.3 Comparison of Different Simulated AF Dynamics	154
11.5 Baseline Modulation	156
11.6 Conclusion	158
12 Electrogram Morphology: Effect of the Substrate	161
12.1 Effect of Tissue Properties	161
12.1.1 Membrane Model	161
12.1.2 Conduction Properties	162
12.2 Effect of Anisotropy	163
12.2.1 Working Hypothesis	163
12.2.2 Anisotropy in a Two-Dimensional Tissue	164
12.2.3 Fiber Orientation in the Atrial Model	166
12.3 Effect of Heterogeneity	168
12.3.1 Discontinuity in Conductivity	169
12.3.2 A Heterogeneous Atrial Model	170
12.4 Effect of Tissue Transmural Heterogeneity	173
12.4.1 Plane Wave Propagation in a 3D Tissue	173
12.4.2 Paced Beat in a Multilayer Atrial Model	175
12.5 Conclusion	176
13 Conclusion	179
Bibliography	183
Curriculum Vitae and Publications	197

List of Figures

1.1	The EKG sequence	3
2.1	Illustration of the properties of an excitable system	8
2.2	Electrical response of a cardiac cell: subthreshold and superthreshold stimulation	8
2.3	Membrane current as a function of the membrane potential during the upstroke phase	9
2.4	Action potential shape simulated using different models	10
2.5	Illustration of the propagation of the electrical impulse in the myocardium	11
2.6	S ₁ -S ₂ protocol for computing restitution curves	12
2.7	Example of restitution curves	12
2.8	Geometry of human atria constructed from MR images	13
2.9	Schematic representation of the bottom-up approach for cardiac modeling	14
3.1	Schematic representation of the Luo-Rudy ventricular cell model and Courtemanche <i>et al.</i> human atrial model	15
3.2	Representation of the parameters describing the gating kinetics of the transient outward current (Courtemanche model)	22
3.3	Timecourse of the membrane currents of the Courtemanche <i>et al.</i> model	29
3.4	Schematic representation of fluid compartment models	31
3.5	Timecourse of the ionic concentrations and the intracellular ionic fluxes in the Courtemanche model	32
3.6	Schematic view of the relations between the state variables of a cell	35
4.1	Decomposition into three domains underlying the spatial homogenization process	38
4.2	Geometry of human atria based on MR images	42
4.3	Illustration of the different steps from a fiber trajectory to a complete fiber orientation field	43
4.4	Representation of the gross fiber structure included in the model	43
4.5	Distribution of heterogeneities generated using Markov random fields	44
4.6	Distribution of heterogeneities on the atria using isotropic and anisotropic diffusion	45
4.7	Electrodes configuration in the simulated high density mapping	47
5.1	Nearest neighbors and local topology of a triangular mesh	55
5.2	Domain associated with a vertex	56
5.3	Illustration of the dual basis	59

5.4	Construction of the vector space of scalar fields on a multilayer structure using a tensor product	63
6.1	Block-diagram view of the time stepping scheme	68
7.1	Activation map and isochrones during normal sinus rhythm activation . . .	78
7.2	Examples of simulated unipolar electrograms during sinus rhythm	79
7.3	Comparison of simulated and clinical bipolar electrograms during sinus rhythm	80
7.4	Safety factor map	82
7.5	Distribution of safety factors for meshes of the atrial surface with different spatial resolutions	82
7.6	Relative error on the conduction velocity for different spatial discretizations	84
8.1	Restitution properties of the modified Luo–Rudy model	89
8.2	Restitution properties of the modified Courtemanche model	90
8.3	Restitution properties of the modified Courtemanche model with vagal stimulation	91
8.4	Initiation of simulated AF using a S ₁ –S ₂ –S ₃ protocol	95
8.5	Initiation of simulated AF using a burst pacing protocol	96
8.6	Illustration of the mechanism of conduction block occurring in the right atrium appendage as a result of burst pacing	97
8.7	Mechanism of conduction block simulated on a cable	98
8.8	Effect of the geometry in a tissue with uniform conduction properties	98
8.9	Action potential duration non-uniform alternans in left atrium appendage .	99
8.10	Initiation of simulated AF using the modified Courtemanche model and a ramp protocol	100
8.11	Example of simulated AF initiation in a heterogeneous tissue without rate adaptation	102
9.1	Example of unsustained fibrillation on the baseline model (Luo–Rudy) . . .	106
9.2	Average duration of SAF as a function of the control parameter \overline{G}_{si}	108
9.3	Example of sustained fibrillation obtained after an abrupt remodeling (Luo–Rudy)	110
9.4	Distribution of the number of wavelets during simulated AF	111
9.5	Dynamical action potential duration restitutions	111
9.6	Average duration of simulated AF as a function of the membrane and tissue properties	113
9.7	Example of sustained fibrillation in an isotropic tissue (Courtemanche) . . .	114
9.8	Example of sustained fibrillation in an anisotropic tissue (Courtemanche) .	115
9.9	Example of sustained fibrillation in a heterogeneous tissue (Courtemanche)	116
9.10	Unipolar electrogram and dominant frequency	117
9.11	Stable rotor anchored at a heterogeneity in the left atrium appendage . . .	117
10.1	Simulated unipolar electrograms and activation patterns for different simulated AF dynamics	120
10.2	Simulated unipolar electrograms and activation patterns for different anisotropy ratios	121
10.3	Activation space constant during sinus rhythm and simulated AF	125
10.4	Activation space constant as a function of the signal length	126
10.5	Examples of coherence map	126

10.6	Magnitude squared coherence during sinus rhythm and simulated AF	127
10.7	Mean square linear prediction error during sinus rhythm and simulated AF	128
10.8	Karhunen-Loève decomposition dimension and correlation length	129
10.9	Hypothesis underlying Botteron's estimate of wavelength	131
10.10	Estimated wavelength during simulated AF as a function of the membrane and tissue properties	132
10.11	Simulated AF duration as a function of the wavelength	133
11.1	Characterization of electrogram waveforms: peak detection	138
11.2	Classification of unipolar electrograms into singles, short-doubles, long- doubles and fragmented potentials	139
11.3	Characterization of electrogram waveforms: definition of R and S	139
11.4	Amplitude-versus-asymmetry plot with examples of electrogram waveforms	140
11.5	Example of amplitude-versus-asymmetry diagram during simulated AF . . .	141
11.6	Waveform asymmetry in the experiment of Chorro <i>et al.</i> and in simulated AF	141
11.7	Distribution of dipolar moments on convex and concave wavefronts	143
11.8	Illustration of the method to estimate curvature	144
11.9	Waveform asymmetry as a function of the wavefront curvature in a 2D tissue	145
11.10	Relation of wavefront curvature to waveform asymmetry during pacing in the atria: detailed data	147
11.11	Relation of wavefront curvature to waveform asymmetry during pacing in the atria: summary	148
11.12	Snapshots of simulated high density mapping of AF and corresponding elec- trogram waveforms	149
11.13	Asymmetry statistics in the three classes of wavefronts (convex, plane and concave/colliding)	149
11.14	Waveform asymmetry during a wavefront collision in a unidimensional fiber	150
11.15	Waveform asymmetry near the end of a unidimensional fiber	151
11.16	Effect of wavefront collision on waveform asymmetry in the atrial model . .	151
11.17	Relation between the peak sodium current and waveform amplitude	152
11.18	Activation map of a conduction block with selected corresponding electro- grams	153
11.19	Amplitude-versus-asymmetry diagrams for the 4 different simulated AF dy- namics	155
11.20	Effect of wavelength on average waveform asymmetry	156
11.21	Example of baseline modulation	157
11.22	Illustration of baseline modulation in presence of repolarization gradients .	157
11.23	Representation of the regions in an amplitude-versus-asymmetry diagram associated with a class of activation patterns	158
12.1	Electrogram waveforms for different membrane models	162
12.2	Electrogram waveforms for different set of parameters affecting conduction velocity	162
12.3	Distribution of dipolar moments on convex and concave wavefronts	164
12.4	Lines of equal waveform asymmetry in a center-paced beat initiated in a 2D sheet of tissue with different anisotropy ratios	165
12.5	Decomposition of electrograms into an axial and a conormal component . .	166
12.6	Effect of anisotropy on amplitude-versus-asymmetry plots for sinus rhythm and four different dynamics of simulated AF	167
12.7	Percentage of rS patterns during simulated AF with different anisotropy ratios	169

12.8	Electrogram waveform in presence of conduction velocity heterogeneities simulated in a cable	170
12.9	Fragmentation map indicating fraction of fragmented waveforms during SAF in the presence of heterogeneity	172
12.10	Waveform morphology distribution during SAF in homogeneous and inhomogeneous atria	173
12.11	Schematic representation of the 3D heterogeneous tissue model	173
12.12	Effect of wavefront angle on electrogram asymmetry in a 3D tissue	174
12.13	Effect of transmural gradients of conductivity on the waveform asymmetry distribution in a multilayer model of the atria	175
12.14	Representation of the different regions in an amplitude-vs-asymmetry diagram that can be associated with a class of activation patterns (anisotropic and heterogeneous case)	177

List of Tables

1.1	Comparison between real and virtual experiment characteristics.	2
3.1	Ionic currents defined in the Luo–Rudy phase I model	16
3.2	Ionic currents defined in the Courtemanche <i>et al.</i> model	16
5.1	Main discretization schemes with a few selected references	52
5.2	Finite differences discretization formulae	54
6.1	Lowest order Padé approximants of e^{-z}	69
6.2	Time integration schemes based on lowest-order Padé approximants	70
7.1	Typical tissue parameters for simulations.	76
7.2	Spatial resolution and number of vertices of the meshes	76
7.3	Time steps used in the present study for structured and unstructured meshes	77
7.4	Dispersion of safety factor on meshes of the atrial surface with different spatial resolutions	83
8.1	Stimulation protocols: S_1 – S_2 – S_3 , burst-pacing and ramp protocols	93
8.2	Initiation of simulated AF in models with different restitution dynamics	99
9.1	Relations between the initial state and simulated AF duration	107
9.2	Mean number of wavelets and phase singularities, AF cycle length and excitable gap during simulated AF	109
9.3	Parameter sets chosen for the remodeled tissue	112
9.4	Qualitative description of the SAF models	118
11.1	Characteristics of waveform morphology and wavelet dynamics for 4 different simulated AF	154
12.1	Percentage of rS patterns in a center-paced 2D model for different anisotropy ratios	165
12.2	Mean wavefront asymmetry in presence of a transmural gradient of conductivity	176

Dissertation

Introduction

1.1 Motivations and Problem Statement

Atrial Fibrillation

Atrial fibrillation (AF) is a disorder of heart rhythm (*arrhythmia*) usually associated with rapid heart rate in which the upper heart chambers (the *atria*) quiver instead of beating effectively.¹ The abnormal heart rhythm diminishes the delivery of blood and its nutrients to the brain and other organs, which can cause symptoms such as weakness, fatigue, shortness of breath, syncope, and palpitations.² While not directly life-threatening, AF has a natural tendency to turn into a chronic disease, often leading to severe complications. Notably, since blood is not pumped completely out of the atria, blood clots may form. If a piece of blood clot leaves the heart and becomes lodged in an artery in the brain, a stroke results.³

According to recent statistics collected in the United States,⁴ AF is the most common cardiac arrhythmia observed in clinical practice, affecting approximately 2.2 millions of people. The rate of AF increases with age, from less than 1% among persons younger than 60, up to 10% for persons aged 80 and older. Treatments of AF include: medications that slow down rapid heart rate associated with AF (anti-arrhythmic drugs), electrical cardioversion (an electric shock is applied), radio-frequency catheter ablation used in order to restrain the pathway of abnormal electrical propagation, and implanted atrial pacemakers that regulate the heart rhythm.

Integrated Research

While clinical studies and animal experiments have provided significant information on the electrophysiological processes associated with AF, the mechanisms underlying its initiation and maintenance remain unclear. Hence the treatment of atrial arrhythmias is still based on empirical considerations.

In order to facilitate the development of innovative therapeutic strategies, there is a need to better *integrate* knowledge and progresses from both clinical research and basic science.⁵ Computer models of heart electrophysiology⁶ are an example of such *integrated research*. Rooted in mathematics, biophysics, engineering, electrophysiology and cardiology, these models are constructed from data collected at several spatial scales (ionic channels, cell, tissue, organ) and help bridge these scales. For instance, the effect of a modification at

the cellular level (such as a pharmacological intervention) on an arrhythmia (organ level) can be investigated.

Despite their inherent limitations due to trade-offs between accuracy of the representation of the electrophysiological details and computational requirements, computer models are believed to provide a framework to test hypotheses and suggest new experimental or clinical studies. Numerical simulations (experiments performed *in silico*) would then become a complementary approach to *in vivo* and *in vitro* experimentations.

***In Silico* Experimentation**

The ever-increasing computer power made it possible to simulate models of full organs (ventricles or atria) with a realistic size and a detailed description of the cellular electrophysiological properties.⁷⁻¹¹ Table 1.1 presents a comparison of the advantages and the drawbacks of both computer models and experiments, demonstrating their complementarity.

	Computer Models	Experiments
Reproducibility	yes	difficult
Access to data	every variable, at any time, at any location	limited to some variables (e.g., electrical signals); some regions may be inaccessible
Tissue preparation (alteration of tissue properties)	easy and reliable; clean substrates can be prepared	difficult; requires a careful validation
Experiment duration	typically more than 1000 times slower than real time	real time; follow-up studies over several months are possible
Relevance to human AF	questionable; model validation is crucial	some limitations in the case of animal models

Table 1.1 — Comparison between real and virtual experiment characteristics.

Atrial Electrograms

Clinical assessment of heart electrophysiology mainly relies on electrical signals like electrocardiograms.¹ These signals constitute a natural link between computer models and experimental data. In the absence of a torso model, electrical signals measured on the atrial surface (*atrial electrograms*) are considered, corresponding to (endocardial) catheter electrode recordings¹² or electrical mapping.¹³

As an anecdotal illustration of the relevance of mathematical models to studying cardiac electrograms, Fig. 1.1 displays the result of a recreational problem of number theory, the so-called “EKG sequence,” showing some (really unexpected) similarities with electrograms recorded during AF.

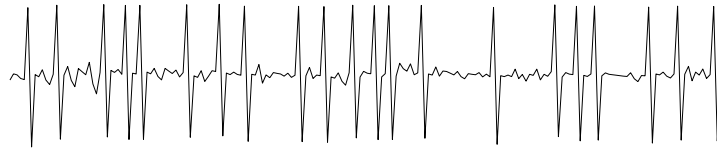


Figure 1.1 — The EKG sequence $\{a_n\}$ is defined by $a_1 = 1$, $a_2 = 2$ and, for $n \geq 3$, a_n is the smallest natural number not yet in the sequence with the property that $\gcd(a_n, a_{n-1}) > 1$, where \gcd stands for greatest common divisor (see Peterson¹⁴). For the sake of illustration, the detrended and normalized form $b_n = (1 + \frac{1}{3 \ln n}) - a_n/n$ is plotted for $100 \leq n \leq 300$.

Objectives

The objectives of the present study are:

- to develop a computer model of AF in which the mechanisms of AF initiation and maintenance can be identified and studied;
- to characterize the dynamics of simulated AF in terms of activation patterns, wavelength and spatiotemporal organization;
- to compute atrial electrograms during AF and study their time course and their morphology.

The ultimate goal of the project would be to help unlock the mechanisms underlying AF and propose new diagnostic tools and therapeutic strategies, keeping in mind that cardiology aims at treating diseases and curing patients.

1.2 Organization of the Dissertation

This dissertation is divided into four parts:

- I. **Modeling:** After a description of the methodology (chapter 2), a bottom-up approach for cardiac modeling is detailed, from cell models (chapter 3) to an atrial model (chapter 4).
- II. **Numerical Methods:** Spatial and temporal discretization schemes involved to solve the reaction-diffusion system representing electrical propagation in the heart are presented in chapters 5 and 6 respectively. Implementation, parameter settings and numerical accuracy are discussed in chapter 7.
- III. **Simulated Atrial Fibrillation:** Different mechanisms leading to initiation and maintenance of AF are isolated and investigated in chapters 8 and 9 respectively. The resulting dynamics are then analyzed in terms of activation patterns, spatial organization and wavelength (chapter 10).
- IV. **Electrogram Morphology:** Electrograms are studied to relate features of the signals to the underlying dynamics and tissue substrate. Chapter 11 concentrates on the effect of wavefront dynamics (wavefront shape and curvature, collisions, refractoriness, conduction blocks) on electrogram morphology. Chapter 12 describes the impact of changes in conduction properties (anisotropy and heterogeneity).

1.3 Original Contributions

This main contributions* of this work are:

- A reformulation of the finite volume method for handling triangular mesh of 3D-surface in the context of reaction-diffusion systems.
 - ▷ Inhomogeneous and anisotropic diffusion can be included.
 - ▷ The spatial discretization scheme was shown to be stable in the general case.
- A computer model of the atria able to simulate more than 20 seconds of AF.
 - ▷ The geometry was derived from magnetic resonance images.
 - ▷ Clinically relevant initiation protocols were used.
 - ▷ Simulated AF was shown to be inducible even in a *uniform* tissue.
 - ▷ Unsustained and sustained episodes of simulated AF were obtained by including the effect of remodeling.
 - ▷ Factors promoting initiation and perpetuation of simulated AF were studied.
 - ▷ Spatiotemporal organization of simulated AF was assessed.
- Analysis of the factors affecting unipolar electrogram morphology.
 - ▷ The effects of wavefront shape (curvature), wavelet dynamics (collisions, refractoriness, conduction blocks) and conduction properties (anisotropy, heterogeneity) were studied.
 - ▷ A mechanism for electrogram fractionation based on heterogeneity was investigated.

*See also the list of publications at the end of the text.

Part I

Modeling

The first part of this thesis presents the modeling aspects necessary for the construction of a computer model of atrial fibrillation. In the first chapter of this part, the basic concepts of cardiac electrophysiological models are introduced. The next chapter gives a mathematical description of the cardiac cell models based on the biophysics of ionic fluxes through the cell membrane. The last chapter of this part finally shows how to integrate a cell model and a model of electrical propagation into an anatomical model of the atria.

Modeling Heart Electrophysiology

The aim of this work is to use computer models to simulate the electrical activity of cardiac tissues. Models are simplification of the actual physical system and rely on our knowledge and our understanding of this system. We may try to integrate in the model all the scientific information currently available about heart electrophysiology. However, such a complex model would be difficult to study and to understand (possibly as difficult as animal experiments), and, in addition, could be computationally intractable. On the other hand, too simple models are likely to fail to reproduce basic phenomena. Therefore, the level of details which should be included in the model *depends on the questions* we want to investigate, following the principle of parsimony (“Things should be made as simple as possible, but not any simpler.” A. Einstein).

The questions investigated in this study concern initiation and maintenance of AF and analysis of atrial electrograms. The key elements for the construction of such a model are¹⁵⁻¹⁷:

- cell excitability,
- action potential shape,
- impulse propagation,
- restitution properties,
- atrial geometry.

This chapter describes the modeling requirements and electrophysiological phenomena we would like to reproduce in a mathematical model of atrial fibrillation (AF). The ingredients mentioned above will be separately discussed in the subsequent sections, with a special emphasis on modeling concepts. A detailed and mathematical presentation of the construction of a model of human atria will be given in the next two chapters.

2.1 Cell Excitability

Excitable Dynamical Systems

Cardiac cells are *excitable*. This means that, as a dynamical system, cardiac cells have the following properties,¹⁸ illustrated in Fig. 2.1:

1. There is a globally attracting steady state (rest state).

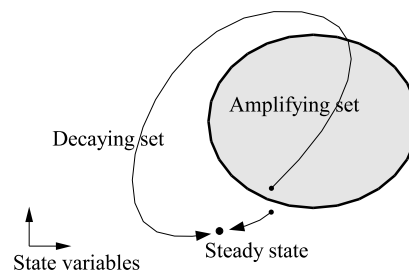


Figure 2.1 — Illustration of the properties of an excitable system.

- The state space can be partitioned into a *decaying set* and an *amplifying set*. The frontier between these sets is called the *threshold region*. Any evolution starting from a state in the decaying set returns to the steady state without significant growth in any of the state variables. In contrast, evolutions starting from the amplifying set can lead to large changes in one or more of the state variables before return to the steady state.

Thus, an impulsive perturbation of the steady state that leaves the state in the decaying set has little impact on the dynamics (*subthreshold response*). If the state is carried into the amplifying set, however, a long orbit eventually reaching the steady state will follow (*superthreshold response*).

Cardiac Cell Models

In cardiac cells, the steady state corresponds to resting conditions, and perturbations are applied by injecting current through the cell membrane (electrical stimulation). The cell response is then observed by measuring the membrane potential (difference in electric potential between the intracellular and the extracellular media). A subthreshold stimulation (Fig. 2.2, response A) does not lead to cell excitation. A superthreshold stimulation triggers an *action potential* (Fig. 2.2, response B) consisting of 5 phases: an upstroke phase where the membrane rapidly depolarizes (phase 0), an early repolarization (phase 1), a plateau (phase 2), a late repolarization (phase 3), and a final repolarization (phase 4).

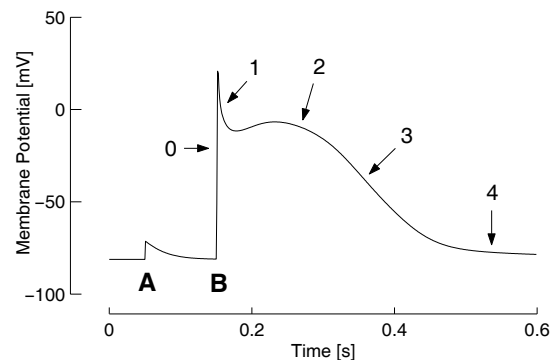


Figure 2.2 — Electrical response of a cardiac cell. (A) Subthreshold stimulation. (B) Superthreshold stimulation. The different phases of the resulting action potential are indicated by a number (from 0 to 4) and explained in the text.

phase characterized by a dome (phase 2), a late repolarization (phase 3), and finally the return to resting potential (phase 4). In atrial cells, phase 2 can be almost inexistent.

Cell excitability changes during the different phases of the action potential. Phases 1, 2 and most of phase 3 are characterized by the impossibility to generate new action potentials (*effective refractory period*). After this period, a sufficiently large stimulus can again initiate an action potential (*relative refractory period*).

If the state of a cell is described by the membrane potential V_m and by some other variables merged into a vector variable \mathbf{s} , the generic evolution equation is written as

$$\frac{dV_m}{dt} = f(V_m, \mathbf{s}) + f_{\text{ext}}(t) \quad (2.1)$$

$$\frac{d\mathbf{s}}{dt} = \mathbf{g}(V_m, \mathbf{s}) \quad (2.2)$$

where f and \mathbf{g} are phenomenological functions of state, and f_{ext} is an external driving force (e.g. representing a stimulation current). This equation expresses that the instantaneous variation (time derivative) of the state is a function of state, but does not make any hypothesis about the underlying processes.

Fig. 2.3 shows a typical example of voltage-dependence of the function f (computed here from a single cell simulation using the Beeler–Reuter model¹⁹). The shape of the curve is well represented by a cubic (dashed curve of Fig. 2.3) and characterizes the excitability property: if Eq. (2.2) is temporarily discarded in order to study the activation process separately, $V_m = -60$ mV becomes an unstable fixed point of the evolution equation (the slope at -60 mV is >0) and represents the threshold for cell activation.^{20–22}

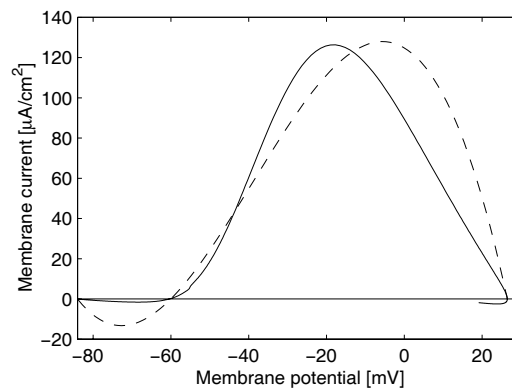


Figure 2.3 — Voltage-dependence of the function f , representing the membrane current as a function of the membrane potential during the upstroke phase of an action potential simulated using the Beeler–Reuter model.¹⁹ In addition, a cubic (dashed curve) is fitted to this curve.

The simplest models accounting for the excitability properties and the depolarization–repolarization cycle are two-variable models such as the FitzHugh–Nagumo model^{23–25} (this model uses a cubic for the function f) and some of its variations.^{22, 26, 27}

2.2 Shape of the Action Potential

Significant differences in repolarization dynamics are observed for the different cell types (e.g. ventricular and atrial cells, Purkinje fiber etc.). Since the maintenance of the AF

activity heavily involves repolarization dynamics,^{28–30} the study of initiation and perpetuation of AF requires an adequate reconstruction of the action potential. Moreover, membrane currents are the sources that will be used for computing atrial electrograms,³¹ and a correct description of the action potential shape is also necessary to account for the electrogram morphology observed during AF.

Variations of the membrane potential are actually caused by ionic fluxes through membrane channels, pumps and ion exchangers.³² The development of experimental techniques such as patch clamp methods³³ made it possible to study single channel ionic current and lead to quite accurate single channel models. The changes in membrane potential are then obtained by summing the contribution of all the channel currents (see next chapter for a detailed description). Inspired by the work of Hodgkin and Huxley³⁴ on the giant squid axon, numerous mathematical models of cardiac cells have been developed following this approach.

The simplest ionic-based models try to reproduce the basic ionic flows (Na^+ , K^+ and Ca^{2+} membrane currents). The Beeler–Reuter model,^{19,35–37} the Luo–Rudy model³⁸ (sometimes called Luo–Rudy phase I) of mammalian ventricular cells, the McAllister *et al.* model³⁹ belong to this class.

Later, a lot of effort was devoted to the construction of a second generation of cardiac cell models taking into account many specific ionic channels, variations in ionic concentrations and intracellular calcium dynamics (in relation to the sarcoplasmic reticulum). The Noble *et al.* model,⁴⁰ the DiFrancesco–Noble model^{41,42} of Purkinje fiber cells and the so-called dynamic Luo–Rudy model^{43,44} of guinea pig ventricular cell and its revised versions^{45–50} were the basis for many other models. Thanks to a large amount of available experimental data, such models could be constructed for various cell types (atrial and ventricular cells, Purkinje fiber, sino-atrial node) and species (human, guinea pig, rabbit, dog, etc.). Ventricular cell models are now available for dogs,^{51,52} guinea pigs,^{53,54} rats,⁵⁵ and human cells.⁵⁶ The research on atrial cells first focused on the sino-atrial node.^{57–68} More recently, models for human,^{69–71} canine^{72–74} and rabbit^{75–77} atrial cells and for human atrio-ventricular node⁷⁸ have been published. Fig. 2.4 displays the action potential shape for some of these models. These simulated action potentials are comparable to published measured monophasic action potentials.^{70,79}

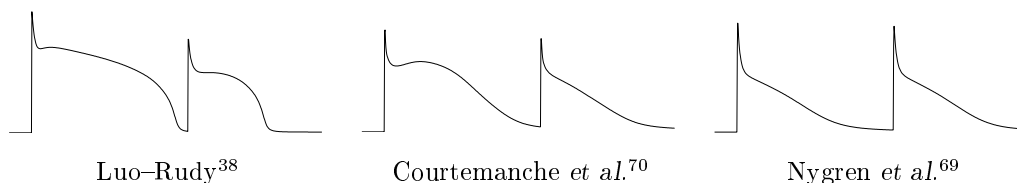


Figure 2.4 — Illustration of action potential shape simulated using the Luo–Rudy ventricular model, and the Courtemanche *et al.* and the Nygren *et al.* atrial models. Two stimuli, S_1 and S_2 , are applied to a single cell model with a S_1 – S_2 interval of 400 ms.

2.3 Impulse Propagation

An important property of cardiac tissue is the cell-to-cell propagation of membrane excitation.³¹ The cardiac cell geometry is similar to a cylinder 30–100 μm long and 8–20 μm wide.⁶ The intracellular media of neighboring cells are directly interconnected through gap junctions (see Fig. 2.5). When a superthreshold electrical stimulation applied to a cell triggers a fast inward flux of sodium (Fig. 2.5, step ①), the cell membrane depolarizes. The resulting voltage difference between the intracellular medium of the cell and that of its neighboring cells generates a current through the gap junctions (step ②). If the neighboring cell is not refractory, this cell-to-cell stimulation will be sufficient to induce a depolarization in this cell (step ③) and the excitation will propagate further (step ④).

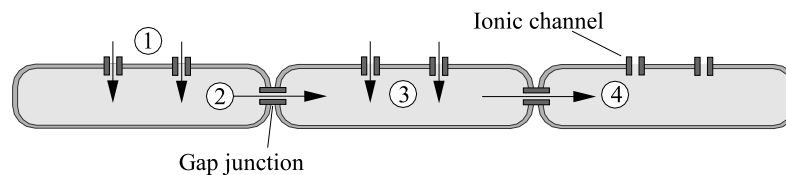


Figure 2.5 — Illustration of the propagation of the electrical impulse in the myocardium. See text for an explanation of the steps ① to ④.

The propagation of the electrical impulse therefore relies on a cell-to-cell diffusion process. *Non-linearity* in the cell dynamics and cell energy consumption are necessary to enable wave propagation without damping. Wave propagation in non-linear dissipative systems is common and arises for instance in burning processes²⁰ like flame propagation in a candle²¹ or like forest fire models.⁸⁰

The simplest model of impulse propagation in a cardiac fiber considers a homogenized tissue structure.^{6,20,31} Cell-to-cell coupling is present as a diffusion term in the partial differential equation describing electrical propagation in a fiber (x is the coordinate along the fiber)

$$\frac{\partial V_m}{\partial t} = D \frac{\partial^2 V_m}{\partial x^2} + f(V_m, \mathbf{s}) + f_{\text{ext}}(t) \quad (2.3)$$

where the diffusion coefficient D is associated with the conduction velocity of the resulting wave.^{20,81} This propagation equation can be generalized to two- and three-dimensional heterogeneous anisotropic tissue⁶ (see chapter 4).

2.4 Restitution Properties

The duration of the effective refractory period (ERP) is a crucial factor for the occurrence of re-entries and arrhythmias since the cells are not excitable during that period and prevent any electrical impulse from propagating further. Estimation of ERP requires to stimulate the cell several times with a different timing until the excitability threshold is found. This protocol is usually not well adapted for ERP estimation during a simulated arrhythmia. The *action potential duration* (APD) is often used instead because it is directly related to ERP⁸² and is easily computed from the membrane potential time-course. APD can be *defined* as the time interval between the upstroke and the 90% repolarization level,⁶ or,

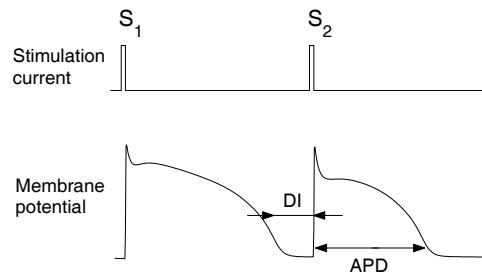


Figure 2.6 — S_1 - S_2 protocol for computing restitution curves. Diastolic interval (DI) and action potential duration (APD) are shown to illustrate the definition.

more simply, by the time the membrane potential remains above a given threshold, -60 mV for instance.⁸²

The APD depends on the preceding *diastolic interval* (DI), defined as the time interval between the end of the previous action potential and the upstroke of the current one (see Fig. 2.6). This dependence is described by the APD *restitution curve* revealed by applying a so-called S_1 - S_2 stimulation protocol (see Fig. 2.6). For the sake of illustration, a S_1 - S_2 protocol was applied at the extremity of a one-dimensional fiber of length 1.5 cm whose membrane kinetics was simulated using either the Luo-Rudy³⁸ or the Courtemanche model.⁷⁰ Fig. 2.7A-B displays the resulting ERP and APD as a function of the DI. The conduction velocity (CV) of the wavefront initiated by the S_2 stimulus is also affected by the preceding DI and is represented in Fig. 2.7C-D.

Restitution properties have an important impact on depolarization wave dynamics. It

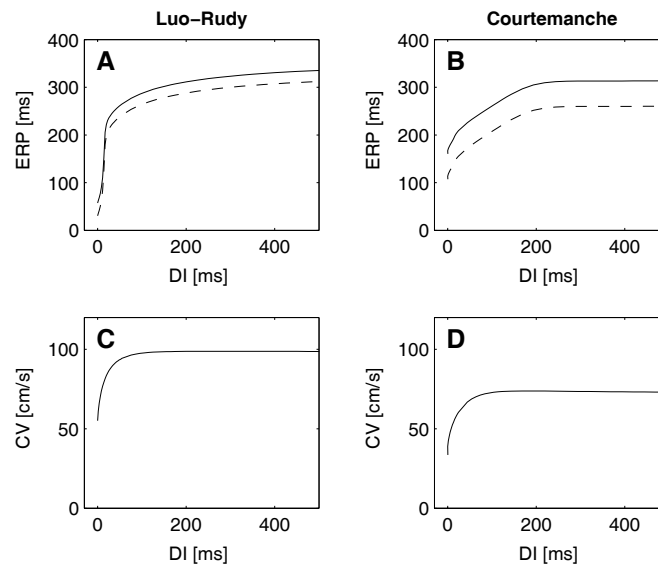


Figure 2.7 — Example of restitution curves computed on a 1D cable (length 1.5 cm, space step $150 \mu\text{m}$, resistivity $200 \Omega \text{ cm}$) using the Luo-Rudy (panels A and C) and the Courtemanche model (panels B and D). (A)-(B) ERP restitution curve (solid curve) obtained using an additional S_3 stimulation, and APD restitution curve (dashed curve) computed with a threshold at -60 mV. (C)-(D) Conduction velocity (CV) restitution curves.

has been shown that the stability of re-entries and spiral/scroll waves depends on APD restitution.^{28–30} For instance, the analysis of the conditions promoting APD alternans^{83–85} demonstrated the influence of the steepness of the APD restitution curve.^{86–89} Based on a systematic study of the relations between APD restitution and the resulting electrical activity, different dynamical regimes or spiral phenotypes (stable spirals, quasiperiodic meandering spirals, chaotic hypermeandering spirals, spiral breakups) and routes from simple toward complex dynamics were exhibited.^{84,90–92} The relevance of these results for drug development has been assessed.^{90,93–95}

Since APD restitution curves have been experimentally measured in the ventricles⁹⁶ and in the atria,⁷⁹ cardiac cell models can be adjusted to a particular clinical condition, experimental setup, or dynamical regime. When investigating questions dominated by the effect of restitution, the formulation of the cell kinetics can even be simplified, while keeping the restitution properties intact, leading to reduced models.^{28,97,98}

2.5 Atrial Geometry

From the anatomical viewpoint, the atria are complex structures including non-propagating regions due to blood vessels and valves. Fig. 2.8 shows a representation of human atria constructed from segmented magnetic resonance images of a normal human subject. This figure highlights the anatomical structures behaving like obstacles (or like holes) for cardiac impulse propagation.

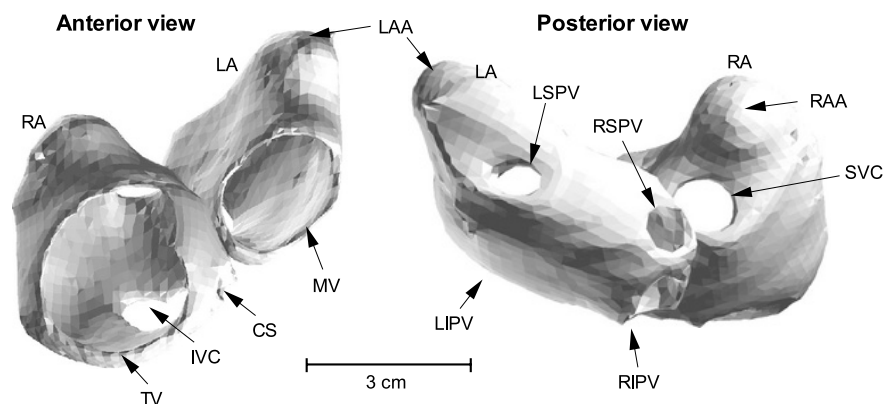


Figure 2.8 — Geometry of human atria constructed from MR images: anterior view (on the left) and posterior view (on the right). The left/right atrium appendages are indicated by LAA/RAA. Anatomical obstacles are shown: tricuspid valve (TV), mitral valve (MV), inferior vena cava (IVC), superior vena cava (SVC), left/right superior pulmonary vein (LSPV/RSPV), left/right inferior pulmonary vein (LIPV/RIPV), and coronary sinus (CS). In this display, the valves are too large here as a result of the difficulty to segment the region in contact with the ventricles.

Several models of electrical propagation in the atria have been recently developed.^{7–9,99,100} They differ in the accuracy of the representation of electrophysiological and anatomical details. This helped demonstrate that the topology and the geometry play an crucial role in the occurrence of (anatomical) reentries and atrial arrhythmias, confirming the results based on simpler geometries including holes.^{101,102}

The atria are thin-walled. Unlike the ventricles, where transmural effects (intramural

re-entries, scroll waves, *etc.*) are present during ventricular fibrillation,^{28, 103–105} considering the atria as a monolayer surface folded on a 3D structure seems to be a reasonable assumption,^{81, 100} at least as a first approximation. This hypothesis underlies several published atrial models^{8, 9, 99} and will be assumed throughout this work. On the other hand, anatomical structures such as Bachmann’s bundle, pectinate muscle and crista terminalis have been shown to have an impact on the activation sequence.⁷ Even a small thickness may also affect the electrogram time-course. The limitations due to the effect of 3D structures will therefore be discussed.

2.6 Conclusion

This chapter briefly overviewed the major elements which will have to be included in a computer model of atrial fibrillation. It appeared that a *bottom-up* modeling approach was adequate for such a complex dynamical system. According to this approach (see Fig. 2.9), the modeling process starts at the microscopic scale with membrane models. Cell models are then integrated into a tissue structure to eventually reconstruct heart geometry.

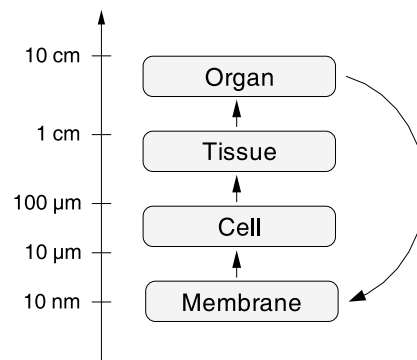


Figure 2.9 — Schematic representation of the *bottom-up* approach for cardiac modeling, with an order of magnitude of the corresponding spatial scale. The curved arrow represents a *top-down* adjustment of the membrane parameters.

Considerations about restitution properties finally highlighted the interest of a complementary *top-down* modeling in which membrane parameters are adjusted in order to reproduce observed macroscopic dynamics.

A bottom-up construction of a model of human atria is presented in detail in the next two chapters.

From Ion Electrodifusion to Cell Models

Cardiac electrophysiological modeling is generally performed by following a bottom-up approach. The procedure starts at the *molecular level*, where channel gating kinetics is modeled. Ionic currents, pumps and ion exchangers are then integrated into a model of membrane (*membrane level*). The contribution of each ionic current is summed up, and its effect on ionic concentration is taken into account (*cell level*). Afterwards, the cells are coupled in order to form a tissue (*tissue level*). Tissue structure is constructed to reproduce the cardiac anatomy (*organ level*). Finally experimental setups (e.g. electrical mapping) are simulated in the model (*experimentalist's level*).

This chapter explains the development of single cell electrophysiological models based on a biophysical model of their constitutive elements (ionic channels, pumps, ion buffers, *etc.*). The construction of a computer model of anatomical structures like the atria is the topic of the next chapter. The approach taken here gives an emphasis on the concepts, methods and mathematical formulations common to most of the published models rather than on the characteristics and physiological relevance specific to each model. As a result, the text will concentrate on the description of the models, and less on a detailed presentation of

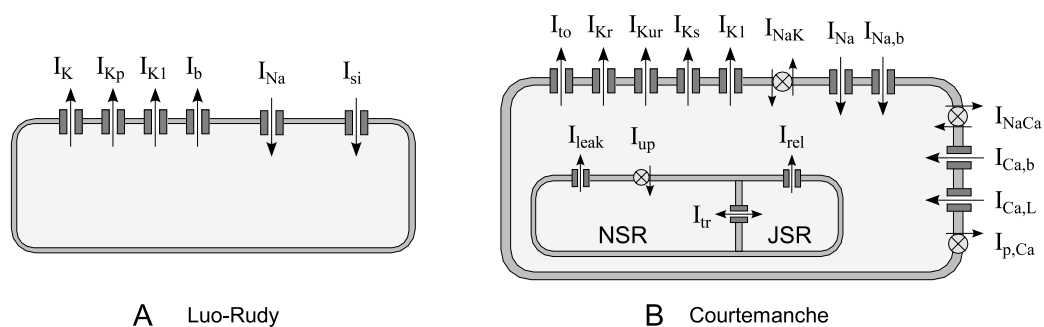


Figure 3.1 — Schematic representation of the Luo–Rudy ventricular cell model and Courtemanche et al. human atrial model. (A) The Luo–Rudy model includes 6 membrane currents listed in Table 3.1. (B) The Courtemanche et al. model includes 16 membrane currents, listed in Table 3.2, a fluid compartment model composed of the intracellular and extracellular media, and a sarcoplasmic reticulum (SR) subdivided into the network SR (NSR) and the junctional SR (JSR).

Symbol	Current	Direction
<i>Sodium channel</i>		
I_{Na}	fast inward Na^+ current	$E \rightarrow I$
<i>Potassium channels</i>		
I_{K1}	time-independent outward K^+ current	$I \rightarrow E$
I_b	time-independent outward background K^+ current	$I \rightarrow E$
I_{Kp}	time-independent outward plateau K^+ current	$I \rightarrow E$
I_K	time-dependent outward K^+ current	$I \rightarrow E$
<i>“Calcium” channel^a</i>		
I_{si}	slow inward current	$E \rightarrow I$

^a Actually, I_{si} is a generic slow inward current driven by the gradient of calcium electrochemical potential.

Table 3.1 — Ionic currents defined in the Luo–Rudy phase I model. In the column “Direction”, E stands for extracellular space and I for intracellular space, e.g. $E \rightarrow I$ means for inward current.

Symbol	Current	Direction
<i>Sodium channels</i>		
I_{Na}	fast inward Na^+ current	$E \rightarrow I$
$I_{Na,b}$	background Na^+ current	$E \rightarrow I$
<i>Potassium channels</i>		
I_{to}	transient outward K^+ current	$I \rightarrow E$
I_{Kr}	rapid delayed rectifier K^+ current	$I \rightarrow E$
I_{Kur}	ultrarapid delayed rectifier K^+ current	$I \rightarrow E$
I_{Ks}	slow delayed rectifier K^+ current	$I \rightarrow E$
I_{K1}	inward rectifier K^+ current	$E \rightarrow I$
<i>Calcium channels</i>		
$I_{Ca,L}$	L-type inward Ca^{2+} current	$E \rightarrow I$
$I_{Ca,b}$	background Ca^{2+} current	$E \rightarrow I$
<i>Pumps</i>		
$I_{p,Ca}$	sarcolemmal Ca^{2+} pump current	$I \rightarrow E$
I_{NaK}	$Na^+ - K^+$ pump current	$I \rightarrow E$
<i>Ion exchanger</i>		
I_{NaCa}	Na^+ / Ca^{2+} exchanger current	$E \rightarrow I$
<i>Sarcoplasmic reticulum fluxes</i>		
I_{leak}	Ca^{2+} leak current	$NSR \rightarrow I$
I_{up}	Ca^{2+} uptake current	$I \rightarrow NSR$
I_{tr}	Ca^{2+} transfer current	$NSR \rightarrow JSR$
I_{rel}	Ca^{2+} release current	$JSR \rightarrow I$

Table 3.2 — Ionic currents defined in the Courtemanche et al. model. The column “Direction” indicates the origin and the destination of the flux. Abbreviation of compartment names: E stands for extracellular space, I for intracellular space, NSR for network sarcoplasmic reticulum and JSR for junctional sarcoplasmic reticulum.

the underlying physiological phenomena or topics such as structure and characterization of membrane channels, which can be found in reference textbooks (Hille,³² Stein,¹⁰⁶ and

DeFelice³³) and in review articles (Catterall,^{107,108} Yellen,¹⁰⁹ Roden¹¹⁰ and Sabah^{111–114}).

The step-by-step description of the typical equation set included in electrophysiological models will be illustrated by a presentation of the Luo–Rudy (phase I) ventricular cell model³⁸ and Courtemanche *et al.* human atrial model,⁷⁰ as well as, in some instances, other models. The former model includes 6 membrane currents and one time-dependent ionic concentration (8 variables in total, that is, 8 differential equations), while the latter, more detailed, takes into account 16 membrane currents, 5 time-dependent ionic concentrations and a two-compartment model of sarcoplasmic reticulum (21 variables in total). In order to give a brief overview of the components included in those cardiac cell models, Fig. 3.1 displays a schematic representation of currents and fluxes. Their membrane currents are listed in Table 3.1 and 3.2.

3.1 Molecular Level : Kinetics

The processes taking place in cell membranes are generally induced by macromolecule (e.g. proteins) dynamics. Their kinetics is of critical importance for membrane current modeling. This section presents the tools used as a starting point for building complex chemical kinetic models, in particular formulae for reaction rates.

3.1.1 Chemical Kinetics and Markov Models

Signals representing current flow through a single channel of a membrane are apparently randomly fluctuating.³² Typically, random transitions between a few discrete levels are observed. Statistical signal processing provides appropriate tools for modeling those signals, in particular (continuous-time) hidden Markov models.¹¹⁵

Let us assume that the value of a signal $I(t)$ (e.g. a single channel current) depends on an internal “hidden” state. To each possible (discrete) state s_i , $i = 1, \dots, n$, is associated a value I_i for the signal. Usually, $I_i = 0$ for some “closed” or “deactivated” states and $I_i = I_{\max}$ for the other “open” states. The evolution of the internal state is supposed to be a Markov random process, so that the probability $p(s_i, t)$ for the system to be in state s_i at time t satisfies

$$\frac{d}{dt}p(s_i, t) = \sum_{j=1}^n k_{j \rightarrow i} p(s_j, t) - p(s_i, t) \sum_{j=1}^n k_{i \rightarrow j} \quad (3.1)$$

where $k_{i \rightarrow j}$ is the transition rate (probability of transition per unit time) from state s_i to state s_j . The first term represents an evolution *toward* state s_i and the second one transitions *from* the state s_i . The *ensemble-averaged* value of the signal reads

$$\langle I(t) \rangle = \sum_{i=1}^n p(s_i, t) I_i \quad (3.2)$$

and is compared to the corresponding experimental averaged signals. This parametric statistical model is defined by the number n of states, the signal values I_i and by the transition rates $k_{i \rightarrow j}$. The number of states is chosen as small as possible by considering the following remark: a n -state system is characterized by $n - 1$ independent relaxation times.³² Parameter estimation can be performed by Bayesian estimation from a set of experimental data.¹¹⁶

In the case of reactions arising in cell membrane, the transition rates may depend on the membrane potential or on the presence of drugs or inactivators.

In addition to signal modeling considerations, a physical interpretation is possible. In the language of statistical physics, the states s_i are microscopic configurations, the set of all p_i 's define the macroscopic state, $I(t)$ is an observable, and Eq. (3.1) is called the *master equation* and describes the relaxation toward thermodynamic equilibrium. The *detailed balance* equation¹¹⁷⁻¹¹⁹ relates the forward and backward rates

$$\frac{k_{i \rightarrow j}}{k_{j \rightarrow i}} = \exp\left(-\frac{G_j - G_i}{RT}\right) \quad (3.3)$$

where G_i is the free energy per mole of the state s_i , R the universal gaz constant and T the temperature, reflects the microscopic reversibility of the underlying processes.

Despite some studies on chaotic deterministic channels¹²⁰ and stochastic fractal channels,^{121,122} the vast majority of the published membrane kinetic models uses Markov models.^{38,43,52,53,69,70,123,124}

3.1.2 Reaction Rates

Once the different states are identified, transition rates have to be determined. Their voltage dependence is of particular relevance for membrane kinetics. This subsection gives some arguments to justify the fitting formulae found in the literature.

Transition-state theory

In 1935, the chemists H. Eyring, M. G. Evans and M. Polanyi proposed a theory of reaction rates now referred to as *conventional transition-state theory*.¹²⁵⁻¹²⁷ For an elementary* reaction $A + B \rightarrow C$, they assumed the existence of an activated complex C^\ddagger associated with an energy barrier such that the reaction mechanism is $A + B \rightleftharpoons C^\ddagger \rightarrow C$, where $A + B \rightleftharpoons C^\ddagger$ is at chemical (quasi)equilibrium and $C^\ddagger \rightarrow C$ is described by a classical motion over an energy barrier (see Laidler¹²⁷ for more details about the hypotheses and the methods). Under these hypotheses, the absolute reaction rate k was calculated using a semi-classical statistical mechanical approach and lead to *Eyring's formula*

$$k = \kappa \frac{k_B T}{2\pi\hbar} \exp\left(-\frac{\Delta G^\ddagger}{RT}\right) \quad (3.4)$$

where ΔG^\ddagger is the Gibbs free energy of activation, k_B the Boltzmann constant, \hbar the reduced Planck constant and κ is called the transmission coefficient, often equal to 1. Notice that the form of Eq. (3.4) is compatible with the general constraint imposed by the detailed balance relation (3.3).

In presence of an electric field, $\Delta G^\ddagger = \Delta G_0^\ddagger + zF\Delta\phi^\ddagger$ where z represents the electric charge participating to the reaction, $\Delta\phi^\ddagger$ is the difference of electric potential between the initial condition and the region of the energy barrier, and F is the Faraday constant. When the reaction takes place in a cell membrane, the potential $\Delta\phi^\ddagger$ is assumed to be a fraction η of the membrane potential V_m , that is, $\Delta\phi^\ddagger = \eta V_m$. The dimensionless parameter η , the

*An *elementary reaction* is a reaction that occurs in a single step, with no experimentally detectable reaction intermediates.¹²⁷

electrical distance, is related to the position of the energy barriers. The voltage dependence of reaction rates of elementary reactions in membranes now appears to be

$$k(V_m) = k_0 \exp\left(-\eta \frac{zFV_m}{RT}\right) \quad (3.5)$$

where k_0 is a voltage-independent constant. This relation explains the presence of numerous exponentials of V_m in the equations of models describing membrane kinetics (see for instance Luo–Rudy⁴³ or Courtemanche *et al.*⁷⁰).

Composite Reactions

The mono-exponential form for the voltage dependence of the reaction rates holds only for elementary reactions. More complex kinetics are observed during composite reactions. In this paragraph, two simple examples of possible mechanisms for the reaction $A \rightleftharpoons B$ are briefly examined:

- *Competition between two routes for the transition* (e.g. two different pathways for a membrane protein folding). If the forward and backward reaction rates are k_i and k_{-i} for the routes $i = 1, 2$, the reaction kinetics is now governed by a linear combination of rates¹¹⁹

$$\frac{d[A]}{dt} = (p_1 k_{-1} + p_2 k_{-2}) [B] - (p_1 k_1 + p_2 k_2) [A] \quad (3.6)$$

where p_i , the probability of the route i , is related to the difference ΔG_b between the activation free energies of the routes by¹¹⁹

$$p_1 = \frac{1}{1 + \exp(-\Delta G_b/RT)} \quad \text{and} \quad p_2 = 1 - p_1 \quad (3.7)$$

so that the route with the lowest activation energy will be more frequently chosen.

- *Transition through an intermediate step*. The process $A \rightleftharpoons I^* \rightleftharpoons B$, with reaction rates k_1 and k_{-1} (resp. k_2 and k_{-2}) associated with $A \rightleftharpoons I^*$, (resp. $I^* \rightleftharpoons B$), obeys in the steady-state regime ($[I^*] = \text{const.}$) the equation¹²⁷

$$\frac{d[A]}{dt} = \frac{k_{-1}k_{-2}}{k_{-1} + k_2} [B] - \frac{k_1k_2}{k_{-1} + k_2} [A] \quad (3.8)$$

In both cases, if the elementary reaction rates k_i are written as exponential function of the voltage, the reaction rates of $A \rightleftharpoons B$ have a voltage dependence expressed as a rational function of exponentials. Most models use this kind of voltage dependence for the transition rates arising in channel gating kinetics (see for instance Luo–Rudy⁴³ or Courtemanche *et al.*⁷⁰). Gating kinetics will be considered in subsection 3.2.2 and some explicit examples will be given.

3.2 Membrane Level : Channels, Pumps and Exchangers

The electrical activity of excitable cells is the consequence of ion fluxes through the cell membrane. This section describes how mathematical models of ionic channels, pumps and ion exchangers are derived. A membrane model, and later a cell model, will be built by combining those elementary components.

3.2.1 Ionic Channels

Ionic channels are the elementary excitable elements of the cardiac cell, capable of producing or transducing ionic fluxes through the cell membrane.³² The structure of a channel is modeled by a sequence of independent elements, each one associated with a specific function:

1. a *selectivity filter*: only a restricted set of ion types (in most models, a single type) is allowed to go through the channel;
2. an *aqueous pore*, whose properties are summarized by an intrinsic voltage-current relation $I_{\text{pore}}(V_m)$;
3. a *gate* that randomly opens and closes: a statistical signal modeling of the probability of opening (using the tools of section 3.1) is used to account for these stochastic fluctuations similar to a “random telegraph” signal;¹¹⁷
4. possibly *receptors* for channel inactivation (e.g. drug-receptors or calcium-induced inactivation mechanism).

The single-channel electric current I_{channel} is equal to $I_{\text{pore}}(V_m)$ if the channel is neither closed nor inactivated, and zero otherwise. The *ensemble-averaged* single-channel electric current $\langle I_{\text{channel}} \rangle$ is therefore given by

$$\langle I_{\text{channel}} \rangle = \text{Prob}\{\text{Open}\} \cdot \text{Prob}\{\text{Not inactivated}\} \cdot I_{\text{pore}}(V_m) \quad (3.9)$$

provided that inactivation is independent from the gating process. The usually large number of membrane channels (order of magnitude 10^2 – 10^3 channels per μm^2 are not uncommon, although it strongly depends on cell and channel type³²) allows the use of the *law of large numbers*¹¹⁸ to calculate the membrane ionic current I_{membr} generated by the given channel from the ensemble-averaged single-channel current³³

$$I_{\text{membr}} = \#\{\text{Channels}\} \cdot \langle I_{\text{channel}} \rangle \quad (3.10)$$

where $\#\{\text{Channels}\}$ is the number of channels on the cell membrane. Each factor of Eq. (3.9) will be studied separately in the following subsections.

3.2.2 Gating Kinetics

A gate can be either open or closed/inactivated. The probability for the gate to be open is usually modeled using a Markov model, as described in section 3.1. There may be several closed or inactivated states,^{123,124,128} while most models include only one open state. The simplest case with a single closed state will be presented first in this subsection, and then it will be shown how those models are combined to build more complex models.

Two-State Model

The simplest gate y can be either in the open (O) or the closed (C) state.³² If the forward (resp. backward) rate of the reaction $C \rightleftharpoons O$ is denoted by α_y (resp. β_y), Eq. (3.1) leads to the following equation for the fraction $y(t)$ of open gates at time t

$$\frac{dy}{dt} = \alpha_y(1 - y) - \beta_y y = \frac{y_\infty - y}{\tau_y} \quad (3.11)$$

where

$$\tau_y = \frac{1}{\alpha_y + \beta_y} \quad \text{and} \quad y_\infty = \frac{1}{1 + \beta_y/\alpha_y} . \quad (3.12)$$

A variable satisfying Eq. (3.11) will be called a *gating variable*.

At equilibrium, the ratio of the probability y_∞ for the channel to be in the open state and the probability $1 - y_\infty$ for the channel to be in the closed state is given by the Boltzmann distribution¹¹⁸

$$\frac{y_\infty}{1 - y_\infty} = \exp\left(\frac{\Delta G_y}{RT}\right) . \quad (3.13)$$

The quantity ΔG_y denotes the free energy difference between the open and closed state and can be expressed as $\Delta G_y = \Delta G_y^0 + z_y F V_m$. The first term ΔG_y^0 is due to the conformation energy and entropy changes while the second term $z_y F V_m$ is associated with the redistribution of charge during the transition.¹¹⁹ The voltage dependence of y_∞ finally reads

$$y_\infty(V_m) = \frac{1}{1 + \lambda_y \exp(-b_y V_m)} \quad (3.14)$$

where $\lambda_y = \exp(-\Delta G_y^0/RT)$ and $b_y = z_y F/RT$. The rates α_y and β_y , and therefore the relaxation time τ_y , can be modeled by one of the formulae suggested by subsection 3.1.2.

EXAMPLE: The Courtemanche *et al.* model⁷⁰ includes 12 voltage-dependent gating variables. Nine of them, namely o_a , o_i , u_a , u_i , x_r , x_s , d , f and w , have a steady-state value given by Eq. (3.14). The three remaining gating variables (m , h and j), associated with the fast inward sodium channel I_{Na} , have a more complex voltage dependence identical to the Luo–Rudy phase I model.³⁸ In particular, the transient outward K^+ current I_{to} depends on two gating variables o_a and o_i (the index a stands for activation and i for inactivation), whose kinetics is determined by the steady-state values $o_{a,\infty}$ and $o_{i,\infty}$, and the relaxation times τ_{o_a} and τ_{o_i} :

$$o_{a,\infty} = \left[1 + \exp\left(-\frac{V_m + 20.47}{17.54}\right)\right]^{-1} \quad (3.15)$$

$$\tau_{o_a} = \frac{1}{K_{Q_{10}}(\alpha_{o_a} + \beta_{o_a})} \quad (3.16)$$

$$\alpha_{o_a} = 0.65 \left[\exp\left(-\frac{V_m + 10}{8.5}\right) + \exp\left(-\frac{V_m - 30}{59}\right) \right]^{-1} \quad (3.17)$$

$$\beta_{o_a} = 0.65 \left[2.5 + \exp\left(\frac{V_m + 82}{17}\right) \right]^{-1} \quad (3.18)$$

$$o_{i,\infty} = \left[1 + \exp\left(\frac{V_m + 43.1}{5.3}\right)\right]^{-1} \quad (3.19)$$

$$\tau_{o_i} = \frac{1}{K_{Q_{10}}(\alpha_{o_i} + \beta_{o_i})} \quad (3.20)$$

$$\alpha_{o_i} = \left[18.53 + \exp\left(\frac{V_m + 113.7}{10.95}\right)\right]^{-1} \quad (3.21)$$

$$\beta_{o_i} = \left[35.56 + \exp\left(-\frac{V_m + 1.26}{7.44}\right)\right]^{-1} \quad (3.22)$$

where $K_{Q_{10}}$, a temperature scaling factor, is equal to 3. Fig. 3.2 displays these curves as a function of the membrane potential V_m .

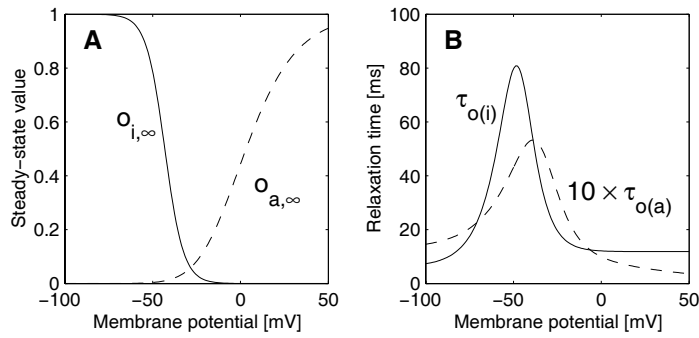


Figure 3.2 — Representation of the parameters describing the gating kinetics of the transient outward K^+ current in the Courtemanche et al. model. (A) Steady-state curves, and (B) relaxation times for the gating variables o_i (solid curves) and o_a (dashed curves).

Gate Models Combined in Series

Let us combine in series two statistically independent gates y_1 and y_2 following the first-order kinetics (3.11). The resulting gate is open if and only if both y_1 and y_2 are open. The probability for the gate to be open is thus $y_1 \cdot y_2$. The combined gate has 3 relaxation times τ_{y_1} , τ_{y_2} and $\tau_{y_1}\tau_{y_2}/(\tau_{y_1} + \tau_{y_2})$, but only two are independent.³² Combination of gates in series enables the construction of complex gating models with many different relaxation times, while keeping the number of independent parameters moderate.

In the particular case where n independent identical gates y are combined in series, the number of states can be reduced from 2^n to $n + 1$. Since only the number of open gates matters, the states are redefined as the number of open gates (from 0 to n). Then, if a gate is open with probability y , the combined gate is open with probability y^n .

EXAMPLE 1: The Hodgkin–Huxley model³⁴ of a giant squid axon includes 3 currents: a sodium current I_{Na} , a potassium current I_K , and a leakage current I_L . The gate of I_{Na} is of the form n^4 where n is a gating variable (two-state gate). The diagram of the kinetic states reads

$$n_0 \rightleftharpoons n_1 \rightleftharpoons n_2 \rightleftharpoons n_3 \rightleftharpoons \boxed{n_4}$$

The state n_k means that k gates out of 4 are open. The box indicates an open state. The kinetics of the K^+ channel depends on two gating variables m and h with a m^3h kinetics. The diagram of the kinetic states is now

$$\begin{array}{ccccccc} m_0h_0 & \rightleftharpoons & m_1h_0 & \rightleftharpoons & m_2h_0 & \rightleftharpoons & m_3h_0 \\ \Downarrow & & \Downarrow & & \Downarrow & & \Downarrow \\ m_0h_1 & \rightleftharpoons & m_1h_1 & \rightleftharpoons & m_2h_1 & \rightleftharpoons & \boxed{m_3h_1} \end{array}$$

When $h = 0$, the channel is inactivated. Finally, the leakage current I_L has no gate.

EXAMPLE 2: The Luo–Rudy phase I model³⁸ includes 6 gating variables, namely m , h , j , x , d , f , and 2 additional gates at steady-state, x_i and k_1 . The current I_{Na} has a gate kinetics m^3hj , I_K has a kinetics xx_i , and I_{si} has a gate kinetics df . The currents I_{K1} , I_{Kp} , and I_b are time-independent, i.e. have no gating kinetics (just possibly a gate at steady state like I_{K1}).

EXAMPLE 3: The Courtemanche *et al.* model⁷⁰ includes 15 gating variables: $m, h, j, o_a, o_i, u_a, u_i, x_r, x_s, d, f, f_{Ca}, u, v$ and w . The current I_{Na} has a gate kinetics m^3hj , I_{to} a kinetics $o_a^3o_i$, I_{Kur} a kinetics $u_a^3u_i$, I_{Kr} a kinetics x_r , I_{Ks} a kinetics x_s^2 , and $I_{Ca,L}$ has a kinetics $df f_{Ca}$. The transition rates of the gating variables are rational functions of exponentials of the membrane potential as described in subsection 3.1.2 (see the original paper⁷⁰ for the complete set of equations). An exception is the calcium-induced inactivation factor f_{Ca} of the L-type Ca^{2+} current which depends on the intracellular calcium concentration. In the membrane of the sarcoplasmic reticulum, the current I_{rel} has a gating kinetics u^2vw .

3.2.3 Pore Conductance

This subsection explains the derivation of most of the popular channel current-voltage relationships, including Ohm's law, classical electrodiffusion and barrier models.

Reversal Potential

At equilibrium, the membrane potential is negative inside the cell, because the intra- and extracellular media contain different concentrations of each ion. Collective ionic movement is driven by gradients of electrochemical potential, combining the effects of both electric field and thermic diffusion. For a dilute solution of the chemical species S of valence z_S , the electrochemical potential reads (see Callen¹²⁹)

$$\mu_S(T, [S], \phi) = \mu_S^0(T) + RT \ln[S] + z_S F \phi \quad (3.23)$$

where T is the temperature, ϕ the electric potential, and $\mu_S^0(T)$ an intrinsic chemical potential, so that the equilibrium condition $\mu_S(T, [S]_o, \phi_o) = \mu_S(T, [S]_i, \phi_i)$ between the intracellular (index i) and extracellular (index o) medium becomes

$$\phi_i - \phi_o = \frac{RT}{z_S F} \ln \frac{[S]_o}{[S]_i} = E_S \quad (3.24)$$

The potential E_S associated with the ion S is known as the *Nernst potential*. When $V_m = E_S$, the current through a pore perfectly selective to ion S is zero, because the electrochemical potential of the ion S is the same inside and outside the cell. This potential at which the current vanishes is called *reversal potential*.

EXAMPLE: In the Courtemanche *et al.* model,⁷⁰ the reversal potentials of the Na^+ , K^+ and Ca^{2+} membrane currents are respectively given by

$$E_{Na} = \frac{RT}{F} \ln \frac{[Na]_o}{[Na]_i} \quad , \quad E_K = \frac{RT}{F} \ln \frac{[K]_o}{[K]_i} \quad \text{and} \quad E_{Ca} = \frac{RT}{2F} \ln \frac{[Ca]_o}{[Ca]_i} \quad (3.25)$$

An exception is the reversal potential of the L-type calcium current $I_{Ca,L}$, whose dependence in calcium concentration is neglected. An experimentally-measured fixed value, 65 mV, is used instead of formula (3.24).

The case of pore permeable to several ions is much more difficult because it belongs to the class of equilibrium problems that cannot be solved using only equilibrium theory.¹²⁹ Electrochemical transport has to be considered (see below the Goldman–Hodgkin–Katz voltage equation).

Ohm's Law

Since the current through the pore vanishes at reversal potential E_{rev} , the simplest phenomenological current-voltage relation linearly depends on the deviation from the equilibrium value (*Ohm's law*)

$$I_S = g_S(V_m - E_{\text{rev}}) \quad (3.26)$$

The parameter g_S is the pore conductance. Because of its simplicity, this relation is commonly used in ionic channel models.

EXAMPLE: The currents I_{Na} , I_b , and I_{si} of the Luo–Rudy phase I model³⁸ verifies an Ohm's law. In the Courtemanche *et al.* model,⁷⁰ the membrane currents I_{Na} , $I_{\text{b,Na}}$, I_{to} , I_{Ks} , $I_{\text{Ca,L}}$, $I_{\text{b,Ca}}$ are based on Ohm's law.

Nernst–Planck Electrodiffusion

Classical electrodiffusion theory states that the ionic flux density J_S of a substance S follows the gradient of electrochemical potential, according to the *Nernst–Planck equation* coming from Eq. (3.23)

$$J_S = -L_S [S] \nabla \mu_S = -L_S RT \left(\nabla [S] + \frac{z_S F [S]}{RT} \nabla \phi \right) \quad (3.27)$$

where L_S is a coupling constant*. The expression $L_S RT$ is shown to be equal to the diffusion coefficient D_S by comparison with Fick's law of diffusion $J_S = -D_S \nabla [S]$ valid in absence of electric field. The electrical current density is then calculated using the relation $I_S = z_S F J_S$.

Goldman–Hodgkin–Katz Equations

Between 1943 and 1949, Goldman, Hodgkin and Katz developed a formalism for describing membrane selectivity and permeability based on classical electrodiffusion. They assumed that ions cross independently an homogeneous pore where a constant electric field is present. Under these hypotheses, the Nernst–Planck equation (3.27) is integrated over the membrane thickness to give the electrodiffusion current generated by an ion S through a pore (*Goldman–Hodgkin–Katz current equation*)³²

$$I_S = P_S z_S^2 \frac{F^2 V_m}{RT} \frac{[S]_i^* - [S]_o^* \exp(-z_S F V_m / RT)}{1 - \exp(-z_S F V_m / RT)}. \quad (3.28)$$

The membrane permeability $P_S = D_S / \ell$ is the diffusion coefficient D_S divided by the membrane thickness ℓ . The concentration $[S]_i^*$ (resp. $[S]_o^*$) is the concentration of S just at the entrance (resp. at the exit) of the pore and is generally written as $[S]_i^* = \gamma_i [S]_i$ (resp. $[S]_o^* = \gamma_o [S]_o$) where γ_i (resp. γ_o) is the partition coefficient, often set to 1. The resulting current-voltage curve is non-linear and accounts for the rectification observed experimentally.¹¹² A similar theory was developed for Mott transition in semiconductors.¹³⁰

EXAMPLE: Eq. (3.28) is used for instance in the dynamic Luo–Rudy model⁴³ for the L-type calcium current $I_{\text{Ca,L}}$.

*The factor $[S]$ has to be included since J_S is a flux per unit volume while μ_S is a Gibbs free energy per mole (see Callen¹²⁹).

In a pore permeable to several ions, the total electric current is the sum of the separate contributions of each ion (*independence hypothesis*). The reversal potential of that pore is obtained by setting this sum to zero. For the monovalent ions Na^+ , K^+ and Cl^- with partition coefficients set to 1, the reversal potential is given by the *Goldman-Hodgkin-Katz voltage equation*³²

$$E_{\text{rev}} = \frac{RT}{F} \ln \frac{P_{\text{Na}} [\text{Na}^+]_o + P_{\text{K}} [\text{K}^+]_o + P_{\text{Cl}} [\text{Cl}^-]_i}{P_{\text{Na}} [\text{Na}^+]_i + P_{\text{K}} [\text{K}^+]_i + P_{\text{Cl}} [\text{Cl}^-]_o} . \quad (3.29)$$

Note that only ratios of permeabilities are needed.

EXAMPLE: The Luo-Rudy phase I model³⁸ uses this formulation for the reversal potential associated with the time-dependent outward K^+ current I_K , in order to take into account the permeability to the Na^+ ions. The dynamic Luo-Rudy^{43,44} adds a non-specific current I_{ns} permeable to both Na^+ and K^+ . The chlorine is, however, discarded in both cases.

Energy Barrier Models

Energy barrier models suppose that the pore has one or several internal binding sites. An ion has to successively bind to them before getting out of the pore. For a channel with a single binding site X processing one ion at a time, the steps for permeation are



where S_i (resp. S_o) represents the ion S inside (resp. outside) the cell. The forward and backward reaction rates are called k_1 and k_{-1} for the first reaction and k_2 and k_{-2} for the second one. Steady-state current, *i.e.* when $\frac{d}{dt}[XS] = 0$, is obtained from chemical kinetics³²

$$I_S = z_S F [X] \frac{k_{-1}k_{-2}[S]_i - k_1k_2[S]_o}{k_{-1} + k_2 + k_1[S]_o + k_{-2}[S]_i} . \quad (3.31)$$

The current I_S vanishes at Nernst potential because $I_S = 0$ implies

$$\frac{[S]_o}{[S]_i} = \frac{k_{-1}}{k_1} \frac{k_{-2}}{k_2} = \exp\left(\frac{z_S F V_m}{RT}\right) \quad (3.32)$$

where the last equality comes from the detailed balance relation (3.3). The flux saturates at high concentrations. However if the ion S is assumed to stay only a very short time in the pore, *i.e.* if $k_{-1} + k_2 \gg k_1[S]_o + k_{-2}[S]_i$, the saturation effect is negligible and the formula becomes

$$I_S = z_S F [X] \frac{k_{-1}k_{-2}}{k_{-1} + k_2} \left([S]_i - [S]_o \exp(-z_S F V_m / RT) \right) \quad (3.33)$$

$$= z_S F [X] \frac{k_{-2}}{1 + k_2/k_{-1}} [S]_i \left(1 - \exp(-z_S F (V_m - E_S) / RT) \right) \quad (3.34)$$

Some convenient approximate formulae can now be derived assuming that the voltage dependence of the rates k_i is exponential. For instance, after linearization of the last factor, the current-voltage relationship can be expressed as

$$I_S = \frac{g_S}{1 + \lambda \exp(b V_m)} (V_m - E_S) \quad (3.35)$$

with g_S , λ and b being three parameters, and is equivalent to an Ohm's law combined with a two-state gate at steady-state, as suggested by DeFelice.³³ In contrast to Eq. (3.28), notice the positive sign ($\lambda > 0$) in the denominator.

EXAMPLE: In the Courtemanche *et al.* model,⁷⁰ the time-independent K^+ current I_{K1} and the rapid delayed outward rectifier K^+ current I_{Kr} have a current-voltage relationship following Eq. (3.35). The ultrarapid delayed rectifier K^+ current I_{Kur} uses a similar formula (a constant conductance is added). In the Luo–Rudy phase I model,³⁸ the time-independent outward potassium current I_{Kp} is also formulated as Eq. (3.35).

3.2.4 Active Transport

In order to maintain the ionic concentration imbalance between intra- and extracellular media necessary for cell excitability, ionic pumps use the chemical energy provided by ATPase to carry ions against the concentration gradient. The molecular structure and functional mechanism of these carriers are different from ionic channels. Their kinetics model, however, are similar except that the ionic flux is usually smaller ($\approx 10^4$ instead of 10^6 ions/s).^{32,106} A simple model of pump can be described by³³

$$I_{\text{pump}} = \#\{\text{Transporters}\} \cdot \text{Prob}\{\text{Occupied entrance site(s)}\} \cdot I_{\text{transporter}}(V_m) \quad (3.36)$$

The flux $I_{\text{transporter}}$ is associated with the duration of the transport of an ion through the membrane. The probability of having an occupied entrance site is responsible for the behavior at low concentration near the entrance site.

Receptor-Ligand Reaction

Before being transported through the membrane, an ion S usually has to bind to the carrier X . This process can be modeled by the Hill's equation¹³¹ for the receptor-ligand reaction $nS + X \rightleftharpoons S_nX$ at equilibrium leading to

$$\text{Prob}\{\text{Occupied site}\} = \frac{1}{1 + (K_{m,S}/[S])^n} \quad (3.37)$$

The parameter $K_{m,S}$ is the equilibrium constant of the reaction. The exponent n is called the Hill's coefficient. It is generally fitted to an experimental curve, and may be non-integer for that reason.

Ionic Pumps

The simplest pump model uses a voltage-independent current and processes one ion at a time ($n = 1$). In this case, the pump current (3.36) becomes*

$$I_{p,S} = \frac{I_{p,S(\max)}}{1 + K_{m,S}/[S]} \quad (3.38)$$

where $I_{p,S(\max)}$ is the maximal value and $K_{m,S}$ the concentration at half-saturation value.

EXAMPLE: In the Courtemanche *et al.* model,⁷⁰ two pumps ensure low Ca^{2+} concentration at rest in the intracellular medium, $I_{p,Ca}$ and I_{up} , the former releasing Ca^{2+} in the extracellular domain and the latter in the uptake compartment of the sarcoplasmic reticulum. Both follow Eq. (3.38)

$$I_{p,Ca} = \frac{I_{p,Ca(\max)}}{1 + K_{p,Ca}/[Ca^{2+}]_i} \quad \text{and} \quad I_{up} = \frac{I_{up(\max)}}{1 + K_{up}/[Ca^{2+}]_i} \quad (3.39)$$

*This equation is very similar to the Michaelis–Menten equation for enzyme action rate.³²

Na⁺-K⁺ Ionic Pump

The Na⁺-K⁺ pump carries simultaneously Na⁺ and K⁺ in the opposite direction in order to maintain stable low intracellular concentration [Na⁺]_i and low extracellular concentration [K⁺]_o at rest. While 3 Na⁺ are moving outside the cell, 2 K⁺ are entering. The probability of occupied entrance sites now factorizes into Prob{Occupied Na sites} × Prob{Occupied K sites} since the mechanism needs both the ions Na⁺ and K⁺ to proceed. Formula (3.37) can be used to model these probabilities.

EXAMPLE: In the Courtemanche *et al.* model,⁷⁰ the Hill coefficient is 3/2 for Na⁺ and 1 for K⁺:

$$I_{\text{NaK}} = I_{\text{NaK(max)}} f_{\text{NaK}}(V_m) \frac{1}{1 + (K_{m,\text{Na}_i}/[\text{Na}^+]_i)^{3/2}} \frac{1}{1 + K_{m,\text{K}_o}/[\text{K}^+]_o} \quad (3.40)$$

where $I_{\text{NaK(max)}}$ is a constant and the current-voltage relationship reads

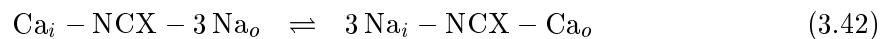
$$f_{\text{NaK}} = (1 + 0.1245 \exp(-0.1FV_m/RT) + 0.0365\sigma \exp(-FV_m/RT))^{-1} . \quad (3.41)$$

Moreover, a dependence in the extracellular sodium concentration [Na⁺]_o is included through the parameter $\sigma = \frac{1}{7}(\exp([\text{Na}^+]_o/67.3) - 1)$, where [Na⁺]_o is expressed in mM.

3.2.5 Ion Exchangers

Ion exchangers alternately bind ions on opposite sides of the membrane, so that the flow of an ion one way across the cell membrane is coupled with another ion flowing in the opposite direction. In cardiac cells, most notable among these is the Na⁺/Ca²⁺ exchanger which uses the energy of Na⁺ influx (along its electrochemical gradient) to remove Ca²⁺ from the cell. During each cycle, one ion Ca²⁺ leaves the cell while 3 ions Na⁺ enter the cell, or the opposite, leading to a net charge flux.

A simplified way to describe this process is to consider the chemical equation



where NCX denotes the Na⁺/Ca²⁺ exchanger and the indices i and o are related to intra- and extracellular binding sites. The current associated with the forward reaction (outward Ca²⁺ flux and inward Na⁺ flux) is expressed as

$$I_{\text{NaCa}}^{\rightarrow} = - [\text{NCX}] F \cdot k^{\rightarrow}(V_m) \cdot \text{Prob}\{\text{Occupied Na}_o \text{ sites}\} \text{Prob}\{\text{Occupied Ca}_i \text{ site}\} \\ \times \text{Prob}\{\text{Free Na}_i \text{ sites}\} \text{Prob}\{\text{Free Ca}_o \text{ site}\} \quad (3.43)$$

where [NCX] is the concentration of ion exchangers, k^{\rightarrow} the forward reaction rate and F the Faraday constant. A minus sign is present, because in this case the net current flow is inward-oriented, and, by convention, outward currents are positive. The probabilities express the fact that the exchange is possible only if 3 ions Na⁺ are bounded at the extracellular side of the membrane, one Ca²⁺ ion is bounded in the intracellular side, and if free sites are available on the opposite sides of the membrane. These probabilities can be estimated using

Eq. (3.37) with Hill's coefficients corresponding to the stoichiometry:

$$\text{Prob}\{\text{Occupied Na}_i \text{ sites}\} = \frac{1}{1 + (K_{m,\text{Na}}/[\text{Na}^+]_i)^3} \approx ([\text{Na}^+]_i/K_{m,\text{Na}})^3 \quad (3.44)$$

$$\text{Prob}\{\text{Occupied Ca}_i \text{ site}\} = \frac{1}{1 + K_{m,\text{Ca}}/[\text{Ca}^{2+}]_i} \approx [\text{Ca}^{2+}]_i/K_{m,\text{Ca}} \quad (3.45)$$

$$\text{Prob}\{\text{Occupied Na}_o \text{ sites}\} = \frac{1}{1 + (K_{m,\text{Na}}/[\text{Na}^+]_o)^3} \quad (3.46)$$

$$\text{Prob}\{\text{Occupied Ca}_o \text{ site}\} = \frac{1}{1 + K_{m,\text{Ca}}/[\text{Ca}^{2+}]_o} \quad (3.47)$$

and obviously $\text{Prob}\{\text{Free site}\} = 1 - \text{Prob}\{\text{Occupied site}\}$. Because intracellular Na^+ and Ca^{2+} concentrations are small, saturation effects are neglected as shown by the development in Eqs. (3.44–3.45), and $\text{Prob}\{\text{Free intracellular sites}\}$ is considered to be 1. The ionic concentration explicit dependence of the $\text{Na}^+/\text{Ca}^{2+}$ exchanger current appears now

$$I_{\text{NaCa}}^{\rightarrow} = - [\text{NCX}] F \cdot k^{\rightarrow}(V_m) \times \frac{1}{1 + (K_{m,\text{Na}}/[\text{Na}^+]_o)^3} \cdot \frac{[\text{Ca}^{2+}]_i}{K_{m,\text{Ca}}} \cdot 1 \cdot \frac{1}{1 + [\text{Ca}^{2+}]_o/K_{m,\text{Ca}}} \quad (3.48)$$

Equivalently, the current associated with the backward reaction (outward Na^+ flux and inward Ca^{2+} flux) reads

$$I_{\text{NaCa}}^{\leftarrow} = [\text{NCX}] F \cdot k^{\leftarrow}(V_m) \times ([\text{Na}^+]_i/K_{m,\text{Na}})^3 \cdot \frac{1}{1 + K_{m,\text{Ca}}/[\text{Ca}^{2+}]_o} \cdot \frac{1}{1 + ([\text{Na}^+]_o)/K_{m,\text{Na}})^3} \cdot 1 \quad (3.49)$$

Further simplifications are made possible by the detailed balance relation (3.3)

$$k^{\leftarrow}/k^{\rightarrow} = \exp(-FV_m/RT) \quad (3.50)$$

By superposition, $I_{\text{NaCa}} = I_{\text{NaCa}}^{\rightarrow} + I_{\text{NaCa}}^{\leftarrow}$ leads to the following form for the $\text{Na}^+/\text{Ca}^{2+}$ exchanger current:

$$I_{\text{NaCa}} = [\text{NCX}] F k^{\rightarrow}(V_m) \frac{\exp(FV_m/RT) [\text{Na}^+]_i^3 [\text{Ca}^{2+}]_o - [\text{Na}^+]_o^3 [\text{Ca}^{2+}]_i}{(K_{m,\text{Na}}^3 + [\text{Na}^+]_o^3) (K_{m,\text{Ca}} + [\text{Ca}^{2+}]_o)} \quad (3.51)$$

EXAMPLE: The dynamic Luo–Rudy^{43,44} model and the Courtemanche *et al.* model⁷⁰ both include a $\text{Na}^+/\text{Ca}^{2+}$ exchanger based on Eq. (3.51). The forward reaction rate is modeled by

$$[\text{NCX}] F k^{\rightarrow}(V_m) = \frac{I_{\text{NaCa(max)}}}{k_{\text{sat}} + \exp(\eta FV_m/RT)} \quad (3.52)$$

where k_{sat} and η are non-dimensional constants. This formula is characterized by a saturation at low V_m and, at higher V_m , by a behavior similar to a single energy barrier as shown by comparison with Eq. (3.5).

3.3 Cellular Level : Cell Models

Membrane models were assembled using the elementary components presented above: ionic channels, pumps and ion exchangers. This section shows how balance equations for charge and mass lead to cell models which account for variations in membrane potential and in ionic concentrations (possibly in several compartments including ion buffering).

3.3.1 Membrane potential

The cell membrane, consisting of a dielectric lipid bilayer, acts as a capacitor. The electric charge $Q_m = C_m V_m$ accumulated at the membrane surface (per unit area of membrane) of an isolated cell is proportional to the membrane potential V_m , with C_m being the membrane capacitance per unit area of membrane. The total ionic current I_{ion} (again per unit area of membrane) through the channels, pumps and ion exchangers (by convention, positive currents are outward currents) is responsible for the variations of V_m according to the evolution equation

$$C_m \frac{dV_m}{dt} = -I_{\text{ion}}(V_m, \mathbf{s}) + I_{\text{stim}}(t) \quad (3.53)$$

$$\frac{d\mathbf{s}}{dt} = \mathbf{g}(V_m, \mathbf{s}) \quad (3.54)$$

where \mathbf{s} summarizes all dynamical variables of the cell (gating variables, ionic concentrations) and the function \mathbf{g} describes the dynamics of those variables, e.g. gating variable equations (3.11) or ion balance equation (see next subsection). An external stimulus current I_{stim} is used to trigger an action potential.

EXAMPLE: In the Courtemanche *et al.* model,⁷⁰ I_{ion} is the sum of all Na^+ , K^+ and Ca^+ currents

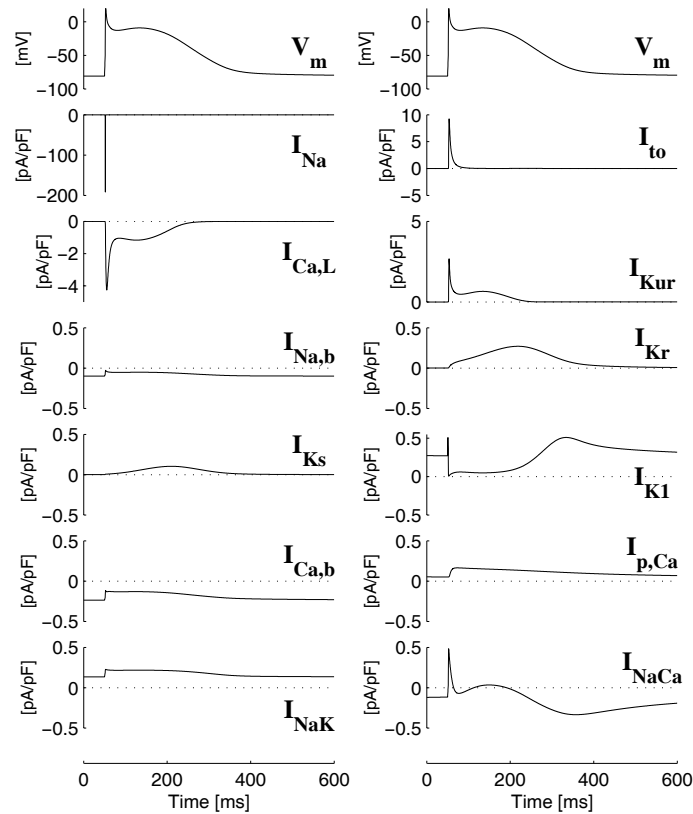


Figure 3.3 — Timecourse of the membrane potential and of the 12 membrane currents of the Courtemanche *et al.* model recorded in a single cell simulation after 10 s of stable pacing with a cycle length of 1 s. The currents are given in pA/pF, as in the original paper, because they actually represent currents divided by the membrane capacitance C_m .

including pumps and ion exchangers

$$I_{\text{ion}} = I_{\text{Na}} + I_{\text{Na,b}} + I_{\text{K1}} + I_{\text{to}} + I_{\text{Ks}} + I_{\text{Kr}} + I_{\text{Kur}} + I_{\text{Ca,L}} + I_{\text{p,Ca}} + I_{\text{Ca,b}} + I_{\text{NaK}} + I_{\text{NaCa}} \quad (3.55)$$

The time-course of these 12 membrane currents during slow and stable pacing are shown in Fig. 3.3. Then, \mathbf{s} is the vector formed by concatenation of 15 gating variables and 5 ionic concentrations (see next subsection).

3.3.2 Fluid Compartment Model

Membrane currents are generated by ionic fluxes through pores, channels, pumps and ion exchangers. These fluxes alter the corresponding ionic concentrations and may significantly modify reversal potential or gating inactivation of channels. The cell models take this possibly important effect into account by considering several compartments or domains (typically intra- and extracellular spaces) that exchange ions. Then ionic concentrations become state variables of the cell.

Division in Compartments

Since the ionic concentrations of Na^+ , K^+ and Ca^{2+} are significantly different inside and outside the cell, at least two domains have to be considered: the intra- and the extracellular space. The intracellular space may also include additional compartments to account for complex features of the calcium dynamics related to the sarcoplasmic reticulum (SR).

The common complexity levels of fluid compartment models are listed below and are schematically represented on Fig. 3.4:

- *Reduced or qualitative models*: all ionic concentrations are constant (e.g. FitzHugh–Nagumo,^{23–25} reduced Priebe–Beukelman⁹⁷);
- *Single compartment model*: the variations in intracellular Ca^{2+} are taken into account. Other intracellular concentrations and extracellular concentrations, however, remain constant. (e.g. Beeler–Reuter,¹⁹ Luo–Rudy³⁸);
- *Simplified SR model*: in addition to the intracellular Ca^{2+} concentration, the Ca^{2+} in the SR is considered (e.g. Fox *et al.*⁵¹);
- *2-compartment SR*: the SR is now divided into two sub-compartments: the network and junctional SR (e.g. dynamic Luo–Rudy,^{43,44} Courtemanche *et al.*⁷⁰);
- *2-compartment SR and cleft concentrations*: the cleft concentrations (extracellular region close to the membrane) are now time-dependent while the bulk concentrations (far from the membrane) are still constant. (e.g. Rasmusson *et al.*,^{68,76} Lindblad *et al.*,⁷⁷ Nygren *et al.*⁶⁹).

A compartment model defines the dynamical variables corresponding to ionic concentrations.

EXAMPLE: The Courtemanche *et al.* model⁷⁰ incorporates a 2-compartment SR model like in Fig. 3.4C. Five ionic concentrations are time-dependent: the intracellular concentrations $[\text{Na}^+]_i$, $[\text{K}^+]_i$ and $[\text{Ca}^{2+}]_i$, the concentration $[\text{Ca}^{2+}]_{\text{up}}$ in the uptake compartment (network SR, NSR) and the concentration $[\text{Ca}^{2+}]_{\text{rel}}$ in the release compartment (junctional SR, JSR). The extracellular concentrations $[\text{Na}^+]_o$, $[\text{K}^+]_o$ and $[\text{Ca}^{2+}]_o$, however, remain constant.

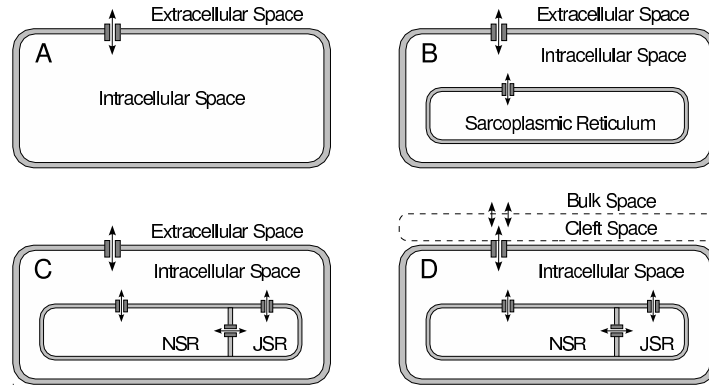


Figure 3.4 — Schematic representation of fluid compartment models of increasing complexity. (A) 2 domains: intra- and extracellular space; (B) 3 domains: intra- and extracellular space, and the sarcoplasmic reticulum; (C) 4 domains: the sarcoplasmic reticulum (SR) is divided into two compartments, the network (NSR) and the junctional (JSR) sarcoplasmic reticulum compartment; (D) 5 domains: the cleft space represents the region in the vicinity of the membrane.

Evolution equations for these variables have to be derived by considering mass conservation. But the ionic flows between compartments will be discussed first.

Ionic Flow Between Compartments

Compartments communicate through channels, pumps and ion exchangers current. In membranes where the effect of electric field can be considered negligible as a first approximation (like the membrane of the sarcoplasmic reticulum), ionic flow through channels is induced by a gradient of ionic concentration. The flux $I_{S,a \rightarrow b}$ of a substance S from a compartment a to a compartment b is written as

$$I_{S,a \rightarrow b} = k_{a \rightarrow b} \text{Prob}\{\text{Open channel}\} ([S]_a - [S]_b) \quad (3.56)$$

where $k_{a \rightarrow b}$ is the flow rate and the probability accounts for a possible gating mechanism of the channel connecting the compartments.

EXAMPLE: In the Courtemanche *et al.* model,⁷⁰ calcium can flow between the intracellular, uptake and release compartments, as illustrated by Fig. 3.4C. The leak current I_{leak} leaving the uptake compartment is modeled by

$$I_{\text{leak}} = \frac{[\text{Ca}^{2+}]_{\text{up}}}{[\text{Ca}^{2+}]_{\text{up}(\text{max})}} I_{\text{up}(\text{max})} \quad (3.57)$$

where $I_{\text{up}(\text{max})}/[\text{Ca}^{2+}]_{\text{up}(\text{max})}$ is the (constant) flow rate. In contrast with Eq. (3.56), the concentration $[\text{Ca}^{2+}]_i$ is not included because it remains much smaller than $[\text{Ca}^{2+}]_{\text{up}}$ at any time during a cardiac cycle.⁷⁰ This current is compensated by a pump I_{up} (uptake current) given by Eq. (3.39). In the same model, the uptake and release compartments exchange Ca^{2+} ions through the transfer (or translocation) current described by the simple formula

$$I_{\text{tr}} = \frac{[\text{Ca}^{2+}]_{\text{up}} - [\text{Ca}^{2+}]_{\text{rel}}}{\tau_{\text{tr}}} \quad (3.58)$$

where τ_{tr} is a diffusion relaxation time. The release current I_{rel} from the release compartment is intended to introduce a calcium-induced calcium release in the intracellular space and is

formulated according to Eq. (3.56)

$$I_{\text{rel}} = k_{\text{rel}} u^2 v w ([\text{Ca}^{2+}]_{\text{rel}} - [\text{Ca}^{2+}]_i) \quad (3.59)$$

where k_{rel} is the flow rate and u , v and w are gating variables controlling the release of Ca^{2+} . The transition rates of the gating variables u and v are functions of the sarcoplasmic Ca^{2+} flux signal*

$$F_n = V_{\text{rel}} I_{\text{rel}} - \frac{1}{2F} \left(\frac{1}{2} I_{\text{Ca,L}} - \frac{1}{5} I_{\text{NaCa}} \right) \quad (3.60)$$

The coefficients $1/2$ and $1/5$ as well as the absence of the calcium currents $I_{\text{p,Ca}}$, $I_{\text{b,Ca}}$, I_{up} and I_{leak} reflect their relative importance with respect to calcium-induced calcium release. This trigger mechanism results in a transient activation of the SR Ca^{2+} release current in response to a suprathreshold Ca^{2+} flux. and is a convenient alternative to the formulation including explicit thresholds proposed by Luo and Rudy.⁴³ The voltage-dependent gating variable w inactivates the channel at high membrane potential. Notice finally that I_{up} and I_{leak} are expressed in $\text{mol s}^{-1}/V_{\text{up}}$ and I_{rel} and I_{tr} in $\text{mol s}^{-1}/V_{\text{rel}}$.

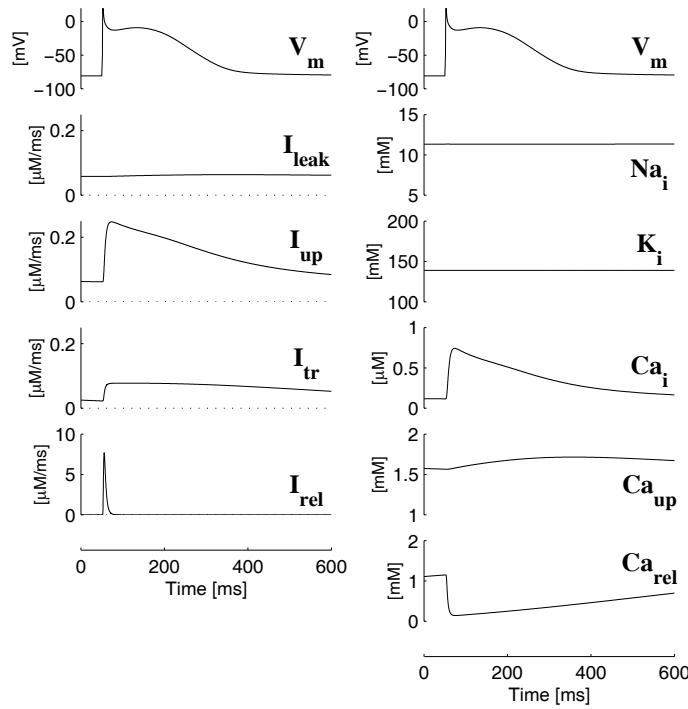


Figure 3.5 — Time-course of the membrane potential, the ionic concentrations and the intracellular ionic fluxes in the Courtemanche et al. model recorded in a single cell simulation after 10 s of slow and stable pacing with a cycle length of 1 s.

Ionic Balance

From mass conservation of the substance S , the variation of the concentration $[S]$ is due to either outward fluxes $J_{S, \text{flux}}$ of the substance or to chemical reactions producing or absorbing S inside the compartment at a rate $J_{S, \text{rxn}}$

$$\frac{d}{dt}[S] = -J_{S, \text{flux}} + J_{S, \text{rxn}} \quad (3.61)$$

*The prefactor 10^{-12} present in the original paper⁷⁰ was left out here for the sake of clarity.

The flux $J_{S, \text{flux}}$ is related to the total current $I_{S, \text{tot}}$ flowing out of the compartment by the equation $J_{S, \text{flux}} = I_{S, \text{tot}}/z_S F V_{\text{cpt}}$, where z_S is the valence of the ion S , F is the Faraday constant and V_{cpt} is the volume of the compartment.* The source term $J_{S, \text{rxn}}$ usually arises in presence of ion buffering (see next paragraph).

EXAMPLE 1: In the Beeler–Reuter¹⁹ and Luo–Rudy³⁸ models, the intracellular Ca^{2+} concentration is computed according to the simplified equation

$$\frac{d}{dt}[\text{Ca}^{2+}]_i = -\frac{\gamma I_{\text{si}}}{2FV_i} + \frac{[\text{Ca}^{2+}]_{\text{eq}} - [\text{Ca}^{2+}]_i}{\tau} \quad (3.62)$$

where γ represents the fraction of the slow inward current I_{si} that carries calcium, and V_i is the volume of the intracellular compartment. The second term ensures that the concentration eventually comes back to its equilibrium value $[\text{Ca}^{2+}]_{\text{eq}}$ with a relaxation time τ .

EXAMPLE 2: In the Courtemanche *et al.* model,⁷⁰ variations in Na^+ and K^+ intracellular concentration, and in Ca^{2+} concentration in the uptake compartment (NSR) are governed by the equations

$$\frac{d}{dt}[\text{Na}^+]_i = \frac{-3I_{\text{NaK}} - 3I_{\text{NaCa}} - I_{\text{b,Na}} - I_{\text{Na}}}{FV_i} \quad (3.63)$$

$$\frac{d}{dt}[\text{K}^+]_i = \frac{2I_{\text{NaK}} - I_{\text{K1}} - I_{\text{to}} - I_{\text{Ks}} - I_{\text{Kr}} - I_{\text{Kur}}}{FV_i} \quad (3.64)$$

$$\frac{d}{dt}[\text{Ca}^{2+}]_{\text{up}} = I_{\text{up}} - I_{\text{leak}} - \frac{V_{\text{rel}}}{V_{\text{up}}} I_{\text{tr}} \quad (3.65)$$

where V_i (resp. V_{rel} and V_{up}) is the volume of the intracellular compartment (resp. release and uptake compartment), and $J_{\text{Na, rxn}} = J_{\text{K, rxn}} = J_{\text{Ca}_{\text{up}}, \text{rxn}} = 0$. Recall that the fluxes I_{up} and I_{leak} are expressed in $\text{mol s}^{-1}/V_{\text{up}}$ and I_{tr} in $\text{mol s}^{-1}/V_{\text{rel}}$. The ratio $V_{\text{rel}}/V_{\text{up}}$ accounts for the dilution of Ca^{2+} when flowing toward a compartment with a different volume. The stoichiometric coefficients are taken into account for pump and exchanger currents.

Ion Buffering Dynamics

Buffering is a mechanism for temporarily storing an ion S in a binding site B so that it becomes unavailable for electrodiffusion through the cell membrane. Its kinetics can be simply modeled by the reaction $B + S \rightleftharpoons BS$. Because the ions S leaving the binding site are released in the compartment, the reaction flux is calculated from $J_{S, \text{rxn}} = -\frac{d[BS]}{dt}$.

Assuming first-order kinetics, the variation of buffered S is given by

$$\frac{d[BS]}{dt} = \alpha_B [S][B] - \beta_B [BS] \quad (3.66)$$

After introduction of the occupancy number $O_B = [BS]/[B]_{\text{max}}$, where $[B]_{\text{max}}$ is the concentration of binding sites, the kinetics is expressed in terms of only $[S]$ and O_B

$$\frac{dO_B}{dt} = \alpha_B [S](1 - O_B) - \beta_B O_B \quad (3.67)$$

$$J_{S, \text{rxn}} = -[B]_{\text{max}} \frac{dO_B}{dt} \quad (3.68)$$

*In models where the membrane currents are expressed as current per unit membrane area, this relation becomes $J_{S, \text{flux}} = A_{\text{cap}} I_{S, \text{tot}}/z_S F V_{\text{cpt}}$, where A_{cap} is the capacitive area of the cell membrane.

When two different ions (e.g. Ca^{2+} and Mg^{2+}) can be bound to the same buffer, the system is straightforwardly generalized for the equations $B + S_1 \rightleftharpoons BS_1$ and $B + S_2 \rightleftharpoons BS_2$. Compartment models incorporating several buffers are built by linear superposition of the corresponding fluxes.

EXAMPLE: The Rassmusson *et al.*,^{68,76} Lindblad *et al.*,⁷⁷ Nygren *et al.*⁶⁹ models all include a buffering dynamics in the intracellular space. Calcium can be buffered in calmodulin- Ca^{2+} buffer, troponin- Ca^{2+} buffer and troponin- Mg^{2+} buffer. Differential equations describing this process are derived from (3.67).

Ion Buffering at Equilibrium

If the buffer is supposed to be instantaneously in equilibrium with the rest of the compartment, the equations are reduced by adiabatic elimination of the occupancy number. The equilibrium occupancy number $O_{B,\text{eq}}$ is obtained by setting $\frac{dO_B}{dt} = 0$ in Eq. (3.67) so that

$$O_{B,\text{eq}} = \frac{[S]}{K_{m,B} + [S]} \quad (3.69)$$

$$J_{S,\text{rxn}} = -[B]_{\text{max}} \frac{dO_{B,\text{eq}}}{dt} = -\frac{[B]_{\text{max}} K_{m,B}}{(K_{m,B} + [S])^2} \frac{d[S]}{dt} \quad (3.70)$$

where $K_{m,B}$ is defined as β_B/α_B . Then the reaction flux (3.70) can be integrated directly in the mass conservation equation (3.61). This gives a concentration equation corrected for taking into account buffering

$$\frac{d}{dt}[S] = -\left(1 + \frac{[B]_{\text{max}} K_{m,B}}{(K_{m,B} + [S])^2}\right)^{-1} J_{S,\text{flux}} \quad (3.71)$$

The variations of $[S]$ are therefore slowed down by the presence of buffers.

EXAMPLE: The Courtemanche *et al.* model⁷⁰ incorporates two Ca^{2+} buffers in the intracellular compartment: Troponin (Trpn) and Calmodulin (Cmdn) buffers. As a consequence, the intracellular Ca^{2+} concentration verifies the equation

$$\frac{d}{dt}[\text{Ca}^{2+}]_i = -\left(1 + \frac{[\text{Trpn}]_{\text{max}} K_{m,\text{Trpn}}}{([\text{Ca}^{2+}]_i + K_{m,\text{Trpn}})^2} + \frac{[\text{Cmdn}]_{\text{max}} K_{m,\text{Cmdn}}}{([\text{Ca}^{2+}]_i + K_{m,\text{Cmdn}})^2}\right)^{-1} J_{\text{Ca}_i,\text{flux}} \quad (3.72)$$

In the junctional sarcoplasmic reticulum compartment, only one buffer, the Calsequestrin (Csqn) buffer, is present, leading to the following equation

$$\frac{d}{dt}[\text{Ca}^{2+}]_{\text{rel}} = -\left(1 + \frac{[\text{Csqn}]_{\text{max}} K_{m,\text{Csqn}}}{([\text{Ca}^{2+}]_{\text{rel}} + K_{m,\text{Csqn}})^2}\right)^{-1} J_{\text{Ca}_{\text{rel}},\text{flux}} \quad (3.73)$$

The outward Ca^{2+} fluxes are given by

$$J_{\text{Ca}_i,\text{flux}} = \frac{-2I_{\text{NaCa}} + I_{\text{p,Ca}} + I_{\text{Ca,L}} + I_{\text{b,Ca}}}{2FV_i} + \frac{V_{\text{up}}}{V_i} (I_{\text{up}} - I_{\text{leak}}) - \frac{V_{\text{rel}}}{V_i} I_{\text{rel}} \quad (3.74)$$

$$J_{\text{Ca}_{\text{rel}},\text{flux}} = I_{\text{rel}} - I_{\text{tr}} \quad (3.75)$$

Recall that I_{up} and I_{leak} are expressed in $\text{mol s}^{-1}/V_{\text{up}}$ and I_{rel} and I_{tr} in $\text{mol s}^{-1}/V_{\text{rel}}$.

3.4 Conclusion

In this chapter, a mathematical description of the cardiac cell electrophysiological models used in the present study was given. In summary, the cell state is defined by the membrane potential, gating variables and ionic concentrations. These state variables are coupled as followed (see Fig. 3.6):

1. Channel gates are voltage-dependent (subsection 3.2.2).
2. Ionic currents are driven by channel gates and include ionic channels (subsection 3.2.1), pumps (subsection 3.2.4) and ion exchangers (subsection 3.2.5).
3. Ionic channels depend on the membrane potential through their intrinsic current-voltage relationship (subsection 3.2.3).
4. Variations in membrane potential is due to ionic currents (subsection 3.3.1).
5. Ionic currents produce changes in ionic concentration (subsection 3.3.2).
6. Ionic concentrations have an impact on ionic currents through the Nernst potentials (subsection 3.2.3).

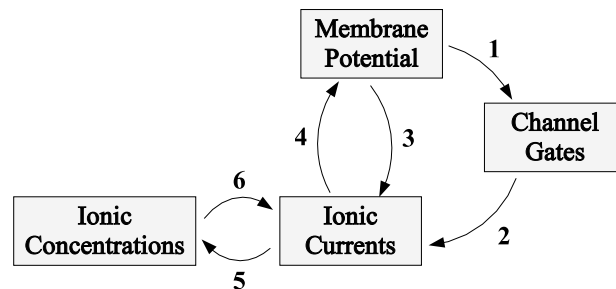


Figure 3.6 — Schematic view of the relations between the state variables of a cell: membrane potential, gating variables and ionic concentrations. The nature of the coupling is explained in the text in the point corresponding to the number near the arrow on the figure.

Despite the increasing accuracy of the included experimental data and the electrophysiological properties successfully reproduced, these models modestly confirm R. Feynman's words: "*Theory is the best guess.*"

From Cell to Organ

In this chapter, the last three levels of the bottom-up approach for cardiac electrophysiological modeling are presented. At the tissue level, the equations of electrical propagation are derived. At the organ level, the anatomy is described, including the geometry, the conduction properties and the fiber structure. Finally, at the experimentalist's level, simulation of electrical mapping is considered.

4.1 Tissue Level : Propagation Equations

The first step from cell models toward full organ electrophysiological modeling is the derivation of the equations describing the propagation of the electrical impulse on a fiber or a piece of cardiac muscle. This section explains how spatial homogenization of diffusion through gap junctions leads to the bidomain and monodomain continuous propagation models.

4.1.1 Cell-to-Cell Coupling

A *gap junction* is a channel (aqueous pore) of large diameter and low selectivity bridging the intracellular medium of two neighboring cells.^{32,33} It provides a cell-to-cell coupling through a direct inter-cellular pathway.

Experimental evidences^{132,133} and theoretical models¹³⁴ have demonstrated that the instantaneous and the steady-state current-voltage relationship of a gap junction coincide and are linear provided the voltage difference between the neighboring cells is no greater than about 10–20 mV. During normal propagation, the order of magnitude of the maximal voltage difference is estimated by: upstroke maximal slope \times cell size / conduction velocity $\approx 10^2$ mV/ms $\cdot 10^{-1}$ mm $\cdot 1$ ms/mm ≈ 10 mV (actually only a fraction of this voltage difference applies across the gap junction due to the intracellular medium resistivity). A gap junction channel will therefore be reasonably modeled by a resistance, leading to a linear cell-to-cell diffusion of the charges. More complex gap junction models including gate kinetics have been proposed and are useful for the study of pathological conduction.^{134,135}

4.1.2 Spatial Homogenization

From the electrical point of view, a cardiac tissue is a set of excitable cells interconnected with their neighbors through gap junctions. Ionic current can flow directly from cell to cell by this pathway, or through membrane channels between the intracellular space and the

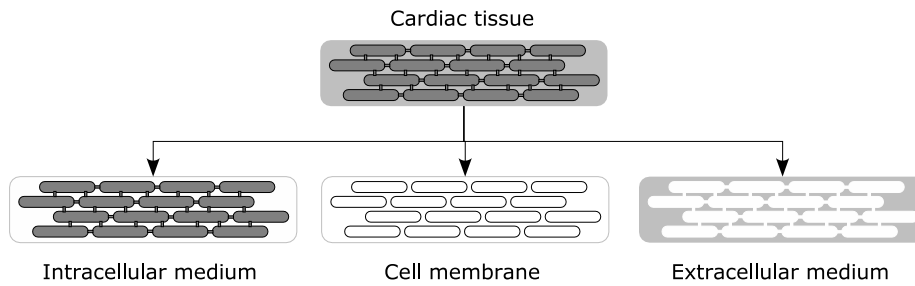


Figure 4.1 — *Decomposition into three domains underlying the spatial homogenization process: the intracellular medium, the cell membranes and the extracellular medium will become three continuous media occupying the same physical space.*

extracellular or interstitial space. Moreover, current flows inside both the intra- and extracellular media. Models taking into account the discrete nature of the electrical propagation require a lot of information about the tissue microstructure (cell geometry, fiber structure, distribution of gap junctions). They are generally restricted to linear strands of cells.^{135–138}

Excitable media are generally modeled by continuous models resulting from a local spatial homogenization.¹³⁹ The intracellular medium, the cell membranes and the extracellular medium are virtually extracted from the cardiac excitable tissue (see Fig. 4.1) and then homogenized by mesoscopic averaging¹⁴⁰ so that the three domains occupy the same continuous physical space called Ω_{active} . The intracellular potential ϕ_i , the cell state \mathbf{s} and the extracellular potential ϕ_e of the cells now become fields $\phi_i(\mathbf{x})$, $\mathbf{s}(\mathbf{x})$ and $\phi_e(\mathbf{x})$ defined on Ω_{active} . Charge diffusion in the intra- and extracellular media is described in the continuous media by coarse-grained conductivity tensor fields $\sigma_i(\mathbf{x})$ and $\sigma_e(\mathbf{x})$ which summarize all the information about the microstructure and the distribution of gap junction over the cell membranes, including anisotropic properties of the tissue.

Wave propagation in such a continuous excitable medium is eventually described by partial differential equations (see next subsection). Solving those equations numerically requires a spatial discretization of the domain, but the discrete elements composing the mesh can now be designed without having to fit their size and shape to real cardiac cells (e.g. triangular elements significantly larger than a real cell).

4.1.3 Bidomain Theory

The *bidomain theory*^{6,139} states the propagation equations in a continuous model of excitable tissue composed of an intra- and an extracellular medium. The evolution equations are simply derived from the law of conservation of charge.

Conservation Laws

If the intracellular medium is considered continuous, the current flows are described by a continuity equation expressing the conservation of electric charge

$$\frac{\partial \rho_i}{\partial t} + \nabla \cdot \mathbf{j}_i = I_{\text{src},i} \quad (4.1)$$

where ρ_i is the charge density, \mathbf{j}_i is the current density in the intracellular medium and I_{src} is a current source term. A similar equation holds for the extracellular medium.

The charge density is given by $\rho_i = V_m C_m S_v$, that is, charge density per unit volume = membrane potential \times membrane capacitance per unit area of membrane \times area of membrane per unit volume. Assuming a linear relationship between gradient of potential and current density, Ohm's law reads

$$\mathbf{j}_i = -\boldsymbol{\sigma}_i \nabla \phi_i \quad (4.2)$$

where $\boldsymbol{\sigma}_i$ is the symmetric positive definite conductivity tensor. Finally, the source current (*inward* current) per unit volume $I_{\text{src},i}$ is given by $-I_{\text{ion}} S_v$, the ionic current through the membrane (by convention, *outward-oriented* if positive) per unit area of membrane \times area of membrane per unit volume, leading to the equation

$$C_m \frac{\partial V_m}{\partial t} = S_v^{-1} \nabla \cdot \boldsymbol{\sigma}_i \nabla \phi_i - I_{\text{ion}} \quad . \quad (4.3)$$

In the extracellular medium, the charges are located on the other side of the capacity, so that $\rho_e + \rho_i = 0$ and $I_{\text{src},e} + I_{\text{src},i} = 0$. The current density is also supposed to satisfy Ohm's law $\mathbf{j}_e = -\boldsymbol{\sigma}_e \nabla \phi_e$, and the continuity equation becomes

$$-C_m \frac{\partial V_m}{\partial t} = S_v^{-1} \nabla \cdot \boldsymbol{\sigma}_e \nabla \phi_e + I_{\text{ion}} \quad . \quad (4.4)$$

The complete system is generally written as

$$S_v^{-1} \nabla \cdot \boldsymbol{\sigma}_i \nabla \phi_i = C_m \frac{\partial V_m}{\partial t} + I_{\text{ion}} \quad (4.5)$$

$$\nabla \cdot (\boldsymbol{\sigma}_i \nabla \phi_i + \boldsymbol{\sigma}_e \nabla \phi_e) = 0 \quad (4.6)$$

where $V_m = \phi_i - \phi_e$. The former equation is a parabolic reaction-diffusion equation, while the latter is an elliptic equation.

Boundary Conditions

These equations have to be solved simultaneously in the domain Ω_{active} representing the active tissue. No current can flow out of the intracellular medium through gap junctions, that is, a von Neumann boundary condition is used

$$\mathbf{n}^\top \cdot \boldsymbol{\sigma}_i \nabla \phi_i = 0 \quad \text{on} \quad \partial\Omega_{\text{active}} \quad (4.7)$$

where \mathbf{n} is a unit vector normal to the boundary $\partial\Omega_{\text{active}}$. In the extracellular medium, however, current can flow outside the active cardiac tissue, provided the surrounding medium (called hereafter the *bath*) is conductive. In this domain Ω_{bath} , characterized by a conductivity tensor field $\boldsymbol{\sigma}_b$ and by the absence of any current source, the electric potential ϕ_b satisfies the elliptic equation

$$\nabla \cdot \boldsymbol{\sigma}_b \nabla \phi_b = 0 \quad \text{in} \quad \Omega_{\text{bath}} \quad . \quad (4.8)$$

On the exterior boundary $\partial\Omega_{\text{bath}}^{\text{ext}}$ of the bath domain Ω_{bath} , a no-flux boundary condition is also assumed, as it is the case for instance when $\partial\Omega_{\text{bath}}^{\text{ext}}$ corresponds to the body surface

$$\mathbf{n}^\top \cdot \boldsymbol{\sigma}_b \nabla \phi_b = 0 \quad \text{on} \quad \partial\Omega_{\text{bath}}^{\text{ext}} \quad . \quad (4.9)$$

Other boundary conditions are possible,^{6,139} for instance when modeling defibrillation. The link between the active tissue and the bath is established through a continuity condition for potentials and currents

$$\phi_b = \phi_e \quad \text{and} \quad \boldsymbol{\sigma}_b \nabla \phi_b = \boldsymbol{\sigma}_e \nabla \phi_e \quad \text{in} \quad \partial\Omega_{\text{active}} . \quad (4.10)$$

The final set of equations describing a bidomain model with a surrounding bath is composed of the partial differential equations (4.5), (4.6) and (4.8), the boundary conditions (4.7) and (4.9), and the continuity conditions (4.10). Moreover, the current I_{ion} depends on the membrane state $\mathbf{s}(\mathbf{x}, t)$ which has also to satisfy a set of ordinary differential equations.

4.1.4 Monodomain Approximation

If the anisotropy ratios are equal, *i.e.* if $\boldsymbol{\sigma}_e(\mathbf{x}) = \kappa \boldsymbol{\sigma}_i(\mathbf{x})$ where κ is a constant, the bidomain equations (4.5) and (4.6) can be decoupled. Only one medium has then to be considered, leading to the so-called *monodomain propagation equation*.^{6,139}

Equal Anisotropy Ratios

Under the assumption of equal anisotropy ratios, the linear combination $(\kappa + 1)^{-1} \kappa \times [\text{Eq. (4.3)}] - (\kappa + 1)^{-1} \times [\text{Eq. (4.4)}]$ gives the monodomain propagation equation

$$C_m \frac{\partial V_m}{\partial t} = S_v^{-1} \nabla \cdot \boldsymbol{\sigma} \nabla V_m - I_{\text{ion}} + I_{\text{stim}} \quad (4.11)$$

where the effective conductivity tensor is defined as $\boldsymbol{\sigma}^{-1} = \boldsymbol{\sigma}_e^{-1} + \boldsymbol{\sigma}_i^{-1}$. An externally driven stimulation current $I_{\text{stim}}(t)$ is introduced to overcome the impossibility to apply stimulations from the extracellular space in this reduced formulation. The boundary condition (4.7) is then expressed as

$$\mathbf{n}^\top \cdot \boldsymbol{\sigma} \nabla V_m = -(\kappa + 1)^{-1} \mathbf{n}^\top \cdot \boldsymbol{\sigma}_e \nabla \phi_e \quad \text{in} \quad \partial\Omega_{\text{active}} . \quad (4.12)$$

In order to completely decouple the membrane potential equation from the other equations involving the extracellular potential, the following no-flux boundary condition will be used instead

$$\mathbf{n}^\top \cdot \boldsymbol{\sigma} \nabla V_m = 0 \quad \text{in} \quad \partial\Omega_{\text{active}} . \quad (4.13)$$

This equation is equivalent to the previous one in the limit $\kappa \gg 1$ of large extracellular conductivity.

Extracellular Potential

Once the membrane potential V_m has been computed using the monodomain propagation equation, the extracellular potential (and bath potential) can be determined from the membrane potential. Eq. (4.6), when expressed in terms of V_m and ϕ_e , becomes

$$\nabla \cdot \boldsymbol{\sigma}_e \nabla \phi_e = -\nabla \cdot \boldsymbol{\sigma} \nabla V_m . \quad (4.14)$$

This equation has to be solved simultaneously with the bath equation (4.8) and the boundary conditions (4.9) and (4.10).

The bath equation and the extracellular potential equation can be merged together. If I_m is defined as $S_v^{-1} \nabla \cdot \boldsymbol{\sigma} \nabla V_m$ in Ω_{active} and 0 everywhere else, $\boldsymbol{\sigma}_0$ is defined as $\boldsymbol{\sigma}_b$ in Ω_{bath} and $\boldsymbol{\sigma}_e$ in Ω_{active} and ϕ_0 is defined as ϕ_b in Ω_{bath} and ϕ_e in Ω_{active} the equations are summarized as

$$\nabla \cdot \boldsymbol{\sigma}_0 \nabla \phi_0 = -S_v I_m . \quad (4.15)$$

Current Source Approximation

If the conductivity tensor $\boldsymbol{\sigma}_0$ can be considered homogeneous and isotropic, i.e. $\boldsymbol{\sigma}_0 = \sigma_0 \mathbb{I}$, an explicit formula can be derived for an infinite bath domain. The solution of the Poisson equation

$$\sigma_0 \nabla^2 \phi_0 = -S_v I_m \quad (4.16)$$

with boundary condition $\phi_0(\mathbf{x}, t) \rightarrow 0$ when $\|\mathbf{x}\| \rightarrow \infty$ is

$$\phi_0(\mathbf{x}, t) = \frac{1}{4\pi\sigma_0} \int_{\Omega_{\text{active}}} d\mathbf{y} \frac{S_v I_m(\mathbf{y}, t)}{\|\mathbf{x} - \mathbf{y}\|} \quad (4.17)$$

and will be referred to as the current source approximation.³¹ This equation will be used to simulate electrical signals measured by electrodes.

4.2 Organ Level : Anatomy

The previous section described the propagation equations for a given tissue geometry with known conduction properties. This section will be devoted to the construction of an anatomical shell model of human atria. Methods to introduce a simplified fiber architecture and some heterogeneities will be also presented, assuming a monodomain approach.

4.2.1 Geometry

In order to define the tissue domain Ω_{active} , medical imaging modalities such as magnetic resonance imaging (MRI) have already proved their usefulness.^{7,9,11,141} Here, the steps involved in the construction of a model of human atria are detailed:

- *Data acquisition:* MRI acquisition was performed *in vivo* on a normal human male subject.*
- *Segmentation:* The epicardial surface of the atria was semi-automatically segmented slice-by-slice and a 3D atrial structure was reconstructed, resulting in a coarse triangular mesh. This mesh, however, suffered from several geometrical problems¹⁵: badly segmented valves and appendages, mesh irregularities, and ambiguously defined septal wall (see Fig. 2.8). High level correction were therefore necessary to make the model suitable for partial differential equation solvers.
- *Surface design:* The surface was smoothed and parametrized using 3D splines.[†] The sizes of appendages, veins and valves were corrected and set to values corresponding to the literature.^{142–144} A septal wall was created.¹⁵

*The raw data were kindly furnished by Ryan Lahm, Dr. Josée Morissette and Dr. Arthur Stillman (Medtronic Inc.). The segmentation was also done by the same group.

[†]The software Ideas (SRDC, Inc.) was used for the 3D geometrical manipulations and meshing.

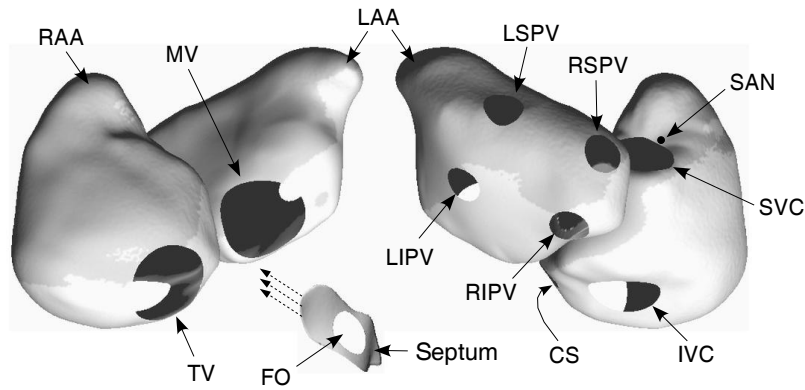


Figure 4.2 — Geometry of human atria based on MR images: anterior view (on the left) and posterior view (on the right). The left/right atrium appendages are indicated by LAA/RAA. The major anatomical obstacles are included: tricuspid valve (TV), mitral valve (MV), inferior vena cava (IVC), superior vena cava (SVC), left/right superior pulmonary vein (LSPV/RSPV), left/right inferior pulmonary vein (LIPV/RIPV), and coronary sinus (CS). A cut of the septum is represented with the fossa ovalis (FO). The location of the sino-atrial node (SAN) is represented as a black dot.

- *Meshing*: From the parametrized surface, several triangular meshes at different spatial resolutions were generated. The discretization and the resulting mesh quality will be discussed in chapter 7.

The final geometry is a monolayer 3D-surface shown in Fig. 4.2. It includes right and left atrial chambers, and openings corresponding to the location of veins and valves. The surface area of both the mitral and tricuspid valves is 4.5 cm^2 , the surface area of the superior and inferior vena cava are 2.8 cm^2 and 3.1 cm^2 , respectively, the surface area of each of the pulmonary veins is 1 cm^2 and the surface area of the coronary sinus is 0.5 cm^2 . The septum has a hole (non-propagating zone) of 1 cm^2 for the fossa ovalis (see Fig. 4.2). The total excitable area of the right atrium (resp. left atrium) is 84 cm^2 (resp. 72 cm^2).

4.2.2 Conduction Properties and Fiber Orientation

Isotropic Conduction

The monodomain propagation equation requires the definition of a conductivity tensor field. When no *a priori* information is available about the conduction properties, or for the sake of simplicity, it is natural to choose an isotropic homogeneous conductivity tensor

$$\boldsymbol{\sigma} = \rho^{-1} \mathbb{I} \quad (4.18)$$

where ρ is the scalar resistivity. This passive resistivity determines the conduction velocity (CV), according to the approximate power law $\rho \propto CV^{-2}$ (see Winfree⁸¹). The value for ρ was selected as a function of the target conduction velocity, because numerous data for the conduction velocity exist.^{145–148}

Anisotropic Conduction

Because anisotropy is expected to have an impact on both wavefront propagation and electrical signals,¹⁴⁹ a fiber structure was included. Using data from histology on excised atria,^{144,146,150–152} a gross fiber structure was manually drawn on the atrial surface, as in Zemlin *et al.*⁹ and Vigmond *et al.*⁸ The fiber orientation was determined by the following steps:

- The trajectory of some selected fibers (about 15) covering the whole surface were drawn on the surface as a sequence of points (Fig. 4.3A).
- On each point of a fiber, the fiber orientation was computed as the unit vector oriented toward the next point of the fiber (Fig. 4.3B).
- The unit vectors describing the fiber orientation were then interpolated on each vertex of the mesh. Since this is a difficult task on a large unstructured mesh,¹⁵³ a nearest neighbor interpolation was used. Each resulting fiber orientation vector was projected on the plane tangent to the surface and is normalized (Fig. 4.3C).
- The vector field is finally smoothed using a (spatially low-pass) nearest-neighbor filter (Fig. 4.3D) and is again projected on the tangent plane and normalized.

The fiber orientation included in the atrial model is represented in Fig. 4.4.

The conductivity tensor can be calculated from the longitudinal (along a fiber) resistivity ρ_l , the transverse (across a fiber) resistivity ρ_t , and the local fiber orientation unit vector

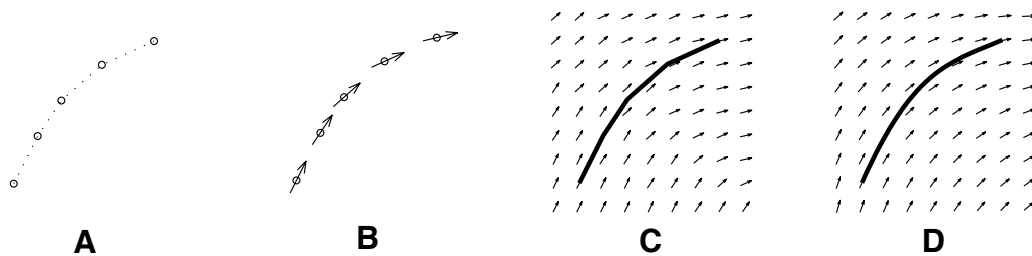


Figure 4.3 — Illustration of the different steps from a fiber trajectory to a complete fiber orientation field. (A) Trajectory of a fiber. (B) Orientation vector along the fiber. (C) Field interpolation. (D) Field smoothing.

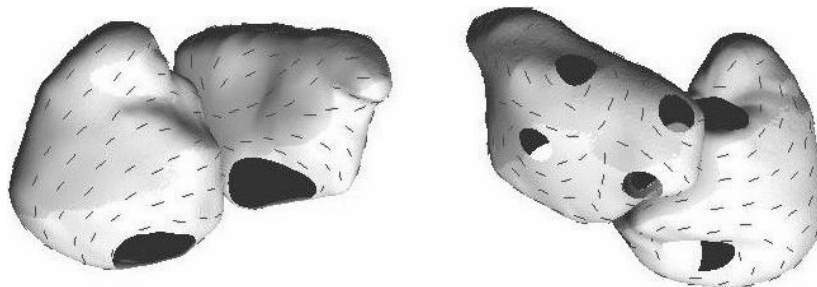


Figure 4.4 — Representation of the gross fiber structure included in the model: anterior view (on the left) and posterior view (on the right). The fiber orientation is represented at some selected locations by a segment.

\mathbf{a} according to the formula¹¹

$$\boldsymbol{\sigma} = \rho_t^{-1} \mathbb{I} + (\rho_t^{-1} - \rho_t^{-1}) \mathbf{a} \mathbf{a}^\top \quad (4.19)$$

where the transverse coupling is assumed to be the same in all angular directions orthogonal to the fiber axis. The ratio $\rho_l^{-1} : \rho_t^{-1}$ is called *anisotropy ratio* and reported experimental values lie in the range 1:1 to 10:1.^{146,148}

4.2.3 Heterogeneities

The presence of heterogeneities is expected to be an arrhythmogenic factor.^{154,155} It may also impact the electrical signals. Although the literature reports the electrophysiological properties (conduction velocity, ionic channels alterations) of various types of heterogeneities, little is known about their spatial distribution. As a consequence, most numerical studies have assumed simple heterogeneity distributions like spatially weakly correlated random distributions,^{156,157} rectangular/circular patches,^{158,159} gradients^{160,161} or smooth transitions.^{74,162} In this study, the purpose was to generate, on a general 3D-surface, random patchy heterogeneity distributions depending only on a few control parameters.

Random texture generation is a well-known topic in image processing and pattern recognition. Simulation of Markov and Gibbs random fields^{163,164} was previously used for that purpose with applications notably in segmentation^{165,166} and image restoration.¹⁶⁷ Fig. 4.5 presents a few examples generated on a square grid by such method (see Cross *et al.*¹⁶⁴).

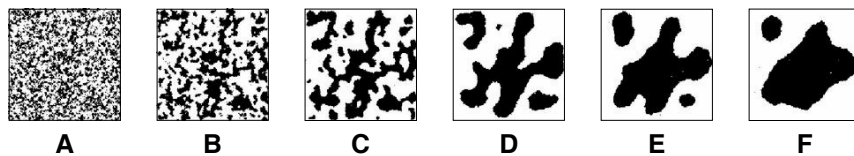


Figure 4.5 — Distribution of heterogeneities in a 150-by-150 2D-grid using Markov random fields. (A–F) successive states after 1, 15, 100, 1000, 5000, 10000 iterations.

Although Markov random fields can also be defined and simulated on any surface, it was more convenient to use another method a bit closer to the reaction–diffusion systems describing biological pattern formation.¹⁶⁸ Basically, a spatially uncorrelated random distribution was generated on the surface. After application of a Gaussian filter introducing a spatial correlation, regions were selected by thresholding. More precisely,

- A random field $u_0(\mathbf{x})$ is generated on the 3D-surface. The random variables $u_0(\mathbf{x})$ are independent and uniformly distributed on $[0, 1]$.
- Filtering is performed through a parabolic partial differential equation to be solved in the time interval $[0, T]$

$$\frac{\partial u}{\partial t} = \nabla \cdot \mathbf{D} \nabla u \quad (4.20)$$

with a no-flux boundary condition and $u(\mathbf{x}, 0) = u_0(\mathbf{x})$ as initial condition. Solving this equation is a difficult task, but the solvers developed for the monodomain propagation equation can be used directly.

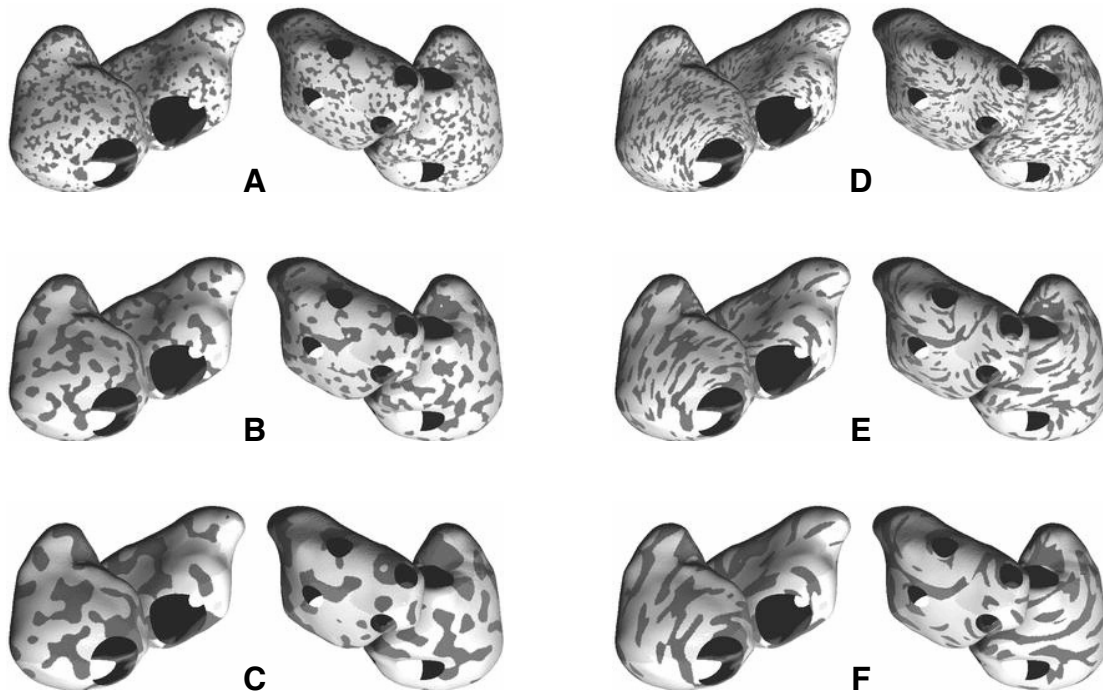


Figure 4.6 — Distribution of heterogeneities using isotropic (A–C) and anisotropic (D–F) diffusion. The spatial length scale of the heterogeneities is 2 mm (A,D), 1 cm (B,E) and 2 cm (C,F). In the anisotropic case, the fiber orientation field was taken from Fig. 4.4.

- The region $\{\mathbf{x} \mid u(\mathbf{x}, T) > u_{th}\}$ was finally chosen as a target for alteration of the tissue properties. The threshold u_{th} was automatically selected so that this region has a given area (a percentage of the total area).

The resulting random patterns are specified by only two parameters: the characteristic length scale of the patches ($\sqrt{D \cdot T}$) and the area of the region. Examples of such patterns computed from the same initial condition but different length scales are displayed on Fig. 4.6. In this procedure, locally anisotropic diffusion can be included (Fig. 4.6D–F).

4.3 Experimentalist's Level : Electrical Mapping

The last level considered in our bottom-up approach of cardiac modeling is the experimentalist's level and concerns the numerical counterparts of the various experimental measurement setups.

4.3.1 Optical and Electrical Mapping

Most of the information about tissue depolarization and repolarization dynamics collected in animal experiments come from optical¹⁶⁹ and electrical^{13,170} mapping, sometimes both simultaneously:¹⁷¹

- *Optical mapping* visualizes the *wavelet dynamics*. The cardiac tissue is stained with fluorescent voltage-sensitive dyes. Through appropriate illumination, variations of

membrane potential are detected as variations in fluorescence by a high-speed CCD video camera. If necessary, the fluorescence maps are converted into phase maps to better reveal the depolarization-repolarization cycle.¹⁷²

- *Electrical mapping* focuses on the *depolarization process*. A set of electrodes, sometimes arranged in a grid, are directly applied on the epicardium (e.g. spoon-shaped grid of electrode¹³) or on the endocardium (e.g. basket catheter¹²), and the electric potential is recorded.

In computer experiments, a direct access to membrane potentials, and therefore to phase maps, is available, so that comparison with optical mapping data is relatively easy. The remaining of this section will focus on simulation of electrical mapping.

4.3.2 Model of Electrode

A *unipolar electrode* is modeled by a point measurement of the (extracellular) electric potential. In contrast to experimental sensors, this idealized electrode cannot damage the tissue or cause disruptions, and it cannot in any way alter the current sources or the propagation of depolarization waves. Moreover, its application on the tissue does not modify the tissue surface geometry. The reference electrode (zero potential) is located at infinity. The distance to the surface (typically 1 mm, see section 7.2) can be understood as a parameter controlling the characteristic length of the region the electrode considers for averaging. It is actually the only parameter describing the model of electrode.

A *bipolar electrode* is modeled as the difference in electric potential between two points close to each other (typically 2 mm) and both at the same distance from the tissue surface.

4.3.3 Simulated High Density Mapping

The objective of this section is to design a simulated electrical mapping system similar to experimental setups. Digital cardiac mapping systems^{173–180} typically include 240–256 channels with a sampling rate of 1–2 kHz. For instance, Konings *et al.*^{13,170,181} used a handheld spoon-shaped mapping electrode to record unipolar electrograms sampled at 1 kHz in the right atrium free wall in Wolff-Parkinson-White patients undergoing cardiac surgery. The mapping system consisted of 244 unipolar electrodes in a spoon of diameter 3.6 cm and an inter-electrode distance of 2.25 mm. A silver plate in the thoracic cavity served as reference electrode.

In order to enable comparisons between computer model data and experimental mapping data, unipolar electrograms were computed in the model at approximately the same location as those recorded in the human patients of Konings *et al.*¹³ Fig. 4.7A represents the virtual spoon-shaped electrode used in computer simulations. The diameter of the virtual spoon was 3.2 cm with an inter-electrode distance of 2 mm and 256 unipolar electrodes in total. The electrodes are positioned 1 mm from the atrial surface. Since the surface is curved, this condition is in competition with the constant inter-electrode distance of 2 mm. As a consequence, a trade-off was necessary to limit the distortions of the grid of electrodes projected on the curved surface.

Figs. 4.7B–C show examples of visualization created from the simulated mapping data: fiber orientation in the mapping area, and an electrogram map during normal sinus rhythm.

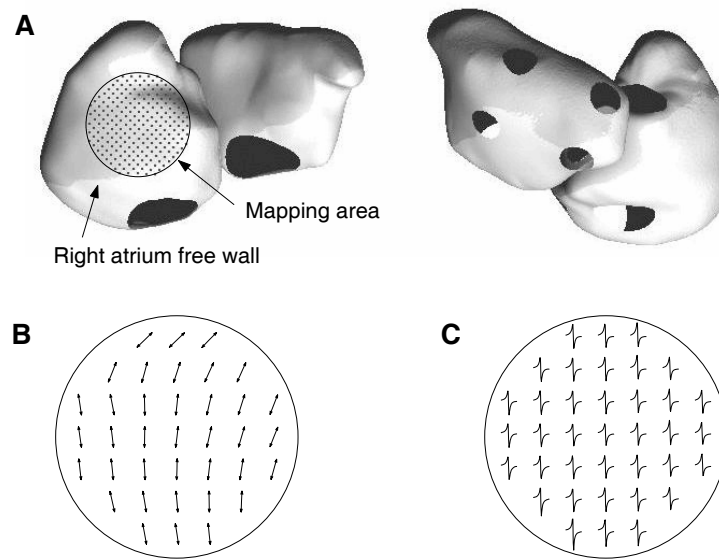


Figure 4.7 — *Electrodes configuration in the simulated high density mapping. (A) Position of the mapping area in the right atrium free wall. The electrodes are located 1 mm from the tissue. (B) Representation of the fiber orientation in the mapping area. (C) Example of electrogram waveforms during normal sinus rhythm.*

4.4 Conclusion

This chapter ends the presentation of the bottom-up approach to cardiac modeling, from cell membrane electrodiffusion to full heart modeling. The construction of a computer model of human atria was explained. The different possible levels of detail in the description of each layer were highlighted:

- *Ionic currents*: reduced model, simple generic model, or detailed specific model;
- *Ionic concentrations*: constant or time-dependent, compartmental model;
- *Tissue physical model*: monodomain or bidomain model;
- *Tissue structure*: discrete (microstructure model) or continuous, presence of fiber orientation or heterogeneities;
- *Anatomy*: 2D sheet or anatomical model, shell or full 3D model;
- *Electrograms*: current source approximation or torso model.

Each choice influences the complexity of the model, and therefore the computational expense of its numerical implementation. Results obtained on a complex model may also be more difficult to interpret. In this work, we will usually start by studying the simplest models capable of demonstrating the phenomena we would like to reproduce, before trying to generalize to more complex situations.

Part II

Numerical Methods

This second part concerns the discretization methods involved to solve numerically the partial/ordinary differential systems presented in the previous chapters. Spatial and temporal discretization are considered separately for a better readability. The first chapter of this part presents a mathematical description of the spatial discretization schemes applied to cardiac modeling in this work. The second chapter shows how the time discretization can be performed, notably with the help of adaptive time steps. Finally, in the third and last chapter of this part, examples of practical computer simulations are given, with a special emphasis on the selection of parameters, on the assessment of accuracy and mesh quality, and on the simulation of electrograms.

Spatial Discretization

The topic of this chapter is the discretization of the diffusion equation with no-flux boundary condition

$$\frac{\partial u}{\partial t} = \nabla \cdot \mathbf{D} \nabla u + f \quad \text{in } \Omega \quad (5.1)$$

$$\mathbf{n} \cdot \mathbf{D} \nabla u = 0 \quad \text{in } \partial\Omega \quad (5.2)$$

defined on a domain Ω with boundary $\partial\Omega$ (\mathbf{n} is a unit vector normal to the boundary). This system will be reduced to the semi-discretized form

$$M \frac{d\mathbf{u}}{dt} + K\mathbf{u} = \mathbf{s} \quad (5.3)$$

where \mathbf{u} gives a finite-dimensional approximation of the field u associated with a mesh constructed on the domain Ω and \mathbf{s} is a source term related to f . The matrices M and K are called *mass matrix* and *stiffness matrix* respectively. It is often more convenient, although restrictive, to have a mass matrix M easy to invert in order to enable efficient explicit time integration. This chapter will focus on this particular case.

The main spatial discretization approaches used in cardiac modeling are briefly overviewed in section 5.1. Then, sections 5.2 and 5.3 describe the numerical schemes used in the present study for structured meshes (2D grids) and for unstructured meshes (triangular mesh of a 3D-surface). Section 5.4 finally presents a possible extension to multi-layer structures.

5.1 Discretization Strategies

The development of a numerical scheme for the diffusion equation involves several steps:

1. *Definition of the domain*: it can be a 1D cable, a 2D rectangular sheet, a 3D box or a surface or volume derived from various medical imaging modalities. In this chapter, in addition to 1D/2D models, a shell model (3D-surface) of human atria based on a MRI dataset is considered.
2. *Mesh construction*: the domain has to be meshed in order to define the discretized field \mathbf{u} . For this purpose, different approaches are available: structured meshes (2D/3D grids, possibly distorted) or unstructured meshes (triangular or tetrahedral elements). The method chosen depends on the shape of the domain and its boundaries, and on the original data format used to code the geometry. Numerical methods may also impose restrictions on the geometry of the mesh (e.g. Delaunay triangulation).

3. *Discretization of the diffusion operator*: a discretization scheme is used to derive the matrices M and K of Eq. (5.3). Many possible methods (finite differences, finite volume, finite elements, etc.) exist and have been extensively studied and applied notably in structure mechanics, fluid dynamics and heat transfer. The main discretization ap-

Reference	Geometry/Methods
<i>Structured meshes</i>	
Finite difference ^{182, 183}	
▷ Fenton <i>et al.</i> ²⁸	3D anisotropic parallelepiped
▷ Saleheen <i>et al.</i> ^{184, 185}	3D bidomain
▷ Gray <i>et al.</i> ¹⁰⁰	1D, 2D, 3D grids, 3D anatomical model of canine ventricles and simplified model of the atria (all with regular cubic elements)
▷ Winslow <i>et al.</i> ¹⁰	
Yung ¹⁸⁶	
Holden <i>et al.</i> ¹⁴¹	3D anisotropic ventricular models (regular cubic elements)
Panfilov <i>et al.</i> ¹¹	
Huiskamp ¹⁸⁷	
▷ Blanc <i>et al.</i> ⁹⁹	simplified shell geometry of the atria
Finite volume ¹⁸⁸	
▷ Harrild <i>et al.</i> ^{7, 189, 190}	3D model of human atria (hexaedral mesh)
Finite elements ^{191, 192}	
▷ Samie <i>et al.</i> ⁵⁴	2D grid using Lagrange polynomial elements ^a
▷ Rogers <i>et al.</i> ¹⁹³	collocation-Galerkin finite elements method
Hunter <i>et al.</i> ¹⁹⁴	
▷ Oniboni <i>et al.</i> ¹⁹⁵	1D finite elements with proper orthogonal decomposition
Adaptative mesh	
▷ Quan <i>et al.</i> ¹⁹⁶	domain decomposition
▷ Cherry <i>et al.</i> ¹⁹⁷	adaptative mesh refinement algorithm
<i>Unstructured meshes</i>	
Generalized finite differences ^b	
▷ Zemlin <i>et al.</i> ⁹	3D shell model of human atria (triangular mesh)
Finite volume-based methods	
▷ Rose <i>et al.</i> ¹⁹⁸	method for triangular meshes
▷ Zozor <i>et al.</i> ¹⁹⁹	3D shell model of human atria (triangular mesh)
Finite Elements	
▷ Vigmond <i>et al.</i> ²⁰⁰	3D first-order tetrahedral elements
<i>Other approaches</i>	
Interconnected cable network	
▷ Leon <i>et al.</i> ²⁰¹	2D/3D anisotropic model
Vigmond <i>et al.</i> ^{200, 202}	
▷ Vigmond <i>et al.</i> ⁸	multilayer model of canine atria

^a see especially the online material.

^b here the term finite volume method is reserved for methods involving a complete tiling of the surface.

Table 5.1 — *Main discretization approaches used in cardiac modeling with some selected references. However, most of the simulation studies found in the literature are still based on finite difference discretization of structured meshes.*

proaches (with some selected references) used in cardiac modeling are summarized in Table 5.1.

4. *Time integration*: finally, a time-stepping scheme has to be proposed to solve Eq. (5.3).

In the remaining of this chapter, the geometry and the mesh (step 1 and 2) are supposed to be already generated, so that the text will focus on discretization of diffusion operators (step 3). Time integration (step 4) will be the topic of the next chapter.

5.2 Structured Mesh

This section recalls the standard finite difference methods used to discretize a diffusion operator applied on a one- or two-dimensional rectangular structured mesh (an extension to the third dimension is straightforward in this simple case). Explicit formulae for the matrices M and K of Eq. (5.3) are given.

5.2.1 Spatial Discretization

Consider a rectangular sheet of size $L_x \times L_y$ regularly discretized. The mesh is composed of points $\mathbf{x}_{i,j} = (i \cdot \Delta x, j \cdot \Delta y)$ with $i = 1, \dots, n_x$, $j = 1, \dots, n_y$ where $(n_x + 1)\Delta x = L_x$ and $(n_y + 1)\Delta y = L_y$. The discrete potential field $\mathbf{u} = (u_{i,j})$ gives an approximation to $u(\mathbf{x}_{i,j}, t)$. The diffusion tensor field is also discretized, i.e. $\mathbf{D}_{i,j} = \mathbf{D}(\mathbf{x}_{i,j})$.

5.2.2 Finite Difference Operators

Forward and backward finite difference operators in the x and y direction are defined as

$$(\delta_{x+}\mathbf{u})_{i,j} = u_{i+1,j} - u_{i,j} \quad \text{and} \quad (\delta_{x-}\mathbf{u})_{i,j} = u_{i,j} - u_{i-1,j} \quad (5.4)$$

$$(\delta_{y+}\mathbf{u})_{i,j} = u_{i,j+1} - u_{i,j} \quad \text{and} \quad (\delta_{y-}\mathbf{u})_{i,j} = u_{i,j} - u_{i,j-1} \quad (5.5)$$

where the von Neumann no-flux boundary conditions are taken into account by setting $u_{0,j} = u_{1,j}$, $u_{i,0} = u_{i,1}$, $u_{n_x+1,j} = u_{n_x,j}$ and $u_{i,n_y+1} = u_{i,n_y}$. The centered finite difference operators are given by

$$\delta_x = \frac{1}{2}(\delta_{x+} + \delta_{x-}) \quad \text{and} \quad \delta_y = \frac{1}{2}(\delta_{y+} + \delta_{y-}) . \quad (5.6)$$

The second order centered finite difference operators are defined by

$$\delta_x^2 = \delta_{x+}\delta_{x-} = \delta_{x-}\delta_{x+} \quad \text{and} \quad \delta_y^2 = \delta_{y+}\delta_{y-} = \delta_{y-}\delta_{y+} . \quad (5.7)$$

5.2.3 Approximation of Diffusion Operators

Finite difference operators help build approximations to differential operators. Some common finite difference formulae for second order derivatives are listed in Table 5.2. A combination of them is sufficient to solve the problems encountered in this study. For instance, the equation

$$\frac{\partial u}{\partial t} = D_x \frac{\partial^2 u}{\partial x^2} + D_y \frac{\partial^2 u}{\partial y^2} + f \quad (5.8)$$

Discretization formula	Order
Second order partial derivative	
$\frac{\partial^2}{\partial x^2} u(\mathbf{x}_{i,j}) = \frac{1}{\Delta x^2} (\delta_x^2 \mathbf{u})_{i,j}$	$+ \mathcal{O}(\Delta x^2)$
2D-Laplacian	
$\nabla^2 u(\mathbf{x}_{i,j}) = \frac{1}{\Delta x^2} (\delta_x^2 \mathbf{u})_{i,j} + \frac{1}{\Delta y^2} (\delta_y^2 \mathbf{u})_{i,j}$	$+ \mathcal{O}(\Delta x^2)$
Mixed partial derivatives	
$\frac{\partial^2}{\partial x \partial y} u(\mathbf{x}_{i,j}) = \frac{1}{\Delta x \Delta y} (\delta_x \delta_y \mathbf{u})_{i,j}$	$+ \mathcal{O}(\Delta x^2)$
Inhomogeneous diffusion operator	
$\frac{\partial}{\partial x} D \frac{\partial}{\partial x} u(\mathbf{x}_{i,j}) = \frac{1}{\Delta x^2} (\delta_{x+} \mathbf{D} \delta_{x-} \mathbf{u})_{i,j}$	$+ \mathcal{O}(\Delta x)$
$\frac{\partial}{\partial x} D \frac{\partial}{\partial y} u(\mathbf{x}_{i,j}) = \frac{1}{\Delta x \Delta y} (\delta_x \mathbf{D} \delta_y \mathbf{u})_{i,j}$	$+ \mathcal{O}(\Delta x)$

Table 5.2 — Finite differences discretization formulae for second order derivatives.^{28, 182, 183} Here the operator \mathbf{D} has to be understood as a point-wise multiplication, i.e. $(\mathbf{D}\mathbf{u})_{i,j} = (\mathbf{D})_{i,j}(\mathbf{u})_{i,j}$. The method's order given here assumes $\Delta y = \mathcal{O}(\Delta x)$.

is approximated by $\mathbf{du}/dt = A\mathbf{u} + \mathbf{f}$ where

$$A = \frac{D_x}{\Delta x^2} \delta_x^2 + \frac{D_y}{\Delta y^2} \delta_y^2 \quad \text{and} \quad f_{i,j} = f(\mathbf{x}_{i,j}) \quad (5.9)$$

that is, the discretization scheme is defined by $M = \mathbb{I}$, $K = -A$ and $\mathbf{s} = \mathbf{f}$ in Eq. (5.3).

5.2.4 Stability and Resistor Interpretation

The source-free discretized system $\mathbf{du}/dt = A\mathbf{u}$ is said to be *stable*²⁰³ if and only if the eigenvalues of A have a non-positive real part and the eigenvalues with zero real part have equal algebraic and geometric multiplicity. The former condition prevents exponential divergence and the latter polynomial divergence. This property can usually be shown in finite difference-based discretization schemes through a resistor interpretation.

Namely, if \mathbf{u} is a constant field, $A\mathbf{u} = \mathbf{0}$ because the gradient of a constant is zero. The sum of each line of A is therefore zero. If, moreover, the matrix A is symmetric with non-negative off-diagonal elements, its elements can be written as

$$A_{mn} = r_{mn} = r_{nm} \geq 0 \quad \text{if } m \neq n \quad (5.10)$$

$$A_{nn} = -\sum_p r_{np} \leq 0, \quad (5.11)$$

leading to the system

$$\frac{du_n}{dt} = \sum_{p \neq n} r_{np} (u_p - u_n). \quad (5.12)$$

This system can be interpreted as the evolution equation of the potential in a circuit of resistors, where u_n is the potential at node n and r_{mn} is the resistance of the connector between nodes m and n , each node being connected to the ground through a unit capacity.

This matrix is clearly *diagonally dominant*, i.e. for all n ,

$$|A_{nn}| \geq \sum_{p \neq n} |A_{np}| . \quad (5.13)$$

Its eigenvalues are then shown to be real non-positive²⁰⁴ when the diagonal elements are negative. Since A is diagonalizable, algebraic and geometric multiplicities are always equal and the system is stable.

5.3 Triangular Mesh

This section presents a discretization scheme based on a finite volume approach to solve a general inhomogeneous anisotropic diffusion equation on a 3D-surface defined by a triangular mesh, reformulating and extending some results from Zozor *et al.*¹⁹⁹ and Shao.²⁰⁵ The resulting discretized system is shown to be stable without any restriction on the mesh.

5.3.1 Spatial Discretization

A triangular mesh on a 3D-surface is described by a set \mathcal{M} of N vertices indexed by i . Vertex $i \in \mathcal{M}$ is located at $\mathbf{x}_i \in \mathbb{R}^3$. A neighborhood relation is introduced through the set \mathcal{N}_i containing the nearest neighbors of the vertex i . A vertex cannot be its own neighbor ($i \notin \mathcal{N}_i$) and the neighborhood relation is symmetric ($j \in \mathcal{N}_i \iff i \in \mathcal{N}_j$). An edge is a couple of vertices (i, j) such that $j \in \mathcal{N}_i$. The corresponding edge vector is denoted by $\mathbf{x}_{ij} = \mathbf{x}_j - \mathbf{x}_i$. The maximal edge length is denoted by Δx in this section. A triple (i, j, k) forms a triangular element of the mesh if (i, j) , (j, k) and (k, i) are edges, that is, when $j \in \mathcal{N}_i$ and $k \in \mathcal{N}_i \cap \mathcal{N}_j$. The set of all triangles is denoted by \mathcal{T} . The number of elements of the set $\mathcal{N}_i \cap \mathcal{N}_j$, denoted by $|\mathcal{N}_i \cap \mathcal{N}_j|$, determines the local topology around the edge (i, j) : if $|\mathcal{N}_i \cap \mathcal{N}_j| = 1$, the edge is a boundary of the domain (Fig. 5.1A); if $|\mathcal{N}_i \cap \mathcal{N}_j| = 2$, the edge is located in the bulk (Fig. 5.1B), and finally if $|\mathcal{N}_i \cap \mathcal{N}_j| > 2$, the edge belongs to a connection line where several surfaces are meeting (Fig. 5.1C).

The scalar fields u and f are approximated by vectors \mathbf{u} and \mathbf{f} whose components are $u_i = u(\mathbf{x}_i)$ and $f_i = f(\mathbf{x}_i)$. For each triangle (i, j, k) , the 3×3 diffusion tensor evaluated at

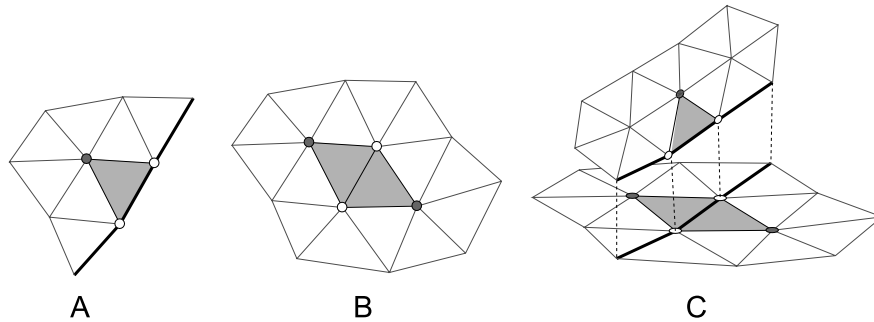


Figure 5.1 — Nearest neighbors and local topology of a triangular mesh. The white circles represent the vertices i and j , while the filled circles represent the set $\mathcal{N}_i \cap \mathcal{N}_j$. (A) $|\mathcal{N}_i \cap \mathcal{N}_j| = 1$, i and j are on a boundary; (B) $|\mathcal{N}_i \cap \mathcal{N}_j| = 2$, i and j are in the bulk of the surface, and (C) $|\mathcal{N}_i \cap \mathcal{N}_j| = 3$, i and j are in the intersection of two surfaces.

the center of gravity of the triangle is called \mathbf{D}_{ijk} . Two independent eigenvectors of \mathbf{D}_{ijk} are assumed to be in the plane defined by the triangle.

5.3.2 Semi-Discretized Equation

Following a finite volume approach, the surface is tiled by assigning a region to each vertex. The flux conservation equation is then applied to each region and leads to the desired matrix form (5.3) for the evolution equation.

Tiling of the Surface

The surface Ω is decomposed into N disjoint regions Ω_i of area $|\Omega_i|$ and boundary $\partial\Omega_i$, for each $i \in \mathcal{M}$. For this purpose, each triangle is divided into 3 quadrilateral domains of equal area. The division lines are drawn from the center of gravity of the triangle to the midpoint of each edge (Fig. 5.2A).

The segment between the center of gravity of (i, j, k) and the midpoint of (i, j) is denoted by S_{ijk} and its length by ℓ_{ijk} . The vector \mathbf{n}_{ijk} is defined as the unit vector perpendicular to the segment S_{ijk} , contained in the plane (i, j, k) and outward-oriented with respect to i , i.e. so that $\mathbf{n}_{ijk}^\top \mathbf{x}_{ij} > 0$. In summary, the contour $\partial\Omega_i$ is the union of all segments S_{ijk} with $j \in \mathcal{N}_i$ and $k \in \mathcal{N}_i \cap \mathcal{N}_j$, and the vectors \mathbf{n}_{ijk} are normal to that contour and outward-oriented (Fig. 5.2B–D).

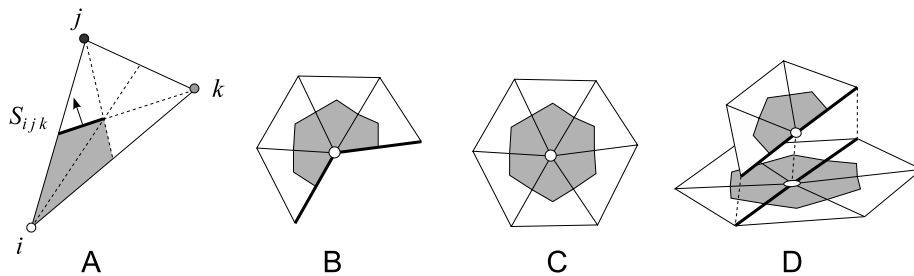


Figure 5.2 — Domain associated with a vertex. (A) In the triangle (i, j, k) , the 3 medians are drawn with dashed lines. The segment S_{ijk} is the thick black line between the gravity center and the midpoint of (i, j) . The arrow illustrates the unit vector \mathbf{n}_{ijk} . The gray zone is the domain assigned to the vertex i . (B) domain associated with a vertex in a boundary, (C) domain associated with a vertex in the bulk, and (D) domain associated with a vertex in the intersection of two surfaces.

Application of Flux Conservation

The flux conservation equation derived from the diffusion equation (5.1) with the help of the divergence theorem and applied to the domain Ω_i reads

$$\frac{dQ_i}{dt} + J_i = s_i, \quad (5.14)$$

that is, variations of the charge Q_i present in Ω_i come from the total outward flux J_i or from the source s_i . These quantities are defined as

$$Q_i = \int_{\Omega_i} d\Omega u, \quad s_i = \int_{\Omega_i} d\Omega f \quad \text{and} \quad J_i = \oint_{\partial\Omega_i} d\ell \mathbf{n}^\top \cdot \mathbf{j} \quad (5.15)$$

where $d\Omega$ is an infinitesimal surface element, $d\ell$ is an infinitesimal length element, $\mathbf{n}(\mathbf{x})$ is normal to the boundary $\partial\Omega_i$ at point \mathbf{x} , and $\mathbf{j} = -\mathbf{D} \nabla u$ is the flux density. Since those integrals are linear with respect to u or f , their discretized forms are expressed as vector equations

$$\mathbf{Q} = M \mathbf{u} \quad , \quad \mathbf{s} = M \mathbf{f} \quad \text{and} \quad \mathbf{J} = K \mathbf{u} \quad (5.16)$$

where M and K are identified with the mass and stiffness matrix of Eq. (5.3). These matrices M and K are obtained through approximate quadrature formulae.

Mass Matrix

The integrals defining Q_i and s_i are estimated by a first-order quadrature formula exact for fields that are constant in Ω_i , leading to the lumping approximations*

$$\int_{\Omega_i} d\Omega u = \Omega_i u_i + \mathcal{O}(\Delta x) \quad \text{and} \quad \int_{\Omega_i} d\Omega f = \Omega_i f_i + \mathcal{O}(\Delta x) . \quad (5.17)$$

Under these assumptions, the mass matrix is diagonal

$$M = \mathbf{\Omega} = \text{diag}(\Omega_1, \dots, \Omega_N) \quad (5.18)$$

and therefore easily invertible. More accurate quadrature formulae would lead to a non-diagonal mass matrix.

Stiffness Matrix

The integral expressing the flux J_i splits into a sum of integrals over each segment S_{ijk}

$$J_i = \sum_{j \in \mathcal{N}_i} \sum_{k \in \mathcal{N}_i \cap \mathcal{N}_j} \int_{S_{ijk}} d\ell \mathbf{n}_{ijk}^\top \cdot \mathbf{j} . \quad (5.19)$$

In order to approximate these integrals, the flux \mathbf{j} and the diffusion tensor \mathbf{D} are considered constant in each triangle.²⁰⁵ Consequently, the gradient of u in the triangle (i, j, k) is evaluated by linear interpolation of the values of u at \mathbf{x}_i , \mathbf{x}_j , and \mathbf{x}_k . Because the gradient is a linear operator, its (local) discrete form is written as

$$\nabla u \left(\frac{\mathbf{x}_i + \mathbf{x}_j + \mathbf{x}_k}{3} \right) = \nabla_{ijk} \mathbf{u} + \mathcal{O}(\Delta x) \quad (5.20)$$

where ∇_{ijk} is a $3 \times N$ sparse matrix. A more explicit expression is derived in the next subsection. The flux integral over the segment S_{ijk} now becomes

$$\int_{S_{ijk}} d\ell \mathbf{n}_{ijk}^\top \cdot \mathbf{j} = -\ell_{ijk} \mathbf{n}_{ijk}^\top \mathbf{D}_{ijk} \nabla_{ijk} \mathbf{u} + \mathcal{O}(\Delta x) . \quad (5.21)$$

After summation over j and k , an approximation for the flux J_i is obtained

$$J_i = - \sum_{j \in \mathcal{N}_i} \sum_{k \in \mathcal{N}_i \cap \mathcal{N}_j} \ell_{ijk} \mathbf{n}_{ijk}^\top \mathbf{D}_{ijk} \nabla_{ijk} \mathbf{u} + \mathcal{O}(\Delta x) . \quad (5.22)$$

*When no confusion is possible, the area of the domain Ω_i is also called Ω_i .

We are now able to write down the expression of the stiffness matrix K of Eq. (5.3) using the canonical basis $\{\mathbf{e}_i\}$ of \mathbb{R}^N as well as the notation $\ell_{ijk} = \ell_{ijk}\mathbf{n}_{ijk}$:

$$K = - \sum_{i \in \mathcal{M}} \sum_{j \in \mathcal{N}_i} \sum_{k \in \mathcal{N}_i \cap \mathcal{N}_j} \mathbf{e}_i \ell_{ijk}^\top \mathbf{D}_{ijk} \nabla_{ijk} . \quad (5.23)$$

Each term of the sum is of the form $(N \times 1)(1 \times 3)(3 \times 3)(3 \times N) = (N \times N)$. Thus, K is a $N \times N$ time-independent sparse matrix. The quantities Ω_i , ℓ_{ijk} , \mathbf{n}_{ijk} and ∇_{ijk} are geometrical parameters depending only on the mesh, while \mathbf{D}_{ijk} is associated with the diffusive properties.

5.3.3 Structure of the Stiffness Matrix

After simplification of Eq. (5.23), the stiffness matrix K will appear to be symmetric positive semidefinite. The stability of the discrete system will be deduced from this property.

Element-based Symmetric Form

Each term of Eq. (5.23) depends *only* on the triangle (i, j, k) . We are going to group together the terms corresponding to the same triangle, so that the structure and the symmetries of the matrix will naturally appear.

The sum over $i \in \mathcal{M}$, $j \in \mathcal{N}_i$, $k \in \mathcal{N}_i \cap \mathcal{N}_j$, is a sum over the set \mathcal{T} of all triangles, each of them considered 6 times, one for each permutation of ijk

$$\sum_{i \in \mathcal{M}} \sum_{j \in \mathcal{N}_i} \sum_{k \in \mathcal{N}_i \cap \mathcal{N}_j} a_{ijk} = \sum_{(i,j,k) \in \mathcal{T}} \sum_{\pi \in \mathcal{S}_3(i,j,k)} a_{\pi(i),\pi(j),\pi(k)} \quad (5.24)$$

where the permutation group of $\{i, j, k\}$ is called $\mathcal{S}_3(i, j, k)$. The matrices \mathbf{D}_{ijk} and ∇_{ijk} are invariant under the permutations of ijk . Thus, the symmetrized form of the matrix K reads

$$K = - \sum_{(i,j,k) \in \mathcal{T}} L_{ijk} \mathbf{D}_{ijk} \nabla_{ijk} \quad (5.25)$$

where the $N \times 3$ matrix L_{ijk} is defined as

$$L_{ijk} = \sum_{\pi \in \mathcal{S}_3(i,j,k)} \mathbf{e}_{\pi(i)} \ell_{\pi(i),\pi(j),\pi(k)}^\top \quad (5.26)$$

$$= \mathbf{e}_i (\ell_{ijk}^\top + \ell_{ikj}^\top) + \mathbf{e}_j (\ell_{jik}^\top + \ell_{jki}^\top) + \mathbf{e}_k (\ell_{kij}^\top + \ell_{kji}^\top) . \quad (5.27)$$

The gradient $\nabla_{ijk}\mathbf{u}$ and the normals vectors ℓ_{ijk} have now to be calculated in terms of the local coordinate system $\{\mathbf{x}_{ij}, \mathbf{x}_{ik}\}$. However, because these vectors are covariant, their components are more naturally expressed in the dual basis of the basis $\{\mathbf{x}_{ij}, \mathbf{x}_{ik}\}$ associated with the triangle edges, a tool widely used in crystallography,²⁰⁶ solid state physics²⁰⁷ and signal processing²⁰⁸ when dealing with non-orthonormal bases.

Dual Basis

Let (\mathbf{a}, \mathbf{b}) be an ordered basis in a plane of an euclidean space. Its *dual basis* $(\mathbf{a}^*, \mathbf{b}^*)$, in the same plane, is defined by the relations²⁰⁶

$$\mathbf{a}^\top \mathbf{a}^* = \mathbf{b}^\top \mathbf{b}^* = 1 \quad \mathbf{a}^\top \mathbf{b}^* = \mathbf{b}^\top \mathbf{a}^* = 0 \quad (5.28)$$

and is computed using cross-products (see Fig. 5.3)

$$\mathbf{a}^* = \mathbf{b} \wedge \mathbf{c} \quad \text{and} \quad \mathbf{b}^* = \mathbf{c} \wedge \mathbf{a} \quad \text{where} \quad \mathbf{c} = \frac{\mathbf{a} \wedge \mathbf{b}}{\|\mathbf{a} \wedge \mathbf{b}\|^2} . \quad (5.29)$$

Notice that the unit of \mathbf{a}^* (e.g. cm^{-1}) is the inverse of the unit of \mathbf{a} (e.g. cm) and that any

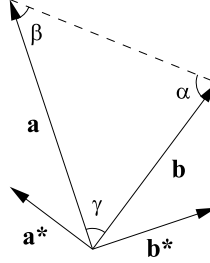


Figure 5.3 — Illustration of the construction of the dual basis: $(\mathbf{a}^*, \mathbf{b}^*)$ is the dual basis of (\mathbf{a}, \mathbf{b}) , and reciprocally (\mathbf{a}, \mathbf{b}) is the dual basis of $(\mathbf{a}^*, \mathbf{b}^*)$. Notice that \mathbf{a}^* is perpendicular to \mathbf{b} and \mathbf{b}^* is perpendicular to \mathbf{a} .

vector \mathbf{v} in the plane generated by $\{\mathbf{a}, \mathbf{b}\}$ can be written as

$$\mathbf{v} = (\mathbf{a}^\top \mathbf{v})\mathbf{a}^* + (\mathbf{b}^\top \mathbf{v})\mathbf{b}^* . \quad (5.30)$$

The following identity will turn out to lead to important simplifications

$$\frac{\|\mathbf{a}\|}{\|\mathbf{b}^*\|} = \frac{\|\mathbf{b}\|}{\|\mathbf{a}^*\|} = \|\mathbf{a} \wedge \mathbf{b}\| \quad (5.31)$$

and is proved by noting that

$$\|\mathbf{b}^*\| \cdot \|\mathbf{a} \wedge \mathbf{b}\| = \|\mathbf{b}^* \wedge (\mathbf{a} \wedge \mathbf{b})\| = \|\mathbf{a}(\mathbf{b}^\top \mathbf{b}^*) - \mathbf{b}(\mathbf{a}^\top \mathbf{b}^*)\| = \|\mathbf{a}\| . \quad (5.32)$$

The *metric tensor*²⁰⁶ in the dual space will also be needed. Some trigonometrical and algebraic manipulations lead to

$$\begin{aligned} \begin{pmatrix} \mathbf{a}^{*\top} \mathbf{a}^* & \mathbf{a}^{*\top} \mathbf{b}^* \\ \mathbf{b}^{*\top} \mathbf{a}^* & \mathbf{b}^{*\top} \mathbf{b}^* \end{pmatrix} &= \begin{pmatrix} \mathbf{a}^\top \mathbf{a} & \mathbf{a}^\top \mathbf{b} \\ \mathbf{b}^\top \mathbf{a} & \mathbf{b}^\top \mathbf{b} \end{pmatrix}^{-1} = \frac{1}{\|\mathbf{a} \wedge \mathbf{b}\|^2} \begin{pmatrix} \|\mathbf{b}\|^2 & -\mathbf{a}^\top \mathbf{b} \\ -\mathbf{a}^\top \mathbf{b} & \|\mathbf{a}\|^2 \end{pmatrix} \\ &= \frac{1}{\|\mathbf{a} \wedge \mathbf{b}\|} \begin{pmatrix} \frac{\|\mathbf{b}\|}{\|\mathbf{a}\| \sin \gamma} & -\cot \gamma \\ -\cot \gamma & \frac{\|\mathbf{a}\|}{\|\mathbf{b}\| \sin \gamma} \end{pmatrix} = \frac{1}{\|\mathbf{a} \wedge \mathbf{b}\|} \begin{pmatrix} \cot \gamma + \cot \alpha & -\cot \gamma \\ -\cot \gamma & \cot \gamma + \cot \beta \end{pmatrix} \end{aligned} \quad (5.33)$$

where α is the angle between $\mathbf{a} - \mathbf{b}$ and $-\mathbf{b}$, β is the angle between $\mathbf{b} - \mathbf{a}$ and $-\mathbf{a}$, and γ is the angle between \mathbf{a} and \mathbf{b} (see Fig. 5.3).

Discrete Gradient Operator

The vector $\nabla_{ijk} \mathbf{u}$ is easily expressed in the dual basis using (5.30)

$$\nabla_{ijk} \mathbf{u} = (\mathbf{x}_{ij}^\top \nabla_{ijk} \mathbf{u}) \mathbf{x}_{ij}^* + (\mathbf{x}_{ik}^\top \nabla_{ijk} \mathbf{u}) \mathbf{x}_{ik}^* = (u_j - u_i) \mathbf{x}_{ij}^* + (u_k - u_i) \mathbf{x}_{ik}^* . \quad (5.34)$$

A matrix form is obtained using $u_i = \mathbf{e}_i^\top \mathbf{u}$

$$\nabla_{ijk} = -(\mathbf{x}_{ij}^* + \mathbf{x}_{ik}^*) \mathbf{e}_i^\top + \mathbf{x}_{ij}^* \mathbf{e}_j^\top + \mathbf{x}_{ik}^* \mathbf{e}_k^\top , \quad (5.35)$$

a matrix directly constructed with the components of the dual basis vectors.

Discrete Divergence Operator

Let ℓ_i (resp. ℓ_j and ℓ_k) be the vector perpendicular to \mathbf{x}_{jk} (resp. \mathbf{x}_{ik} and \mathbf{x}_{ij}), outward-oriented with respect to the triangle (i, j, k) and with a norm $\|\ell_i\| = \|\mathbf{x}_{jk}\|$ (resp. $\|\ell_j\| = \|\mathbf{x}_{ik}\|$ and $\|\ell_k\| = \|\mathbf{x}_{ij}\|$). Since for a closed curve in a plane $\oint d\ell \mathbf{n} = \mathbf{0}$, then

$$\ell_{ijk} + \ell_{ikj} + \frac{1}{2} \ell_j + \frac{1}{2} \ell_k = \mathbf{0} \quad (5.36)$$

The matrix L_{ijk} can then be written as

$$L_{ijk} = -\frac{1}{2} \left(\mathbf{e}_i (\ell_j^\top + \ell_k^\top) + \mathbf{e}_j (\ell_i^\top + \ell_k^\top) + \mathbf{e}_k (\ell_i^\top + \ell_j^\top) \right) \quad (5.37)$$

The covariant vector ℓ_j is easily expressed in the dual basis $\{\mathbf{x}_{ij}^*, \mathbf{x}_{ik}^*\}$ using the identity (5.31). Because $\ell_j^\top \mathbf{x}_{ik} = 0$, ℓ_j is proportional to \mathbf{x}_{ij}^*

$$\ell_j = -\|\mathbf{x}_{ik}\| \frac{\mathbf{x}_{ij}^*}{\|\mathbf{x}_{ij}^*\|} = -\|\mathbf{x}_{ij} \wedge \mathbf{x}_{ik}\| \mathbf{x}_{ij}^* = -2 \Omega_{ijk} \mathbf{x}_{ij}^* \quad (5.38)$$

where Ω_{ijk} is the area of the triangle (i, j, k) . This vector is outward-oriented since $\ell_j^\top \mathbf{x}_{ij} = -2\Omega_{ijk} < 0$. Similarly, simple formulae for ℓ_k and ℓ_i are obtained

$$\ell_k = -2 \Omega_{ijk} \mathbf{x}_{ik}^* \quad (5.39)$$

$$\ell_i = -\ell_j - \ell_k = 2 \Omega_{ijk} (\mathbf{x}_{ij}^* + \mathbf{x}_{ik}^*) \quad (5.40)$$

The matrix L_{ijk} now reads

$$L_{ijk} = -\Omega_{ijk} \left(-\mathbf{e}_i (\mathbf{x}_{ij}^{*\top} + \mathbf{x}_{ik}^{*\top}) + \mathbf{e}_j \mathbf{x}_{ij}^{*\top} + \mathbf{e}_k \mathbf{x}_{ik}^{*\top} \right) \quad (5.41)$$

and reveals its structure

$$L_{ijk} = -\Omega_{ijk} \nabla_{ijk}^\top \quad (5.42)$$

Note that in the derivation of this result, we only used the fact that the boundary of Ω_i crosses each segment at its midpoint. The other point defining the boundary (located at the gravity center of the triangle) could be moved anywhere else in the triangle. Actually, the boundary could even be curved inside each triangle.

Final Expression

The final expression of the stiffness matrix K is obtained by collecting the results of Eqs. (5.23), (5.25) and (5.42) :

$$K = \sum_{(i,j,k) \in \mathcal{T}} \Omega_{ijk} \nabla_{ijk}^\top \mathbf{D}_{ijk} \nabla_{ijk} \quad (5.43)$$

The diffusion tensor \mathbf{D}_{ijk} is symmetric positive definite, so that there exists a symmetric positive definite square root matrix $\mathbf{D}_{ijk}^{1/2}$. The matrix

$$\Omega_{ijk} \nabla_{ijk}^\top \mathbf{D}_{ijk} \nabla_{ijk} = (\Omega_{ijk}^{1/2} \mathbf{D}_{ijk}^{1/2} \nabla_{ijk})^\top (\Omega_{ijk}^{1/2} \mathbf{D}_{ijk}^{1/2} \nabla_{ijk}) \quad (5.44)$$

is clearly symmetric positive semidefinite. This property is preserved under the addition of such matrices. Therefore, K is symmetric positive semidefinite.

5.3.4 Practical Formulation

Since the mass matrix is invertible, the semi-discretized equation (5.3) can be written as

$$\frac{d\mathbf{u}}{dt} = A\mathbf{u} + \mathbf{f} \quad , \quad (5.45)$$

a formulation more convenient both for time integration and numerical implementation provided that M is easily invertible. The matrix A is given by

$$A = -M^{-1}K = -\mathbf{\Omega}^{-1} \sum_{(i,j,k) \in \mathcal{T}} \Omega_{ijk} \nabla_{ijk}^{\top} \mathbf{D}_{ijk} \nabla_{ijk} \quad . \quad (5.46)$$

The matrix $-\nabla_{ijk}^{\top} \mathbf{D}_{ijk} \nabla_{ijk}$ is a (local) discrete form of the differential operator $\nabla \cdot \mathbf{D} \nabla$. Notice the minus sign due to the fact that the diffusion operator (on a bounded domain with appropriate boundary conditions) has *non-positive* eigenvalues.²⁰⁴ The ratios Ω_{ijk}/Ω_l reflect the interplay between the *vertex-centered* balance equation and the *element-centered* estimation of the flux.

This formulation (5.45-5.46) will be used as a starting point for the development of time integration schemes and then for the resulting computer implementations.

5.3.5 Stability

Recall that the discretized system $d\mathbf{u}/dt = A\mathbf{u}$ is said to be *stable* if and only if the eigenvalues of A have a non-positive real part and the eigenvalues with zero real part have equal algebraic and geometric multiplicity. The structure of the final expression (5.43) will show that the system is stable for every mesh and for every diffusion tensor field.

Since M is symmetric positive definite, $M^{1/2}$ and $M^{-1/2}$ are well defined. The *congruence transformation*²⁰⁴

$$K \mapsto K' = M^{-1/2} K M^{-1/2} \quad (5.47)$$

does not preserve the eigenvalues, but preserves their sign (Sylvester Law of Inertia²⁰⁴). Then, the *similarity transformation*²⁰⁴

$$K' \mapsto M^{-1/2} K' M^{1/2} = M^{-1} K = -A \quad (5.48)$$

preserves the eigenvalues. Thus, the eigenvalues of A are all real and non-positive.

Finally, the only eigenvalue of A with zero real part is zero. The algebraic and geometric multiplicity of zero as an eigenvalue of K are equal because K is diagonalizable. But the similarity and congruence transformations preserve the algebraic multiplicity of zero (Sylvester Law of Inertia) and the geometric multiplicity of zero ($\text{rank}(A) = \text{rank}(K)$). Therefore, the eigenvalues of A are real non-positive, the algebraic and geometric multiplicity of zero are equal, and the system is always stable.

5.3.6 Computing the Matrix A

In summary, the construction of the matrix A is performed as follows:

- Inputs: read vertex positions \mathbf{x}_i and the list of triangles (i, j, k) with the corresponding diffusion tensor \mathbf{D}_{ijk} .

- Initialization: $A \leftarrow \mathbf{0}$ and $\Omega_i \leftarrow 0$ for $i = 1, \dots, N$.
- Loop: for each triangle $(i, j, k) \in \mathcal{T}$
 - compute the local basis $(\mathbf{x}_{ij}, \mathbf{x}_{ik})$, its dual basis $(\mathbf{x}_{ij}^*, \mathbf{x}_{ik}^*)$ using Eq. (5.29), and the area Ω_{ijk} of the triangle.
 - update the elements area: $\Omega_l \leftarrow \Omega_l + \Omega_{ijk}/3$ for $l = i, j, k$.
 - construct the 3×3 block matrix $\tilde{\nabla}_{ijk} = \left(-\mathbf{x}_{ij}^* - \mathbf{x}_{ik}^* \mid \mathbf{x}_{ij}^* \mid \mathbf{x}_{ik}^* \right)$
 - compute the product $\tilde{K}_{ijk} = \Omega_{ijk} \tilde{\nabla}_{ijk}^\top \mathbf{D}_{ijk} \tilde{\nabla}_{ijk}$, embed the resulting matrix in the N -dimensional space and subtract it from A , that is, $A \leftarrow A - P_{ijk} \tilde{K}_{ijk} P_{ijk}^\top$ where P_{ijk} is defined as $P_{ijk} = \mathbf{e}_i (1 \ 0 \ 0) + \mathbf{e}_j (0 \ 1 \ 0) + \mathbf{e}_k (0 \ 0 \ 1)$.
- for $i = 1, \dots, N$, divide line i of A by Ω_i .
- Output: write matrix A .

Any entry A_{ij} of the matrix A is zero as soon as $i \neq j$ and $i \notin \mathcal{N}_j$. The storage format for this matrix has to take into account its sparsity.

5.3.7 The Isotropic Case

When the tissue conduction properties are isotropic, *i.e.* when $\mathbf{D}_{ijk} = D_{ijk} \mathbb{I}$, the algorithm of the last subsection is simplified. In that case,

$$\tilde{\nabla}_{ijk}^\top \tilde{\nabla}_{ijk} = \begin{pmatrix} (\mathbf{x}_{ij}^* + \mathbf{x}_{ik}^*)^\top (\mathbf{x}_{ij}^* + \mathbf{x}_{ik}^*) & -(\mathbf{x}_{ij}^* + \mathbf{x}_{ik}^*)^\top \mathbf{x}_{ij}^* & -(\mathbf{x}_{ij}^* + \mathbf{x}_{ik}^*)^\top \mathbf{x}_{ik}^* \\ -\mathbf{x}_{ij}^{*\top} (\mathbf{x}_{ij}^* + \mathbf{x}_{ik}^*) & \mathbf{x}_{ij}^{*\top} \mathbf{x}_{ij}^* & \mathbf{x}_{ij}^{*\top} \mathbf{x}_{ik}^* \\ -\mathbf{x}_{ik}^{*\top} (\mathbf{x}_{ij}^* + \mathbf{x}_{ik}^*) & \mathbf{x}_{ik}^{*\top} \mathbf{x}_{ij}^* & \mathbf{x}_{ik}^{*\top} \mathbf{x}_{ik}^* \end{pmatrix} \quad (5.49)$$

is evaluated using the components of the metric tensor (5.33) in the dual space and gives

$$\begin{aligned} \tilde{K}_{ijk} &= \Omega_{ijk} D_{ijk} \tilde{\nabla}_{ijk}^\top \tilde{\nabla}_{ijk} \\ &= \frac{D_{ijk}}{2} \begin{pmatrix} \cot \theta_{kij} + \cot \theta_{jik} & -\cot \theta_{kij} & -\cot \theta_{jik} \\ -\cot \theta_{kij} & \cot \theta_{kij} + \cot \theta_{ijk} & -\cot \theta_{ijk} \\ -\cot \theta_{jik} & -\cot \theta_{ijk} & \cot \theta_{jik} + \cot \theta_{ijk} \end{pmatrix} \end{aligned} \quad (5.50)$$

where $\theta_{ijk} = \theta_{ikj}$ is the angle between \mathbf{x}_{ij} and \mathbf{x}_{ik} . This formula with the cotangents now appears to be consistent with Zozor *et al.*¹⁹⁹ and Shao.²⁰⁵

Some off-diagonal coefficients may be negative if $\theta_{ijk} > \pi/2$, although one can directly verify that this matrix is always positive semidefinite. Thus, a resistor interpretation (as in subsection 5.2.4) is hard to formulate. This is due to the fact that the gradient is estimated using a three-point formula and not a two-point formula as we would expect for a network of resistances.

5.4 Multi-Layer Triangular Mesh

A simple way for adding thickness to a monolayer geometry (shell model) is to replace each vertex by a cable (1D structured mesh) and complete the connections in each layer. This procedure is mathematically formalized using a tensor product (see Fig. 5.4) and is a first step toward full 3D modeling. This tool will enable us to evaluate the impact of wall thickness on cardiac impulse propagation and on electrical signals, without having to build a 3D mesh of a complex 3D structure.

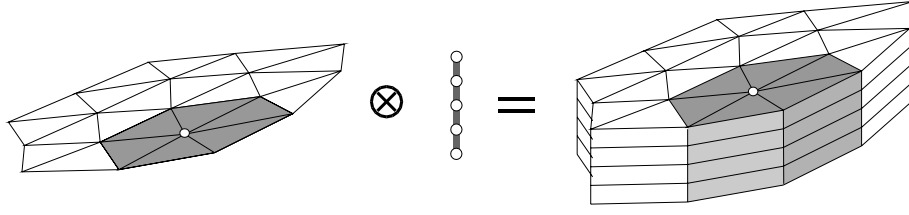


Figure 5.4 — Construction of the vector space of scalar fields on a multilayer structure using a tensor product. A field on a monolayer surface including N vertices is in \mathbb{R}^N , a field on a cable of length L is in \mathbb{R}^L , and a field on a multilayer structure including N vertices and L layers is in \mathbb{R}^{NL} , which is isomorphic to $\mathbb{R}^N \otimes \mathbb{R}^L$.

5.4.1 Spatial Discretization

Suppose that L layers have to be created with a distance Δz between them. It is assumed that the thickness $L\Delta z$ is small compared to the size of the geometry. The layers are labeled by an index k from 0 (epicardium) to $L - 1$ (endocardium), that is, $k \in \mathcal{L} = \{0, \dots, L - 1\}$. To each vertex $i \in \mathcal{M}$ of the 3D-surface mesh (epicardial mesh) are associated L vertices located at

$$\mathbf{x}_i^{(k)} = \mathbf{x}_i - k\Delta z \cdot \mathbf{n}(\mathbf{x}_i) \quad (5.51)$$

where $\mathbf{n}(\mathbf{x}_i)$ is a unit vector normal to the surface at \mathbf{x}_i and outward-oriented. It is more robust, although approximative, to set

$$\mathbf{n}(\mathbf{x}_i) = \frac{\mathbf{x}_i - \bar{\mathbf{x}}}{\|\mathbf{x}_i - \bar{\mathbf{x}}\|} \quad (5.52)$$

where $\bar{\mathbf{x}}$ is a reference point inside the atria, typically at the center of gravity (a different $\bar{\mathbf{x}}$ can be selected for each atrium).

If $\mathbf{u}^{(k)} \in \mathbb{R}^N$ represents the discretized field u in the layer k for all $k \in \mathcal{L}$, the complete discretized field in the whole structure is constructed as a tensor product (see Fig. 5.4)

$$\mathbf{u} = \sum_{k \in \mathcal{L}} \mathbf{u}^{(k)} \otimes \mathbf{e}_k \in \mathbb{R}^N \otimes \mathbb{R}^L \cong \mathbb{R}^{NL} \quad (5.53)$$

where $\{\mathbf{e}_k\}$ is the canonical basis of \mathbb{R}^L . Reciprocally, every field can be written in this form. A similar construction holds for the source term \mathbf{f} .

5.4.2 Semi-discretized Equation

If the discretized diffusion operator A_{surf} of Eq. (5.46) acts on the vector space \mathbb{R}^N , and if the 1D diffusion operator (see subsection 5.2.3)

$$A_{1D} = \frac{D_z}{\Delta z^2} \delta_z^2 \quad (5.54)$$

acts on \mathbb{R}^L , then the semi-discretized equation on the multi-layer geometry reads again $d\mathbf{u}/dt = \mathbf{A}\mathbf{u} + \mathbf{f}$ where the $NL \times NL$ -matrix \mathbf{A} is now given by

$$\mathbf{A} = A_{\text{surf}} \otimes \mathbb{I} + \mathbb{I} \otimes A_{1D} \quad (5.55)$$

and is computed through *Kronecker products* (matrix direct products). The former term accounts for diffusion in each layer and the latter for the diffusion between the layers. Because of this formulation, however, the fiber orientation vector is restricted to lie in the tangent plane of the surface.

5.4.3 Stability

The stability of the system $\mathbf{du}/dt = A\mathbf{u}$ directly derives from the following formula expressing the evolution operator*

$$\exp(At) = \exp(A_{\text{surf}} \otimes \mathbb{I} t + \mathbb{I} \otimes A_{1D}t) = \exp(A_{\text{surf}}t) \otimes \exp(A_{1D}t) \quad (5.56)$$

because a system is stable if and only if any orbit $\mathbf{u}(t) = \exp(At)\mathbf{u}(0)$ is bounded for $t \rightarrow +\infty$. Therefore, if A_{surf} and A_{1D} define stable systems (it was shown to be the case), so does A .

5.5 Conclusion

In this chapter, discretization schemes for reaction–diffusion equations were presented. Both structured and unstructured meshes were considered. Methods based on finite differences and finite volumes lead to algorithms for computing the mass matrix and the stiffness matrix. A new mathematical reformulation of a discretization scheme for a triangular mesh of a general 3D-surface was notably developed. This scheme has by construction several advantages:

- the weight matrix can be easily and efficiently computed,
- a true tiling of the domain is constructed so that no-flux boundary conditions are correctly taken into account,
- inhomogeneous and anisotropic diffusion properties can be introduced,
- exact conservation of current is ensured for all mesh resolutions (this is of particular importance to compute electrograms based on those current sources),
- the finite-dimensional dynamical system resulting from the spatial discretization was shown to be stable when no reaction term is present,
- efficient explicit time integration schemes can be implemented.

The most important properties of diffusive systems, namely conservation of current and stability, are therefore preserved after spatial discretization. This means that in both the continuous and the discretized model, whatever the initial condition, the solution tends toward a homogeneous state in the absence of reaction and external stimulation.

Finally, a simple extension to multi-layer structures was proposed as a first step toward full 3D modeling.

*It relies on the identities: $\exp(A + B) = \exp(A)\exp(B)$ if $AB = BA$, and $\exp(A \otimes \mathbb{I}) = \exp(A) \otimes \mathbb{I}$.

Time Integration

After spatial discretization, the monodomain propagation equations for an active tissue become an initial value problem of the form (see subsection 3.3.1 and 5.3.4)

$$\frac{d\mathbf{u}}{dt} = A\mathbf{u} + \mathbf{f}(\mathbf{u}, \mathbf{s}, t) \quad (6.1)$$

$$\frac{d\mathbf{s}}{dt} = \mathbf{g}(\mathbf{u}, \mathbf{s}, t) \quad (6.2)$$

where \mathbf{u} represents the membrane potential field, \mathbf{s} the state of all cells, A the discretized diffusion operator, \mathbf{f} the aggregate membrane current and \mathbf{g} is associated with the membrane kinetics. Numerical integration of these equations is performed through a time discretization $t = 0, \Delta t, 2\Delta t, 3\Delta t \dots$ and an iterative scheme of the form

$$\left(\mathbf{u}^{(k)}, \mathbf{s}^{(k)} \right) \mapsto \left(\mathbf{u}^{(k+1)}, \mathbf{s}^{(k+1)} \right) \quad (6.3)$$

where $\mathbf{u}^{(k)}$ (resp. $\mathbf{s}^{(k)}$) is an approximation of $\mathbf{u}(k\Delta t)$ (resp. $\mathbf{s}(k\Delta t)$).

This chapter describes the schemes used in the present study to solve Eqs. (6.1) and (6.2). An operator-splitting method is introduced (section 6.1) in order to divide the problem into a diffusion step (section 6.2) and a reaction step (section 6.3).

6.1 Operator Splitting

In some situations, it is fruitful to consider separately reaction and diffusion. This is a common procedure in advection–reaction–diffusion systems arising in atmospheric pollution modeling,²⁰⁹ reacting flows^{210,211} and in viscoelastic fluid mechanics.²¹² Similar methods were introduced in cardiac modeling by Qu *et al.*²¹³ and applied to a 3D ventricular model by Yung.^{10,186} The resulting scheme enables an adaptive choice of the time step, a property highly desirable when a large range of time constants are present, like in cardiac tissue models.

6.1.1 Principle

Let us consider a dynamical system which splits into a sum (see Lanser²⁰⁹ or Budd²¹⁴)

$$\frac{d\mathbf{x}}{dt} = \mathbf{h}(\mathbf{x}) = \mathbf{h}_1(\mathbf{x}) + \mathbf{h}_2(\mathbf{x}) \quad (6.4)$$

Here \mathbf{h}_1 may represent the diffusion term and \mathbf{h}_2 the reaction term. If we assume that a convenient or efficient method is known to solve both $d\mathbf{x}/dt = \mathbf{h}_1(\mathbf{x})$ and $d\mathbf{x}/dt = \mathbf{h}_2(\mathbf{x})$ through an updating scheme $\mathbf{x}^{(k+1)} = \mathcal{U}_{\Delta t}^{(1)}(\mathbf{x}^{(k)})$ and $\mathbf{x}^{(k+1)} = \mathcal{U}_{\Delta t}^{(2)}(\mathbf{x}^{(k)})$ respectively, we would then suggest to solve Eq. (6.4) by combining both schemes

$$\mathbf{x}^{(k+1)} = \mathcal{U}_{\Delta t}^{(1)}\left(\mathcal{U}_{\Delta t}^{(2)}\left(\mathbf{x}^{(k)}\right)\right) \quad \text{or} \quad \mathbf{x}^{(k+1)} = \mathcal{U}_{\Delta t}^{(2)}\left(\mathcal{U}_{\Delta t}^{(1)}\left(\mathbf{x}^{(k)}\right)\right), \quad (6.5)$$

that is, by alternating the updating schemes $\mathcal{U}_{\Delta t}^{(1)}$ and $\mathcal{U}_{\Delta t}^{(2)}$. The remaining of this section will show why and how such a method is applicable to reaction–diffusion systems. Some mathematical notations concerning ordinary differential equations will be first introduced.

6.1.2 Flow Operators

The *flow operator* $\Phi_{\Delta t}^{(\mathbf{h})}$ associated with an ordinary differential equation $d\mathbf{x}/dt = \mathbf{h}(\mathbf{x})$ is a function defined by the relation²¹⁵

$$\mathbf{x}(t + \Delta t) = \Phi_{\Delta t}^{(\mathbf{h})}(\mathbf{x}(t)) \quad (6.6)$$

where $\mathbf{x}(t)$ is a solution of the differential equation. When the equation is linear, i.e. if $\mathbf{h}(\mathbf{x}) = B\mathbf{x}$, the flow operator is given by $\Phi_{\Delta t}^{(\mathbf{h})}(\mathbf{x}) = \exp(B\Delta t)\mathbf{x}$. In the general non-linear case, it is surprisingly still possible to write the flow in an exponential form. This form, briefly explained below, turns out to be crucial for the derivation of splitting methods.

The *Lie derivative* (associated with the vector field \mathbf{h}) of a function $\mathbf{F}(\mathbf{x})$ is a function defined as

$$(\mathcal{D}_{\mathbf{h}}\mathbf{F})(\mathbf{x}) = \frac{\partial \mathbf{F}}{\partial \mathbf{x}} \mathbf{h}(\mathbf{x}) \quad (6.7)$$

where $\partial \mathbf{F}/\partial \mathbf{x}$ is the Jacobian matrix. Using that definition, the successive Lie derivatives of the identity function $\mathbb{I}(\mathbf{x}) = \mathbf{x}$ are

$$(\mathcal{D}_{\mathbf{h}}\mathbb{I})(\mathbf{x}) = \mathbf{h}(\mathbf{x}) \quad \text{and} \quad \left(\mathcal{D}_{\mathbf{h}}^{k+1}\mathbb{I}\right)(\mathbf{x}) = \frac{\partial}{\partial \mathbf{x}}\left(\mathcal{D}_{\mathbf{h}}^k\mathbb{I}\right)\mathbf{h}(\mathbf{x}) . \quad (6.8)$$

When evaluated at $\mathbf{x}(t)$, a solution of $d\mathbf{x}/dt = \mathbf{h}(\mathbf{x})$, Eq. (6.8) becomes

$$(\mathcal{D}_{\mathbf{h}}\mathbb{I})(\mathbf{x}(t)) = \mathbf{h}(\mathbf{x}(t)) = \frac{d\mathbf{x}(t)}{dt} \quad (6.9)$$

$$\left(\mathcal{D}_{\mathbf{h}}^{k+1}\mathbb{I}\right)(\mathbf{x}(t)) = \frac{d}{dt}\left(\left(\mathcal{D}_{\mathbf{h}}^k\mathbb{I}\right)(\mathbf{x}(t))\right) = \frac{d^{k+1}\mathbf{x}(t)}{dt^{k+1}} . \quad (6.10)$$

The flow operator can now be calculated from its Taylor expansion with respect to Δt

$$\Phi_{\Delta t}^{(\mathbf{h})}(\mathbf{x}(t)) = \sum_{k \geq 0} \frac{d^k \mathbf{x}}{dt^k} \frac{\Delta t^k}{k!} = \sum_{k \geq 0} \frac{\Delta t^k}{k!} \left(\mathcal{D}_{\mathbf{h}}^k\mathbb{I}\right)(\mathbf{x}(t)) = \left(\exp(\Delta t \mathcal{D}_{\mathbf{h}})\mathbb{I}\right)(\mathbf{x}(t)) \quad (6.11)$$

and the desired exponential form appears

$$\Phi_{\Delta t}^{(\mathbf{h})} = \exp(\Delta t \mathcal{D}_{\mathbf{h}})\mathbb{I} \quad (6.12)$$

General splitting methods are based on this formula.

6.1.3 Splitting Formulae

A *splitting formula* is an approximate relation between $\Phi_{\Delta t}^{(\mathbf{h}_1+\mathbf{h}_2)}$, $\Phi_{\Delta t}^{(\mathbf{h}_1)}$ and $\Phi_{\Delta t}^{(\mathbf{h}_2)}$. In the linear case $\mathbf{h}(\mathbf{x}) = B_1\mathbf{x} + B_2\mathbf{x}$, those flows are respectively $\exp(\Delta t(B_1 + B_2))$, $\exp(\Delta t B_1)$ and $\exp(\Delta t B_2)$. Those three exponentials are related through the following splitting formulae^{209,214,216}

$$e^{(B_1+B_2)\Delta t} = e^{B_1\Delta t} e^{B_2\Delta t} + \mathcal{O}(\Delta t^2) \quad (6.13)$$

$$= e^{B_1\Delta t/2} e^{B_2\Delta t} e^{B_1\Delta t/2} + \mathcal{O}(\Delta t^3). \quad (6.14)$$

The former approximation is known as *Lie–Trotter splitting* and the latter *Strang splitting*. Both are a direct corollary of the *Baker–Campbell–Hausdorff’s* formula^{209,214,217} for factorization of exponentials. This formula reads $\exp(hX) \exp(hY) = \exp(hZ)$, where Z is given by

$$Z = X + Y + \frac{h}{2}[X, Y] + \frac{h^2}{12}([X, [X, Y]] + [Y, [Y, X]]) + \mathcal{O}(h^3) \quad (6.15)$$

and the commutator is defined as $[X, Y] = XY - YX$.

In the general case, by analogy with the linear case, the Strang splitting naturally generalizes to

$$\Phi_{\Delta t}^{(\mathbf{h}_1+\mathbf{h}_2)} = \Phi_{\Delta t/2}^{(\mathbf{h}_1)} \circ \Phi_{\Delta t}^{(\mathbf{h}_2)} \circ \Phi_{\Delta t/2}^{(\mathbf{h}_1)} + \mathcal{O}(\Delta t^3). \quad (6.16)$$

As a matter of fact, using the exponential form (6.12), the left and the right hand side of Eq. (6.16) become

$$\Phi_{\Delta t}^{(\mathbf{h}_1+\mathbf{h}_2)} = \exp(\Delta t \mathcal{D}_{\mathbf{h}_1} + \Delta t \mathcal{D}_{\mathbf{h}_2}) \mathbb{I} \quad (6.17)$$

$$\Phi_{\Delta t/2}^{(\mathbf{h}_1)} \circ \Phi_{\Delta t}^{(\mathbf{h}_2)} \circ \Phi_{\Delta t/2}^{(\mathbf{h}_1)} = \exp(\Delta t \mathcal{D}_{\mathbf{h}_1}/2) \exp(\Delta t \mathcal{D}_{\mathbf{h}_2}) \exp(\Delta t \mathcal{D}_{\mathbf{h}_1}/2) \mathbb{I} \quad (6.18)$$

since $\mathcal{D}_{\mathbf{h}_1+\mathbf{h}_2} = \mathcal{D}_{\mathbf{h}_1} + \mathcal{D}_{\mathbf{h}_2}$. Baker–Campbell–Hausdorff’s formula also applies in this case* and leads to the result anticipated above.

6.1.4 Application to Reaction–Diffusion Systems

Let us now apply this operator splitting procedure to the reaction–diffusion system (6.1)–(6.2). First, since the differential system depends *explicitly* on time, a new state variable τ associated with the equation $\frac{d\tau}{dt} = 1$ has to be included in order to make the system autonomous. The state vector is now $\mathbf{x} = (\mathbf{u}, \mathbf{s}, \tau)$. With these notations, Eqs. (6.1) and (6.2) become

$$\frac{d\mathbf{x}}{dt} = \mathbf{h}_1(\mathbf{x}) + \mathbf{h}_2(\mathbf{x}) \quad \text{where} \quad \mathbf{h}_1(\mathbf{x}) = \begin{pmatrix} A\mathbf{u} \\ 0 \\ 0 \end{pmatrix} \quad \text{and} \quad \mathbf{h}_2(\mathbf{x}) = \begin{pmatrix} \mathbf{f}(\mathbf{u}, \mathbf{s}, \tau) \\ \mathbf{g}(\mathbf{u}, \mathbf{s}, \tau) \\ 1 \end{pmatrix}. \quad (6.19)$$

If the flow operators are written

$$\Phi_{\Delta t}^{(\mathbf{h}_1)}(\mathbf{x}) = \begin{pmatrix} \exp(A\Delta t)\mathbf{u} \\ \mathbf{s} \\ \tau \end{pmatrix} \quad \text{and} \quad \Phi_{\Delta t}^{(\mathbf{h}_2)}(\mathbf{x}) = \begin{pmatrix} \phi_{\Delta t}(\mathbf{u}, \mathbf{s}, \tau) \\ \psi_{\Delta t}(\mathbf{u}, \mathbf{s}, \tau) \\ \tau + \Delta t \end{pmatrix}, \quad (6.20)$$

*Although in Eq. (6.15) X , Y and Z were implicitly supposed to be matrices, Baker–Campbell–Hausdorff’s formula is still valid in general Lie algebra with the exponential map defined accordingly (see Varadarajan²¹⁷)

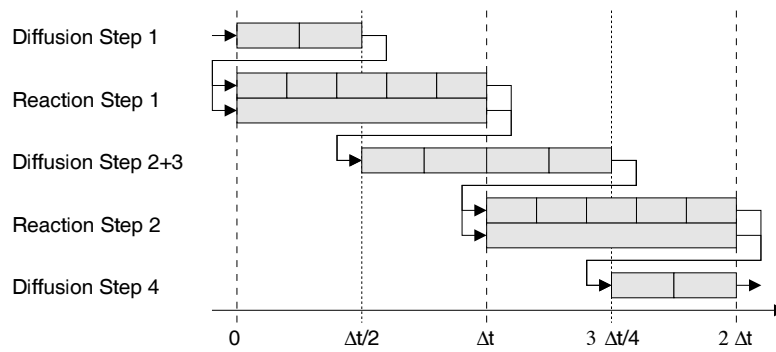


Figure 6.1 — Block-diagram view of the time stepping scheme for the two first time steps. Diffusion step 1: only diffusion is considered during $\Delta t/2$; this step is divided here into two sub-time steps. Reaction step 1: only reaction equations are solved (separately for each cell); here this step is divided into 5 sub-time steps in a sub-group of cells and performed in a single step for the others. Diffusion step 2+3: two successive diffusion steps are combined together. Reaction step 2: reaction equations are again considered . . .

then the Strang splitting (6.16) leads to

$$\begin{cases} \mathbf{u}(t + \Delta t) &= \exp(A\Delta t/2) \phi_{\Delta t} \left(\exp(A\Delta t/2) \mathbf{u}(t), \mathbf{s}(t), t \right) + \mathcal{O}(\Delta t^3) \\ \mathbf{s}(t + \Delta t) &= \psi_{\Delta t} \left(\mathbf{u}(t), \mathbf{s}(t), t \right) + \mathcal{O}(\Delta t^3) \end{cases} \quad (6.21)$$

where $\tau(t) = t$ has been substituted.

Section 6.2 will be devoted to find approximations of $\exp(A\Delta t)$, and section 6.3 to find approximations of the functions $\phi_{\Delta t}$ and $\psi_{\Delta t}$.

6.1.5 Adaptive Time Steps

Most cardiac cell models are described by a set of *stiff*²¹⁸ ordinary differential equations. This usually requires a very small time step to solve the stiff reaction equations. Operator splitting enables us to choose small time steps only when and where necessary.

In practice, the splitting time step Δt can be divided into an integer number of sub-time steps usually different for diffusion (subsection 6.2.3) and for reaction (subsection 6.3.2). Moreover, since cell coupling is present only in the diffusion equation, a different number of reaction sub-time steps can be associated with each cell. Typically, cells in the fast activation phase will be attributed smaller sub-time steps than cells in the slow recovery phase. The time stepping scheme becomes therefore space- and time-adaptive. Its sequence of operations is illustrated in Fig. 6.1.

6.2 The Diffusion Step

The purpose of this section is to integrate the diffusion equation $d\mathbf{u}/dt = A\mathbf{u}$ in the time interval $[t, t + \Delta t]$. The analytical solution is known to be $\mathbf{u}(t + \Delta t) = \exp(A\Delta t)\mathbf{u}(t)$. This section is therefore devoted to the construction of appropriate approximations F , of order $n + 1$, for the exponential operator

$$e^{A\Delta t} = F(A\Delta t) + \mathcal{O}(\Delta t^{n+1}) \quad (6.22)$$

	q = 0	q = 1
p = 0	1	1 - z
p = 1	$\frac{1}{1+z}$	$\frac{1-z/2}{1+z/2}$

Table 6.1 — Lowest order Padé approximants of e^{-z} .

in order to define a time integration scheme*

$$\mathbf{u}(t + \Delta t) = e^{A\Delta t}\mathbf{u}(t) = F(A\Delta t)\mathbf{u}(t) + \mathcal{O}(\Delta t^{n+1}) \quad . \quad (6.23)$$

The function F will typically be a rational function.

6.2.1 Padé Approximants

Padé approximants^{183,219} of a function $f(z)$ are rational local approximations of the form $n_{p,q}(z)/d_{p,q}(z)$ satisfying the relation

$$f(z) = \frac{n_{p,q}(z)}{d_{p,q}(z)} + \mathcal{O}(|z|^{p+q+1}) \quad (6.24)$$

where $n_{p,q}(z)$ and $d_{p,q}(z)$ are polynomials of degree q and p respectively.

Numerical schemes can be easily derived from the Padé approximants of the exponential function e^{-z} around $z = 0$ listed in Table 6.1:

$$e^{A\Delta t} = d_{p,q}(-A\Delta t)^{-1} n_{p,q}(-A\Delta t) + \mathcal{O}(\Delta t^{p+q+1}) \quad . \quad (6.25)$$

The corresponding scheme, of order $p + q$, is *consistent* if $p + q > 0$, *implicit* if $p > 0$, and *unconditionally stable* if $p \geq q$ (see Varga²¹⁹ and Strikwerda¹⁸²). Table 6.2 summarizes the most common schemes based on Padé expansions with $p \leq 1$ and $q \leq 1$: forward Euler, backward Euler and Crank–Nicholson. The forward Euler scheme will typically be used with complex unstructured meshes for which the sparse structure of the matrix A would require specific (and possibly computationally extensive, *i.e.*, slower) tools for implicit integration (bandwidth reduction, iterative solvers, . . .). Structured meshes, however, enable an efficient use of the Crank–Nicholson scheme with the help of a mathematical development presented just below.

6.2.2 Alternating Direction Implicit

Suppose that the matrix A splits into a sum of two commuting matrices A_1 and A_2 . Then

$$A_1 A_2 = A_2 A_1 \quad \implies \quad e^{A\Delta t} = e^{A_1 \Delta t} e^{A_2 \Delta t} \quad (6.26)$$

This is the case when an (orthotropic anisotropic) diffusion operator is discretized, *i.e.* when $A_1 = D_x \delta_x^2$ and $A_2 = D_y \delta_y^2$. Eq. (6.26) is however verified up to the second order in Δt even if A_1 and A_2 do not commute.

*Notice that in spite of an error term in $\mathcal{O}(\Delta t^{n+1})$, this scheme is of order n in Δt since $\frac{\mathbf{u}(t+\Delta t) - \mathbf{u}(t)}{\Delta t} = \frac{F(A\Delta t) - \mathbb{1}}{\Delta t} + \mathcal{O}(\Delta t^n)$

$p = 0, q = 1$	Forward Euler scheme
Approximation:	$e^{A\Delta t} = \mathbb{I} + A\Delta t + \mathcal{O}(\Delta t^2)$
Scheme (1st order):	$\mathbf{u}^{(k+1)} = (\mathbb{I} + A\Delta t) \mathbf{u}^{(k)}$
$p = 1, q = 0$	Backward Euler scheme
Approximation:	$e^{A\Delta t} = (\mathbb{I} - A\Delta t)^{-1} + \mathcal{O}(\Delta t^2)$
Scheme (1st order):	$(\mathbb{I} - A\Delta t) \mathbf{u}^{(k+1)} = \mathbf{u}^{(k)}$
$p = 1, q = 1$	Crank–Nicholson scheme
Approximation:	$e^{A\Delta t} = (\mathbb{I} - A\Delta t/2)^{-1} (\mathbb{I} + A\Delta t/2) + \mathcal{O}(\Delta t^3)$
Scheme (2nd order):	$(\mathbb{I} - A\Delta t/2) \mathbf{u}^{(k+1)} = (\mathbb{I} + A\Delta t/2) \mathbf{u}^{(k)}$
Other formulation:	$(\mathbb{I} - A\Delta t/2) \mathbf{u}^{(k+1/2)} = \mathbf{u}^{(k)}$ $\mathbf{u}^{(k+1)} = 2\mathbf{u}^{(k+1/2)} - \mathbf{u}^{(k)}$

Table 6.2 — Well-known schemes based on lowest-order Padé approximants: Forward Euler, Backward Euler and Crank–Nicholson. Thanks to a mathematical trick, Crank–Nicholson scheme reduces to a backward Euler step followed by a linear combination (like a predictor-corrector scheme), thus increasing the backward Euler scheme’s accuracy with little additional computational effort.²²⁰

The factors $e^{A_1\Delta t}$ and $e^{A_2\Delta t}$ can be approximated separately. A Crank–Nicholson approximation of each one

$$e^{A\Delta t} = (\mathbb{I} - A_1\Delta t/2)^{-1} (\mathbb{I} + A_1\Delta t/2) (\mathbb{I} - A_2\Delta t/2)^{-1} (\mathbb{I} + A_2\Delta t/2) + \mathcal{O}(\Delta t^3) \quad (6.27)$$

leads to the second order *Peaceman–Rachford scheme*^{182, 219, 221, 222}

$$(\mathbb{I} - A_1\Delta t/2) \mathbf{u}^{(k+1/2)} = (\mathbb{I} + A_1\Delta t/2) \mathbf{u}^{(k)} \quad (6.28)$$

$$(\mathbb{I} - A_2\Delta t/2) \mathbf{u}^{(k+1)} = (\mathbb{I} + A_2\Delta t/2) \mathbf{u}^{(k+1/2)} \quad (6.29)$$

The variable $\mathbf{u}^{(k+1/2)}$ should be thought of as a temporary variable and not as an approximation of \mathbf{u} at time $t + \Delta t/2$. This method is widely used for 2D parabolic problems,^{223, 224} and in particular in cardiac modeling.^{28, 97} Extension to three-term splitting for 3D diffusion is straightforward.^{28, 219}

In a rectangular 2D geometry with homogeneous diffusion properties, $A_1 = D_x \delta_x^2$ and $A_2 = D_y \delta_y^2$, and there exists a permutation matrix P such that both A_1 and $A'_2 = P^{-1} A_2 P$ are tridiagonal matrices in a certain basis. The scheme is now based only on tridiagonal systems

$$(\mathbb{I} - A_1\Delta t/2) \mathbf{u}^{(k+1/4)} = (\mathbb{I} + A_1\Delta t/2) \mathbf{u}^{(k)} \quad (6.30)$$

$$\mathbf{u}^{(k+1/2)} = P^{-1} \mathbf{u}^{(k+1/4)} \quad (6.31)$$

$$(\mathbb{I} - A'_2\Delta t/2) \mathbf{u}^{(k+3/4)} = (\mathbb{I} + A'_2\Delta t/2) \mathbf{u}^{(k+1/2)} \quad (6.32)$$

$$\mathbf{u}^{(k+1)} = P \mathbf{u}^{(k+3/4)} \quad (6.33)$$

It is called *Alternating Direction Implicit*²²³ because the first step involves only diffusion in the x -axis, and the second step in the y -axis. This method and its variants are popular

because solving a tridiagonal systems and permuting the components of a vector are easily and efficiently implemented.^{182, 224}

6.2.3 Time Step Subdivision

Suppose an approximation $F(A\Delta t)$, of order $n + 1$, for the exponential $\exp(A\Delta t)$ is known. A more precise approximation (but of the same order) is obtained by N_d iterations:

$$\exp(A\Delta t) = F^{N_d}\left(\frac{A\Delta t}{N_d}\right) + \mathcal{O}(\Delta t^{n+1}) \quad . \quad (6.34)$$

For instance, the refined forward Euler scheme reads

$$\exp(A\Delta t) = \left(\mathbb{I} + \frac{A\Delta t}{N_d}\right)^{N_d} + \mathcal{O}(\Delta t^2/N_d) \quad . \quad (6.35)$$

This formula is useful when the splitting time step Δt does not give an adequate accuracy for the diffusion step or even when Δt is larger than the stability limit (in the case of an explicit scheme). Although higher order explicit schemes with the same number of matrix multiplications are available (e.g., Taylor expansion of the exponential), approximation (6.35) has an advantage: the stability limit for Δt is multiplied by N_d . The number N_d of time step subdivisions is generally time-independent, and will be typically set to 3 in practice when dealing with a large unstructured mesh (see next chapter).

6.3 The Reaction Step

Because the cells are coupled only through the membrane potential u , the reaction equations can be solved independently for each cell in the time interval $[t, t + \Delta t]$

$$\frac{du}{dt} = f(u, \mathbf{s}, t) \quad \text{and} \quad \frac{d\mathbf{s}}{dt} = \mathbf{g}(u, \mathbf{s}, t) \quad (6.36)$$

where \mathbf{s} represents here the state of a single cell. This enables a refinement of the time discretization only when and where needed.

6.3.1 Forward Euler Update

The main requirement for the corresponding numerical scheme is a high efficiency, while only a moderate accuracy is needed.²²⁵ Since the functions f and \mathbf{g} are usually very time consuming, their evaluations have to be limited. Although high-order schemes have been proposed, including Newton method with Steffenson optimization¹⁹⁶ and variants of Runge-Kutta,²²⁵ the explicit Euler scheme satisfies these conditions and has been widely used for this purpose:

$$u^{(k+1)} = u^{(k)} + \Delta t \cdot f\left(u^{(k)}, \mathbf{s}^{(k)}, t\right) \quad (6.37)$$

$$\mathbf{s}^{(k+1)} = \mathbf{s}^{(k)} + \Delta t \cdot \mathbf{g}\left(u^{(k)}, \mathbf{s}^{(k)}, t\right) \quad . \quad (6.38)$$

The structure of some equations, in particular gating variables (subsection 6.3.3), makes possible an improvement in accuracy without increase of computational effort. On the other hand, some slow variables (subsection 6.3.4) can be integrated with larger time steps so that the computational time is reduced without significant decrease in accuracy.

6.3.2 Time-Adaptive Stepping

Suppose $\mathcal{U}_{\Delta t}$ gives an updating scheme to solve Eq. (6.36)

$$\left(u^{(k+1)}, \mathbf{s}^{(k+1)}\right) = \mathcal{U}_{\Delta t} \left(u^{(k)}, \mathbf{s}^{(k)}\right) \quad (6.39)$$

More accuracy can be achieved by iterating this scheme N_k times

$$\left(u^{(k+1)}, \mathbf{s}^{(k+1)}\right) = \left(\mathcal{U}_{\Delta t/N_k} \circ \cdots \circ \mathcal{U}_{\Delta t/N_k}\right) \left(u^{(k)}, \mathbf{s}^{(k)}\right) \quad (6.40)$$

The number of sub-time steps N_k may be time-dependent (as indicated by the index k). It is usually an integer between 1 and 10. The choice of N_k can be related to the time derivative of the potential²¹³

$$N_k = \left\lfloor \alpha \left| \frac{du}{dt} \right| \right\rfloor \quad (6.41)$$

where α is a scaling constant, together with the constraint $1 \leq N_k \leq N_{max}$.

But the range of du/dt is wide because of the steep upstroke so that this method tends to select most of the time $N_k = 1$ and $N_k = N_{max}$. It is therefore more convenient to choose only two different sub-time steps, one for the upstroke and the other one for the repolarization phase.⁹⁷ Selection is done by thresholding

$$N_k = \begin{cases} 1 & \text{if } \frac{du}{dt} \leq \dot{u}_{thres} \\ N_{max} & \text{if } \frac{du}{dt} > \dot{u}_{thres} \end{cases} . \quad (6.42)$$

6.3.3 Gating variables: Rush–Larsen Scheme

A *gating variable* y satisfies an equation of the form (see subsection 3.2.2)

$$\frac{dy}{dt} = \frac{y_{\infty}(u) - y}{\tau_y(u)} . \quad (6.43)$$

If the dependence in u in the gate equation can be neglected in the time interval $[t, t + \Delta t]$, an analytical solution is obtained

$$y(t + \Delta t) = y_{\infty} + (y(t) - y_{\infty}) e^{-\Delta t/\tau_y} . \quad (6.44)$$

This suggests the *Rush–Larsen scheme*^{226,227}

$$y^{(k+1)} = y_{\infty}(u^{(k)}) + (y^{(k)} - y_{\infty}(u^{(k)})) e^{-\Delta t/\tau_y(u^{(k)})} \quad (6.45)$$

$$= a_y(u^{(k)}, \Delta t) y^{(k)} + b_y(u^{(k)}, \Delta t) \quad (6.46)$$

where $a_y(u, \Delta t) = e^{-\Delta t/\tau_y(u)}$ and $b_y(u, \Delta t) = y_{\infty}(u) (1 - e^{-\Delta t/\tau_y(u)})$. This method has several decisive advantages:

1. *Accuracy*: the scheme accuracy only depends on the variations of u in the time interval $[t, t + \Delta t]$ and not on the time derivative of y . As a consequence, the time step can be chosen regardless the time derivative of the gating variables. This is of special importance during the repolarization phase where the membrane potential u decreases slowly while some gates may open or close quickly.

2. *Stability*: if $0 \leq y^{(k)} \leq 1$, then necessarily $0 \leq y^{(k+1)} \leq 1$ (under the natural assumptions $0 \leq y_\infty \leq 1$ and $\tau_y > 0$).
3. *Efficiency*: if Δt is limited to a restricted set of values (e.g. only two), lookup tables of both $a_y(u, \Delta t)$ and $b_y(u, \Delta t)$ can be created for each possible time step. The resulting updating step includes now only one multiplication and one addition (plus some memory accesses).

6.3.4 Slow Variables

If the component s_i of the cell state vector \mathbf{s} varies very slowly, an update every Δt may not be necessary. A forward Euler update every N_{s_i} time steps is then formalized as

$$s_i^{(k+1)} = s_i^{(k)} + \begin{cases} N_{s_i} \Delta t \cdot g_i(\mathbf{s}^{(k)}, t) & \text{if } k \equiv 0 \pmod{N_{s_i}} \\ 0 & \text{otherwise} \end{cases}. \quad (6.47)$$

For instance, the slowly drifting Na^+ and K^+ intracellular concentrations belong to that class of variables. A time-dependence of N_{s_i} can be easily introduced if more accuracy is needed during the upstroke phase (e.g. for variables associated with the Ca^{2+} dynamics).

6.4 Conclusion

When dealing with a large set of stiff differential equations, an efficient time integration scheme is necessary. By considering reaction and diffusion separately, the operator splitting procedure leads to adaptive time stepping schemes capable of speeding up computations during the slow repolarization phase, while keeping a sufficiently accurate description of the depolarization process.

The diffusion step can be performed using the common forward/backward Euler or Crank–Nicholson schemes. Explicit or implicit time integration is preferred depending on the computational effort required to solve the linear system involved. For instance, the alternating direction implicit scheme is adequate for structured meshes, but an explicit Euler scheme may be faster for a complex triangular mesh when the stability limit for the time step is not too small.

The reaction step generally consists in a simple forward Euler update because of the large number of computationally expensive functions involved. Gating variables and some slowly drifting variables are given a special attention since a better trade-off between speed and accuracy is possible.

Numerical Methods in Action

This chapter describes how the numerical methods presented in the two previous chapters were used in this study. The whole process of simulation from parameters configuration to post-processing is illustrated by a simple example, a simulation of normal sinus rhythm in a computer model of human atria. A special emphasis will be given to the computation of electrograms and to the analysis of numerical accuracy.

7.1 Running Simulations

The steps involved in a computer simulation of electrophysiology are briefly overviewed in this section. Guidelines for the selection of parameters are presented and illustrated in an example of sinus rhythm.

Selection of the Mathematical Model

First, the full set of equations governing the system dynamics has to be selected. This implies the choice of a geometry (and thus a mesh describing this geometry), a cell model, and a framework to combine cell excitability and impulse propagation, here the monodomain formulation.

In the simple example of sinus rhythm, a monodomain tissue model based on the normal Courtemanche *et al.* human atrial cell model was used on a geometry of human atria based on MR images.

Definition of Tissue Properties

The equations of the mathematical model depend on many electrophysiological parameters characterizing the *substrate*: conduction properties (tissue resistivity), anisotropy (fiber orientation), cell membrane (membrane capacitance, channel conductances, parameters of the channel gates, . . .), and also the presence of heterogeneities possibly both in conduction and membrane properties. Typical value of some of the generic parameters are reported on Table 7.1 and are used by default.

An advantage of computer models is precisely that these parameters can be easily and reliably assigned to any value at any location in the tissue. In our example of sinus rhythm, an isotropic homogeneous tissue with a resistivity of $\rho = 80 \Omega \text{ cm}$ and based on uniform unmodified cellular properties was considered. The resistivity was chosen so as to obtain a ho-

Parameter	Symbol	Value
Membrane capacitance	C_m	$1 \mu\text{F}/\text{cm}^2$
Cell surface-to-volume ratio	S_v	$0.24 \mu\text{m}^{-1}$
Tissue resistivity	ρ	$80\text{--}800 \Omega \text{ cm}$

Table 7.1 — *Typical tissue parameters for simulations.*

mogeneous conduction velocity of about 90 cm/s corresponding to normal conditions^{228,229} (see section 4.2.2).

Stimulation Protocol

Most simulated dynamics, from sinus rhythm to atrial fibrillation, were initiated by a programmed stimulation protocol (no model of sino-atrial node and ectopic beats was included). Stimulations are applied by injecting intracellular current through the membrane.

In the case of sinus rhythm, a stimulus current of amplitude $I_{\text{stim}} = 80 \mu\text{A}/\text{cm}^2$ and duration 2 ms is periodically applied to a region with an approximate area of 3 mm^2 and located near the anatomical location of the sino-atrial node. The cycle length was set to 500 ms.

Spatial Discretization

The mathematical problem is well posed and numerical approximations of the solution have to be found. The choice of appropriate solvers depends on the geometry, and therefore on the mesh. In a two-dimensional rectangular geometry discretized using a regularly spaced structured mesh, a finite difference method combined with an alternating direction implicit scheme was used because of the efficiency and the stability of its semi-implicit time integration. For the unstructured triangular mesh representing the atrial surface, the finite volume method proposed in section 5.3 was preferred because it enables fast explicit time integration by avoiding having to solve a large linear system.

4×4-cm sheet		Atrial geometry	
Δx	N	Δx	N
1000 μm	1.6k	1000 μm	17k
800 μm	2.5k	- μm	-
600 μm	4.4k	600 μm	50k
500 μm	6.4k	500 μm	68k
400 μm	10k	400 μm	100k
300 μm	17.8k	300 μm	200k
200 μm	40k	200 μm	400k
100 μm	160k	- μm	-

Table 7.2 — *Average spatial resolution (Δx) and approximated number of vertices (N) for each mesh of a 4×4-cm sheet of tissue and for each mesh of the atrial geometry used in the present study (atrial meshes with $\Delta x = 100$ or $800 \mu\text{m}$ were not constructed). The suffix k means 1000, i.e. 100k=100 000.*

After the choice of a numerical scheme, the spatial resolution Δx has to be carefully selected. In the general case, Δx is defined as the average edge length of the mesh. In a regular structured mesh, Δx is simply the size of a square element. For both the rectangular geometry and the atrial model, meshes with spatial resolution ranging from 100 to 1000 μm were constructed and their accuracy was analyzed and compared (see below, section 7.3). Table 7.2 shows the relation between the spatial resolution and the resulting mesh size. The final choice of Δx is a trade-off between accuracy and computer power requirements. Standard simulations are run with $\Delta x = 150\text{--}200 \mu\text{m}$ in the rectangular sheet of tissue and with $\Delta x = 400 \mu\text{m}$ in the atrial model. Finer meshes are used to check the consistency of the results and to ensure the absence of artifacts.

Time integration

Operator splitting was used to separate diffusion and reaction. In this case, several time steps are defined. The splitting time step Δt_{split} is subdivided into several diffusion time steps Δt_{diff} (sub-time steps for the diffusion part), into several reaction time steps $\Delta t_{\text{react}\uparrow}$ during the upstroke phase (sub-time steps for the reaction part) and into several reaction time steps $\Delta t_{\text{react}\downarrow}$ during the repolarization phase.

Table 7.3 shows the values of the time steps used in the present study. Qu and Garfinkel verified that a splitting time step of $\Delta t_{\text{split}} = 100 \mu\text{s}$ leads to sufficiently small splitting error.²¹³ This value is therefore used for structured meshes. The diffusion time step may be, however, restricted to smaller values because of the stability limit when explicit time integration is chosen. For instance, in the triangular mesh of the atria, the diffusion time step was reduced from 17 to 10 μs and the splitting time step from 50 to 30 μs when the spatial discretization is refined from $\Delta x = 400$ to $\Delta x = 300$ or 200 μm . The reaction time step was always in the range 10–12.5 μs during depolarization, and to the largest admissible value ($\Delta t_{\text{react}\downarrow} = \Delta t_{\text{split}}$) during repolarization. These remarks are consistent with those of Yung *et al.*^{10, 186}

Time step	Structured mesh	Triangular mesh ($\Delta x \geq 350 \mu\text{m}$)	Triangular mesh ($\Delta x < 350 \mu\text{m}$)
Δt_{split}	100 μs	50 μs	30 μs
Δt_{diff}	100/1 = 100 μs	50/3 \approx 17 μs	30/3 = 10 μs
$\Delta t_{\text{react}\uparrow}$	100/8 = 12.5 μs	50/4 = 12.5 μs	30/3 = 10 μs
$\Delta t_{\text{react}\downarrow}$	100/1 = 100 μs	50/1 = 50 μs	30/1 = 30 μs

Table 7.3 — Time steps used in the present study for structured and unstructured meshes: splitting time step (Δt_{split}), diffusion time step (Δt_{diff}), and reaction time steps during upstroke ($\Delta t_{\text{react}\uparrow}$) and repolarization ($\Delta t_{\text{react}\downarrow}$). Because the scheme for triangular meshes is explicit, the time steps have to be reduced when Δx is decreased.

Computer Simulation and Implementation

The simulation code was written in C/C++ and is composed of modules corresponding to cell models, geometries and numerical schemes. This modular approach was found to be efficient and flexible. Membrane kinetics computations were optimized by look-up tables.

On a standard single processor PC (Pentium III Xeon, 1.4 GHz running Linux), 2 hours of CPU time and 48 MB memory are required for a one-second simulation on a 100k-nodes mesh whose membrane kinetics is given by the Courtemanche *et al.* model. The speed is roughly doubled when the Luo–Rudy model is used instead because of its simplified membrane kinetics. The solver spends approximately 25% of the CPU time for the diffusion part and the remaining for the reaction part (Courtemanche *et al.* model). This fraction increases up to 55% when the Luo–Rudy is used. Although parallelization can be efficiently applied to this class of problems,^{230,231} we limited ourselves to sequential processing because very often a large set of simulations with similar protocol and settings had to be launched at the same time on several processes.

The program is able to output the time-course of membrane potential or any other cell variable recorded at any point of the tissue, membrane potential maps dumped typically every 5 ms, activation times, unipolar/bipolar electrograms or electrical mapping data, and finally a dump of the complete tissue state for starting later new simulations with this state as initial condition.

Visualization of Results

The output files are finally loaded in Matlab[®] (The MathWorks, Inc.) for post-processing and plotting. Visualization of potential maps and generation of image sequences were performed in a specific tool written using the OpenGL[®] library (see www.opengl.org).

Fig. 7.1 displays the activation pattern and isochrones in our example of sinus rhythm. The sinus beat propagates from the right to the left atrial tissue. Atrial activation terminates in the left lateral wall below the appendage, where the wavefronts converge. The total activation time is about 110 ms. Despite some differences due to the absence of specialized conductive structures like Bachman’s bundle or crista terminalis, the global behavior of the activation maps is comparable to those available from experimental data²³² or other anatomical models.⁷

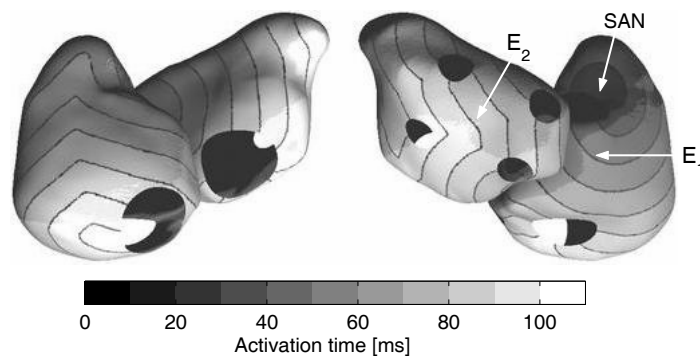


Figure 7.1 — Activation map and isochrones during normal sinus rhythm activation initiated from the sinoatrial node (SAN). Isochrones are drawn every 10 ms. The points denoted by E_1 and E_2 represent the location of unipolar electrodes (see next section).

7.2 Computing Electrograms

Extracellular or bath potential can be estimated in a monodomain formulation by assuming a superposition of potential fields from each of the transmbrane current sources.^{31,233} This approach has been used by Spach *et al.*²³⁴ to compare simulated and experimental signals in thin tissue, and more recently by Gima and Rudy²³⁵ in an inhomogeneous cable. In our case, it is assumed that the tissue is thin and lies in an extensive conductive bath, and that the current sources are located at the surface of the tissue.

Unipolar electrograms are computed according to the current source approximation (4.17) adapted for monolayer models with constant thickness. The extracellular (or bath) potential at \mathbf{x} is given by

$$\phi_0(\mathbf{x}, t) = \frac{1}{4\pi\sigma_0} \int_{\Omega_{\text{epi}}} d\mathbf{y} \delta \frac{S_v I_m(\mathbf{y}, t)}{\|\mathbf{x} - \mathbf{y}\|} \quad (7.1)$$

where Ω_{epi} represents the epicardial surface, $d\mathbf{y}$ is an infinitesimal surface element, δ is the (small) thickness of the tissue, σ_0 the surrounding bath conductivity, I_m the current source per unit area of membrane surface, and S_v the cell surface-to-volume ratio. Numerical quadrature of this integral is performed by lumping the sources. On a mesh \mathcal{M} containing vertices i located at \mathbf{x}_i and associated with a region of area Ω_i , the approximation reads

$$\phi_0(\mathbf{x}, t) = \frac{S_v \delta}{4\pi\sigma_0} \sum_{i \in \mathcal{M}} \Omega_i \frac{I_m(\mathbf{x}_i, t)}{\|\mathbf{x} - \mathbf{x}_i\|} + \mathcal{O}(\Delta x) \quad (7.2)$$

where the factor $S_v \delta / 4\pi\sigma_0$ is a constant. Since only I_m is time-dependent in the right hand side, a unipolar electrogram is computed as a linear combination of current sources. The membrane current I_m is obtained by applying the diffusion operator to the membrane potential field, so that the electrogram is also a linear combination of membrane potentials.^{31,199} Fig. 7.2 shows unipolar electrograms computed during sinus rhythm at sites E_1 and E_2 whose location is displayed on Fig. 7.1.

Only one parameter characterizes a simulated electrode: its distance d to the epi- or endocardial surface (see subsection 4.3.2). This parameter determines the length scale of the averaging effect, *i.e.*, roughly speaking, the region an electrode can see. A value of

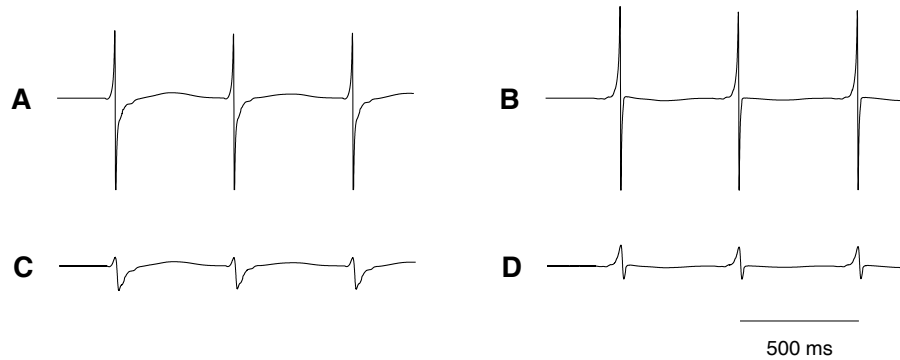


Figure 7.2 — Examples of simulated unipolar electrograms (arbitrary unit) during sinus rhythm with a cycle length of 500 ms. The electrodes are located in the right (A,C) and in the left (B,D) atrium at sites E_1 and E_2 respectively (these sites are shown on Fig. 7.1), 1 mm (A-B) or 5 mm (C-D) from the atrial surface.



Figure 7.3 — Comparison of simulated and clinical bipolar electrograms, both during sinus rhythm. (A) Simulated bipolar electrogram (normalized amplitude) measured in the right atrium. (B) Clinical bipolar electrogram (normalized amplitude) measured during routine intracardiac mapping. In both case, the distance between the unipolar electrodes is 2 mm.

$d = 1$ mm was used to simulated electrodes in contact with the cardiac tissue, in order to compensate the fact that the model of electrode is point-shaped. Notice that this value corresponds to the order of magnitude of the diameter of the sensor in the decapolar catheter electrode (7 French, BARD catheter) which was used to record experimental signals during routine intracardiac mapping for comparison with simulated signals (see below). The choice of the distance d was motivated by the following constraints:

- *Validity of the formula:* The $1/r$ weighting assumes an infinite homogeneous volume conductor. This approximation, used for the sake of simplicity, is only valid for locations close to the heart surface, where the volume-conductor boundary effects and conductor heterogeneities have a limited impact, say, $d \ll 1$ cm.
- *Numerical quadrature:* Comparison with equivalent problems in electrostatics shows that, at a distance of about 1–2 times the average distance Δx between the sources considered as punctual, the field is comparable to that generated by a distributed source density (see Feynman²³⁶). So, a value $d \geq 2\Delta x$ would be enough to sufficiently reduce the differences (in amplitude notably) observed between an electrode located right over a source and an electrode equidistant to two or three sources.
- *Comparison with experimental signals:* Finally, the decisive criterion is the comparison with real electrograms. The distance d determines the width of the peak observed during an activation (a small distance d gives a marked peak with large amplitude and short width, see Fig. 7.2) and is adjusted in order to lead to the experimentally measured peak width.

Fig. 7.3 shows a comparison of simulated bipolar electrograms with 2-mm spacing with those obtained from a decapolar catheter (7 French, BARD catheter with electrode spacing of 2 mm and a sampling rate of 1 kHz) during routine intracardiac mapping of the atria. The simulated and clinical electrograms show an excellent agreement, in particular concerning their shape and peak width, and justify the choice $d = 1$ mm.

7.3 Numerical Accuracy

In every area of numerical analysis, it is of crucial importance to be informed on the accuracy of the numerical solution. In this section, mesh quality and convergence of the numerical

solution are assessed using physiologically relevant quantities.

7.3.1 Mesh Quality

Partial differential equations solvers require a sufficiently regular mesh. Assessing mesh quality is usually performed by geometrical measures depending on mesh elements. It is, however, interesting in specific applications to relate mesh quality to some meaningful physical quantities. For instance, using exactly the same meshes as in the present study, Blanc¹⁵ computed the maximal time step allowed for explicit time integration of the propagation equation, leading to a global measure of mesh quality. Here, we start from the requirement that homogeneous isotropic conduction properties should lead to a regular homogeneous wavefront propagation (curvature effects excepted). For this purpose, the safety factor for conduction is introduced as a tool to detect and localize mesh irregularities susceptible to generate wavefront propagation artifacts (local mesh quality) and as a tool to assess the global mesh quality through the dispersion of safety factor.

Safety Factor

The *safety factor* (SF) for conduction is defined as the ratio of charge generated to charge consumed during the excitation cycle of a cell.^{237,238} The fraction of $SF > 1$ indicates a margin of safety. If I_m is the membrane current, $I_c = C_m \frac{\partial V_m}{\partial t}$ is the capacitive current, I_{in} and I_{out} are inward and outward diffusion currents ($I_m = I_{in} - I_{out} = I_c + I_{ion}$), then SF is computed as

$$SF = \frac{Q_c + Q_{out}}{Q_{in}} \quad (7.3)$$

where each charge is associated with its corresponding current

$$Q_m(t) = \int_0^t dt' I_m(t') \quad \text{and} \quad Q_{c|in|out} = \int_{\{t|Q_m>0\}} dt I_{c|in|out}(t) . \quad (7.4)$$

The domain of integration is the interval during which $Q_m(t) > 0$, that is when the cell consumes charges for its depolarization.

Local Mesh Quality Assessment

For each mesh of the atrial surface, a wavefront propagation is initiated near the sinoatrial node with homogeneous isotropic resistivities set to $\rho = 200 \Omega \text{ cm}$. The SF was then computed at each vertex of the mesh. Fig. 7.4 shows a SF map of a mesh with a spatial resolution of $\Delta x = 400 \mu\text{m}$. Apparently random variations (in the range $SF = 2\text{--}2.5$) are observed because SF depends on the orientation of each triangular element with respect to the wavefront. Notice that this randomness is an advantage of triangular meshes since it prevents the “square wave” effect often seen in structured meshes at coarse resolution,¹⁵ that is, wavefront propagation is more isotropic at the macroscopic level in triangular meshes as compared to structured meshes with similar resolution. A careful analysis reveals a correlation between SF and the mesh structure (the mesh was generated by creating first quadrilateral patches on the surface). Moreover, a comparison with the activation map (Fig. 7.1) shows that SF is smaller in the regions where wavefronts merge, or close to a boundary, because Q_{out} is significantly reduced in those cases.

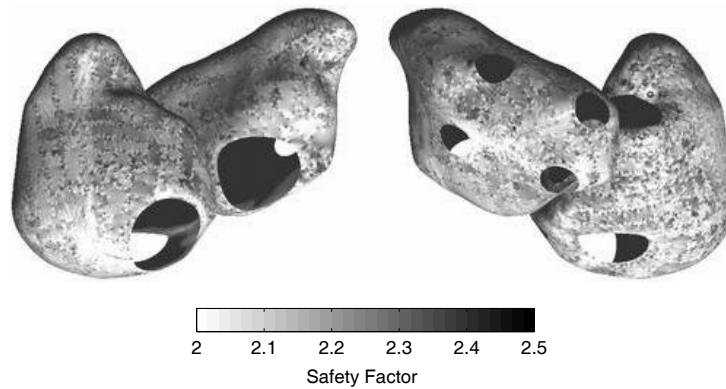


Figure 7.4 — Safety factor map computed on a mesh with $\Delta x = 400 \mu\text{m}$ (100k nodes). Note that the scale is restricted to the range 2–2.5.

Global Mesh Quality Comparison

Fig. 7.5 presents SF statistics and histograms for meshes with average spatial resolution of 200, 300, 400, 500, 600 and 1000 μm . In addition, SF s measured in 1D-cables with similar discretization and conduction properties are displayed on Fig. 7.5A and are consistently slightly higher than the values corresponding to a triangular mesh (conduction is safer in 1D than in 2D). The observed SF range 1.5–3 corresponds to the values reported in the literature.^{237,238} The mean SF increases with the spatial discretization Δx (Fig. 7.5A) due to the smaller coupling (the “vertex-to-vertex” coupling is $\mathcal{O}(\rho^{-1}\Delta x^{-2})$ in the discretized system), in agreement with Shaw and Rudy.²³⁷ Fig. 7.5B shows that the peak of SF

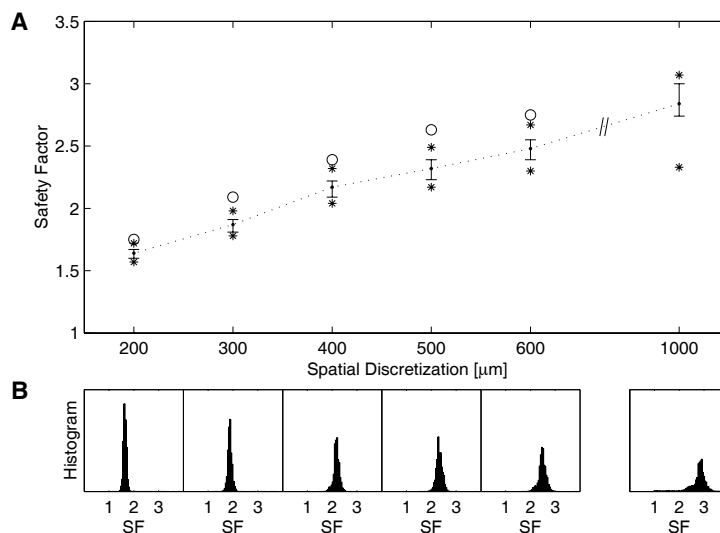


Figure 7.5 — Distribution of safety factors (SF) for meshes of the atrial surface with different spatial resolutions. SF s are computed during a normal sinus beat with a homogeneous isotropic resistivity of $\rho = 200 \Omega \text{cm}$. (A) 25th, 50th, 75th percentile (error bars), 10th and 90th percentile (stars) of SF distribution for each mesh. The circles represent the SF computed on a 1D-cable (linear strand of cells) with the same spatial discretization and conduction properties. (B) SF histograms.

Δx	SD	IQI
1000 μm	14.0 %	9.2 %
600 μm	6.3 %	6.5 %
500 μm	5.8 %	6.9 %
400 μm	5.6 %	6.0 %
300 μm	5.1 %	5.3 %
200 μm	4.3 %	4.2 %

Table 7.4 — Dispersion of safety factor (SF) on meshes of the atrial surface with different spatial resolutions Δx . Standard deviation (SD) and interquartile interval (IQI) of the safety factor are expressed as a percentage of the median of the SF distribution.

distributions is more pronounced for finer resolutions. This is confirmed by Table 7.4 showing that the standard deviations (SD) and interquartile intervals (IQI) of SF distributions, normalized with respect to the median, are smaller in finer meshes, leading to a smoother wavefront propagation. Some dispersion in SF is however expected even for a very fine mesh because of the effect of wavefront curvature on conduction velocity. For spatial discretization $\Delta x \leq 400 \mu\text{m}$ corresponding to the meshes used for the simulations, the dispersion of SF (both SD and IQI) are $\leq 6\%$. These values lead to a sufficiently smooth wavefront propagation as confirmed by visual inspection.

7.3.2 Convergence

In order to appropriately choose the spatial discretization parameters, convergence has to be checked by progressively reducing the maximal element size Δx . Accuracy is then estimated as a function of Δx . In cardiac electrophysiological models, common measures of accuracy of the solution are root-mean square error of the potential field,^{37,200} conduction velocity of a propagating wavefront,^{15,97,213,239,240} characteristics of spiral dynamics^{15,213} (e.g. cycle length or steady-state action potential duration), and diffusion current⁹⁹ (neighborhood stimulating current).

Average conduction velocities (CV) were computed during a simple propagation in a 1-by-1 cm square tissue regularly discretized, and on triangular meshes of the atrial surface, with spatial discretization Δx ranging from 100 to 1000 μm for the square tissue and from 200 to 1000 μm for the atrial model. In all cases, the resistivity is set to $\rho = 200 \Omega \text{cm}$, the membrane capacitance to $C_m = 1 \mu\text{F}/\text{cm}^2$, and the cell surface-to-volume ratio to $S_v = 0.24 \mu\text{m}^{-1}$. The discretization of a monodomain propagation equation is characterized by the parameter $\rho C_m S_v \Delta x^2$, expressed in milliseconds.¹⁵ The golden standard $\Delta x = 45 \mu\text{m}$ proposed by Wu and Zipes²⁴⁰ was used on a 1D cable with the same resistivity to measure the reference CV for the calculation of the relative numerical error on CV .

Fig. 7.6 displays the numerical error on CV as a function of the discretization parameter $\rho C_m S_v \Delta x^2$ for a wavefront propagation initiated from a corner of a square tissue (dashed lines), and for a normal sinus rhythm propagation on the atrial geometry (continuous line). In the square tissue, the numerical error on CV is significantly smaller along the diagonal direction than along the natural grid direction.¹⁵ The numerical error on CV measured on the triangular mesh of the atrial geometry lies between those two curves. With a spatial

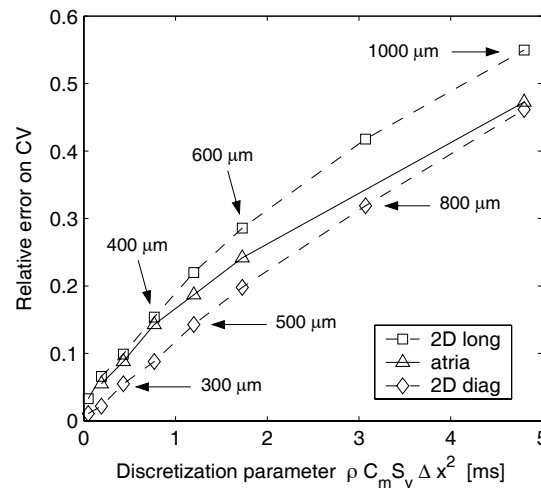


Figure 7.6 — Relative error on the conduction velocity (CV) for different spatial discretizations characterized by the parameter $\rho C_m S_v \Delta x^2$. Recall that Δx is the average spatial discretization in unstructured meshes. Dashed curves represent simulations on a square mesh (propagation initiated from a corner), with CV measured along the diagonal (diamond markers) and in the longitudinal axis along a boundary (square markers). The continuous curve with triangular markers represents simulations on the atrial geometry (propagation initiated from the sino-atrial node). Annotations show the average element size corresponding to the parameters $\rho = 200 \Omega \text{ cm}$, $C_m = 1 \mu\text{F}/\text{cm}^2$ and $S_v = 0.24 \mu\text{m}^{-1}$.

discretization $\Delta x = 400 \mu\text{m}$, a relative error $< 15\%$ is achieved. The error is reduced to about 5% if $\Delta x = 200 \mu\text{m}$. Although these errors are still non-negligible, such coarse discretization levels are commonly used as a trade-off between accuracy and computational requirements (or even tractability) of the numerical problem¹⁵ (see also Table 7.2).

7.4 Conclusion

This chapter described the practical issues concerning computer simulation of cardiac electrophysiology through the chronological sequence of operations from parameters configuration and simulation setups to post-processing and visualization. Then, a method to compute unipolar and bipolar electrograms in a monodomain formulation was discussed. It will be the starting point for most of the attempts toward model validation. Finally, tools for the assessment of numerical accuracy and local/global mesh quality based on physiologically relevant quantities were presented and applied to a computer model of human atria during normal sinus rhythm. Arguments were given to justify *a posteriori* the adequacy of the meshes used in the present work for the simulation of wavefront propagation. Such tools may be used directly during the mesh design phase for a better control over the numerical errors.

Part III

Simulated Atrial Fibrillation

This third part describes several computer models of atrial fibrillation (AF) in which the initiation and maintenance mechanisms can be identified and examined. Different mechanisms of initiation of simulated AF through clinically relevant pacing protocols are discussed in chapter 8. Then, chapter 9 is devoted to AF perpetuation. Models based on multiple independent wavelets, meandering wavelets and mother rotor are successively considered. These dynamics of simulated AF are examined in chapter 10 in terms of activation patterns, spatial organization and wavelength.

Initiation of Atrial Fibrillation

Different mapping techniques have provided experimental clues on the relevant electrophysiological processes initiating or sustaining arrhythmia. Experimental models of atrial fibrillation (AF) usually involve an intervention, such as the application of a drug or chronic pacing²⁴¹⁻²⁴⁴ to create a substrate for arrhythmogenesis. Often interventions cause considerable shortening of both the effective refractory period and spatial wavelengths, increasing the likelihood of arrhythmias. The maintenance of multiple wavelets appears to be a consistent feature of the AF observed in experimental models. Using *in vivo* extracellular recordings, Allesie *et al.*²⁴⁵ showed that AF induced by programmed electrical stimulation (premature beats or rapid pacing) was characterized by 3–4 wavefronts. In a different experimental model of an explanted sheep heart exposed to acetylcholine, Chen *et al.*²⁴⁶ found using higher resolution optical mapping that AF is comprised of a larger number of wavelets that are short lived and rarely completely reenter. They also found that when reentry of wavelets did occur, it was generally observed at a fixed location such as the left atrial appendage or the right atrial free wall.

While both electrical and optical mapping have provided significant insight into the dynamics of animal models of AF, they are limited practically since all regions of the atria cannot be accessed or recorded simultaneously. Computer models offer the advantage of providing information at multiple biological scales and at nearly cellular spatial resolution. Models, however, are limited by the accuracy of the representation of electrophysiological and anatomical details and the computational requirements.

The combined use of anatomically and electrophysiologically realistic computer models and experimental mapping may help unlock the mechanisms underlying AF. In this chapter, mechanisms of AF initiation are investigated in a computer model of the atria. Simulated AF (SAF) will be initiated using programmed electrical stimulation protocols (described in section 8.1) like S_1 – S_2 – S_3 , burst-pacing and ramp protocols in a tissue with uniform conduction properties and a membrane kinetics based on modified versions of the Luo–Rudy³⁸ and the Courtemanche⁷⁰ models. Initiation mechanisms based on action potential duration (APD) restitution and on APD heterogeneity will be explored in sections 8.2 and 8.3 respectively. This study will lead to several different models of SAF whose dynamics will be analyzed in the following chapters.

8.1 Initiation Protocols

Computer models of AF are determined by the tissue substrate (geometry, cell and conduction properties) and by the initiation protocol (electrical stimulation). This section describes the elements composing the framework of the SAF dynamics considered in this study.

8.1.1 Single Cell Model

The selection of a single cell model is determined by the desired accuracy of the representation of the cell electrophysiological properties and by the available computer power. Several sophisticated and computationally demanding models based on membrane ionic channel kinetics have been published for atrial cells.^{69–72,75–77} In this work, membrane kinetics was described by modified versions of the Luo–Rudy model³⁸ and the Courtemanche model⁷⁰ and lead to different models of SAF. This section presents the main characteristics of these models (action potential shape, rate adaptation).

Modified Luo–Rudy Model

For the study of the basic mechanisms of AF initiation and perpetuation, in particular the effect of restitution, we have chosen to use the Luo–Rudy model.³⁸ Developed originally for ventricular cells, it can be seen as a generic ionic model taking into account the major inward and outward ion fluxes through the cell membrane. This choice was motivated by the desire to reduce computational load and to enable simple and flexible alteration of the restitution curves.

To approximate the specific properties of atrial cells, the original Luo–Rudy model was modified. Using previous analyses of the restitution dynamics of this model,^{29,88,90,92} the channel conductances \overline{G}_{Na} , \overline{G}_K and \overline{G}_{si} associated with the membrane currents I_{Na} , I_K and I_{si} (see Table 3.1) were adjusted in order to reproduce reasonable atrial action potential duration (APD).²⁴⁷ To accomplish this, \overline{G}_{Na} was reduced to 16 mS/cm², \overline{G}_K was set to 0.423 mS/cm² and \overline{G}_{si} to 0.085 mS/cm² as in Qu *et al.*⁹² The resulting APD at rest, 245 ms, is in agreement with the range of atrial refractory periods in humans (220 to 260 ms²³²). These modifications constitute the *baseline model* used in the simulations. Any additional modifications will be discussed as they arise. The maximum slow inward conductance, \overline{G}_{si} , is used as a control parameter as in Qu *et al.*⁹² to affect the APD and restitution properties. \overline{G}_{si} is varied from 0.085 to 0.05 mS/cm².

The restitution dynamics were determined for each \overline{G}_{si} computed on a cable (see Fig. 8.1). The action potential shape is shown for different cycle lengths in Fig. 8.1A. The baseline model has APDs in the range 30–245 ms (computed using a threshold at -60 mV), and a steep restitution. The effect of the control parameter \overline{G}_{si} on the APD restitution is presented on Fig. 8.1B. Decreasing values of \overline{G}_{si} correspond to reduced APD and flattened restitution. For values of $\overline{G}_{si} < 0.06$ mS/cm², the maximal slope is smaller than 1. The relationship between steady-state APD and pacing frequency generated by the modified Luo–Rudy model (Fig. 8.1B) is very similar to that measured experimentally on remodeled atrial cells (see Fig. 1C in Li *et al.*²⁴⁷). Fig. 8.1D shows that \overline{G}_{si} has a negligible influence on the conduction velocity which is mainly determined by the sodium current I_{Na} . Fig. 8.1E displays the bifurcation diagram of APD as a function of regular pacing rate. For each

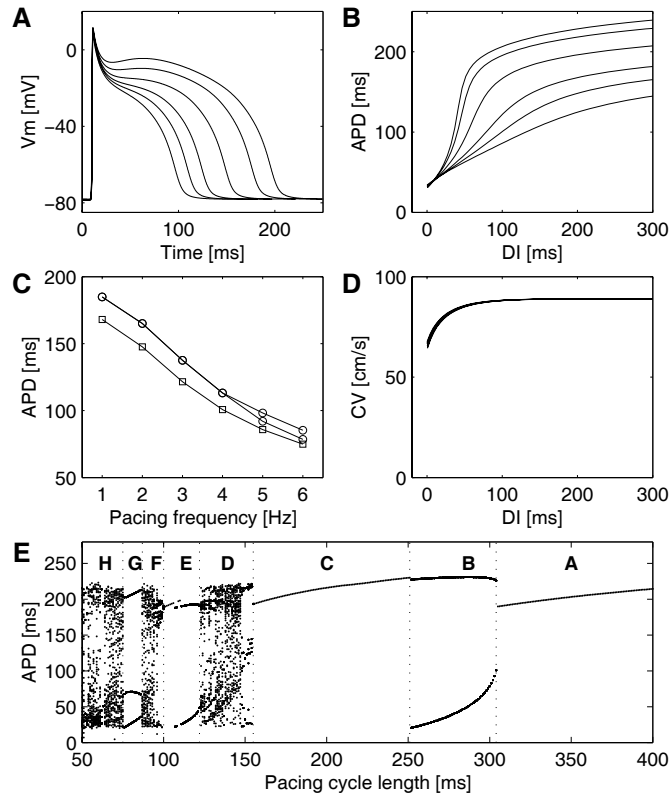


Figure 8.1 — Restitution properties of the modified Luo–Rudy model measured on a 1-cm cable with an element size of $200\ \mu\text{m}$ and a resistivity of $200\ \Omega\text{cm}$. Stimulations are delivered to the first cell with a strength of $2 \times$ diastolic threshold. Diastolic intervals (DIs) and action potential durations (APDs) are measured in the middle of the cable using a $-60\ \text{mV}$ threshold. Protocol: A 100-bpm pacing rate is applied until steady-state is reached. Then a S_2 stimulus with different DIs is delivered. Results: (A) Action potential shapes (with reduced APD, $\bar{G}_{\text{si}} = 0.055\ \text{mS/cm}^2$) are displayed for various cycle lengths from 260 ms to 1000 ms respectively from left to right; (B) APD restitution curves of the modified Luo–Rudy model with $\bar{G}_{\text{si}} = 0.085, 0.08, 0.07, 0.06, 0.055, 0.05\ \text{mS/cm}^2$ respectively from top to bottom; (C) Steady-state APD as a function of the pacing frequency for $\bar{G}_{\text{si}} = 0.055\ \text{mS/cm}^2$ (circles, displaying APD alternans for pacing frequency $\geq 5\ \text{Hz}$) and for $\bar{G}_{\text{si}} = 0.05\ \text{mS/cm}^2$ (squares); (D) Conduction velocity (CV) restitution curves for the same values of \bar{G}_{si} ; (E) Bifurcation diagram of APDs as a function of the pacing cycle length ($\bar{G}_{\text{si}} = 0.085\ \text{mS/cm}^2$). Zones A to H correspond to different dynamical regimes.

pacing cycle length from 50 to 400 ms, the last 50 APDs of 300-beat simulations starting from resting potential were measured and plotted on the figure. At slow rates, one action potential was generated for each stimulus (Fig. 8.1E, zone A). At a cycle length of 310 ms, a period doubling was observed, resulting in a stable alternation of short and long APDs (zone B). For further increase in pacing rate, only one action potential was generated every two stimuli (zone C). At higher rate, additional bifurcations degenerated toward chaotic dynamics (zones D, F and H). Between chaotic zones, stability regions were also observed (zones E and G).

Modified Courtemanche Model

After having investigated the effect of APD restitution on SAF initiation and perpetuation using the modified Luo–Rudy model, a computer model of SAF based on more realistic ionic

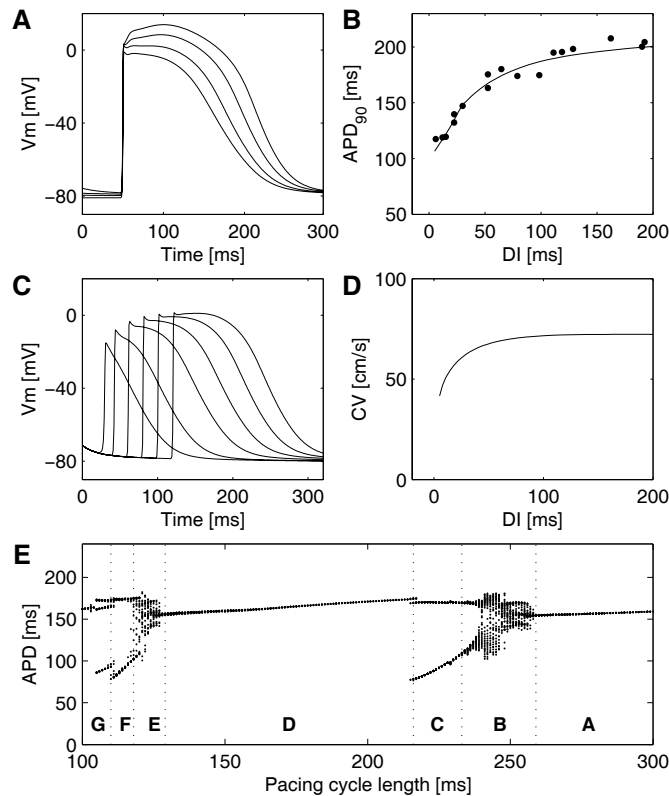


Figure 8.2 — Restitution properties of the modified Courtemanche model measured on a 1-cm cable with an element size of $200\ \mu\text{m}$ and a resistivity of $200\ \Omega\ \text{cm}$. Stimulations are delivered to the first cell with a strength of $2 \times$ diastolic threshold. Diastolic intervals (DIs) and action potential durations (APDs) are measured in the middle of the cable. Protocol: A 100-bpm pacing rate is applied until steady-state is reached. Then a S_2 stimulus with different DIs is delivered. Results: (A) Steady-state action potential shapes are displayed for various pacing rates from 1 Hz to 4 Hz respectively from right to left; (B) APD restitution curve (solid curve) and experimental data from Kim *et al.*,⁷⁹ the APDs being measured in both cases at the 90% repolarization level; (C) Action potential shape for various DIs from 20 to 120 ms; (D) Conduction velocity (CV) restitution curve; (E) Bifurcation diagram of APDs as a function of the pacing cycle length. Zones A to G correspond to different dynamical regimes.

properties and on experimentally measured APD restitution was constructed and studied.

The Courtemanche model,⁷⁰ designed specifically to reproduce human atrial cell electrophysiology, is well adapted for this purpose. When the unmodified Courtemanche model is used, however, the spatial wavelength is too long to sustain SAF for more than one second.²⁴⁸ In order to induce self-sustained SAF, the parameters of the membrane were modified to reasonably reproduce the APD restitution curve of remodeled human atrial cells measured by Kim *et al.* during chronic AF.⁷⁹ The target ionic currents for parameter modification were chosen according to the suggestions of Courtemanche *et al.*⁷¹ The currents I_{to} , I_{CaL} , and I_{Kur} were reduced by 80%, 30% and 90%, and I_{Kr} was increased by 50%, so that APDs were shortened to 210 ms, while the maximal slope of the APD restitution became slightly larger than 1 as described in Kim *et al.*⁷⁹

Fig. 8.2 shows the basic dynamical properties of the modified Courtemanche model. Action potential shape is given for different pacing rates during stable pacing protocol (Fig. 8.2A) and for various diastolic intervals (Fig. 8.2C). APD and CV restitution curves

are plotted on Figs. 8.2B and 8.2D. Experimental data from Kim *et al.*⁷⁹ are superimposed in order to justify the relevance of the membrane parameter modifications. The bifurcation diagram of APD as a function of regular pacing cycle length ranging from 100 to 300 ms (Fig. 8.2E) displays the last 50 APDs of 150-beat simulations run on a cable and illustrates the transitions toward APD alternans (Fig. 8.2E, zone C) and 2:1 block (zone D). Near period doubling bifurcations, the dynamics is characterized by long transients, in agreement with the simulation study of Kneller *et al.*⁷³

Modified Courtemanche Model with Vagal Stimulation

Several experimental models of AF involve exposition to acetylcholine.²⁴⁶ This intervention causes a significant reduction of effective refractory period and a loss of rate adaptation.^{249,250} The resulting AF dynamics is qualitatively different from models characterized by a steeper APD restitution.⁷⁴ The effect of vagal stimulation was added to the modified Courtemanche model in order to analyze different initiation mechanisms arising when APD restitution is flat.

Kneller *et al.*⁷⁴ proposed a mathematical formulation for an acetylcholine-driven potassium current $I_{K(\text{ACh})}$ in a canine atrial cell model based on the Courtemanche model.⁷² The voltage dependence of $I_{K(\text{ACh})}$ was given by (see Fig. 8.3C)

$$I_{K(\text{ACh})} = g_{K(\text{ACh})} \left(0.0517 + \frac{0.4516}{1 + \exp((V_m + 59.53)/17.8)} \right) (V_m - E_K) \quad (8.1)$$

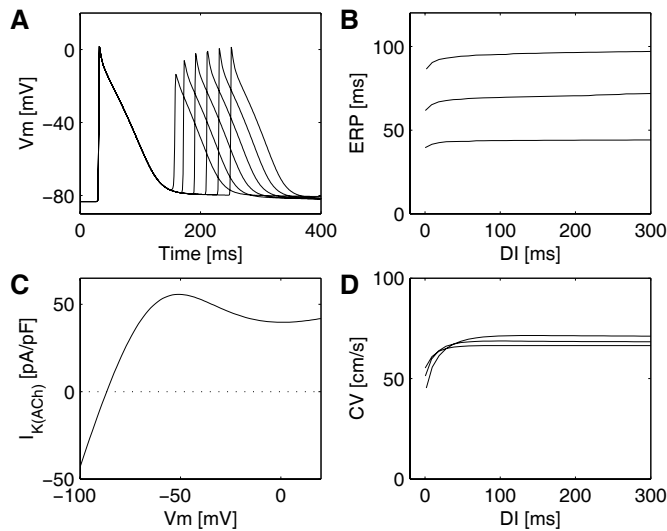


Figure 8.3 — Restitution properties of the modified Courtemanche model with vagal stimulation measured on a 1-cm cable with an element size of $200 \mu\text{m}$ and a resistivity of $200 \Omega \text{ cm}$. Stimulations are delivered to the first cell with a strength of $2 \times$ diastolic threshold. Diastolic intervals (DIs) and action potential durations (APDs) are measured in the middle of the cable. Protocol: A 100-bpm pacing rate is applied until steady-state is reached. Then a S_2 stimulus with different DIs is delivered. Results: (A) Action potential shape for various DIs from 20 to 120 ms; (B) APD restitution curve for $g_{K(\text{ACh})} = 7, 12 \text{ and } 25 \text{ ms}^{-1}$ respectively from top to bottom; (C) Voltage dependence of the current $I_{K(\text{ACh})}$ for $g_{K(\text{ACh})} = 7 \text{ ms}^{-1}$; (D) Conduction velocity (CV) restitution curve for $g_{K(\text{ACh})} = 7, 12 \text{ and } 25 \text{ ms}^{-1}$ respectively from top to bottom.

where V_m is the membrane potential, E_K the reversal potential for potassium channels, and $g_{K(\text{ACh})}$ is a parameter associated with the presence of acetylcholine (ACh). The parameter $g_{K(\text{ACh})}$ is expressed in ms^{-1} because, in the Courtemanche model, currents are given in pA/pF and V_m in mV, and the parameters 0.0517 and 0.4516 are considered to be dimensionless. The value of $g_{K(\text{ACh})}$ will be selected in the range from 0 to 25 ms^{-1} in order to sufficiently reduce the effective refractory period (ERP). This current was added to the list of membrane currents (see chapter 3).

As shown on Fig. 8.3A, the resulting action potential has a triangular shape at all diastolic intervals. Restitution curves (Figs. 8.3A and C) show that the ERP is almost constant when the diastolic interval is varied, and that the CV is only weakly affected by the presence of a vagal stimulation, in agreement with Kneller *et al.*⁷⁴

8.1.2 Conduction Properties

In the simulations of AF initiation presented in this chapter, the conductivities are homogeneous and isotropic. It is then possible to determine whether AF can be initiated in a uniform tissue as a result of only dynamical heterogeneity (repolarization gradients). Inhomogeneities, however, are present in this simplified model due to the anatomical obstacles and the inhomogeneous curvature of the surface.

The resistivity of the model for normal propagation is set to $\rho = 150 \Omega \text{ cm}$ (Luo–Rudy model) or to $\rho = 80 \Omega \text{ cm}$ (Courtemanche model), leading to a conduction velocity (CV) of 90 cm/s (mean value over the atria). For the simulation of arrhythmias, the CV was reduced to values in the range $40\text{--}90 \text{ cm/s}$, in order to decrease wavelength while keeping the CV within physiological (but possibly pathological) range.²⁵¹ Note that a reduction of the CV is perfectly equivalent to a *uniform* dilation of the atria.

8.1.3 Stimulation Protocols

Wavefronts were initiated by injecting intracellular current ($I_{\text{stim}} = 80 \mu\text{A}/\text{cm}^2$) in a small region with a area of about 3 mm^2 during 2 ms (square pulse). Attempts to initiate SAF were performed using the following clinically relevant stimulation protocols illustrated on Table 8.1:

- *Programmed stimulation protocol* ($S_1\text{--}S_2\text{--}S_3$ protocols):^{252,253} Three sites are selected (two sites may coincide). A first stimulus S_1 is applied at site 1. Then, two additional stimuli (premature beats S_2 and S_3) are delivered at site 2 and 3. Both stimulus locations and timing parameters are essential for the success of this method.
- *Burst-pacing protocol*:^{254–258} This protocol simply consists of a 20–50 Hz periodic stimulation of a single site during a few seconds.
- *Ramp protocol*:²⁵⁹ A train of stimuli is delivered to a single site, the time interval between two successive stimuli (*cycle length*, CL) being decremented by Δ after each stimulation. The procedure typically starts with a cycle length such that every stimulus initiates a wavefront propagation. The cycle length is then regularly reduced, *i.e.*, $\text{CL}_{n+1} = \text{CL}_n - \Delta$, until AF is detected.

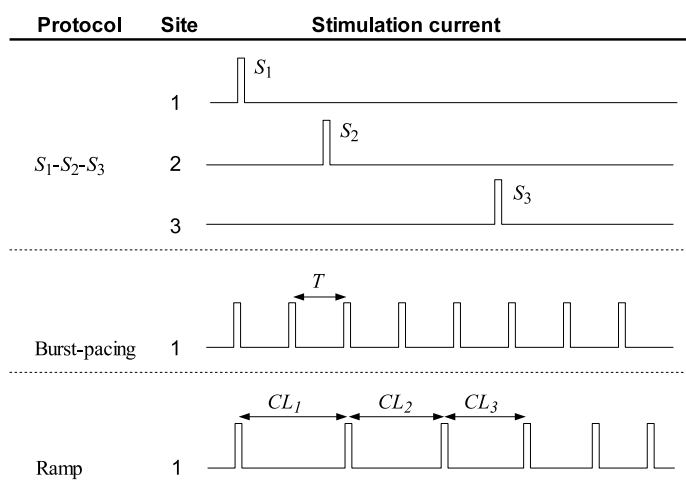


Table 8.1 — Illustration of the stimulation protocols: S_1 - S_2 - S_3 , burst-pacing and ramp protocols. Notations: cycle length (CL), period (T).

The choice of a stimulation protocol for initiating SAF will be based on practical considerations like the efficiency, the difficulty of parameters selection or some limitations of the membrane models.

8.1.4 Output Data and Signal Analysis

To eventually compare data from model simulations with mapping data from animal experiments or human clinical studies, the model was designed to output both transmembrane and extracellular potentials. During simulation, a bipolar electrogram was computed from the difference between the extracellular potential of two points, 2-mm distant from each other and 1 mm from the surface, located in the right atrium free wall. The membrane potential of the node right below the electrode was recorded as well. Membrane potential maps were stored every 5 milliseconds, while electrograms were computed during the simulation every millisecond. In the space plots, action potentials were gray-level-coded, black and white representing respectively 20 and -80 mV.

In addition, phase maps were computed from the membrane potential maps. The phase is an angle variable defined as

$$\theta(\mathbf{x}, t) = \arctan \frac{V_m(\mathbf{x}, t + \tau) - V_m^*}{V_m(\mathbf{x}, t) - V_m^*} \quad (8.2)$$

where V_m^* is a reference potential and τ is a time delay suitable for reconstructing the dynamics from a single signal.¹⁷² In this study, we used $V_m^* = -60$ mV and $\tau = 5$ ms. Because of its angular nature, the phase variable characterizes the state of the cell with respect to the cardiac cycle. At some locations, the phase is not well-defined and the neighboring sites exhibit a continuous progression of phase over the whole range $[0, 2\pi]$ in such a way that¹⁷²

$$\oint \nabla \theta \cdot d\ell = \pm 2\pi \quad (8.3)$$

where the integral is defined over a small closed path surrounding the singularity. Such points are called a *phase singularities* and occur at the tip of a spiral. Localizing and tracking phase singularities was found to be useful to describe the complexity of the dynamics in simple two- and three-dimensional models.^{28, 74, 172, 260}

As a simple measure of complexity and organization, the percentage of excited tissue and the number of wavelets were computed. Cells were considered to be excited when the transmembrane potential exceeded -60 mV. The number of wavelets was defined as the number of connected regions of excited tissue. Non-propagating islands of depolarized tissue were ignored.

8.2 Restitution-Based Simulated Atrial Fibrillation

A key requirement of a computer model of AF is that it produces some number of wavefronts or wavelets that are self-sustaining. One source of instability and induction of wavelet breakup is a steep restitution curve.^{88, 103, 261–264} While spontaneous breakup has been associated with an increase in the slope of the restitution dependence, AF is usually associated with a loss of rate adaption and general flattening of the restitution dependence.^{71, 265} In addition, there is some theoretical evidence that restitution-based breakup may be transient, suggesting that other factors are needed to maintain the arrhythmia.²³⁹

The goal of this study is to investigate the initiation of restitution-based SAF in a model with realistic size and conduction velocity. Programmed stimulation protocols and burst-pacing protocols will be applied to a uniform isotropic tissue using the modified Luo–Rudy model. Different value of the control parameter \bar{G}_{si} ranging from 0.05 to 0.085 mS/cm² will be tested. Then, similar initiation procedures will be investigated with the modified Courtemanche model featuring a more realistic APD range.

8.2.1 S_1 – S_2 – S_3 protocols

Our first attempts to initiate SAF in the model were performed by applying a S_1 – S_2 – S_3 protocol to the baseline model (Luo–Rudy model with $\bar{G}_{si} = 0.085$ mS/cm²) with uniform resistivity set to $\rho = 250$ Ω cm, resulting in a conduction velocity of 70 cm/s. This protocol consists of three stimulations:⁹⁹

- The S_1 stimulus corresponds to a sinus beat and was naturally applied near the anatomical location of the sino-atrial node;
- A first ectopic beat S_2 was then delivered in the right atrium near the superior vena cava with a S_1 – S_2 interval of 310 ms in order to generate repolarization gradients;
- A second ectopic beat S_3 was initiated near the sino-atrial node with a S_2 – S_3 interval ranging from 125 to 145 ms and lead to the first wavebreak.

Fig. 8.4 illustrates the SAF initiation process when the S_2 – S_3 interval is set to 136 ms. After the S_1 , S_2 and S_3 beat propagation (Figs. 8.4A, B and C respectively), a wavebreak occurred and was followed by a figure-of-eight reentry,²⁶⁶ one wavefront extremity being anchored to the superior vena cava (Fig. 8.4D). Further wavebreaks, promoted by the steep restitution as previously demonstrated in 2D and 3D models,^{28–30, 84, 90–92} were observed and helped the fibrillatory activity move toward the left atrium (Figs. 8.4E–H).

Simulations run using the same protocol, but with a S_2 – S_3 interval ranging from 125 to 145 ms showed that the resulting vulnerability window is narrow (between 128 and 129 ms and between 133 and 136 ms). Both location and timing of the stimuli required a careful adjustment. Due to the high sensitivity of the system to these parameters, SAF initiation through S_1 – S_2 – S_3 protocols can be time consuming in a computer model. We will therefore analyze protocols involving less critical parameters, like burst-pacing.

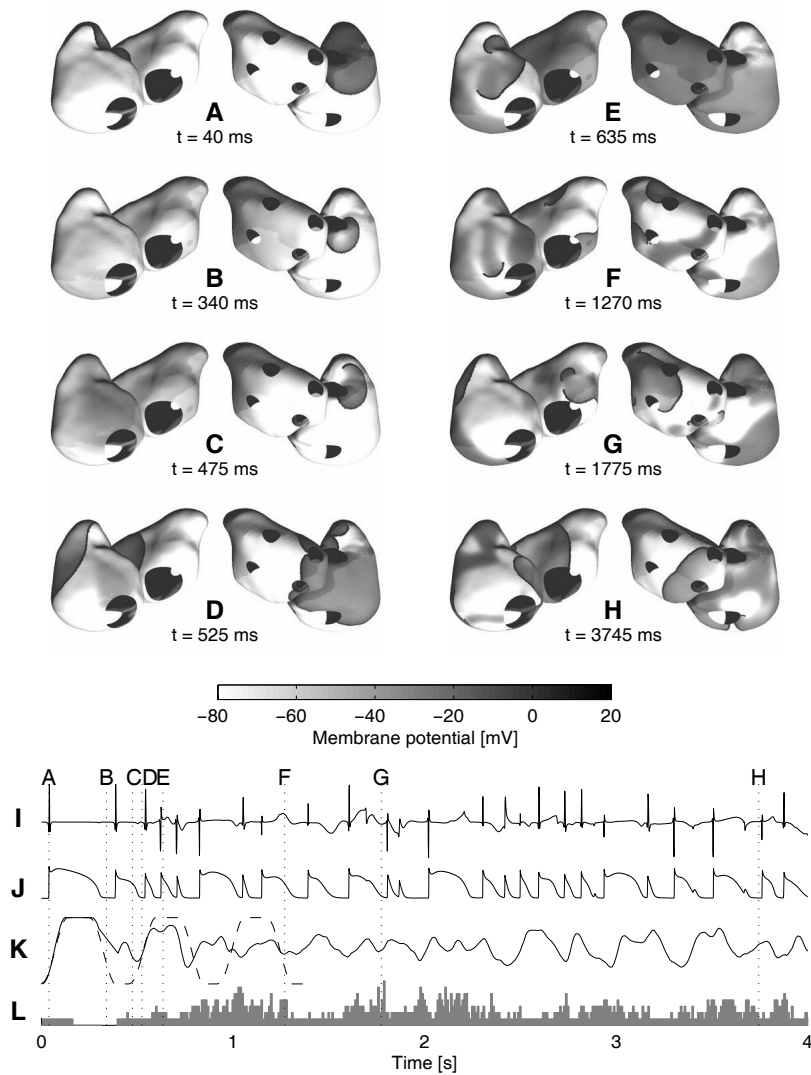


Figure 8.4 — Initiation of SAF in a model with $\bar{G}_{si} = 0.085 \text{ mS/cm}^2$ using a S_1 – S_2 – S_3 protocol. Thick black lines represent wavefronts. (A) First beat showing normal activation with a conduction velocity of 70 cm/s. (B) First ectopic beat. (C) Second ectopic beat. (D) Figure-of-eight reentry around the superior vena cava. (E)–(H) Development of SAF. (I) Bipolar electrogram recorded in the right atrium freewall. (J) Corresponding membrane potential time course. (K) Percentage of excited tissue during SAF initiation (solid line) as well as during sinus rhythm at a cycle length of 470 ms with the same tissue properties (dashed line, range: 0 to 100%). (L) Number of wavelets (range: 0 to 7).

8.2.2 Burst Pacing Protocols

Burst pacing protocols are convenient because they only require a single site paced at a fixed rate. In several animal models of atrial arrhythmia, this initiation protocol was applied during a few seconds in the right atrium or near the pulmonary veins, typically using a pacing frequency of 20 Hz²⁵⁴⁻²⁵⁶ or 50 Hz.^{257,258}

In our computer model ($\bar{G}_{si} = 0.05$ to 0.085 mS/cm², $CV = 70$ cm/s), SAF was initiated by means of a burst pacing protocol consisting of a 20 Hz (or 25 Hz) stimulation applied

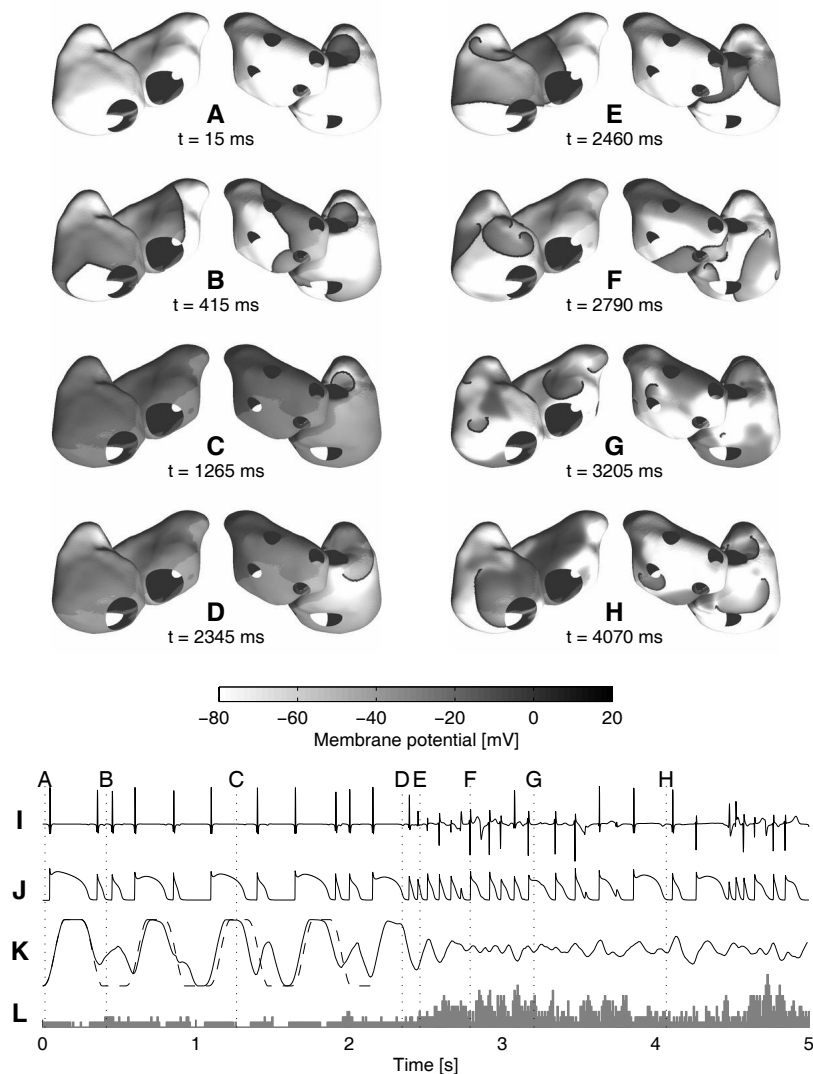


Figure 8.5 — Initiation of SAF in a model with $\bar{G}_{si} = 0.08$ mS/cm² using a burst pacing protocol. These space plots were all stored during burst pacing. Thick black lines represent wavefronts. (A) First beat. (B) Third propagating beat. (C) Seventh propagating beat just before undergoing a functional block. (D) First wavebreak. (E) Figure-of-eight reentry. (F)–(H) Development of SAF. (I) Bipolar electrogram recorded in the right atrium freewall. (J) Corresponding membrane potential time course. (K) Percentage of excited tissue during SAF initiation (solid line) as well as during sinus rhythm at a cycle length of 520 ms with the same tissue properties (dashed line, range: 0 to 100%). (L) Number of wavelets (range: 0 to 10).

near the sino-atrial node for 5 seconds. Due to the refractoriness of the action potentials, most of the stimuli applied during rapid pacing failed to elicit a response and generate a propagating wavefront. As a result, the burst pacing protocol is equivalent to a sequence of premature stimuli, whose diastolic interval at the pacing site is ensured to be shorter than 50 ms (for a 20 Hz pacing), a value lying in the steepest part of the restitution curve (see Fig. 8.1).

Fig. 8.5 illustrates the 20-Hz burst pacing protocol in our atrial model with $\overline{C}_{si} = 0.08$ mS/cm². Fig. 8.5A shows the first beat (equivalent to a sinus beat) and Fig. 8.5B the third one. Figs. 8.5C–H show how after several beats, burst pacing degenerates into multiple independent wavelets traveling randomly in the tissue.

To better understand the mechanism leading to SAF in a homogeneous model, we plotted the evolution of membrane potentials along two lines from the sino-atrial node toward the right atrium appendage. Fig. 8.6 shows a conduction block arising along only one of the two paths, a phenomenon made possible by the symmetry breaking due to the non-planar geometry. It is worth noting that the conduction block can also occur along the whole wavefront, as shown in Fig. 8.5C. The first wavebreak is therefore obtained through a mechanism of non-uniform alternans^{267,268} due to both restitution and geometry. Interactions with the next wavelets initiated at sino-atrial node by the stimulation protocol and with boundaries²⁶⁹ lead to SAF.

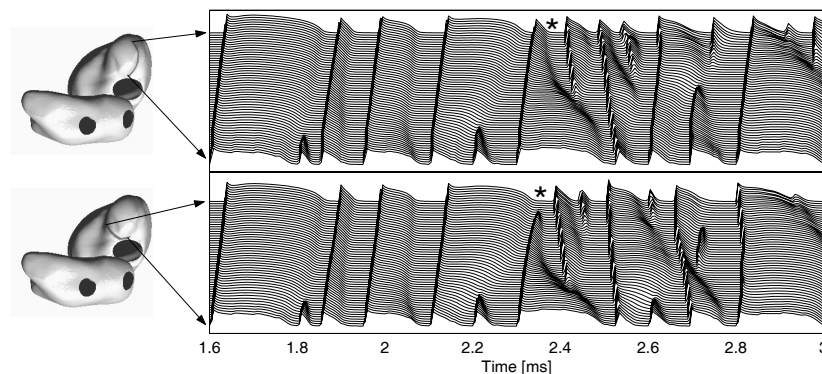


Figure 8.6 — Illustration of the mechanism of conduction block occurring in the right atrium appendage as a result of burst pacing. The membrane potentials along two lines from the sino-atrial node toward the appendage are plotted. The star (\star) indicates the conduction block arising along the second line (bottom panel) and not along the first one (top panel).

But why does the conduction block occur only in some directions? The location and time of a conduction block are actually very sensitive to conduction properties. Fig. 8.7 demonstrates in a 3-cm cable paced at 20 Hz that even a small change in tissue resistivity (here a reduction from 246 to 245 Ω cm) can significantly delay or displace the conduction block. In a uniform tissue, there are no such variations but the geometry alone can play the same role if the curvature of the surface is not constant. As an illustration of the correspondence between geometry and heterogeneity in conduction velocity, isochrones were simulated in a square tissue including a hill-like appendage in the center. Instead of solving a reaction-diffusion system, the activation times were computed using the shortest path algorithm²⁷⁰ in order to exclude non-geometrical effects. Fig. 8.8 displays the isochrones on

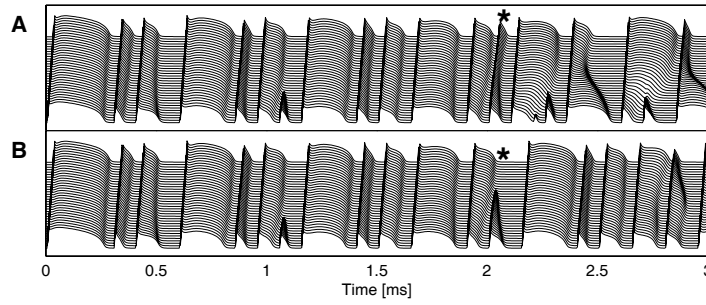


Figure 8.7 — Mechanism of conduction block simulated in a 3-cm cable with a resistivity of 246 Ω cm (panel A) and 245 Ω cm (panel B). A extremity of the tissue is stimulated with a pacing frequency of 20 Hz. The membrane potentials are plotted. The star (*) indicates the conduction block arising in the bottom panel, but not in the top panel.

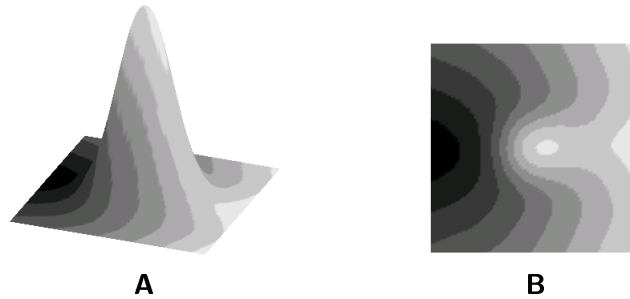


Figure 8.8 — Effect of the geometry in a tissue with uniform conduction properties. Isochrone computed with the shortest path algorithm are plotted on the 3D-surface. Black means early and white late. (A) 3D view. (B) Top view of the same graph.

this 3D-surface. The isochrones seen from above the tissue (top view, Fig. 8.8B) could be equivalently obtained in a planar tissue including a zone of slow conduction. Mathematically, this observation is expressed by a general (non-linear) change of coordinate $\mathbf{x}' = \mathbf{x}'(\mathbf{x})$ leading to exactly the same propagation equation (monodomain formulation) but with a different conductivity tensor $\boldsymbol{\sigma}'(\mathbf{x}') = (\partial\mathbf{x}/\partial\mathbf{x}')^\top \boldsymbol{\sigma}(\mathbf{x}) (\partial\mathbf{x}/\partial\mathbf{x}')$ where $\partial\mathbf{x}/\partial\mathbf{x}'$ is the Jacobian matrix of the transform ($\boldsymbol{\sigma}$ is a rank-2 covariant tensor).

8.2.3 Effect of Restitution

When a burst pacing protocol is applied to the Luo–Rudy-based model, the SAF initiation mechanism was shown to involve an interplay between non-uniform alternans and non-planar geometry. APD restitution is therefore expected to play a key role for SAF initiation in this model.

To quantify the effect of restitution, the same initiation protocol (burst-pacing at 20 Hz and 25 Hz during 5 sec) was used on models with decreasing value of the control parameter \overline{G}_{si} . We successively used $\overline{G}_{\text{si}} = 0.085$ (baseline model), 0.08, 0.07, 0.06, 0.055, 0.05 mS/cm², with all other parameter values remaining the same as in the baseline model. The success of SAF initiation was assessed by considering the time evolution of the number of wavelets.

Table 8.2 summarizes the results of these simulations. For $\overline{G}_{\text{si}} \geq 0.06$ mS/cm², the


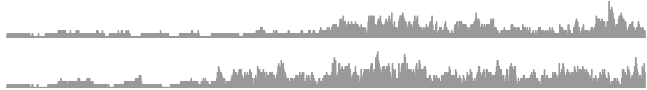
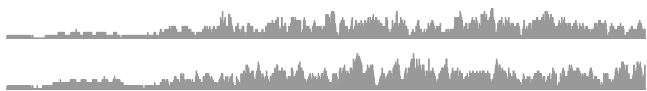
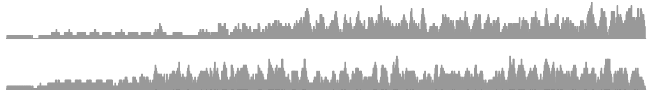


\overline{G}_{si} [mS/cm ²]	max. slope	DI range slope>1	# wavelets (burst-pacing 20 Hz and 25 Hz)
0.085	4.70	64 ms	
0.080	3.68	71 ms	
0.070	2.08	88 ms	
0.060	1.06	90 ms	
0.055	0.76	–	
0.050	0.68	–	

Table 8.2 — Initiation of SAF in models with different restitution dynamics. For each value of the control parameter \overline{G}_{si} , the maximal slope of the static APD restitution curve (i.e., computed using a S_1 - S_2 protocol) and the range of diastolic interval for which the slope is larger than 1 are given. The time evolution of the number of wavelets is shown for two examples of SAF initiation by burst pacing, the first at 20 Hz and the second at 25 Hz.

maximal slope of APD restitution is larger than 1 and SAF could be initiated by both 20 Hz and 25 Hz stimulations. The time of the first wavebreak seems random and actually depends on the precise timing of the propagating beats. When APD restitution is flat, however, SAF could not be initiated (within 5 sec.) in the uniform tissue except in one case with $\overline{G}_{si} = 0.055$ mS/cm² and a pacing frequency of 25 Hz. Interestingly, a detailed analysis of this latter case revealed that the first wavebreak occurred in the left atrium appendage and was preceded by a non-uniform alternans. Fig. 8.9 displays the membrane potential time course recorded close to the left atrium appendage, as well as a reference membrane potential signal simulated in a cable paced at a cycle length of 80 ms.

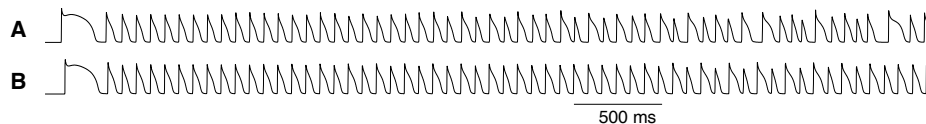


Figure 8.9 — (A) Membrane potential recorded in the left atrium appendage during the 25-Hz burst pacing protocol in a model with $\overline{G}_{si} = 0.055$ mS/cm². (B) Membrane potential recorded during stable pacing with a cycle length of 80 ms in a 1-cm cable with the same conduction and membrane properties as the atrial model.

These results, in agreement with the stable APDs measured at pacing frequencies larger than 4 Hz in a cable (see Fig. 8.1C), suggest that SAF can be initiated in this model provided

that the *dynamic* restitution curve⁹⁶ (APD versus diastolic interval measured during SAF initiation) has a maximal slope larger than 1. The difference between static and dynamic restitution will be studied in subsection 9.1.3.

8.2.4 Ramp Protocols

Now another restitution-based SAF dynamics using the modified Courtemanche model will be initiated in a uniform tissue. Detailed cell models taking into account changes in ionic concentrations (*i.e.*, including memory²⁷¹) like the Courtemanche model may not be well-

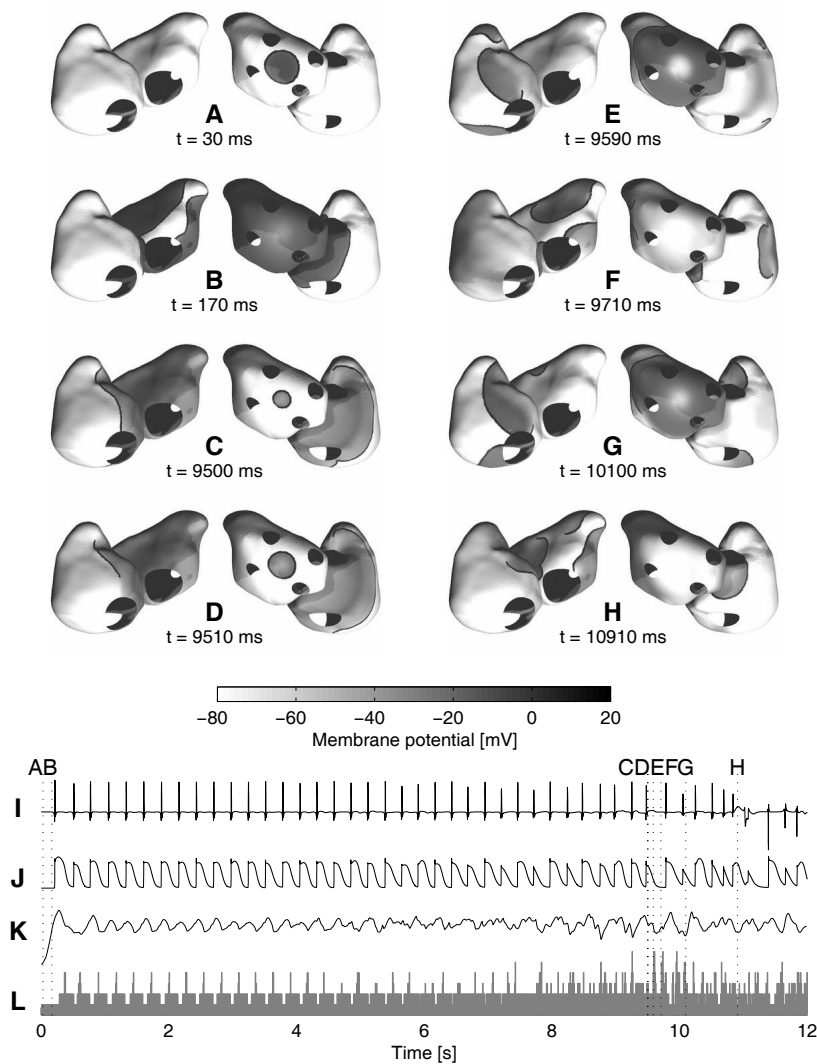


Figure 8.10 — Initiation of SAF using the modified Courtemanche model and a ramp protocol. The cycle length, starting from 260 ms, is decremented by 1 ms every beat. These space plots were all stored during burst pacing. Thick black lines represent wavefronts. (A) First beat. (B) Third propagating beat. (C) Seventh propagating beat just before undergoing a functional block. (D) First wavebreak. (E) Figure-of-eight reentry. (F)–(H) Development of SAF. (I) Bipolar electrogram recorded in the right atrium freewall. (J) Corresponding membrane potential time course. (K) Percentage of excited tissue during SAF initiation. (L) Number of wavelets (range: 0 to 6).

suitable for burst pacing at frequencies ≥ 20 Hz, because high rate pacing involves a large membrane current flow that is not attributed to any ionic species (the stimulation current I_{stim} only appears in the equation expressing the conservation of charge). The effects of this potential violation of the ionic balance equation are still unexplored in this context. In order to remain not too far from the range of pacing rates for which the electrophysiological properties of the cell model were assessed by its authors (cycle lengths between 300 and 1000 ms for the Courtemanche model⁷⁰), a ramp protocol was preferred.

In a tissue with the membrane kinetics of the modified Courtemanche model, a ramp protocol starting with a cycle length of 280 ms was initiated in the pulmonary vein region (or near the sino-atrial node). The stimulation cycle length was decremented by 1 ms every beat. This simulated protocol is comparable to clinical ones. For instance, among many other similar studies, Brignole *et al.*²⁵⁹ induced AF or atrial flutter in patients using ramps with cycle lengths decreased down to 200–240 ms.

The effective refractory period of the modified Courtemanche model is 230 ms at rest and 120 ms for the shortest diastolic interval. As a result, the conduction velocity (CV) had to be reduced in order to sufficiently decrease wavelength and help the maintenance of SAF. With a uniform CV set to 55 cm/s, a transient complex electrical activity lasting for 1–2 s could be initiated. After further reduction of CV to 40 cm/s, long SAF episodes (> 20 sec.) were obtained. These results are in agreement with the simulation study of Cherry *et al.*²⁴⁸ Including anisotropy will enable us to increase the longitudinal CV up to 75 cm/s without preventing SAF dynamics from being self-sustained (see next chapter).

Fig. 8.10 illustrates SAF initiation using a ramp protocol applied in the pulmonary vein region (Figs. 8.10 A–B) in a tissue with uniform conduction velocity reduced to 40 cm/s. The 36th beat (cycle length of 245 ms) lead to a wavebreak (Figs. 8.10 C–D), and then to a reentry and a fibrillatory activity self-perpetuated by 1–3 wavelets (Figs. 8.10 E–H). This first wavebreak was preceded by a non-uniform alternans (see Fig. 8.10J) similar to that observed with the modified Luo–Rudy model in the previous subsections. This process can be followed on the bifurcation diagram of Fig. 8.2E. In the ramp protocol, the cycle length is progressively decreased from the stable region toward APD alternans through the unstable zone dominated by long transients. Ramp protocols applied near the sino-atrial node also induced SAF in the left atrium appendage through a similar mechanism.

8.3 Arrhythmogenic Effect of Heterogeneity

Steep rate adaptation is one mechanism that can lead to initiation and perpetuation of AF. In this case, wavebreaks are induced by dynamical instabilities (APD gradients generated by the restitution dynamics). In general, wavebreaks can also be produced by structural heterogeneities and gradients in APD.⁹¹ Kneller *et al.*⁷⁴ recently developed a two-dimensional computer model of cholinergic AF using a model of canine atrial tissue. Their results suggest that heterogeneities in acetylcholine concentration are sufficient to create fibrillatory conditions despite the complete loss of rate adaptation.

The aim of this section is to illustrate how mechanisms other than rate adaptation can initiate SAF in an anatomical computer model of the atria. The effect of regional heterogeneities in effective refractory period (ERP) on SAF initiation was investigated in the model including vagal stimulation described in subsection 8.1.1. The resulting SAF dynam-

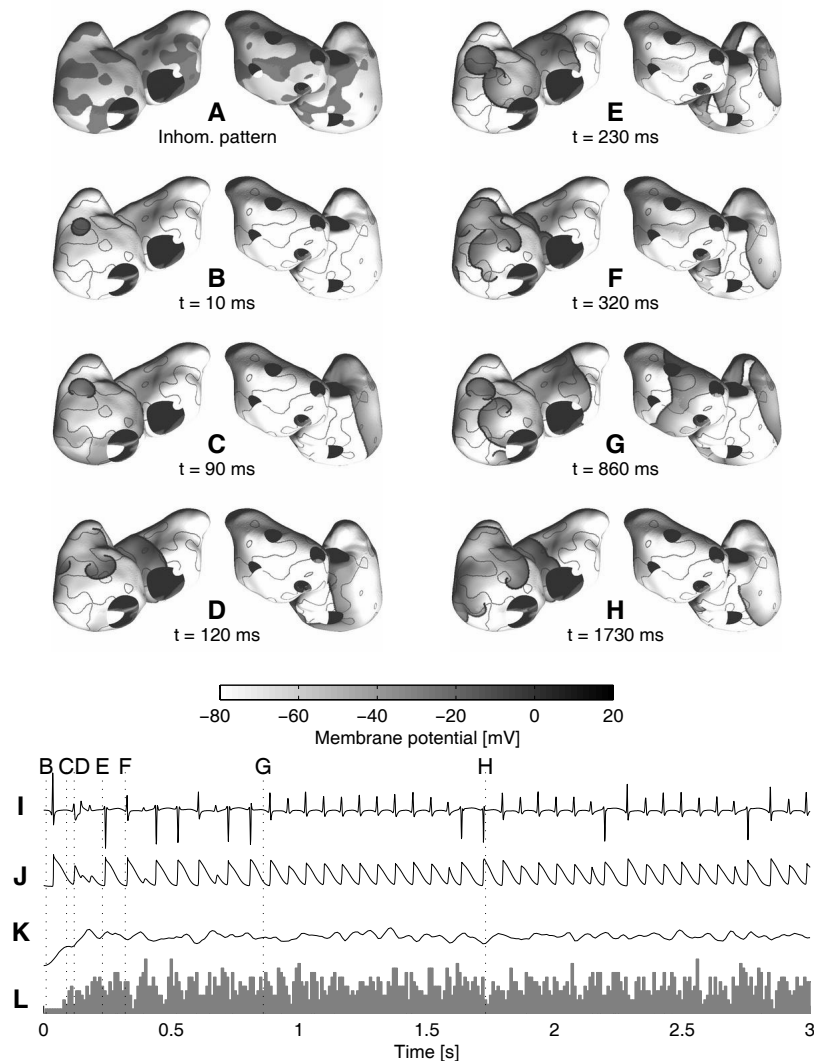


Figure 8.11 — Example of SAF initiation in a heterogeneous tissue using the modified Courtemanche model including vagal stimulation. (A) Distribution of heterogeneity. The ERP is set to 95 ms in the dark regions and to 45 ms everywhere else. (B)–(H) Space plots of membrane potentials during SAF initiation. Thick black lines represent wavefronts. The boundary of the heterogeneity patches is shown as thin gray lines. (I) Bipolar electrogram recorded in the right atrium freewall. (J) Corresponding membrane potential time course. (K) Percentage of excited tissue during SAF. (L) Number of wavelets (range: 0 to 11).

ics, characterized by a significant spatiotemporal organization, was found to be comparable to several animal models.^{246, 272, 273}

In the atrial model, heterogeneities in ERP were introduced by adding an inhomogeneous vagal stimulation to the modified Courtemanche model, using isotropic CV of 90 cm/s. Evidences of such heterogeneity was found experimentally.²⁷⁴ The variations in ERP were controlled by the parameter $g_{K(ACh)}$, as described in Eq. (8.1). In contrast to Kneller *et al.*,⁷⁴ heterogeneity patterns of $g_{K(ACh)}$ were not periodic but assigned randomly with patches having a characteristic length scale in the range 1.5–2.5 cm on the atrial surface (see subsection 4.2.3). An example of such pattern is shown in Fig. 8.11A. The value of $g_{K(ACh)}$

was set to 7 ms^{-1} in those patches and to a constant value between 7 and 25 ms^{-1} everywhere else. The corresponding ERP ranges from 45 ms ($g_{\text{K(ACh)}} = 25 \text{ ms}^{-1}$) to 95 ms ($g_{\text{K(ACh)}} = 7 \text{ ms}^{-1}$) when measured in an isolated cell with the same membrane kinetics. Cell-to-cell coupling introduces an ERP gradient although the spatial variations in $g_{\text{K(ACh)}}$ are discontinuous. Again, these choices were motivated by a previously published model study of cholinergic AF based on *in vitro* measurements performed in canine atrial myocytes.⁷⁴

For a random heterogeneity pattern with patch size approximately in the range 1.5–2.5 cm, and a difference in ERP of the patches and surrounding tissue greater than about 35 ms, a complex reentrant activity could be initiated using a rapid pacing protocol (basic cycle length 70 ms) in the right atrium free wall or in the pulmonary vein region, or by applying a cross-shock stimulation,²⁷⁵ in agreement with Kneller *et al.*⁷⁴ In the absence of sufficient heterogeneity, the SAF converted to a single stable spiral or the wavelets annihilated each other through mutual interaction and collision.

Fig. 8.11 shows an example of SAF initiation by rapid pacing in the right atrium free wall. The ERP is set to 95 ms in the dark regions of Fig. 8.11A and to 45 ms everywhere else. Cell-to-cell coupling creates an APD gradient of about 8 ms/mm in the transition regions. Provided that the pacing site was selected in a region of large APD gradient (near the boundary of a heterogeneity patch) and the basic cycle length (here 70 ms) was chosen between the shortest and longest ERP of the tissue, the second beat already lead to a conduction block (Fig. 8.11B). Interaction with the next propagating beats created new wavelets. Notice that the fibrillatory activity had some difficulty to move from the right to the left atrium, due to the extreme stability of the spirals (Figs. 8.11E–H show simple propagations in the left atrium). Similarly, when the same rapid pacing protocol was applied in the pulmonary vein region, the complex dynamics mainly remained located in the left atrium. SAF extended over the whole atrial surface, when a multisite pacing (*i.e.*, including additional ectopic beats) or a cross-shock stimulation (like in Kneller *et al.*⁷⁴) was applied.

8.4 Conclusion

In this chapter, several models of SAF initiation in a tissue with uniform and isotropic conduction properties were proposed and described. None of them was intended to be completely realistic. Their advantage, however, was that the mechanisms underlying their initiation were reproducible and clearly identified. This specificity illustrates the usefulness of computer model to study the elementary mechanisms underlying AF.

The results showed that the origin of the fibrillatory activity in the model was an initial instability (the *initiator*) created by either a dynamical (*i.e.*, restitution-based) or a structural heterogeneity in tissue refractoriness. In particular, when the maximal slope of the (dynamical) APD restitution curve was larger than 1, SAF could be initiated even in a perfectly homogeneous tissue. In this case, the atrial geometry played an important role by breaking the geometrical symmetry (in contrast to a planar sheet), as illustrated by the fact that the first wavebreaks occurred in the right or left atrial appendage, where large spatial variations in surface curvature are found. Without rate adaptation, however, intrinsic APD gradients were required to generate a dynamics more complex than a periodic activity like a single stable spiral.

This chapter intentionally did not consider SAF perpetuation and focused only on the first wavebreak and the emergence of spatiotemporal complexity. The mechanisms participating to the maintenance of SAF will be investigated in the next chapter.

Perpetuation of Atrial Fibrillation

In the 1960s, Moe proposed the *multiple wavelet hypothesis*²⁷⁶ as a mechanism for the maintenance of atrial fibrillation (AF), motivated by a cellular-automaton computer model of AF.²⁷⁷ This conceptual description of AF postulates that perpetuation of AF relies on several independent wavelets randomly propagating in the atria. Wavelet fractionation, collisions and coalescence would ensure the maintenance of a sufficient number of wavelets like a turbulence process.²⁷⁸ Arrhythmogenic factors are expected increase the number of wavelets while therapeutic interventions should aim at reducing this number. The multiple wavelet hypothesis has been the conceptual basis for most of the experimental studies. For instance, Allesie *et al.*²⁴¹ estimated that a critical number of 3–6 wavelets was required for perpetuation of AF. Konings *et al.*²⁷⁹ showed in a high density mapping of human AF that the right atrium was activated by multiple wavelets separated by lines of block and areas of slow conduction (during AF type III). Wang *et al.*^{280,281} showed that pharmacological termination of AF was preceded by a reduction of the average number of wavelets.

Is AF really made of random propagation of several independent wavelets? Evidences of spatiotemporal organization (and even periodicity) in experimental models of AF^{246, 272, 273} suggested another mechanism for AF perpetuation, the *mother rotor hypothesis*, inspired by the early work of Lewis.²⁸² According to this theory, a single source (or possibly a small number) of stable reentrant wavefronts (“mother rotor”), presumably located in the left atrium, maintains the fibrillatory activity.²⁸³ Such mechanism may be related to the focal activity reported in the pulmonary veins in some patients.²⁸⁴

In the debate “multiple wavelet or mother rotor, or both?,”²⁸⁵ computer models can provide new insights by exhibiting idealized models of AF in which mechanisms of perpetuation can be clearly identified and the arrhythmogenic factors studied separately. This chapter presents three different dynamics of simulated AF (SAF): a model of multiple reentrant wavelets (section 9.1), a model of meandering wavelets (section 9.2) and a model of mother rotor (section 9.3). In all cases, the *wavelength*, defined as the product between conduction velocity (CV) and effective refractory period (ERP), will be shown to play a critical role.

9.1 A Model of Multiple Reentrant Wavelets

In this section, a model of AF based on a modified Luo–Rudy model is used as a tool to investigate questions in the framework of the multiple wavelet hypothesis. SAF initiation by applying burst pacing protocols was presented in subsection 8.2.2. We will now consider

AF perpetuation and self-termination (if it occurs), and in particular the arrhythmogenic factors affecting the duration and the dynamical properties of SAF. Restitution will be a *perpetuator* in this AF model since the dynamical instability caused by the steep restitution leads to creation of new wavelets through wavebreaks.

9.1.1 Unsustained Atrial Fibrillation

Using the baseline model ($\bar{G}_{si} = 0.085 \text{ mS/cm}^2$, see subsection 8.1.1), none of the atrial arrhythmia initiation protocols (S_1 – S_2 – S_3 or burst pacing) succeeded in producing sustained

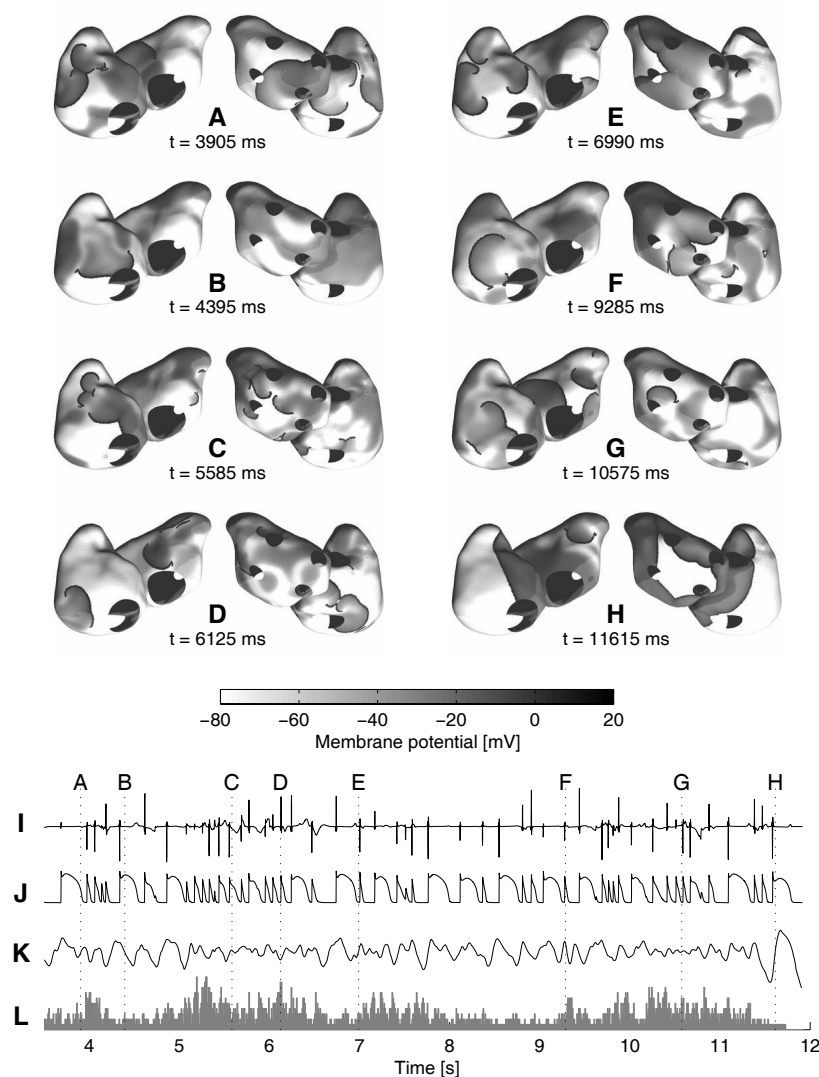


Figure 9.1 — Example of unsustained fibrillation on the baseline model ($\bar{G}_{si} = 0.085 \text{ mS/cm}^2$) using a 20-Hz burst-pacing stimulation protocol applied at the sino-atrial node during 3.5 s. (A)–(G) Space plots of membrane potentials during SAF showing several interacting wavelets. Thick black lines represent wavefronts. (H) Self-termination after 8.4 s of SAF. (I) Bipolar electrogram recorded in the right atrium freewall. (J) Corresponding membrane potential time course. (K) Percentage of excited tissue during SAF. (L) Number of wavelets.

SAF. Most of the simulated arrhythmias were unstable and tended to terminate through mutual interactions of wavefronts or interactions with boundary and refractory tissue. The average SAF duration was approximately 4–5 seconds. This antifibrillatory property in the baseline conditions with long duration action potentials is similar to that observed on the normal human atria, where most AF episodes convert to sinus rhythm after a few seconds.²⁴⁵

Fig. 9.1 shows an example of unsustainable SAF in the baseline model after a 20-Hz burst pacing protocol was applied during 3.5 seconds. This figure displays the activation potential maps, and both the electrogram and transmembrane potential for a cell located in the right atrium free wall. In this example, SAF is sustained for 8.4 seconds and is terminated by a gradual reorganization and a reduction of the number of wavelets and finally by the collision of three wavefronts (see Fig. 9.1H). SAF is observed as multiple interacting wavelets

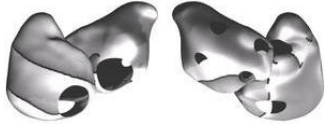







Initial State	Time	% Excited Tissue	Number of Wavelets	SAF Duration
	1.5 s	60%	7	2.5 s
	2.0 s	57%	3	1.1 s
	2.5 s	59%	5	1.1 s
	3.0 s	55%	4	3.5 s
	3.5 s	44%	1	8.4 s
	4.0 s	49%	4	7.8 s
	4.5 s	58%	2	4.3 s
	5.0 s	49%	5	2.7 s

Table 9.1 — Relations between the initial state and SAF duration. “Time” refers to the duration of the stimulation protocol. The percentage of excited tissue (computed with a threshold at -60 mV) and the number of wavelets are measured in the initial state. On the space plots, refractory tissue is colored in dark gray. Black lines represent wave fronts.

undergoing both functional and anatomical reentries. During SAF, the activity oscillates between periods of complex cardiac activity and periods with reduced activity. This slowed activity (at time $t \approx 4.5$ s, $t \approx 6.5$ s and $t \approx 8.5$ s) is characterized by a decreased rate, larger and slower variations of the percentage of excited tissue, and by a small number of wavelets (1 to 3). These situations are similar to those observed near the self-termination of AF. Consequently, a slight perturbation will affect the duration of SAF.

SAF duration, measured as the time between the last burst pacing beat and the repolarization of the whole tissue, was computed for different initial states of tissue just after the end of the stimulation protocol. Table 9.1 summarizes the results, and includes two simple measures of the degree of organization: the percentage of excited tissue and the number of wavelets. The data illustrates the difficulty in predicting the duration of SAF from either the initial state of the tissue or the number of wavelets. No obvious correlation has been found between these measures of degree of organization and duration of SAF, although very short runs of SAF can usually be identified. These results suggest that other indices of complexity or organization are needed.

9.1.2 Effect of Action Potential Duration Restitution

Wavebreak has been shown to be facilitated when using action potential dynamics with a steep restitution curve (*i.e.*, slope greater than 1).^{88,261} The impact of the restitution dynamics of the action potential on the perpetuation of SAF was therefore investigated.

To quantify the effect of APD restitution, the same initiation protocol was used on models with decreasing value of the control parameter \bar{G}_{si} (subsection 8.2.3). We successively used $\bar{G}_{si} = 0.085$ (baseline model), 0.08, 0.07, 0.06, 0.055 and 0.05 mS/cm², with all other parameter values remaining the same as in the baseline model. The resulting flattening of restitution curve is obtained in combination with reduced APD (see Fig. 8.1). For each value of \bar{G}_{si} , 15 burst-pacing protocols with different durations (from 1.5 to 5 s) were applied, and SAF duration was measured. If the SAF duration was at least 20 s, SAF was classified as sustained and the simulation was terminated.

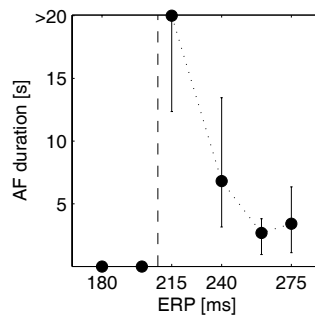


Figure 9.2 — Average duration of SAF as a function of the control parameter \bar{G}_{si} . A duration >20 s was considered as sustained SAF. The circles represent the median of SAF durations distribution, and the error bars are associated with the first and third quartile. For this illustration, \bar{G}_{si} was replaced by its associated effective refractory period (ERP) at rest (conversion table: an ERP of 275, 265, 240, 215, 200, 180 ms is associated with a \bar{G}_{si} of 0.085, 0.08, 0.07, 0.06, 0.055, 0.05 mS/cm² respectively). The vertical dashed line gives the value for which the maximal slope of the corresponding APD restitution curve is 1. Zero SAF duration means that SAF could not be initiated.

Fig. 9.2 displays the median, the first and third quartiles of the resulting distributions of SAF duration. As explained in subsection 8.2.3, when the slope of the APD restitution function was always smaller than 1 ($ERP = 180$ and 200 ms on Fig. 9.2), initiation of AF was usually not possible. Although AF initiation was more difficult with a slope close to 1, the resulting SAF lasted longer because the APD, and thus the wavelength, was shortened.

9.1.3 Remodeling and Sustained Atrial Fibrillation

Significantly longer runs of SAF could be obtained by an abrupt reduction of the APD. Such changes (*remodeling*) in APD are often seen experimentally and clinically after many seconds of AF.²⁶⁵ Remodeled cells were shown to be characterized by shorter APDs and a reduced rate adaptation⁷¹ (flattened APD restitution). The recurrence of AF is then more likely in patients with a long history of AF (AF begets AF²⁸⁶).

In this study, the initiation phase was separated from the perpetuation phase. SAF was induced by applying a burst pacing protocol on the baseline model. After some predefined period, the value of the control parameter \overline{G}_{si} was instantaneously reduced to produce shorter APDs and a flatter restitution (Fig. 8.1). Remodeled values of \overline{G}_{si} were chosen in the range 0.05 to 0.08 mS/cm². Fig. 9.3 shows an example of simulated remodeling where, after 3.5 s of pacing in the baseline model, \overline{G}_{si} was abruptly reduced from 0.085 to 0.07 mS/cm² in the whole tissue. As a result, SAF was sustained for more than 24 seconds, and was maintained by 2 – 5 reentrant wavelets undergoing front-tail interactions and wavebreaks (Figs. 9.3 A–H).

Table 9.2 presents some parameters describing the SAF dynamics for different remodeled values of \overline{G}_{si} . As the APD reduces, the mean number of wavelets and phase singularities^{172,246} increases due to the decrease in wavelength. The lifespan of the phase singularities increases as well,²⁸⁷ suggesting that the wavelets are more stable and break up less often, due to the flatter restitution. Distribution of the number of wavelets is shown in Fig. 9.4 for $\overline{G}_{si} = 0.085$, 0.07 and 0.055 mS/cm². We can also observe that the rate of SAF is increased for reduced values of \overline{G}_{si} , while the excitable gap is decreased (to crudely estimate the excitable gap during SAF, the ERP is approximated by the sum of the average APD and the minimum of the diastolic interval distribution).

\overline{G}_{si}	AFCL	Exc. Gap	# Wav.	# PS	PS lifespan
0.085 mS/cm ²	141 ± 8 ms	43 ± 5 ms	2.7 ± 1.2	8 ± 4	36 ms
0.070 mS/cm ²	120 ± 6 ms	37 ± 4 ms	3.0 ± 1.4	14 ± 5	53 ms
0.060 mS/cm ²	91 ± 4 ms	27 ± 3 ms	3.4 ± 1.5	18 ± 4	78 ms
0.055 mS/cm ²	78 ± 3 ms	22 ± 3 ms	3.6 ± 1.5	19 ± 5	94 ms

Table 9.2 — Mean AF cycle length (AFCL), excitable gap (Exc. Gap), mean number of wavelets (# Wav.), mean number of phase singularities (# PS) and mean phase singularity lifespan (PS lifespan) measured during SAF with a \overline{G}_{si} after remodeling ranging from 0.05 to 0.085 mS/cm². Values for the number and lifespan of phase singularities are those reported in Ducry.²⁸⁷ The number of PS is much larger than twice the number of wavelets because the number of wavelets was computed as the number of excited regions and not the number of wavefronts. The use of various thresholds for automatic detection of PSs may also be a cause.²⁸⁷

Remodeling decreases the wavelength, hence prolonging the duration of SAF. Moreover,

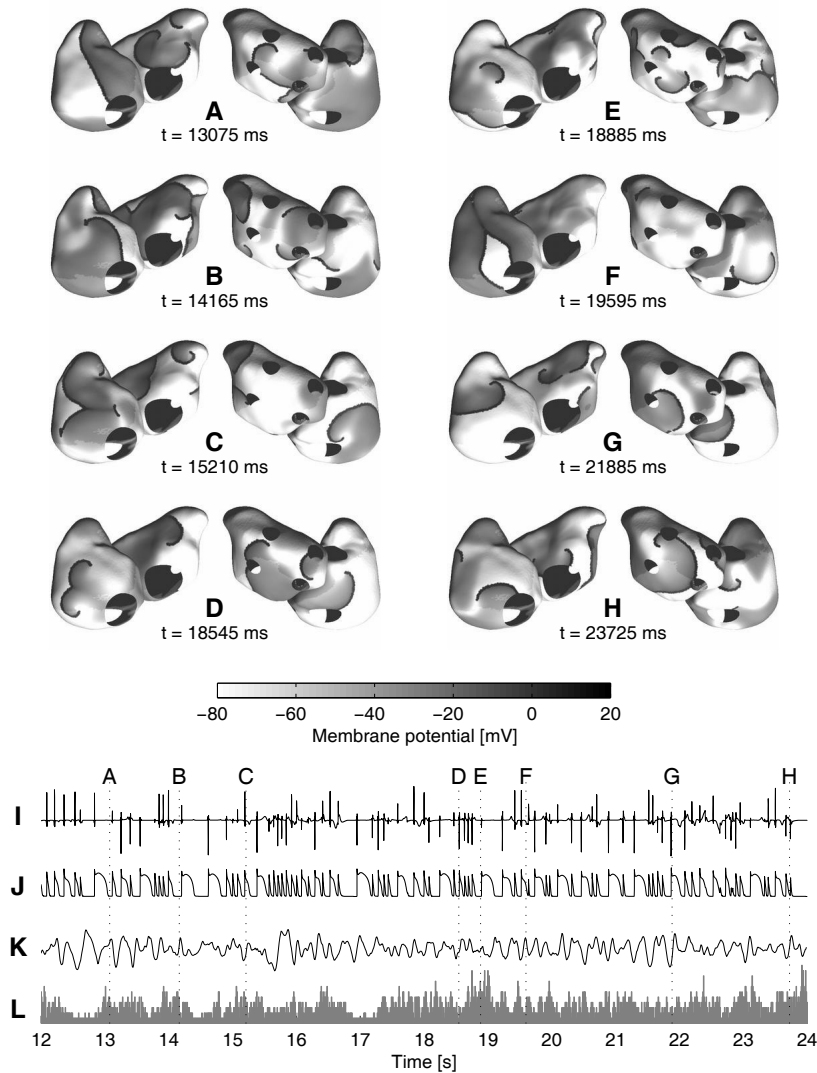


Figure 9.3 — Example of sustained fibrillation obtained after an abrupt remodeling. A 20-Hz burst-pacing stimulation protocol was applied at the sino-atrial node during 3.5 s on the baseline model (exactly as in Fig. 9.3) followed by an abrupt remodeling at time $t = 3.5$ s where the conductance \overline{G}_{si} was instantaneously set to 0.07 mS/cm² (instead of 0.085 mS/cm² in the baseline model). (A)–(H) Space plots of membrane potentials during SAF showing several interacting wavelets. Thick black lines represent wavefronts. (I) Bipolar electrogram recorded in the right atrium freewall. (J) Corresponding membrane potential time course. (K) Percentage of excited tissue during SAF. (L) Number of wavelets.

after further reduction of \overline{G}_{si} , sustained SAF was observed even for values of \overline{G}_{si} for which SAF could usually not be initiated using a burst pacing protocol. The reason for this anomalous behavior is that despite the flat static restitution for this \overline{G}_{si} , wavebreaks can still occur because the dynamical APD restitution has a slope slightly greater than 1 for short DIs. Fig. 9.5A shows the dynamical restitution curve measured during SAF with a remodeled \overline{G}_{si} value of 0.055 mS/cm². This curve is influenced by all the local changes in gradients of APD due to collisions and interactions with boundaries during SAF.

In order to illustrate the transition from the static restitution (S_1 – S_2 protocol) to the

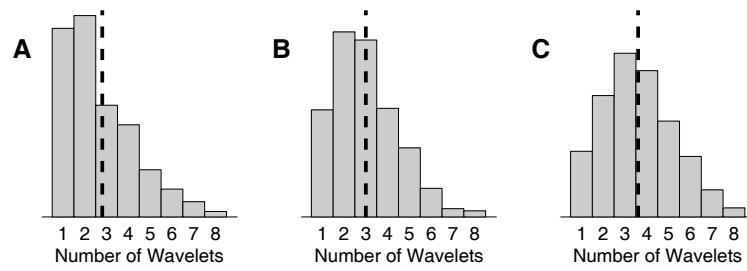


Figure 9.4 — Distribution of the number of wavelets during SAF initiated by a 20-Hz burst pacing at sinoatrial node during 3.5 s on the baseline model. (A) Without remodeling ($\overline{G}_{\text{si}} = 0.085 \text{ mS/cm}^2$), leading to an unsustainable AF of duration 8.4 s and with an average number of wavelets $\langle w \rangle = 2.7$. (B) After remodeling ($\overline{G}_{\text{si}} = 0.07 \text{ mS/cm}^2$), leading to sustained AF with $\langle w \rangle = 3.0$. (C) after remodeling ($\overline{G}_{\text{si}} = 0.055 \text{ mS/cm}^2$), leading to sustained AF with $\langle w \rangle = 3.6$. The vertical dashed line represents the average number of wavelets.

dynamic restitution measured during SAF, a spiral was initiated in the right atrium free wall using a cross-shock stimulation protocol.²⁷⁵ Tissue properties were identical to those of Fig. 9.5A ($\overline{G}_{\text{si}} = 0.055 \text{ mS/cm}^2$). Fig. 9.5B displays the dynamics restitution curve measured before the spiral becomes unstable and breaks up (the resulting time window is about 1 s long, that is, a few turns for the spiral). In contrast with Fig. 9.5A, the cloud of points is now aligned with the static restitution curve, i.e., the slope is < 1 . Notice that, for $\text{DI} > 40 \text{ ms}$, the points are separated into two clusters (one above and one below the static restitution curve), revealing an APD alternans prior to the first wavebreak in agreement with Figs. 8.1C and 8.6.

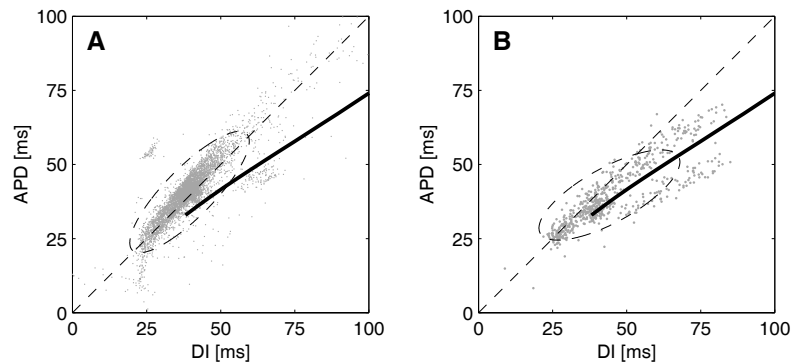


Figure 9.5 — (A) Dynamical APD restitution curve during SAF after remodeling in a model with $\overline{G}_{\text{si}} = 0.055 \text{ mS/cm}^2$ together with the corresponding static restitution curve (plain line). (B) Dynamical APD restitution curve measured in a stable spiral in a tissue with exactly the same properties. The dashed diagonal line has a slope 1. The global orientation of the cloud of points is illustrated by a dashed ellipse computed from a principal component analysis. APDs and diastolic intervals (DI) are measured with a -60 mV threshold and computed over 100 cells located on the epicardial surface in the right atrium free wall. Very short APDs and DIs ($< 30 \text{ ms}$) are mainly due to electrotonic effects produced by wavefront-waveback collisions and cannot be considered as action potentials. The presence and the value of extremely low APD and DI strongly depends on the thresholding method used to compute them.

9.1.4 Factors Promoting Atrial Fibrillation

To investigate the effect of remodeling on SAF duration and evaluate the arrhythmogenic effect of structural changes in conduction properties, a large set of computer experiments with various tissue properties was performed. After SAF was initiated in the baseline model, a combination of the following interventions was applied as an abrupt remodeling in order to alter the wavelength:

- *reduction of ERP* in the range 180–275 ms by changing the control parameter \overline{G}_{si} ,
- *modification of the CV* between 50 and 120 cm/s,
- *increase of the anisotropy ratio* from 1:1 (isotropic) to 9:1 (ratio of conductivities), obtained by decreasing the transverse conductivity according to the fiber orientation described in subsection 4.2.2.

The list of all tissue properties used in the simulations are collected in Table 9.3. For each set of parameters, the simulations were repeated for 8 different burst pacing initiation protocols.

	120 cm/s	100 cm/s	85 cm/s	70 cm/s	60 cm/s	50 cm/s	
275 ms		×	×	×	×	×	0.085 mS/cm ²
260 ms		×		×			0.080 mS/cm ²
240 ms	× (aniso)	×		×			0.070 mS/cm ²
215 ms		×		×			0.060 mS/cm ²
200 ms	× (aniso)	×	×	×	×	×	0.055 mS/cm ²
180 ms		×		×			0.050 mS/cm ²
	80 Ω cm	125 Ω cm	177 Ω cm	250 Ω cm	350 Ω cm	500 Ω cm	

Table 9.3 — *Parameter sets chosen for the remodeled tissue. Each row corresponds to an effective refractory period (on the left) and to a value of \overline{G}_{si} (on the right). Each column corresponds to a conduction velocity (top row) and to a conductivity (bottom row). A cross (×) denotes a parameter set chosen for the simulations (8 different simulations for each cross). The annotation “(aniso)” means that simulations were run with 5 different anisotropy ratios (1:1, 2.25:1, 4:1, 6.25:1 and 9:1), each one with 8 different initiation protocols (40 simulations in total for each “× (aniso)”).*

Fig. 9.6 summarizes the results. SAF duration statistics are plotted as a function of the ERP (Fig. 9.6A), the CV (Fig. 9.6B), and the transverse CV (the longitudinal CV being fixed, Fig. 9.6C).

As a rule, the SAF is prolonged when the ERP or the CV (even only the transverse CV) is reduced, because the wavelength (ERP multiplied by CV) becomes shorter, creating by the way some free space for new wavelets. This effect is in agreement with experimental^{242,288} and clinical^{289–291} studies and will be further analyzed in section 10.3.

9.2 A Model of Meandering Wavelets

This section presents a SAF dynamics based on the modified Courtemanche model and initiated through a ramp protocol (see subsection 8.2.4). While the previous model was characterized by high rates and large beat-to-beat variations in AF cycle length, the rhythm will be slower and more regular in this model, mainly because the APDs range from 100 to

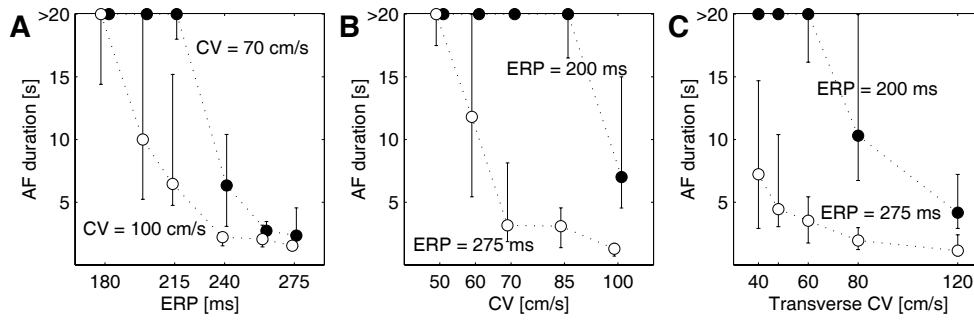


Figure 9.6 — Average duration of SAF as a function of the membrane and tissue properties. A duration >20 s was considered as sustained SAF. The circles represent the median of SAF durations distribution, and the error bars are associated with the first and third quartile. For this illustration, \bar{G}_{si} was replaced by its associated effective refractory period (ERP) at rest (conversion table: an ERP of 275, 265, 240, 215, 200, 180 ms is associated with a \bar{G}_{si} of 0.085, 0.08, 0.07, 0.06, 0.055, 0.05 mS/cm² respectively). (A) SAF duration as a function of the ERP (at rest) with a CV of 70 cm/s (white dots) and 100 cm/s (filled dots). (B) SAF duration as a function of the CV with an ERP (at rest) of 275 ms (white dots) and 200 ms (filled dots). (C) SAF duration as a function of the transverse CV in an anisotropic tissue with a longitudinal CV of 120 cm/s and with an ERP (at rest) of 275 ms (white dots) and 200 ms (filled dots).

200 ms (see Fig. 8.2B). From the dynamical viewpoint, activation wavefronts will propagate like spirals in the hypermeandering regime.^{84,91,92}

Ramp protocols applied near the sino-atrial node or in the pulmonary veins region succeeded in inducing SAF in a homogeneous and isotropic model using the modified Courtemanche model. As explained in subsection 8.2.4, the conduction velocity had to be reduced to 40 cm/s to initiate a complex activity in a uniform tissue with ERP larger than 120 ms. Although the majority of the SAF episodes converted to sinus rhythm after 5–10 s, episodes self-sustained for more than 20 s could be initiated. SAF duration depended on the tissue state when the pacing is stopped, as discussed in subsection 9.1.1 for the Luo–Rudy model.

Fig. 9.7 illustrates the resulting dynamics. SAF was maintained by 1–2 (rarely 3) meandering wavelets undergoing front-tail interactions, sometimes wavebreaks, collisions (Fig. 9.7D in the left atrium free wall) and anchoring to valves (tricuspid valve in Fig. 9.7H) or veins (pulmonary vein in Fig. 9.7A, but in this case for less than one turn). Alternation of long and short APDs (e.g. Fig. 9.7J, between $t = 21$ s and $t = 24$ s) was a mechanism leading to the destabilization of the wavelets. For instance, the spiral in the right atrium free wall of Fig. 9.7G was anchored to the tricuspid valve and its liberation was preceded by APD alternans. APD restitution, whose maximal slope is here slightly >1 , is therefore also a perpetuator in this model.

Including anisotropic conduction is a way to introduce more realistic conduction velocity without preventing SAF inducibility. A set of anisotropy ratios (longitudinal conductivity over transverse conductivity) ranging from 1:1 (isotropic) to 9:1 was successively considered and the fiber orientation of Fig. 4.4 was used. The longitudinal to transverse conduction velocity ratio was set to approximately 40:40, 50:33, 60:30, 67:27 and 75:25 cm/s when the anisotropy ratio is 1:1, 2.25:1, 4:1, 6.25:1 and 9:1 respectively in order to approximately preserve the average wavelength. Runs of SAF with durations similar to the isotropic case were obtained on these anisotropic models. Fig. 9.8 shows an example of SAF in a model with an anisotropy ratio of 4:1 where SAF was initiated using a ramp protocol during 11 s.

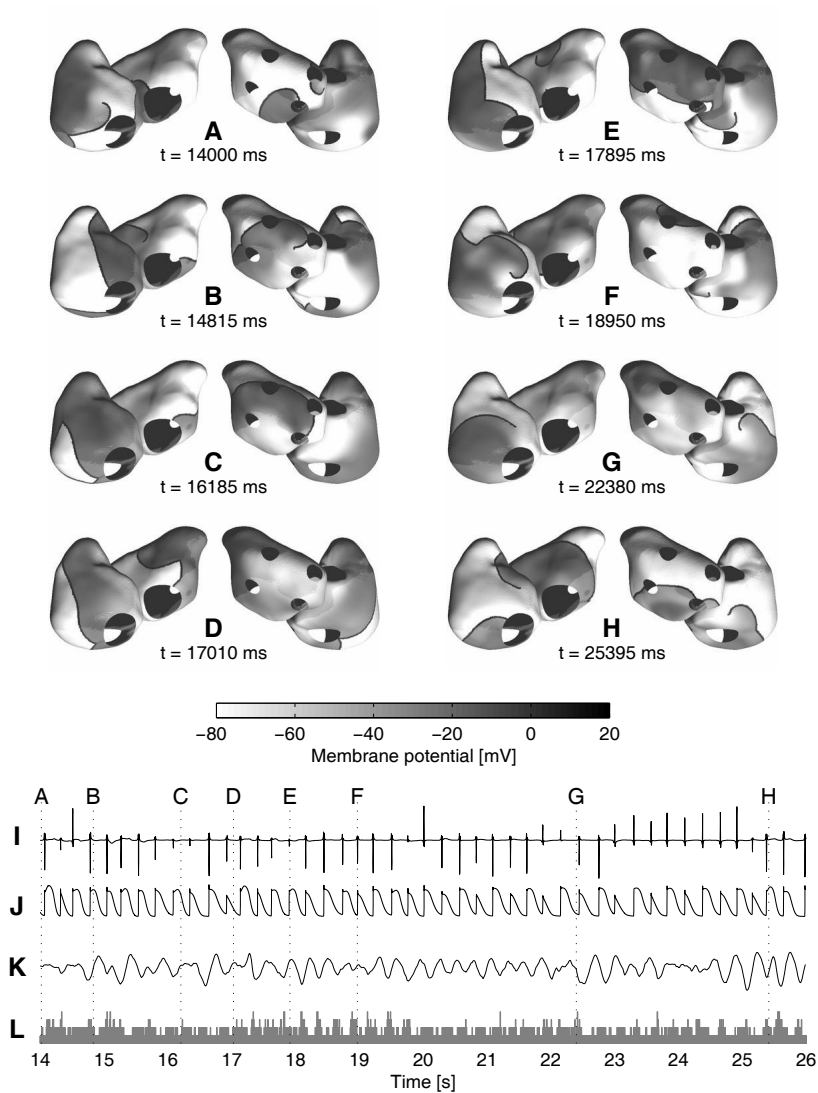


Figure 9.7 — Example of sustained fibrillation in an isotropic tissue using the modified Courtemanche model. A ramp stimulation protocol was applied in the pulmonary veins region during 10 s. (exactly as in Fig. 8.10). (A)–(H) Space plots of membrane potentials during SAF showing one or several meandering wavelets. Thick black lines represent wavefronts. (I) Bipolar electrogram recorded in the right atrium freewall. (J) Corresponding membrane potential time course. (K) Percentage of excited tissue during SAF. (L) Number of wavelets.

Again, SAF was observed as 1–2 (sometimes 3) meandering wavelets. Wavefront shape was elongated along the fiber (see for in the right atrium free all of Figs. 9.8 B, C, G). This episode self-terminated at $t \approx 24$ s after the dynamics became more organized: a wavelet with long wavelength got anchored to the tricuspid valve (Fig. 9.8H) and the other extremity of the wavefront eventually collided with a refractory region.

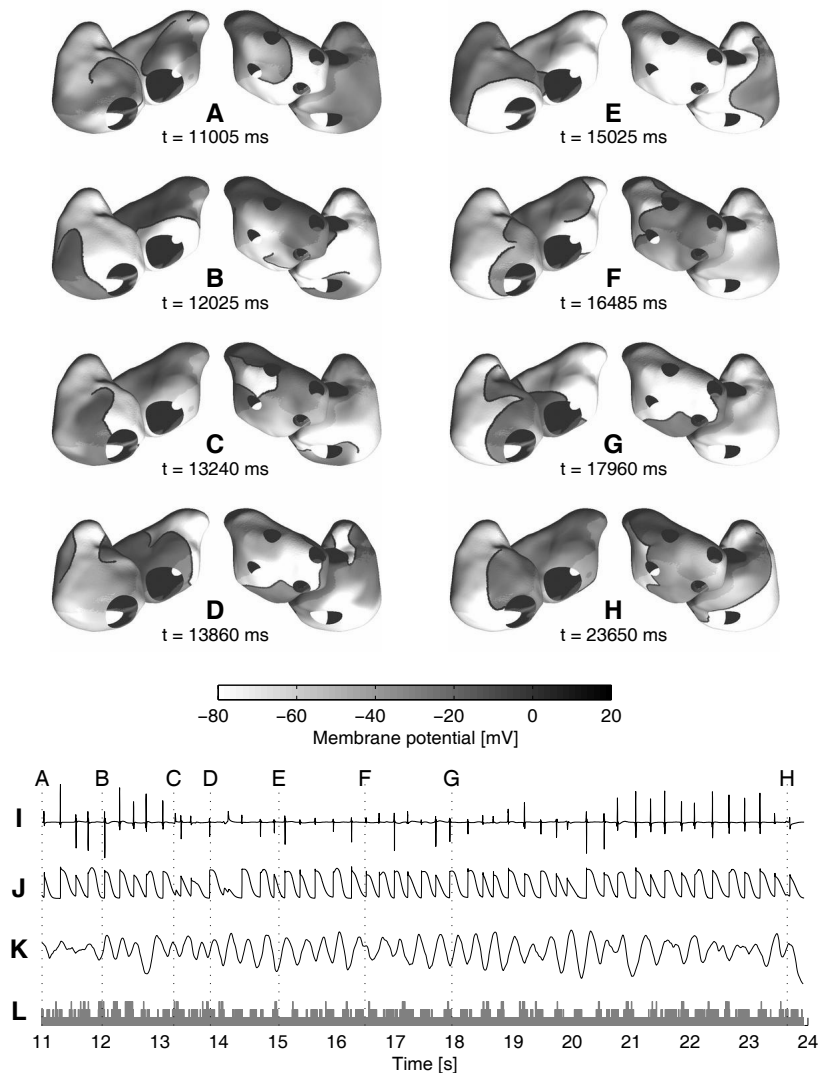


Figure 9.8 — Example of sustained fibrillation in an anisotropic tissue using the modified Courtemanche model. A ramp stimulation protocol was applied in the pulmonary veins region during 10 s. (exactly as in Fig. 8.10). (A)–(H) Space plots of membrane potentials during SAF showing one or several meandering wavelets. Thick black lines represent wavefronts. (I) Bipolar electrogram recorded in the right atrium freewall. (J) Corresponding membrane potential time course. (K) Percentage of excited tissue during SAF. (L) Number of wavelets.

9.3 A Model of Mother Rotor

Even in the absence of rate adaptation, sufficient heterogeneity in ERP was shown to create fibrillatory conditions (section 8.3). In this section, the resulting SAF dynamics is analyzed. Due to the completely flat restitution, the spirals initiated by collision with regions of long ERPs were stable and helped maintain an organized and sustained SAF activity. This model provides a tool to evaluate the mother rotor hypothesis and its impact on atrial electrograms.

In a Courtemanche-based model including inhomogeneous vagal stimulation, SAF was induced using a cross-shock stimulation (see section 8.3). The ERPs were set to 95 ms

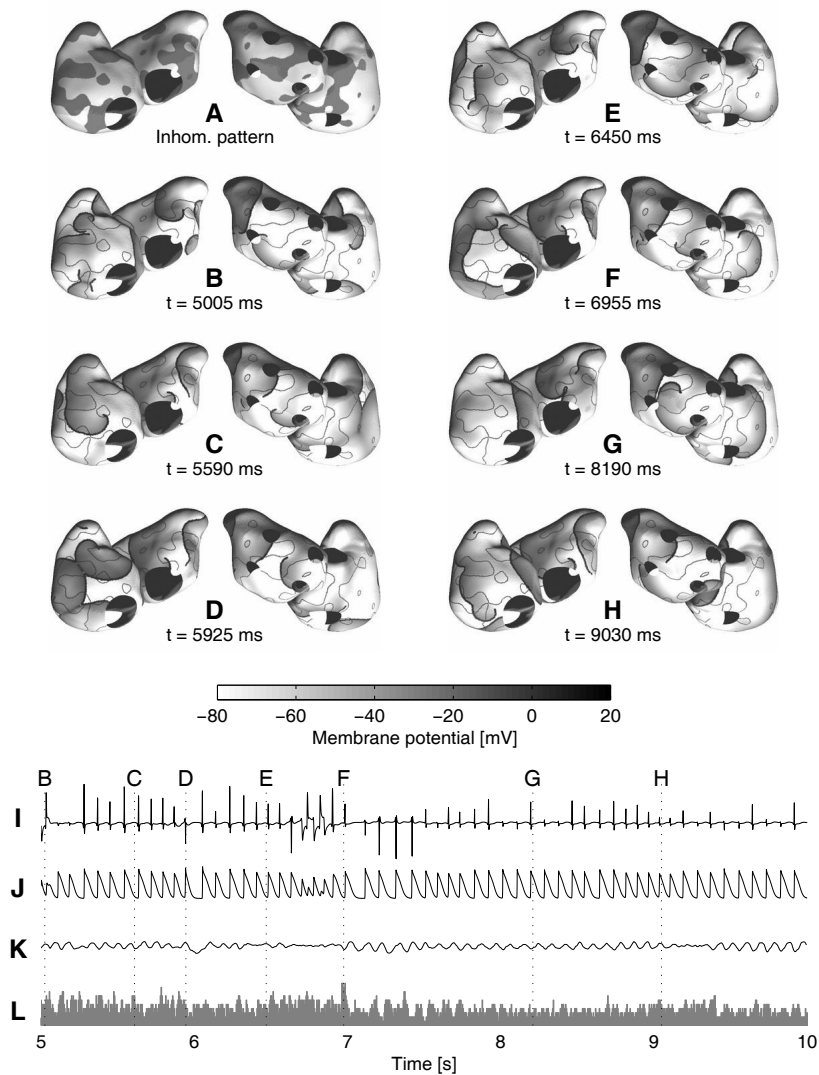


Figure 9.9 — Example of sustained fibrillation in a heterogeneous tissue using the modified Courtemanche model including vagal stimulation. (A) Distribution of heterogeneity. The ERP is set to 95 ms in the dark regions and to 45 ms everywhere else. (B)–(H) Space plots of membrane potentials during SAF showing several wavelets/spirals. Thick black lines represent wavefronts. The boundary of the heterogeneity patches is shown as thin gray lines. (I) Bipolar electrogram recorded in the right atrium freewall. (J) Corresponding membrane potential time course. (K) Percentage of excited tissue during SAF. (L) Number of wavelets.

in the dark regions on the heterogeneity pattern displayed on Fig. 9.9A, and to 45 ms everywhere else. An isotropic conduction velocity of 90 cm/s was used. As a result, a fibrillatory activity lasting for more than 20 s was observed. Figs. 9.9B–H shows space plots of membrane potentials during SAF. The sustained SAF was characterized by 4.5 ± 1.5 spiral-like interacting wavelets undergoing both functional and anatomical reentries. A few of the reentries served as a stable source of wavelets, mostly located in the left atrium. Notice that the phase singularities are almost always found in regions with longer ERPs. As a matter of fact, the spirals often tend to propagate around refractory zones characterized by an increased ERP. This dynamics is similar to that described in Kneller *et al.*⁷⁴

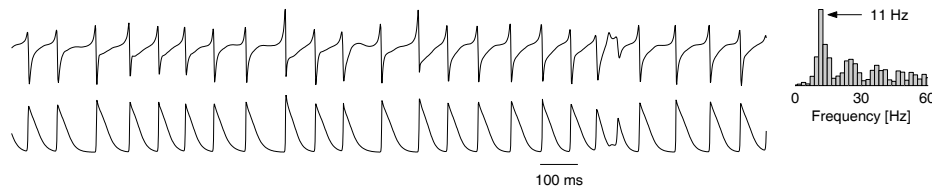


Figure 9.10 — Left panel: Example of unipolar electrogram during SAF and its corresponding membrane potential. Right panel: Power spectral density of the electrogram.

Because the dynamics mainly consists of stable interacting spirals with an ERP almost constant along the wavefront, the local electrical activity includes a significant periodic component. Fig. 9.10 displays an example of unipolar electrogram as well as the corresponding membrane potential time course. Spectral analysis reveals the presence of a dominant frequency between 11 and 12 Hz. This spatio-temporal organization during SAF is consistent with the experimental data from Berenfeld *et al.*²⁹² Average dominant frequencies of 14.7 ± 3.8 Hz (left atrium) and 10.3 ± 2.1 Hz (right atrium) were found in the isolated sheep heart.²⁷³

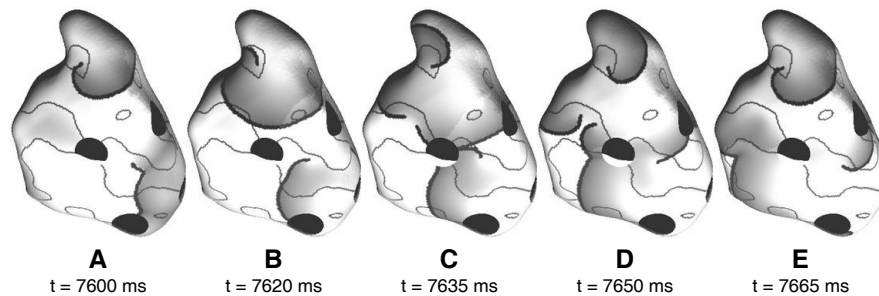


Figure 9.11 — Stable rotor anchored at a heterogeneity in the left atrium appendage. (A)–(E) Space plots of membrane potentials during SAF. Only the left atrium is shown: the appendage is on the top and the septum on the bottom; the four black circles correspond to the location of the pulmonary veins. Thick black lines represent wavefronts. The boundary of the heterogeneity patches is shown as thin gray lines.

Fig. 9.11 shows a stable source of wavelets (mother rotor) anchored at a heterogeneity with a diameter of about 1.1 cm (approximately the size of the non-propagating region created by a pulmonary vein) located in the left atrium appendage. This rotor had a cycle length of about 65 ms and lasted for more than 10 s. The stability conditions for this type of rotor in this model appears to be:

- the spiral rotates around a heterogeneity with longer ERP, so that the wavefront is blocked by the refractoriness in the heterogeneity (the phase singularity is trapped in the heterogeneity);
- the heterogeneity has to be sufficiently large because of the smoothing effect of cell-to-cell coupling;
- the heterogeneity should not be too large in order to have a cycle length (and therefore an excitable gap) as short as possible;

- the surrounding tissue should not be too heterogeneous to protect the rotor from the destructive interactions with other wavefronts.

This mechanism is similar to a spiral anchored to a vein and contrasts with the two-dimensional computer model of ventricular fibrillation of Samie *et al.*⁵⁴ in which a unique, very fast (about 33 Hz) and stable rotor is located in a region with very short ERPs and is the perpetuator of the fibrillatory activity in the surrounding tissue.

9.4 Conclusion

In order to study different mechanisms leading to maintenance of AF, three models of SAF were proposed and analyzed. Table 9.4 summarizes their main qualitative characteristics. These models differed by the dynamical regime of their spirals and by their spatiotemporal organization. In the Luo–Rudy-based model reproducing the features of the multiple wavelet hypothesis, the wavelets, continuously in interaction and undergoing wavebreaks, seemed to move randomly over the atrial surface. In contrast, the Courtmanche-based model of slow meandering wavelet was characterized by a more organized dynamics because of its longer wavelength and its more regular rate. Finally, the loss of rate adaptation caused by inhomogeneous vagal stimulation acted to stabilize the spirals around heterogeneities, leading to a spatiotemporal organization with a marked periodic component.

Sect.	Paradigm	Spiral Phenotype	Organization	Typical AFCL
9.1	multiple wavelets	wavebreaks	random	fast (80–140 ms)
9.2	meandering wavelet	hypermeandering	temporal	slow (230–240 ms)
9.3	mother rotor	stable	spatiotemporal	fast (80–90 ms)

Table 9.4 — Qualitative description of the SAF models considered in this chapter (AFCL means average cycle length during SAF).

While SAF initiation required a dynamical instability or heterogeneity, SAF with long durations appeared to be associated with less unstable dynamics. For instance, remodeling, abruptly applied as a flattening of the restitution curve along with a reduction of the APD, prolonged SAF duration by increasing the spiral lifespan. Wavebreaks, although less frequent, were still observed because the dynamical restitution was steep. The mechanism of mother rotor gave another example of sustained SAF maintained by a stable spiral.

Complexity, organization and wavelength were found to be critical factors for SAF perpetuation. The next chapter will concentrate on such analysis of SAF dynamics from the electrophysiologist’s viewpoint by considering unipolar electrograms and simulated mapping data.

Analysis of Simulated Atrial Fibrillation

Computer models can provide information at multiple biological scales and give an access to every region with a high resolution. The previous chapters exploited these advantages to study the factors promoting initiation and perpetuation of atrial fibrillation (AF) in an atrial model. The underlying mechanisms could be identified by tracking the activation wavefronts over the whole atrial surface and analyzing their dynamics.

In contrast, clinical evaluation of the human heart electrophysiology usually involves only electrical signals measured with electrocardiogram leads, an electrode array, a basket catheter or possibly a cardiac mapping system. In order to get closer to the electrophysiologist's viewpoint, data from simulated AF (SAF) will be represented in a form similar to those of experimental and clinical studies. This operation deliberately reduces the amount of information available but is a necessary step toward model validation.

This chapter presents a description of SAF in terms of (unipolar) electrograms and activation patterns (section 10.1), measure of organization (section 10.2) and wavelength (section 10.3). Comparison with published experimental or clinical data will be performed when possible.

10.1 Electrograms and Activation Patterns

In a study of electrically induced AF in humans, Konings *et al.*^{181,279} systematically analyzed activation patterns during AF using a high-resolution epicardial mapping in the free wall of the right atrium. In our atrial model, a similar mapping system was simulated in order to enable comparison with experimental data (see section 4.3.3).

10.1.1 Comparison of Different Simulated Atrial Fibrillation Dynamics

In the previous chapter, different mechanisms of SAF perpetuation were discussed: a model of multiple wavelets (Fig. 9.3), a model of meandering wavelets (Fig. 9.7), and a model of mother wavelet mechanism (Fig. 9.9). Here, unipolar electrogram data are analyzed for each case.

Fig. 10.1 displays atrial electrograms during SAF for each model as well as four different examples of activation patterns showing uniform activation, collisions and conduction

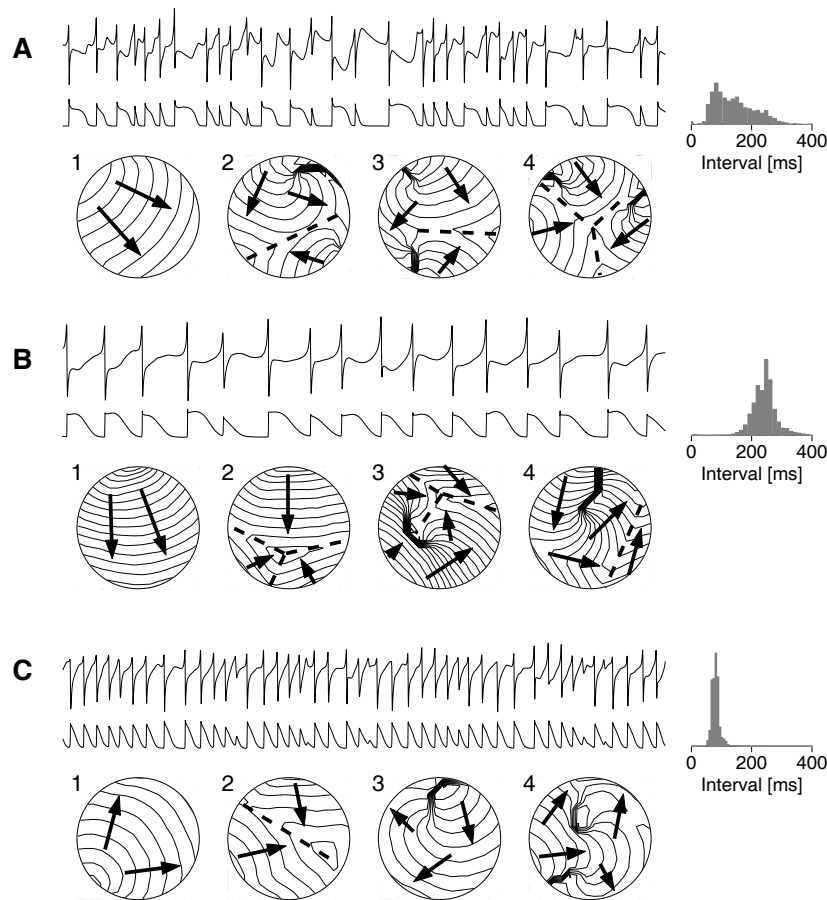


Figure 10.1 — Examples of simulated unipolar electrograms measured in the right atrium free wall during SAF in an isotropic tissue with different dynamics: (A) SAF using the modified Luo–Rudy model ($\bar{G}_{si} = 0.07 \text{ mS/cm}^2$) and a conduction velocity (CV) of 70 cm/s; (B) SAF using the modified Courtemanche model and a CV of 40 cm/s; (C) SAF using the modified Courtemanche model including inhomogeneous vagal stimulation and a CV of 90 cm/s. The same time frame (4 s) is used for all signals and peak-to-peak electrogram amplitudes correspond to approximately 10 mV. Electrograms are recorded at the center of the mapping area. Corresponding timecourse of membrane potential is displayed just below the electrogram. Distributions of beat-to-beat intervals in the right atrium freewall are given on the right panels. For SAF dynamics, four activation patterns are also shown: the diameter of the mapping area is 3.2 cm, isochrones are plotted every 7 ms; arrows illustrate wavefront propagation; dashed lines represent collisions; and thick black lines are conduction blocks. Pattern 1 is a simple propagation, pattern 2 is a wavefront collision, and patterns 3 and 4 involve both collisions and conduction blocks.

blocks. In all the cases, the activation patterns change with each beat, due to the multiple wavelets that continuously change in size, shape and direction.¹³ Due to the uniform tissue substrate, the isochrones are smoother and more regular in the simulations than in typical experimental recordings.¹⁸¹ In contrast to the signals obtained in sinus rhythm (see for instance Fig. 7.2), the electrograms show marked variability in amplitude and symmetry, similar to those recorded in humans.¹⁸¹ The reason for these changes in morphology will be investigated in chapter 11.

The three models of AF differ significantly by their rate and rate variability. The distributions of beat-to-beat intervals based on all measurement sites in the region of the simulated plaque array are displayed on the right panels of Fig. 10.1. The first model (mod-

ified Luo–Rudy model with $\bar{G}_{si} = 0.07 \text{ mS/cm}^2$ and a restitution slope >1) is characterized by large beat-to-beat variations in action potential duration, and thus by a broad distribution of activation intervals ranging from 50 to 300 ms, with an average of about 120 ms (see Fig. 10.1A). The distribution shown in Fig. 10.1B (modified Courtemanche model), however, is roughly Gaussian, as also observed experimentally,²⁷⁹ with an average beat-to-beat interval of about 240 ms during SAF. Finally, the model including vagal stimulation (Fig. 10.1C) has a stable rhythm and activation intervals concentrated in the range 80–90 ms (that is, 11–12 Hz).

Konings¹⁸¹ reported a median of interval distribution ranging from 118 to 212 ms (over 25 patients) in electrically induced human AF, slower rates being consistently associated with less complex activation patterns. The first model and the second one (Figs. 10.1A–B) are at each extremity of this range. The width of the distribution of Fig. 10.1A (modified Luo–Rudy model) is however larger than any experimental data (21–125 ms in Konings,¹⁸¹ measured as the difference between the 5th and the 95th percentile). The third distribution (Fig. 10.1C) is closer to those of animal models of cholinergic AF.^{74, 272, 292}

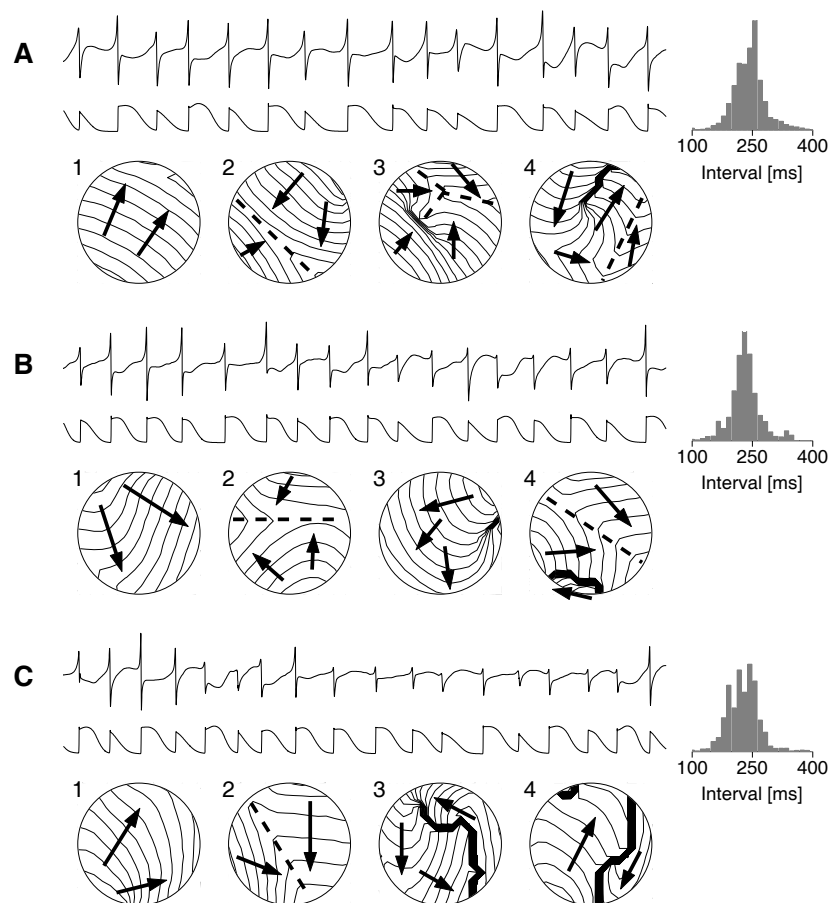


Figure 10.2 — Examples of simulated unipolar electrograms measured in the right atrium free wall during SAF using the modified Courtemanche model in tissue with an anisotropic ratio of (A) 1:1, (B) 2.25:1 and (C) 4:1. Corresponding longitudinal-to-transverse conduction velocity ratios are: (A) 40:40 cm/s, (B) 50:33 cm/s and (C) 60:30 cm/s. The same time frame (4 s) is used for all signals and peak-to-peak electrogram amplitudes correspond to approximately 10 mV. Exactly the same representation as Fig. 10.1 is used.

10.1.2 Effect of Anisotropy

In order to study the effect of anisotropy on unipolar electrograms and on activation patterns, SAF was simulated in the atrial model with different anisotropy ratios using the meandering wavelet dynamics based on the modified Courtemanche model (see section 9.2).

Fig. 10.2 shows examples of the variation in single-site electrograms during SAF in the atrial model with anisotropy ratios ranging from 1:1 (isotropic) to 4:1. The distribution of beat-to-beat intervals displayed on the right panels presents an average beat-to-beat interval in the range 230–240 ms during SAF. The increase in anisotropy ratio acts to make the underlying activity slightly more complex as revealed by a broader distribution of activation times. The average number of wavelets recorded in the plaque region, however, is relatively constant (1–2 wavelets, but rarely 3). Typical activation patterns are also displayed below the signals indicating periods of uniform activation, wavefront collision and conduction blocks. Notice that there is a marked change in the fraction of low amplitude signals with increasing anisotropy. This remark motivated a more detailed study of the effect of anisotropic conduction on electrogram morphology (see chapter 12).

10.2 Measures of Organization and Complexity

Transitions from normal rhythm to AF are associated with significant changes in the complexity and the organization of the dynamics. Arrhythmic regimes like atrial flutter and AF (type I, II and III) are characterized by different levels of organization. Measures of complexity and organization are therefore important tools to detect changes in the dynamics or classify different regimes. Moreover, in computer models, it enables researchers to assess the complexity of simulated arrhythmias and to perform comparisons with experimental models and clinical studies.

10.2.1 Overview of Existing Methods

This subsection presents an overview of existing methods for quantifying the complexity and the organization in dynamical systems. These methods are classified into two categories: measures of complexity computed from a single signal, and measures of organization taking into account the spatial information of mapping data. Although a description both classes of methods is included for the sake of completeness, the remaining of the chapter will concentrate on measures of spatial organization.

Measures of Complexity from a Single Signal

Many different indices of signal complexity have been developed and applied to biomedical signals, and in particular to electrocardiograms or electrograms.²⁹³ These methods come from various areas of signal processing:

- *Frequency analysis*: Everett *et al.*^{294, 295} defined an organization index computed from the area below the dominant peak of the power spectrum and some of its harmonics. This index is especially useful for studying dynamics with a marked periodic component. Variations based on dominant frequency were proposed.²⁸⁵

- *Information theory*: approximate entropy,²⁹⁶ multiresolution entropy²⁹⁷ and different forms of Fisher²⁹⁸ and Tsallis^{297,299} information were used to extract the complexity of the statistical information contained in the signal³⁰⁰ and detect sudden changes in the dynamics. The complexity of a signal can be equivalently related to its ability to be compressed, as illustrated by Zhang *et al.*³⁰¹ using Ziv-Lempel complexity.³⁰²
- *Non-linear analysis and chaos*: correlation dimension and correlation entropy estimated on a reconstructed attractor³⁰³ (embedding) were used as measures of organization^{304–306} and as discriminant parameter for classification of AF type I, II and III³⁰⁷ and assessment of the effect of drugs.^{303,308} Since an embedding dimension of 10 to 20 is common for application to electrograms,³⁰⁷ the available signal length is however often too small (“the curse of dimensionality”). Indicators of chaos like positive Lyapunov exponents^{92,309} and fractal dimension³¹⁰ also lead to valuable measures of complexity.
- *Pattern matching*: When the signal can be considered as a sequence of events or peaks (or waveforms in an electrogram), it is meaningful to compute an estimate of the probability that two randomly selected peaks match, with the matching criterion based on a distance measure³¹¹ (e.g. defined as the angle between the vectors constructed from the samples around the peaks).
- *Other signal processing tools*: wavelet-based methods³¹² and archetypal analysis^{313,314} may also be considered for this purpose.

Measures of Organization from Mapping Data

When several signals are recorded at known locations like in mapping experiments, a measure of spatial organization or spatio-temporal complexity may be defined. A common method is to compute a measure of correlation or similarity between each pair of signals, and then to plot this correlation as a function of the distance between the locations at which the signals are recorded.³¹⁵ This correlation is expected to decrease with the distance. A measure of spatial organization is finally defined as the steepness of that decrease.

The degree of correlation between two signals can be measured using maximal cross-correlation,³¹⁶ frequency-averaged magnitude squared coherence³¹⁷ or mean square error of linear prediction.²⁴³ Mutual information is also a good candidate for this application.³¹⁸ Similar methods were developed in liquid state physics, where the solid-liquid transition is observed using the pair correlation function³¹⁹ (*i.e.* the conditional probability density $g(r)$ to find a particle at a distance r from the origin, given that there is a particle at the origin). This is of particular relevance to define an order parameter describing the phase transition.³²⁰

Another different approach is to apply dimensionality reduction techniques to the set of signals, *i.e.* to describe a large part (for instance 90%) of the signal information using a reduced set of signals. The number of modes needed is related to the complexity of the dynamics. Principal component analysis was widely used for this purpose.^{321,322}

The remaining of this section will concentrate on four methods for which experimental results are available. The procedures described in the corresponding original papers will be followed rigorously to avoid inadequate comparisons. To illustrate the methods, results are shown for an episode of SAF lasting for more than 20 s and described in subsection 9.1.3

(modified Luo–Rudy model with $\overline{G}_{si} = 0.07 \text{ mS/cm}^2$). Its dynamics is characterized by complex activation patterns due to multiple wavelets undergoing front-tail interactions, collisions and wavebreaks. The motivation for this choice was that these measures of organization, based on *statistical* signal processing tools, assume that the system is sufficiently disordered in the sense that (random) variations in beat-to-beat interval should be observed. This issue will be discussed in the next section about wavelength estimation.

10.2.2 Space Constant of Activation

Botteron *et al.*^{290,316,323} proposed a measure of organization based on the *maximal cross-correlation* between pairs of signals. The procedure is as follows:

- Inputs: read N digital signals $x_i(t)$, each one representing a bipolar electrogram recorded by an electrode located at \mathbf{d}_i , sampled at 1 kHz.
- Preprocessing: for each signal x_i :
 - Filter with a 3rd-order zero-phase Butterworth band-pass filter with cut-offs at 40–250 Hz.
 - Take the absolute value of the signal.
 - Filter with a 3rd-order zero-phase Butterworth low-pass filter with cut-off at 20 Hz.
 - Remove the mean and normalize. The resulting filtered signal is called y_i .
- Correlation coefficients: for each pair of signals y_i and y_j :
 - Set the distance $d_{ij} = \|\mathbf{d}_i - \mathbf{d}_j\|$.
 - Compute the cross-correlation $c_{ij}(\tau)$ between y_i and y_j .
 - The *correlation coefficient* C_{ij} is defined as the maximal cross-correlation $C_{ij} = \max_{\tau} c_{ij}(\tau)$.
- Graphical representation: Plot the pairs (d_{ij}, C_{ij}) . Whenever possible, group together the points with the same distance d_{ij} and display instead the mean and standard deviation.
- Space constant of activation δ : Fit the data to the function $C(d) = \exp(-d/\delta)$ to determine the space constant δ .

In the preprocessing step, band-pass filtering and smoothing create a waveform which is used directly as an estimate of the likelihood of activation.³¹⁶ An interesting property of this method is that the resulting space constant δ gives an approximation of the average wavelength λ through the simple formula $\lambda = 2\pi \cdot \delta$ (see Botteron and Smith³¹⁶ and the next section).

Fig. 10.3 shows the decrease of the correlation coefficient as a function of the inter-electrode distance during normal sinus rhythm (control) and during SAF. Electrograms are computed in a 8-by-8 grid of bipolar electrodes located in the right atrium free wall. Sinus rhythm is characterized by nearly identical time-shifted electrogram waveforms, so that the correlation coefficient is close to 1. In contrast, the multiple reentrant wavelets present during SAF significantly decrease the correlation between distant electrodes, leading to short-range correlations similar to measurement in humans during AF.²⁹⁰ The space constant of activation is found to be $\delta = 1.6 \pm 0.3 \text{ cm}$. This value obtained during sustained SAF is consistent with the clinical study of human AF by Botteron *et al.*,²⁹⁰ which reported activation space constants globally in the range 1.48–5.99 cm, and specifically $1.84 \pm 0.36 \text{ cm}$ during chronic AF, $2.80 \pm 1.4 \text{ cm}$ during paroxysmal AF and $3.06 \pm 0.4 \text{ cm}$ in patients with no prior history of AF. This encouraging agreement with experimental data motivated a more extensive study of activation space constant during SAF, discussed in the next section in terms of wavelength.

Because of the low-pass filter with cut-off frequency at 20 Hz, all the filtered waveforms look similar. Thus, the cross-correlation essentially estimates a correlation between the sequences of activation times. Sufficiently long signals are required to accurately estimate this correlation. Botteron and Smith³¹⁶ used segments of 2, 3 and 10 s duration. The duration of the segment depended on the heart rhythm in such a way that at least 10-12 activations were present in each segment. Fig. 10.4 displays the space constant δ computed using SAF signals restricted to a subinterval, with a length ranging from 1 to 16 s, assuming that SAF dynamics is stationary. For short signals, the space constant is overestimated. But if the signal length is larger than about 3–4 s, the method gives a reasonable estimate of the space constant which does not depend anymore on the segment duration.

10.2.3 Coherence Analysis

Sih *et al.*³¹⁷ proposed a measure of organization based on the *frequency-averaged magnitude squared coherence* between pairs of signals. The procedure is as follows:

- Inputs: read N digital signals $x_i(t)$, each one representing a unipolar electrogram recorded by an electrode located at \mathbf{d}_i , sampled at 1 kHz.
- Preprocessing: for each signal x_i :
 - Filter with a 3rd-order zero-phase Butterworth low-pass filter with cut-off at 50 Hz.
 - Downsample by a factor 8 to a final sampling rate of 125 Hz.
 - Remove the mean and normalize. The resulting filtered signal is called y_i .
- Magnitude squared coherence: for each pair of signals y_i and y_j :
 - Set the distance $d_{ij} = \|\mathbf{d}_i - \mathbf{d}_j\|$.
 - Estimate the magnitude squared coherence spectrum $\text{MSC}_{ij}(f)$ between y_i and y_j .

$$\text{MSC}_{ij}(f) = \frac{|S_{y_i y_j}(f)|^2}{S_{y_i y_i}(f) S_{y_j y_j}(f)} \quad (10.1)$$

where $S_{y_i y_i}(f)$ is the power spectrum and $S_{y_i y_j}(f)$ the cross-power spectrum.

- The *magnitude squared coherence* (MSC) is defined as the MSC spectrum averaged in the frequency range 0–50 Hz.

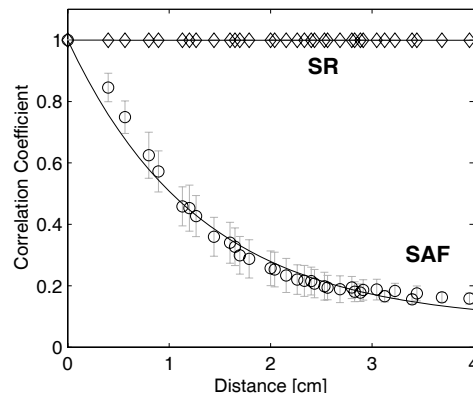


Figure 10.3 — Correlation coefficient as a function of the inter-electrode distance during sinus rhythm (SR, marker: diamond) and SAF (SAF, marker: circle), both simulated using the modified Luo–Rudy model ($\overline{G}_{si} = 0.07 \text{ ms/cm}^2$) and a conduction velocity of 70 cm/s.

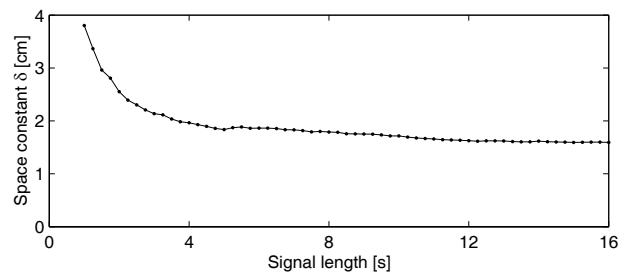


Figure 10.4 — Activation space constant as a function of the time interval over which the space constant is estimated. Signals are measured during SAF simulated using the modified Luo–Rudy model ($\bar{G}_{si} = 0.07 \text{ mS/cm}^2$) and a conduction velocity of 70 cm/s .

- Graphical representation: Plot the pairs $(d_{ij}, \text{MSC}_{ij})$. Whenever possible, group together the points with the same distance d_{ij} and display instead the mean and standard deviation.

Fig. 10.5 displays examples of contour plots of MSC with respect to a reference electrode located at the center of the region (in the right atrium free wall). These coherence maps, computed during SAF, are comparable to experimental maps.^{317,324} Isocoherence contours are approximately circular in an isotropic tissue (Fig. 10.5A). In an anisotropic tissue, however, these circles are elongated into ellipses in about the same direction as fiber orientation, as illustrated in Fig. 10.5B and Fig. 10.5C.

Fig. 10.6 illustrates how MSC decreases with the inter-electrode distance during normal sinus rhythm and during SAF. Signals are computed on a 16-by-16 grid of unipolar electrodes in the right atrium free wall. Experimental studies^{243,317,324} reported a similar behavior. The decrease observed during sinus rhythm is due to the imperfections in coherence estimation, especially at high frequencies.

Compared to the method of space constant of activation, this approach involves an additional averaging over a frequency range, leading to a more robust estimate (*i.e.* a smaller number of signals is needed to estimate the MSC-versus-distance curve). However, MSC decreases quickly with inter-electrode distance, so it is harder to classify different dynamics unless a very high spatial resolution is used for the electrical mapping.

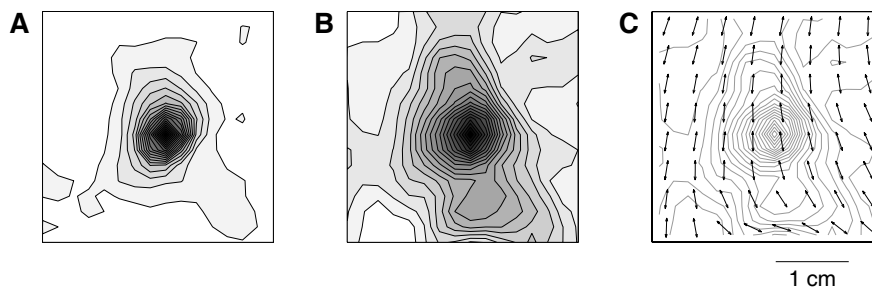


Figure 10.5 — Examples of coherence maps (contour plots). The reference electrode is located at the center. The MSC is gray-level coded from 0 (white) to 1 (black). Signals are measured in the right atrium free wall during SAF simulated using the Luo–Rudy model ($\bar{G}_{si} = 0.07 \text{ mS/cm}^2$). (A) isotropic tissue with a conduction velocity of 70 cm/s . (B) anisotropic tissue with a ratio of longitudinal to transverse conduction velocity of $120:60 \text{ cm/s}$ (anisotropy ratio 4:1). (C) fiber orientation superimposed on the coherence map (B).

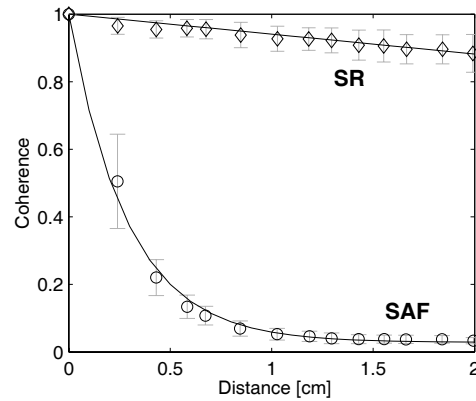


Figure 10.6 — Magnitude squared coherence during sinus rhythm (SR, marker: diamond) and simulated AF (SAF, marker: circle), both simulated using the modified Luo-Rudy model ($\bar{G}_{si} = 0.07 \text{ ms/cm}^2$) and a conduction velocity of 70 cm/s.

10.2.4 Linear Prediction Error

Sih *et al.*^{243,324} estimated the degree of non-linearity in the dynamics by analyzing the *mean-square error of linear prediction* when trying to predict a signal using another one measured at a distant location. A higher temporal resolution is achieved since only short signals are required²⁴³ (about 300 ms). The procedure is as follows (slightly modified from Sih *et al.*²⁴³):

- Inputs: read N digital signals $x_i(t)$, each one representing a unipolar electrogram recorded by an electrode located at \mathbf{d}_i , sampled at 1 kHz.
- Preprocessing: for each signal x_i :
 - Filter with a 3rd-order zero-phase Butterworth low-pass filter with cut-off at 20 Hz.
 - Downsample by a factor 10 to a final sampling rate of 100 Hz.
 - Remove the linear trend and normalize. The resulting filtered signal is called y_i .
- Linear prediction error: for each pair of signals y_i and y_j :
 - Set the distance $d_{ij} = \|\mathbf{d}_i - \mathbf{d}_j\|$.
 - Determine the linear transfer function (filter of order 15) between y_i and y_j in the least mean square sense (predict y_j using y_i).
The resulting mean square error is called $\text{MSE}_{i \rightarrow j}$.
 - Determine the linear transfer function between y_j and y_i (predict y_i using y_j), leading to the mean square error $\text{MSE}_{j \rightarrow i}$.
 - The mean square error associated with the pair (i, j) is $\text{MSE}_{ij} = \min(\text{MSE}_{i \rightarrow j}, \text{MSE}_{j \rightarrow i})$.
- Graphical representation: Plot the pairs $(d_{ij}, \text{MSE}_{ij})$. Whenever possible, group together the points with the same distance d_{ij} and display instead the mean and standard deviation.

Fig. 10.7 illustrates the increase of MSE as a function of the inter-electrode distance during normal sinus rhythm and during SAF where the signals are computed in a 16-by-16 grid of unipolar electrodes in the right atrium free wall. When two electrodes are close together, the corresponding electrograms are linearly related (and thus the MSE is small) since the activations are correlated. For distant electrodes during SAF, however, the activations are triggered by independent wavelets and the MSE reaches its maximal value. Experimental studies^{243,324} reported a similar behavior.

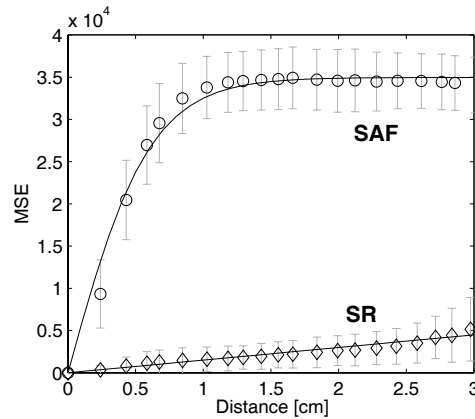


Figure 10.7 — Mean square linear prediction error (MSE) during sinus rhythm (SR, marker: diamond) and simulated AF (SAF, marker: circle), both simulated using the modified Luo–Rudy model ($\bar{G}_{si} = 0.07 \text{ ms/cm}^2$) and a conduction velocity of 70 cm/s.

10.2.5 Principal Component Analysis

Karhunen-Loève decomposition (*principal component analysis*) can be used to quantitatively describe changes in spatial organization in complex dynamics like atrial or ventricular fibrillation.^{321, 322, 325–327} The relevant parameter to extract is the number of principal modes necessary to account for a large fraction (say 90%) of the signal energy. The procedure is as follows:^{321, 328, 329}

- Inputs: read $N = n^2$ digital signals $x_i(t)$ sampled at 1 kHz, recorded by a n -by- n regular grid of unipolar electrodes.
- Preprocessing: for each signal x_i (of length 1 s; if necessary a 1-s segment is extracted):
 - Filter with a 5rd-order zero-phase Butterworth band-pass filter with passband 2–100 Hz.
 - Remove the mean and normalize. The resulting filtered signal is called y_i .
- Karhunen-Loève decomposition (KLD):
 - Construct a matrix Y whose columns are the signals y_i .
 - Determine the eigenvalues $E_1 \geq E_2 \geq \dots \geq E_N$ of the N -by- N matrix $R = Y^T Y$. The eigenvalue E_k represents the energy associated with the k -th mode.
- KLD dimension: Plot the cumulative energy of the first k modes $C_k = E_1 + \dots + E_k$ as a function of k . The KLD dimension D_{KLD} is defined as the number of modes needed to account for a fraction f of the total energy:^{328, 329}

$$D_{\text{KLD}} = \max\{k \mid C_k < f \cdot C_N\} \quad (10.2)$$

The value $f = 0.9$ was used.

- KLD correlation length (if applicable): When the system dynamics is in the *extensive chaos regime*, the KLD dimension becomes an extensive quantity,³²⁹ so that the density of KLD dimension can be considered, leading to the definition of the *KLD correlation length*

$$\xi_{\text{KLD}} = \left(\lim_{A \rightarrow \infty} \frac{D_{\text{KLD}}}{A} \right)^{-1/2} \quad (10.3)$$

where A is the area of the surface covered by the electrodes. Here, in a n -by- n grid of electrodes, $A = n^2 \Delta x^2$ where Δx is the inter-electrode distance.

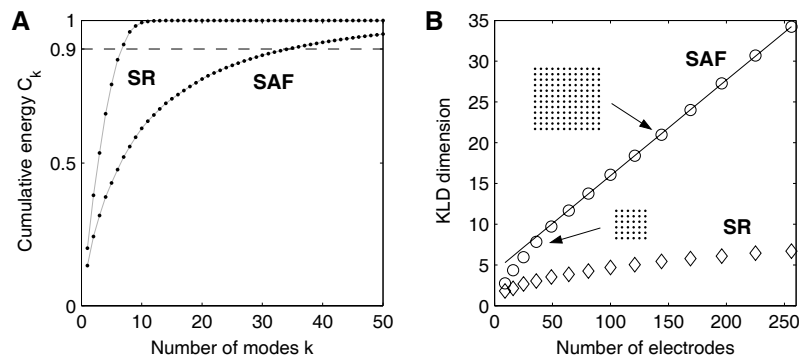


Figure 10.8 — Karhunen-Loève decomposition dimension and correlation length during sinus rhythm (SR, marker: diamond) and simulated AF (SAF, marker: circle), both simulated using the modified Luo–Rudy model ($\bar{G}_{si} = 0.07$ ms/cm²) and a conduction velocity of 70 cm/s.

The steps are illustrated by Fig. 10.8. Signals are recorded in a 16-by-16 grid of unipolar electrodes in the right atrium free wall during normal sinus rhythm and during SAF. Fig. 10.8A presents the cumulative energy C_k of the first k modes computed from the 256 signals. The KLD dimension D_{KLD} is given by the intersection with the horizontal line $C_k = 0.9$. While 256 signals during sinus rhythm require 6 modes to account for 90% of their energy, the complexity of SAF dynamics increases this value to about 35 modes.

KLD dimension depends on the number of electrodes. In order to quantify this dependence, electrode subsets forming a square grid of 3×3 , 4×4 , ..., 16×16 electrodes were successively considered for principal component analysis. Fig. 10.8B shows KLD dimension as a function of the number of electrodes for both sinus rhythm and SAF. The asymptotic linear behavior observed during SAF suggests that the hypothesis of extensive chaos regime is reasonably satisfied. Notice that it is obviously not the case for sinus rhythm. The KLD correlation length ξ_{KLD} can therefore be estimated using (10.3). An average over 20 segments of duration 1 s extracted from the signals recorded during SAF gives $\xi_{\text{KLD}} = 5.4 \pm 0.9$ mm. This value roughly means that 90% of the signals energy can be described by one mode per 5.4×5.4 mm², so that the inter-electrode distance of 2 mm we used in this study is appropriate for electrical mapping of AF.

Bayly *et al.*³²¹ reported KLD dimensions in the range 10–25 during ventricular fibrillation in pigs mapped by a 22×23 array of electrodes covering an area of 2.35×2.46 cm². KLD dimensions can not be directly compared because the inter-electrode distance is different in the computer model. The KLD correlation length, however, does not depend on the electrode configuration. A crude estimate of the KLD correlation length from these experimental data gives values in the range 4.8–7.6 mm. Although a comparison with this experiment is difficult and limited, the order of magnitude is at least consistent.

10.3 Estimation of Wavelength

The wavelength was shown to play a critical role in AF perpetuation both in the computer model (see subsection 9.1.4) and in animal models.²⁸⁸ The difficulty to measure wavelength in patients motivated the development of indirect techniques for wavelength estimation.

Botteron and Smith^{290,316} proposed an estimate of wavelength based on the time correlation between electrograms recorded at different locations (see subsection 10.2.2). They found an estimated wavelength below a critical value, namely 13 ± 3.6 cm, in chronic AF patients and above this value in paroxysmal AF patients. This method and its underlying assumptions will be described in more details and evaluated by means of a computer model of AF.

10.3.1 Hypotheses of Botteron's Method

Botteron's method for wavelength estimation was described in subsection 10.2.2. The arguments and hypotheses underlying the formula $\lambda = 2\pi \cdot \delta$ relating the (estimated) wavelength λ to the activation space constant δ are given here (recall that the procedure uses as input N bipolar electrograms signal x_i , $i = 1, \dots, N$, where x_i is recorded at position \mathbf{d}_i):

1. The filtered and normalized electrograms (denoted by y_i) are used as an estimate of the likelihood of activation.³¹⁶ Examples of such signals are displayed on Fig. 10.9.
2. The cross-correlation $c_{ij}(\tau)$ between y_i and y_j is assumed to represent the probability for the site i to be activated a time interval τ after site j . The correlation coefficient $C_{ij} = \max_{\tau} c_{ij}(\tau)$ is interpreted as the probability for the sites i and j to have a correlated electrical activity (possibly with a delay).
3. Time correlation of the activations is supposed to imply that these activations are elicited by the same wavefronts, that is

$$C_{ij} = \text{Prob}\{\mathbf{d}_i \text{ and } \mathbf{d}_j \text{ belong to the same wavelet domain}\} \quad . \quad (10.4)$$

This probability depends on the wavelength λ and is denoted by $p_{\lambda}(\mathbf{d}_i, \mathbf{d}_j)$.

4. For the sake of simplicity, homogeneity and isotropy is assumed so that the correlation coefficient depends only on a single variable and is written as

$$C_{ij} = p_{\lambda}(\mathbf{d}_i, \mathbf{d}_j) = p(\|\mathbf{d}_i - \mathbf{d}_j\|/\lambda) \quad . \quad (10.5)$$

The space constant of activation δ is defined as the inter-electrode distance for which the correlation coefficient falls to the value $1/e$, so that by definition

$$p(\delta/\lambda) = 1/e \quad . \quad (10.6)$$

5. The function p is estimated in the framework of Allesie's leading circles³³⁰ (see Fig. 10.9). The domain of each wavelet is considered to be a circle whose circumference is the wavelength λ . Then, $p(d/\lambda)$ is the probability for the electrode i to lie in the circle (of radius $\lambda/2\pi$), given that the electrode j lies in the circle and that the distance $\|\mathbf{d}_i - \mathbf{d}_j\|$ is fixed to d . Using this definition for p , it can be shown³¹⁶ that $p(1/2\pi) \approx 1/e$, or, equivalently, $\lambda \approx 2\pi \cdot \delta$ by comparison with (10.6).

The relation $\lambda \approx 2\pi \cdot \delta$ expresses the fact that a more organized dynamics generally corresponds to a longer wavelength. However, this may not be the case depending on the mechanism perpetuating AF (because of hypothesis 3). Suppose that two fixed and stable

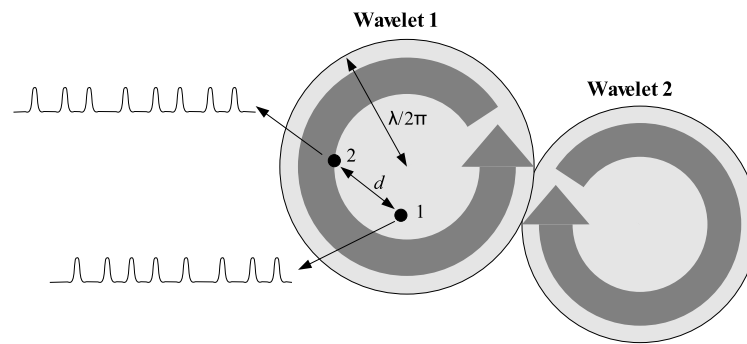


Figure 10.9 — Hypothesis underlying Botteron's estimate of wavelength. Circular regions represent wavelet domains and circular arrows indicate a reentrant activity. Two electrodes (with inter-electrode distance fixed to d) are shown as black dots, as well as their corresponding signal (after filtering and normalization).

rotors with the same frequency coexist in the atria. If two electrograms are recorded, one near each rotor, the correlation coefficient will be close to 1 because their activity is periodic so that the first electrogram is a time-shifted version of the second one. Therefore, this method, based on the *statistical* properties of the activation sequences, is more adapted to AF dynamics perpetuated through a mechanism of multiple interacting wavelets that *randomly* propagate over the whole atrial surface. This last remark motivated the use of Luo–Rudy-based SAF dynamics to evaluate the wavelength estimation method.

10.3.2 Evaluation of Botteron's Method

Botteron and Smith³¹⁶ mentioned that computer models could be used to validate their approach. The consistency of their wavelength estimate was therefore tested in our computer model of AF.

In subsection 9.1.4, different sustained and unsustained SAF dynamics with various wavelengths were simulated using the modified Luo–Rudy model. The effective refractory period (ERP) and the longitudinal conduction velocity (CV) as well as the transverse CV were modified in order to affect wavelength. As a complement to Fig. 9.6 showing SAF duration as a function of the tissue properties, estimated wavelength statistics were plotted as a function of the ERP (Fig. 10.10A), the CV (Fig. 10.10B), and the transverse CV (the longitudinal CV being fixed, Fig. 10.10C). The results show that the variations of the estimated wavelength are consistent with the definition of the wavelength, that is, the estimated wavelength is a monotonic function of both ERP and CV.

Wavelength, however, is overestimated by Botteron's method. First, wavelength estimation is implicitly based on beat-to-beat intervals (AFCL) and not on ERP. According to Table 9.2, taking into account the ERP would reduce the estimated value of wavelength by approximately 30% in the case of the modified Luo–Rudy model. In the example of section 10.2.2 whose estimated wavelength is 10 cm, more direct approaches lead to smaller values. $ERP \times CV$ gives approximately 5.8 cm and $AFCL \times CV$ gives 8.4 cm. In the model of meandering wavelet (using the modified Courtemanche model), the estimated wavelength is 12.7 cm, while $AFCL \times CV$ gives 9.6 cm.

When the SAF dynamics is characterized by a marked spatiotemporal organization, Bot-

teron's method fails to correctly approximate wavelength as explained above. For example, in the model of Courtemanche including inhomogeneous vagal stimulation, the estimated wavelength is 26.5 cm although 4–6 wavelets are present, the AF cycle lengths are in the range 80–90 ms and the CV is 90 cm/s. In this case the activation space constant reflects organization, but not wavelength.

10.3.3 Critical Wavelength of Simulated Atrial Fibrillation

As mentioned above, Botteron and Smith²⁹⁰ used their estimate of wavelength to investigate the relation between wavelength and maintenance of AF. By collecting the data from Figs. 9.6 and 10.10, SAF duration was plotted in Fig. 10.11 as a function of the estimated wavelength for all the simulations considered in the previous subsection.

When the wavelength was reduced (either by decreasing the ERP or the CV), SAF duration increased. Below a critical wavelength, approximately 10 ± 1 cm, SAF duration became larger than 20 s and was considered as sustained.

This phenomenon is in agreement with experimental data. Botteron and Smith²⁹⁰ found a critical wavelength of 13 ± 3.6 in human AF using *exactly the same method* as we used for wavelength estimation. Allesie *et al.*²⁴² estimated that the wavelength should be shorter than 12 cm for human AF to be sustained. Other clinical studies, based on the so-called wavelength index,^{289,291} qualitatively confirmed these findings.

The shorter critical wavelength in the model (especially when considering the wavelength overestimation mentioned in the previous subsection) is interpreted as AF being more difficult to induce in a uniform tissue, *i.e.*, more pronounced alteration of tissue properties are needed in order to maintain SAF (see chapter 8). Additional anatomical structures (like pectinate muscles and other fiber bundles) and heterogeneity not present in the model are expected to enable sustained SAF with a longer wavelength.

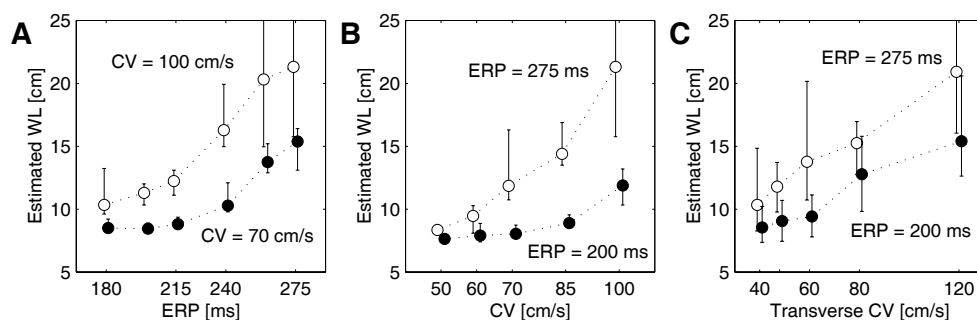


Figure 10.10 — Estimated wavelength during SAF (using Botteron's method) as a function of the membrane and tissue properties (modified Luo–Rudy model). The circles represent the median of wavelength distribution, and the error bars are associated with the first and third quartile. For this illustration, \bar{G}_{si} was replaced by its associated effective refractory period (ERP) at rest (conversion table: an ERP of 275, 265, 240, 215, 200, 180 ms is associated with a \bar{G}_{si} of 0.085, 0.08, 0.07, 0.06, 0.055, 0.05 mS/cm² respectively). (A) Estimated wavelength as a function of the ERP (at rest) with a CV of 70 cm/s (white dots) and 100 cm/s (filled dots). (B) Estimated wavelength as a function of the CV with an ERP (at rest) of 275 ms (white dots) and 200 ms (filled dots). (C) Estimated wavelength as a function of the transverse CV in an anisotropic tissue with a longitudinal CV of 120 cm/s and with an ERP (at rest) of 275 ms (white dots) and 200 ms (filled dots).

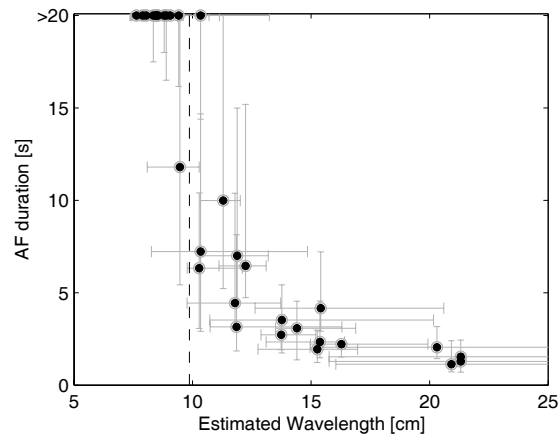


Figure 10.11 — SAF duration as a function of the wavelength estimated using Botteron’s method, obtained by combining the plots of Figs. 9.6 and 10.10. Every data point is an average over 8 different simulations with exactly the same tissue properties. Horizontal and vertical error bars represent the first and third quartile of the resulting distribution of wavelength and SAF duration. The vertical dashed line indicates the critical wavelength.

10.4 Conclusion

This chapter was an attempt to fill the gap between computer modeling and experimental studies. Since electrograms are usually the only measurement accessible in both electrophysiology laboratory and in mathematical models, they are particularly suited for that purpose.

In this chapter, simulated high-density mapping revealed activation patterns similar, although less complex, to those observed experimentally, showing uniform activations, collisions and conduction blocks involving 1–3 wavelets in the mapped area. The spatial organization during SAF was assessed using clinically relevant procedures. The results confirmed that AF is not random but is characterized by a spatial organization whose extent (activation space constant) ranges from 1.3 to 3.2 cm, depending on the wavelength, on SAF duration and the mechanisms maintaining SAF. Botteron’s method for wavelength estimation was evaluated in the computer model. The model study showed the relevance of this approach, despite an overestimation of the wavelength as compared to direct methods ($ERP \times CV$). In particular, this method helped determine the critical wavelength below which SAF was sustained.

Can we extract information about the tissue substrate (conduction properties, anisotropy, heterogeneity) and wavelet dynamics (wavefront shape, wavelength) from only electrogram data or possibly electrical mapping data? Botteron’s estimate of wavelength shows that a positive answer to this question is probable, although *a priori* knowledge about the underlying mechanisms seems to be required. The next two chapters will focus on this question by investigating the effects of tissue structure and AF dynamics on unipolar electrogram morphology.

Part IV

Electrogram Morphology

Atrial fibrillation provides a natural environment to explore electrograms for a wide array of wavefronts with different curvatures and extents, propagating at varying coupling intervals and in different directions. In this part, data from computer models are studied to relate features of the signals to the underlying dynamics and tissue substrate. Computer models enable one to analyze separately the effects of wavefront dynamics and tissue conduction properties. Each one will be presented in a separate chapter. Chapter 11 concentrates on the effect of wavefront dynamics (wavefront shape and curvature, collisions, refractoriness, conduction blocks) on electrogram morphology. Chapter 12 describes the impact of changes in conduction properties (anisotropy and heterogeneity).

Electrogram Morphology: Effect of Wavefront Dynamics

Despite the significant advances in optical methods to indirectly measure electrical activity in the heart, the only technique available for the clinical local evaluation of the human heart is electrical mapping of extracellular potentials or electrograms using contact or non-contact electrode arrays. A number of simulation studies have been performed to determine the effects of tissue anisotropy, conduction block, and collision on the morphology of unipolar and bipolar electrograms during pacing or stable rhythms.^{331–335} In contrast, there is little theoretical guidance to relate single or multisite electrograms to the underlying dynamics during arrhythmias like atrial fibrillation (AF). Electrograms recorded at a single site during AF exhibit significant variation in amplitude and shape.¹⁷⁰ It is unclear, however, what features of the variation are due to the size and orientation of multiple, interacting wavelets maintaining the arrhythmia and what features are due to the underlying substrate.

In this chapter, the simulated substrate is characterized by *uniform and isotropic conduction properties*. The discussion will focus on the impact of wavelet dynamics on electrogram morphology during simulated AF (SAF). The different aspects of wavelet dynamics will be studied separately:

- curved wavefronts and spirals,
- wavefront collisions,
- tissue refractoriness,
- front-tail interactions and conduction blocks.

A hierarchical set of computer models will be used for that purpose, including one-dimensional fibers, 2D sheets of tissue and an atrial model. This chapter aims at providing a better understanding of the relationship between electrogram morphology and the underlying AF dynamics.

11.1 Characterization of Electrogram Waveforms

This section describes how relevant informations about electrogram morphology are extracted from the signals. First, electrogram waveforms will be isolated using a peak detec-

tion scheme. Then, qualitative and quantitative measures of waveform morphology as well as some terminology will be introduced.

11.1.1 Waveform Detection

Numerous automated peak detection schemes have been developed for extracting QRS complexes from experimental ECG signals.³³⁶ These methods can also be applied to atrial electrograms. In our application, a peak (waveform) is considered detected if the majority of the following threshold-based methods can recognize it*: (1) instantaneous frequency analysis,^{337–340} (2) high pass filtering³⁴¹ and (3) adaptive linear prediction error.³⁴² When simulated electrograms are processed, however, the third method alone (with a 3rd-order predictor) is generally sufficient because of the smoothness of the signals (see Fig. 11.1A). In addition, a peak is rejected if it is too close to the previous one (the time interval should be >50 ms, a lower bound for the effective refractory period). This precaution enables a correct detection of waveforms featuring multiple deflections.

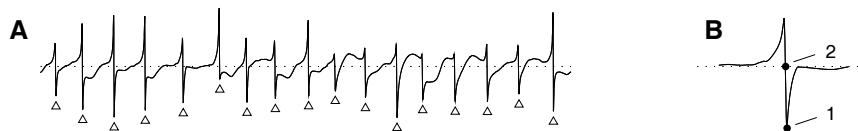


Figure 11.1 — Characterization of electrogram waveforms. (A) Illustration of peak detection in atrial electrograms. (B) Determination of the activation time from electrograms using the position of the negative deflection (point 1) and using the intersection with the x -axis (point 2). The dashed line represents the zero potential.

The *activation time* (temporal localization of the waveform) is the basis for the construction of isochrone maps. It can be approximated by the position of the negative peak. When a higher accuracy is needed and the signal is smooth enough, the activation time is redefined as the intersection with the x -axis just preceding the negative peak (see Fig. 11.1B). This value gives a robust estimate of the position of the maximal slope of the electrogram, which in turn is well aligned with the maximal slope of the membrane potential upstroke.²³⁴ Notice that in the case of fragmented potentials (see next subsection), the activation time may be difficult to determine from electrograms.^{317,343} In computer models, if necessary, the action potential can be used to determine which deflection corresponds to the depolarization.

11.1.2 Waveform Morphology: Qualitative Description

The degree of complexity of a waveform can be qualitatively described by the number of deflections. Following an approach proposed by Konings *et al.*,¹³ unipolar electrogram waveforms were classified into four categories illustrated on Fig. 11.2: (1) *single potentials* are characterized by a single large negative deflection, (2) *short-double potentials* by two negative deflections separated by <10 ms, (3) *long-double potentials* by two negative deflections separated by an interval of >10 ms, and (4) *fragmented potentials* by a complex with multiple negative deflections within 50 ms.

*The peak detection toolbox was implemented by Zenichi Ihara, Signal Processing Institute, EPFL, Lausanne (2002).

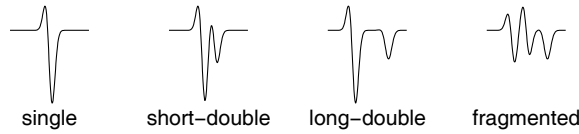


Figure 11.2 — Classification of unipolar electrograms into singles, short-doubles, long-doubles and fragmented potentials. A synthetic example is given for each category.

11.1.3 Waveform Morphology: Quantitative Description

Because even single potentials can display various morphologies,¹⁷⁰ a shape index was developed to compare signals. As shown in Fig. 11.3, the positive deflection (resp. negative deflection) will be called the R wave (resp. S wave) and its amplitude (in absolute value) will be denoted by R (resp. S). The amplitude is measured with respect to the zero potential line. This terminology, found for instance in Villacastin *et al.*,³⁴⁴ in Chorro *et al.*³⁴⁵ and in Fenelon and Brugada,³⁴⁶ should not be confused with the R and S waves of surface ECGs.

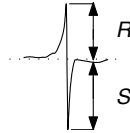


Figure 11.3 — Characterization of electrogram waveforms: illustration of the definitions of R and S . The dashed line represents the zero potential.

The quantitative description of electrogram morphology will be based on two waveform parameters: the total amplitude A and the asymmetry a , respectively defined as

$$A = R + S \quad (11.1)$$

$$a = \frac{R - S}{R + S} = \frac{R/S - 1}{R/S + 1} \quad (11.2)$$

where the second equality for a relates a to the R/S ratio used notably in Villacastin *et al.*³⁴⁴ By its definition, the asymmetry ranges from -1 to 1 . A symmetric waveform has an asymmetry $a = 0$. If $R > S$ (*positive asymmetric* waveform), the asymmetry a is positive, while if $R < S$ (*negative asymmetric* waveform), the asymmetry a is negative.

For simulated signals, the amplitude A will be given in normalized units, in such a way that $0 < A \leq 1$, because only *relative variations* in amplitude will be investigated. The amplitude A will be generally normalized with respect to the amplitude of a waveform generated by a simple propagation in a fully recovered tissue. Since the order of magnitude of electrogram peak-to-peak amplitude is 10 mV (see de Bakker³⁴⁷), the constant prefactor arising in the expression used for computing electrograms (see section 7.2) can be chosen so that a normalized amplitude $A = 1$ corresponds to an amplitude of 10 mV.

When a particular asymmetry predominance has to be emphasized or compared to experimental data, the waveforms will be classified into 4 patterns^{344-346,348}: the QS pattern (essentially negative deflection, $R \ll S$), the rS pattern (negative predominance, $R < S$), the Rs pattern (positive predominance, $R > S$) and the R pattern (essentially positive

deflection, $R \gg S$). An RS pattern can possibly be added to classify separately symmetric waveforms ($R \approx S$). Automatic classification is performed using separation levels at $a = -1/2$, $a = 0$ and $a = 1/2$. These thresholds, corresponding to R/S ratios of 1/3, 1 and 3, were taken from Villacastin *et al.*³⁴⁴

11.1.4 Amplitude-versus-Asymmetry Diagrams

The statistics of electrogram morphology during a complex dynamics like AF was visualized with the help of amplitude-versus-asymmetry diagrams. In this graphical representation, the amplitude and asymmetry are computed for each waveform and a point is drawn at the corresponding location in the diagram. This plot can be combined with histograms of amplitude and asymmetry. Fig. 11.4 gives examples of waveforms with various morphologies arranged in an amplitude-versus-asymmetry diagram.

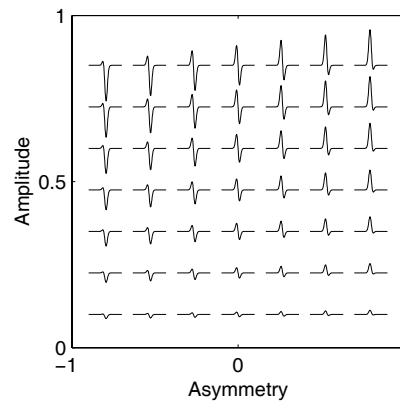


Figure 11.4 — Amplitude-versus-asymmetry plot with examples of electrogram waveforms located at the point corresponding to its morphology. Amplitudes are normalized.

11.2 Wavefront Curvature

This section is devoted to the analysis of the impact of wavefront curvature on waveform asymmetry. Wavefronts of increasing shape complexity will be considered: circular wavefronts in a 2D sheet of tissue, convex and concave wavefronts in the atrial model during stable pacing and then during SAF.

11.2.1 Motivation

In order to motivate the analysis of the effect of wavefront curvature and suggest adequate working hypotheses, recently published experimental data and preliminary simulated results describing waveform morphology are briefly described here.

Sinus rhythm and sustained SAF were simulated in a uniform and isotropic tissue with a modified Luo–Rudy membrane kinetics ($\overline{G}_{si} = 0.07$ mS/cm², see subsection 9.1.3). Electrograms were recorded in the grid (plaque) of 256 electrodes located in the right atrium free wall. Statistical distributions of waveform morphology were constructed. Fig. 11.5 shows the variation of amplitude versus the asymmetry of the electrograms over the entire plaque

for sinus rhythm (left panel) and SAF (right panel). Each point in the scatter plot represents the electrogram amplitude and asymmetry at the 256 sites in the plaque region for a single beat during sinus rhythm and approximately 120 beats during SAF (14 s time window). During sinus rhythm in the isotropic atria, the waveform morphology is similar over the whole atria (Fig. 11.5A) and is revealed as a tight cluster of points centered on an average asymmetry of -0.05. During SAF, however, the morphology distribution is characterized by a larger dispersion of both amplitude and asymmetry in a circular cluster centered on an average asymmetry of -0.2. In addition, a set of positive asymmetric small amplitude waveforms is observed.

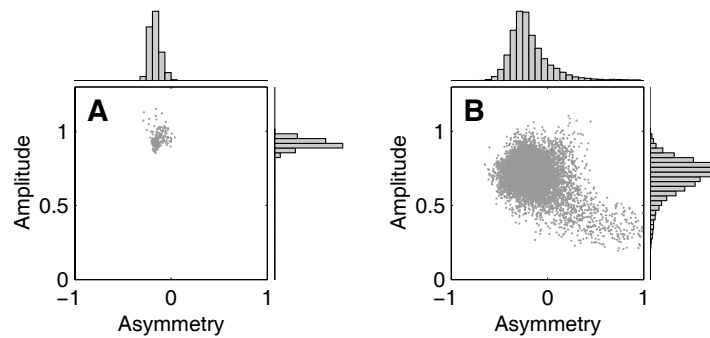


Figure 11.5 — Example of amplitude-versus-asymmetry diagram during (A) sinus rhythm and (B) SAF, combined with the marginal distributions of amplitude and asymmetry. Amplitudes are given in normalized units. An amplitude $A = 1$ can be seen as representing 10 mV.

A first global observation about these simulation results is the predominance of negative over positive asymmetric waveforms, during both sinus rhythm and SAF. Experimental recordings confirm this remark. For instance, most of the signals presented in Konings^{13,181} qualitatively display this predominance. Moreover, in a recent study of electrogram morphology in a rabbit model of ventricular fibrillation, Chorro *et al.*³⁴⁵ recorded 121 unipolar electrograms using a 1.1×1.1-cm grid of electrodes located in the lateral wall of the left ventricle. Electrogram asymmetry, classified by visual inspection into QS, rS, Rs and R patterns, was then reported for three different activation patterns: single broad wavefront propagations, epicardial breakthroughs (centrifugal elliptic isochrones), and conduction blocks. These asymmetry distributions, displayed on Fig. 11.6, revealed a predominance of QS and

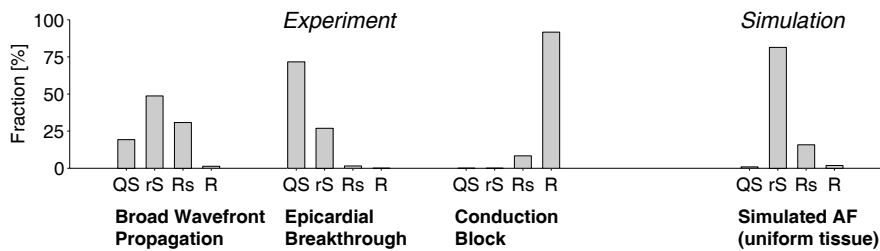


Figure 11.6 — Waveform asymmetry in the experiment of Chorro *et al.*³⁴⁵ (the histograms are constructed from the numerical data given in the original paper) and in SAF run on a tissue with uniform conduction and membrane properties.

rS patterns in the two first classes of activation patterns, while R patterns were specifically associated with conduction blocks. Notice that the negative asymmetry is more pronounced in epicardial breakthrough patterns (high wavefront curvature) than in broad wavefront patterns (low wavefront curvature). These findings are in agreement with Fenelon and Brugada³⁴⁶ reporting, in a study of slow conduction in human typical atrial flutter, QS patterns at onset of activation, R patterns in case of collision or end of activation and essentially rS patterns otherwise.

Therefore, in order to elucidate the origin of waveform morphology, activation patterns with increasing complexity will have to be initiated and related to their corresponding electrograms. The different constitutive elements of the dynamics of AF will be successively analyzed in the subsequent sections: curved wavefronts, wavefront collisions, conduction blocks and effect of wavelength.

11.2.2 Theory of Oblique Dipole Layer

The theory of *oblique dipole layer* gives a theoretical background for the understanding of waveform asymmetry. In this framework, electrograms are shown to be the result of the superposition of dipole fields whose sources are located along the wavefront. The orientation of these dipoles will help describe the relationship between wavefront shape and electrogram morphology. This theory also applies to the anisotropic case studied in the next chapter.

First, wavefront propagation has to be described. In the eikonal approach, the wavefront $\Sigma_{\text{wf}}(t)$ (i.e., the depolarization wave) moves in a fully recovered cardiac tissue along its normal vector with a direction-dependent velocity. (see Colli Franzone *et al.*^{349–352}). This approach is the electrophysiological counterpart of the geometrical optics (eikonal equation and Huygens' principle) in the wave theory of light,³⁵³ or the Wentzel–Kramers–Brillouin semi-classical approximation in quantum mechanics.³⁵⁴ As a result, the eikonal method outputs the isochrones $\Sigma_{\text{wf}}(t)$. Electrograms can then be computed in the bidomain framework from a precomputed action potential shape.³⁵⁵

In this context, convenient approximate formulae for the far-field extracardiac potential were derived by Colli Franzone *et al.*³⁵⁵ Assuming that the action potential upstroke is a step function ($V_m(t) = V_{\text{rest}}$ if $t < t_{\text{activ}}$ and $V_m(t) = V_{\text{rest}} + \Delta V_{\text{max}}$ if $t \geq t_{\text{activ}}$ where t_{activ} is the activation time), an electrogram ϕ_0 measured at location \mathbf{x} outside the wavefront ($\mathbf{x} \notin \Sigma_{\text{wf}}(t)$) is shown to be directly related to the wavefront shape $\Sigma_{\text{wf}}(t)$ through the equation³⁵⁵

$$\phi_0(\mathbf{x}, t) = \Delta V_{\text{max}} \int_{\Sigma_{\text{wf}}(t)} d\ell(\mathbf{y}) \delta \cdot \left(\boldsymbol{\sigma}_i(\mathbf{y}) \mathbf{n}(\mathbf{y}) \right)^\top \cdot \nabla_{\mathbf{y}} G(\mathbf{x}, \mathbf{y}) \quad (11.3)$$

where $d\ell$ is an infinitesimal-length element along the wavefront, δ is the tissue thickness, \mathbf{n} is the unit vector normal to the wavefront and directed toward the resting region, and $\boldsymbol{\sigma}_i$ is the intracellular conductivity tensor. The Green's function $G(\mathbf{x}, \mathbf{y})$ is the potential at position \mathbf{x} generated by a unit punctual source located at \mathbf{y} , that is, $G(\mathbf{x}, \mathbf{y})$ is the solution of

$$\nabla_{\mathbf{x}} \cdot \boldsymbol{\sigma}_0 \nabla_{\mathbf{x}} G(\mathbf{x}, \mathbf{y}) + \delta_3(\mathbf{x} - \mathbf{y}) = 0 \quad (11.4)$$

where $\boldsymbol{\sigma}_0$ is the conductivity tensor of the surrounding medium and δ_3 is the 3D-Dirac distribution. In the framework of the current-source approximation (infinite, homogeneous

and isotropic conductive surrounding medium) this function is given by

$$G(\mathbf{x}, \mathbf{y}) = \frac{1}{4\pi\sigma_0 \|\mathbf{x} - \mathbf{y}\|} . \quad (11.5)$$

In the homogeneous and isotropic case ($\sigma_i = \sigma_i \mathbb{I}$), the electrogram (11.3) is written as a superposition of dipolar fields.³¹ The density of dipolar moment $\boldsymbol{\mu}$ is equal to

$$\boldsymbol{\mu} = \sigma_i \mathbf{n} \quad (11.6)$$

along the wavefront, and is normal to this wavefront. The distribution of dipolar moments along convex and concave wavefronts is illustrated in Fig. 11.7.

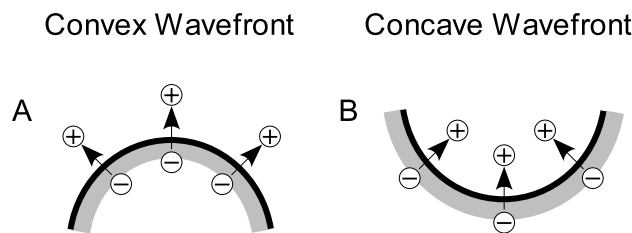


Figure 11.7 — Distribution of dipolar moments on convex (A) and concave (B) wavefronts on a plane tissue with isotropic conduction properties. The black half-circles are wavefronts and the gray regions indicate the zones of activated tissue. The dipoles are displayed as an arrow joining a negative (\ominus) and a positive (\oplus) current source.

11.2.3 Working Hypothesis

Experimental evidences and general considerations in the framework of the eikonal approach suggest that electrogram morphology is related to the wavefront shape, and in particular to its curvature. As a matter of fact, Fig. 11.7 gives an insight into the electrogram morphology since the R wave (resp. S wave) is associated with the density of positive current source \oplus (resp. negative current source \ominus). As a guideline for the subsequent discussion, we hypothesized that:

Curvature hypothesis*: In an isotropic tissue, an electrogram waveform measured close to a *convex* wavefront has a small R wave and a large S wave ($R < S$), i.e., has a *negative asymmetry* ($a < 0$). Reciprocally, a waveform measured close to a *concave* wavefront has a large R wave and a small S wave ($R > S$), i.e., has a *positive asymmetry* ($a > 0$). Symmetric waveforms ($a = 0$) are associated with planar wavefronts.

This statement will be evaluated in two-dimensional plane sheet of tissue and in an atrial model during pacing and during SAF.

11.2.4 Estimation of Local Curvature

Quantification of the relation between waveform asymmetry and wavefront curvature requires a tool to estimate the local curvature of a wavefront defined by the activation times

*The “curvature hypothesis” for waveform asymmetry was formulated by R. Houben, Bakken Research Institute, Maastricht, The Netherlands.

at given locations, typically arranged in a grid. Mathematically, curvature is defined as the inverse of the osculating circle radius.³⁵⁶ Here, curvature is positive for convex wavefronts and negative for concave wavefronts. When a high spatial resolution (< 0.5 mm) for the activation times is available, the wavefront may be directly detected using a threshold and fitted to an appropriate curve, for instance to a spline.³⁵⁷ But in general, and especially with experimental data, it is necessary to fit an activation time map.

Here, electrogram data from electrical mapping (16×16 grid of electrodes with an inter-electrode distance of 2 mm) are considered. Suppose we want to compute the curvature of the wavefront at the black dot in the center of Fig. 11.8. A bivariate second-order polynomial $\tau(x, y)$ is fitted to the activation times of the 3×3 grid of the node considered and its nearest neighbors^{358–360}

$$\tau(x, y) = a_1 + a_2x + a_3y + a_4xy + a_5x^2 + a_6y^2 \quad (11.7)$$

using the local coordinate system xy (see Fig. 11.8). The overdetermined linear system constructed from Eq. (11.7) evaluated at each of the 9 points is solved for the coefficients a_1, \dots, a_6 in the least mean square sense.

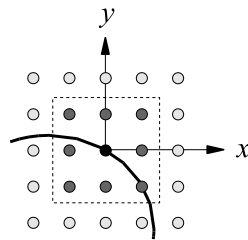


Figure 11.8 — Illustration of the method to estimate curvature. The dots represent the points where the activation times are known. The x - and y -axes define a local coordinate system with respect to the (black) center point. The 9 points enclosed in the dashed square are used to construct the (local) isochrone displayed as a black curve.

The isochrone $y(x)$ crossing the origin is defined by the implicit equation $\tau(x, y(x)) = a_1$. Through the calculation of the derivatives of the implicit function $y(x)$, the absolute value of the curvature \varkappa at the origin $(0, 0)$ is³⁵⁶

$$|\varkappa| = \frac{|y''(0)|}{(1 + y'(0)^2)^{3/2}} = 2 \frac{|a_3^2 a_5 - a_2 a_3 a_4 + a_2^2 a_6|}{(a_2^2 + a_3^2)^{3/2}}. \quad (11.8)$$

In the case $a_2 = a_3 = 0$, the isochrone degenerates into a pair of lines and the curvature is not well-defined. The sign of the curvature is here by convention negative when the wavefront moves toward the center \mathbf{c}_{osc} of its osculating circle, that is

$$\text{sgn}(\varkappa) = -\text{sgn}(\nabla p(0, 0) \cdot \mathbf{c}_{\text{osc}}) \quad (11.9)$$

where sgn is the signum function. Direct and explicit calculation of the osculating circle³⁵⁶ leads to $\text{sgn}(\varkappa) = \text{sgn}(a_3^2 a_5 - a_2 a_3 a_4 + a_2^2 a_6)$, *i.e.*

$$\varkappa = \text{sgn}(\varkappa) \cdot |\varkappa| = 2 \frac{a_3^2 a_5 - a_2 a_3 a_4 + a_2^2 a_6}{(a_2^2 + a_3^2)^{3/2}}. \quad (11.10)$$

This formula was used as an estimate of wavefront local curvature.

11.2.5 Two-Dimensional Circular Wavefronts

To quantify the relationship of wavefront curvature to waveform asymmetry, a simulation was performed on a model of a large 6×6 -cm sheet of tissue with an isotropic resistivity of $200\ \Omega\text{ cm}$. Using this model, wavefronts of time-varying curvatures were created by imposing three different stimulus patterns: a point at the center of the tissue (convex wavefront), the complement (in the sense of set operations) of a large circle (concave wavefront), and an edge (plane wave). The asymmetry was computed for signals measured along the propagation of the wavefront.

For recording points along the diagonal, at a distance of 0.5 mm (dashed line), 1 mm (solid line) and 1.5 mm (dash-dotted line) from the tissue surface, Fig. 11.9 shows the waveform asymmetry as a function of the wavefront curvature. The larger the curvature of a concave or colliding front, the larger the R wave relative to the S wave (positive asymmetry). Similarly, highly curved convex fronts are associated with a larger S wave relative to the R wave, *i.e.*, with a negative asymmetry. This curvature effect is more pronounced in electrograms measured at a larger distance from the tissue surface. These results, obtained in a 2D tissue, are in agreement with our working hypothesis.

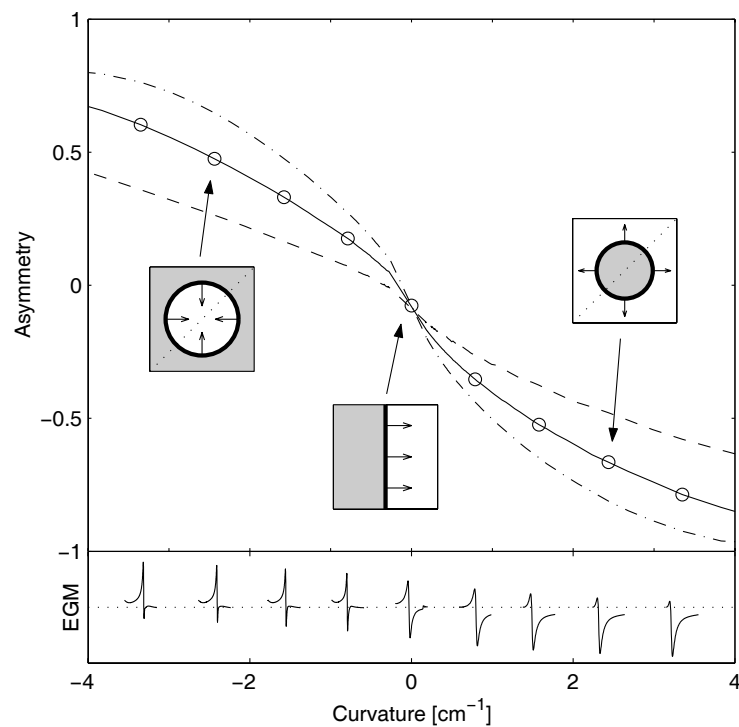


Figure 11.9 — Waveform asymmetry as a function of the wavefront curvature in a 2D tissue. Electrograms are measured along the diagonal, 0.5 mm (dashed line), 1 mm (solid line) and 1.5 mm (dash-dotted line) from the tissue surface. The curvature of a circular wavefront was defined as the inverse of its radius. Negative curvatures correspond to the wavefront propagating from the borders to the center; positive curvature correspond to the wavefront expanding from the center to the boundary; curvature equal to zero correspond to the plane wave. A few examples of electrogram waveforms (EGM), measured 1 mm from the tissue surface, are shown below their corresponding asymmetry (circle mark).

11.2.6 Curved Wavefronts in the Atrial Model

The next step is testing the curvature hypothesis on the atrial model during pacing. Boundary conditions are more natural in this model. Moreover, different activation patterns with non-uniform curvature can be initiated by single site pacing..

Six pacing sites have been selected to generate different activation patterns and variations in wavefront curvature in the zone of the right atrium free wall mapped by the grid of electrodes. These pacing sites were located near the anatomical location of the tricuspid valve, the right atrium appendage, the septum wall, the Bachmann's bundle, the sino-atrial node and the pulmonary veins region. From the 16×16 electrograms (sampled at 10 kHz) recorded 1 mm from the atrial surface, activation times and asymmetries were extracted and the isochrones were reconstructed. The curvature of these isochrones were then computed by Eq. (11.10), assuming that the grid of electrodes is planar and that the inter-electrode distance is constant (this is only approximately the case due to wall curvature).

Fig. 11.10 displays, for each pacing site, the isochrones, the wavefront curvature map, the waveform asymmetry map, and an asymmetry-vs-curvature plot illustrating the negative correlation between asymmetry and curvature. Although the linear correlation coefficient ranges from -0.6 to -0.85 (the data are not strongly linearly correlated), the correlation is systematically negative. In addition, a comparison of columns 2 and 3 of Fig. 11.10 clearly shows a qualitative correspondence between zones of convex wavefronts (resp. concave wavefronts) and zones of negative waveform asymmetry (resp. positive asymmetry).

Fig. 11.11 merges all the asymmetry-vs-curvature scatter plots of Fig. 11.10. The curve obtained with a circular wavefront in 2D tissue is superimposed for comparison. For a curvature in the interval between -1 and 1 cm^{-1} , 2D and 3D-surface models generated waveforms with an asymmetry in the same range. But for highly curved wavefronts, the atrial model did not produce the very asymmetric waveforms predicted by the 2D model. These differences between numerical experiments performed on 2D tissue and on the atrial model can be justified by the following arguments:

- *Non-uniformity of the curvature:* Along the wavefront, the curvature is not constant, in contrast with the circular wavefronts of the previous subsection. The electrode makes an average over a part of the wavefront. As a result, extreme asymmetries are rarely observed since the regions of high curvature are usually small.
- *Distance between the electrodes and the tissue:* The curvature effect is difficult to exhibit in case of complex activation patterns. When the electrodes are close to the atrial surface, the curvature effect is less pronounced. On the other hand, when the electrodes are far from the tissue surface, the averaging process discussed just above complicates the relation between asymmetry and curvature, *i.e.*, asymmetry depends on the whole wavefront shape and not only on its local shape.
- *Not-well-defined curvature:* When two wavefronts (or two different parts of a single wavefront) merge or collide, the isochrone has an edge point where the curvature is infinite. This problem becomes critical during AF in which this event may occur frequently.
- *Wall curvature:* Our estimate of wavefront curvature does not take into account wall curvature. The wavefront actually lies in the 3D-space and its curvature should be

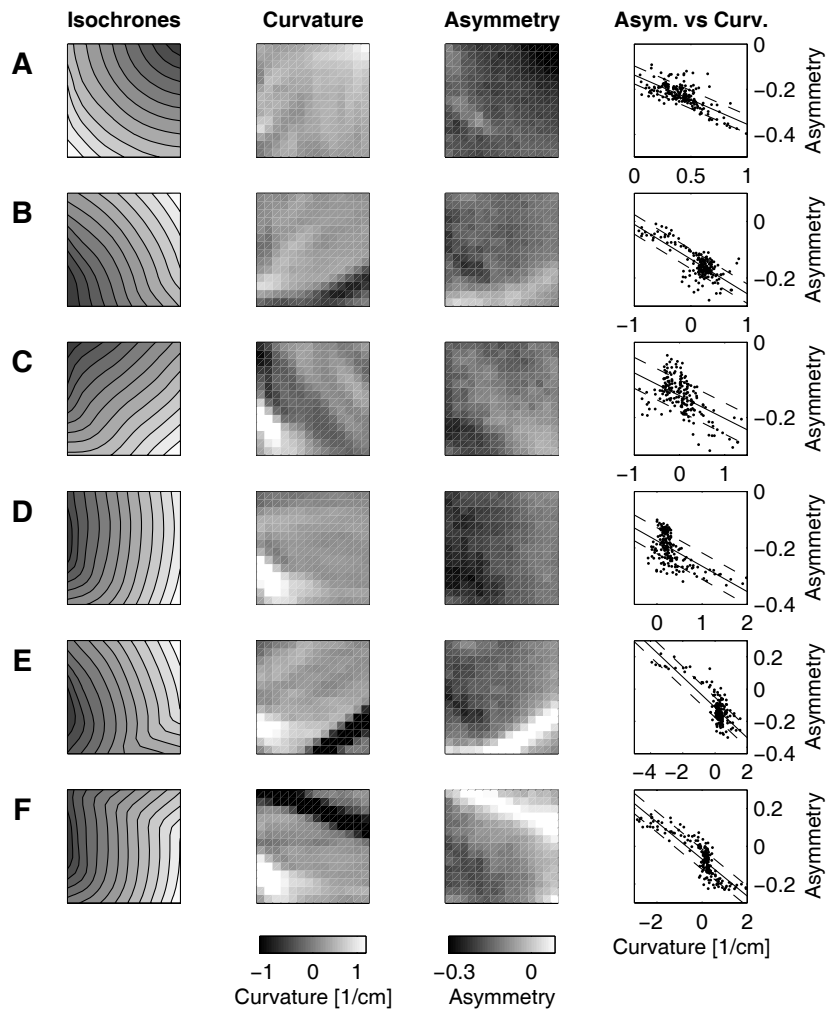


Figure 11.10 — Relation of wavefront curvature to waveform asymmetry during stable pacing in the atria. The mapping area is a 3×3 cm square region located in the right atrium free wall. First column: isochrones. Activation time is gray-level coded (black means early and white late). The stimulus site is located near the anatomical location of the tricuspid valve (A), the right atrium appendage (B), the septal wall (C), the Bachmann’s bundle (D), the sino-atrial node (E) and the pulmonary veins region (F). Second column: corresponding wavefront curvature map computed using Eq. (11.10). Curvature is gray-level coded (white means convex and black concave). Third column: waveform asymmetry map (white means positive asymmetry, gray means symmetric waveform and black means negative asymmetry). Fourth column: asymmetry versus curvature plot summarizing the correlation between the preceding columns. Linear regression line is represented (solid line) as well as error bounds containing at least 50% of the samples (dashed lines).

precisely redefined in this case. In addition, due to wall curvature, the grid of electrodes is slightly distorted, especially in its corners (similarly to an optical aberration of type “pin-cushion distortion”). However, less than 9% of the inter-electrode distances are altered by more than 10%.

- *Numerical accuracy:* Activation times are determined with some uncertainty (the inferior limit being the time step of the solver). Although this has no visual impact on activation maps and isochrones, the curvature involves second order derivatives which are difficult to accurately estimate in presence of noise.

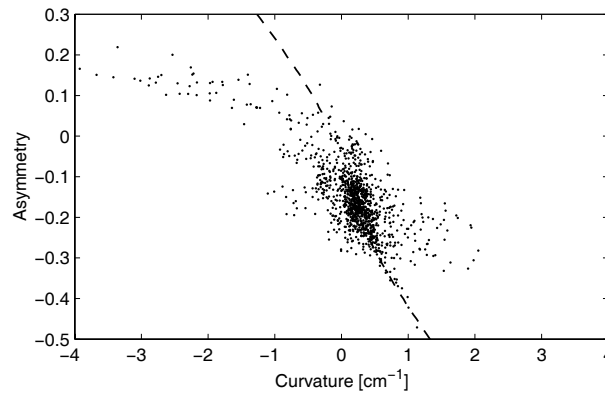


Figure 11.11 — Relation of wavefront curvature to waveform asymmetry during stable pacing in the atria. The asymmetry-vs-curvature scatter plots of Fig. 11.10 are merged. The dashed line represents the curve computed in a 2D tissue (Fig. 11.9) with electrodes located 1 mm from the tissue surface.

Despite the limitations mentioned above, the results show again that convex wavefronts are associated with negative waveform asymmetry and concave wavefront with positive asymmetry. Moreover, when the curvature is near zero, the asymmetry tends to be slightly negative.

11.2.7 Wavefront Classification during Simulated AF

The previous subsection emphasized the relevance of a classification of the wavefronts into three classes: convex wavefronts, plane waves and concave wavefronts. In order to further assess the curvature hypothesis during the more complex wavefront dynamics of AF, 200 activation maps constructed during SAF were analyzed and classified by visual inspection. Among these 200 wavefronts, 64% were convex (e.g. spiral wave), 20% were plane waves, and 16% were concave (mostly wavefronts collision or merging).

Fig. 11.12 gives two typical examples of wavefront shape for each class with their corresponding electrogram waveform and asymmetry. In these examples, convex wavefronts are associated with large negative asymmetry ($a < -0.2$), near-planar wavefronts with slightly negative asymmetry and concave wavefronts with positive asymmetry. In order to estimate how much information about the wavefront can be extracted from an electrogram during AF, statistics of waveform asymmetry inside each class is represented on Fig. 11.13. Separation lines at asymmetry $a = -0.17$ and $a = -0.06$ lead to a classification error of 19%, mainly due to the difficulty to classify near-planar wavefronts. When only the convex and concave classes were considered, the classification error was reduced to 3.5%.

Consequently, waveform asymmetry gives some information about wavefront curvature during SAF in uniform isotropic tissue, but this relationship becomes less reliable when curvature is low.

11.3 Wavefront Collisions

The results shown in the previous section indicates that concave wavefronts observed during SAF are mainly the result of collisions. Waveform morphology close to collision lines

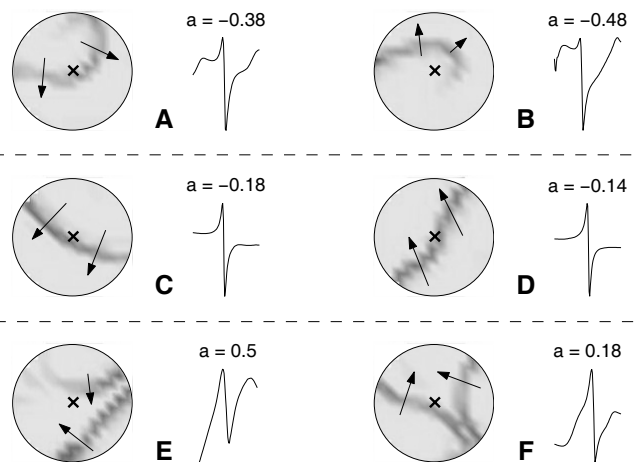


Figure 11.12 — Snapshots of simulated high density mapping of AF and corresponding electrogram waveforms measured at the location indicated by a small cross (\times). Waveform asymmetry (a) is given just above the electrograms. The diameter of the mapping area is 3 cm. Gradients of membrane potential are gray level-coded and the propagation of wavefronts is described by arrows. These examples are classified in three activation pattern classes: (A,B) spiral waves, (C,D) plane waves and (E,F) wavefront collisions.

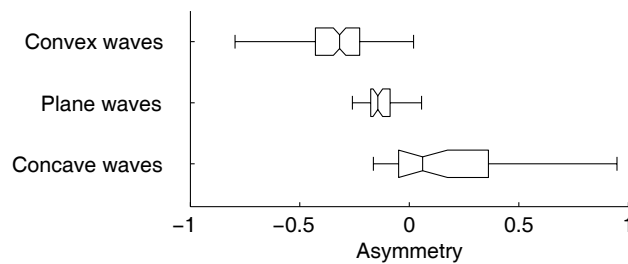


Figure 11.13 — Asymmetry statistics in the three classes of wavefronts (convex, plane and concave/colliding) manually classified during SAF. Medians, quartiles and minimal/maximal values are displayed. The notches represent a robust estimate of the uncertainty on the median.

will be investigated here in order to propose a mechanism for positive asymmetric signals, reformulating the work of Spach and Kootsey²³⁴ in terms of asymmetry.

11.3.1 Collision in a One-dimensional Fiber

The simplest case of collision arises in a one-dimensional fiber. In this configuration (a fiber with a length of 2 cm, a resistivity of 200 Ω cm and a spatial discretization of 100 μ m), both extremities were stimulated at the same time and two wavefronts were initiated in opposite directions which collide and annihilate in the middle of the fiber. A high density array of unipolar electrodes (128 electrodes with 0.1 mm inter-electrode distance, located 0.5, 1 or 2 mm from the fiber) recorded the extracellular electrical activity close to the collision site.

Fig. 11.14 presents the resulting waveform asymmetry as a function of the position with respect to the collision site with some examples of signals. In a region of approximate size 4 mm around the collision point, significantly increased asymmetries up to 0.8 were observed. The waveform amplitude, however, was only slightly reduced. The size of this

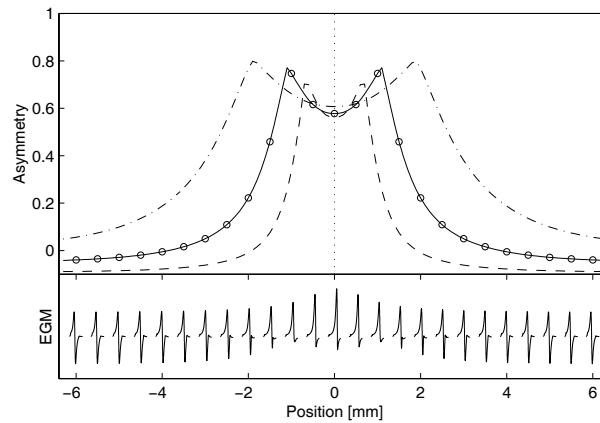


Figure 11.14 — Waveform asymmetry during a wavefront collision in a unidimensional fiber. Asymmetry is plotted as a function of the position on the fiber (the zero is the collision site) for an array of unipolar electrodes located 1 mm (solid curve), 0.5 mm (dashed curve) and 2 mm (dash-dotted curve) from the fiber. Examples of electrograms (EGM) are shown below their corresponding asymmetry value denoted by a circle on the graph.

region increased when the electrodes were moved away from the fiber (see Fig. 11.14) because of the wider averaging effect. Actually, close to the collision (<1 mm), the peak sodium current was reduced and the maximal membrane potential slope was increased, resulting in a positive asymmetry.²³⁴ Further from the collision, the phenomena were dominated by the interaction of the signals generated by each wavefront (see next subsection). Changing the tissue resistivity did not modify much the asymmetry, although signal amplitude was different.

11.3.2 Collision with a Boundary

By symmetry, the membrane potential shows identical changes in shape when the action potential approaches a wavefront collision or a boundary (sealed end of the fiber).²³⁴ In the same simulated fiber as in the previous subsection, electrograms were computed near its end, assuming no-flux boundary conditions (in the intracellular medium).

Fig. 11.15 displays waveform asymmetry as a function of the position with respect to the boundary. Like near a collision and for the same reason, positive asymmetric waveforms were observed close to the end of the fiber, in agreement with Spach and Kootsey.²³⁴ Moreover, beyond the end of the fiber, signals with a quickly decreasing waveform amplitude and an approximately constant positive asymmetry were observed. A careful analysis of the signals shows that the extracellular signals of Fig. 11.14 ($\phi_{0,\text{collision}}$) can be reconstructed from those of Fig. 11.15 ($\phi_{0,\text{boundary}}$) using the symmetry of the wavefront evolution

$$\phi_{0,\text{collision}}(x, t) = \phi_{0,\text{boundary}}(x, t) + \phi_{0,\text{boundary}}(-x, t) . \quad (11.11)$$

The spatial extent of the zone of positive asymmetry near a collision site is therefore related to the decrease in amplitude of the signals measured beyond the end of the fiber.

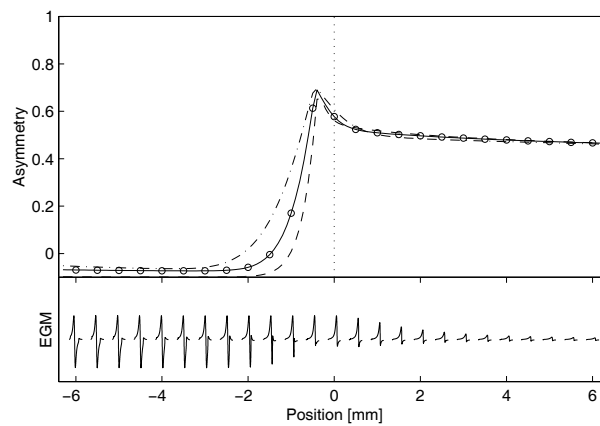


Figure 11.15 — Waveform asymmetry near the end of a unidimensional fiber. Asymmetry is plotted as a function of the position on the fiber (positions < 0 belongs to the fiber, and positions > 0 are outside the tissue, in the surrounding bath) for an array of unipolar electrodes located 1 mm (solid curve), 0.5 mm (dashed curve) and 2 mm (dash-dotted curve) from the fiber. Examples of electrograms (EGM) are shown below their corresponding asymmetry value denoted by a circle on the graph.

11.3.3 Colliding Wavefronts in the Atrial Model

In order to study how the results obtained in a unidimensional fiber generalize in higher dimensions, a wavefront collision was initiated in the atrial model by stimulating two distant sites at the same time. Fig. 11.16 shows activation maps and waveform asymmetry maps for two examples of wavefront collisions occurring in the right atrium free wall. Around the collision line, represented as a dashed line in the activation map, a band of positive asymmetry was observed. The width of this region, approximately 4 mm, was consistent

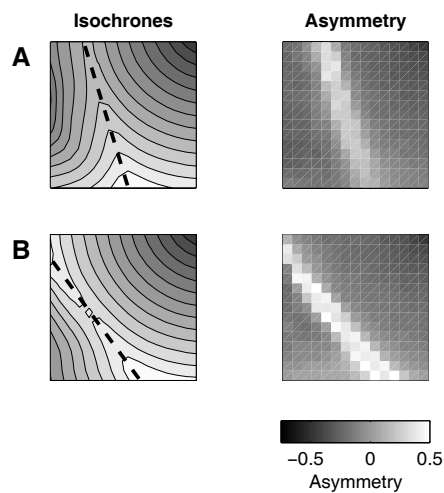


Figure 11.16 — Effect of wavefront collision on waveform asymmetry in the atrial model. Two distant sites are stimulated at the same time: near the anatomical location of the Bachmann's bundle and near the tricuspid valve (A), and in the region of the sino-atrial node and near the tricuspid valve (B). First column: Activation map. The collision line is displayed as a dashed line. Second column: Corresponding waveform asymmetry. The region mapped has a diameter of 3 cm, the inter-electrode distance is 2 mm, and the distance from electrode-to-tissue is 1 mm.

with the 1D results. Notice that the asymmetry was more pronounced for a frontal collision (Fig. 11.16B) than for a collision with an angle, resembling wavefront merging (Fig. 11.16A, especially at the bottom of the activation map), in agreement with the concepts underlying the curvature hypothesis.

11.4 Refractoriness and Front-Tail Interactions

Up to now, wavefront propagation was considered only in a fully recovered tissue. This section will show how the dynamics of AF, especially refractoriness and restitution, affect electrogram morphology. A better understanding of the amplitude-versus-asymmetry diagrams during AF will follow.

11.4.1 Waveform Amplitude and Peak Sodium Current

Even in a tissue with uniform conduction and membrane properties, a dispersion of waveform amplitude is observed during SAF (see Fig. 11.5). Simulation studies have actually demonstrated that wavefront curvature and collision impact the availability of sodium current and, as a result, impact the amplitude of the electrograms.^{234,361} Moreover, because of the front-tail interactions occurring during AF, the wavefronts have to propagate in a partially recovered tissue characterized by a slower conduction velocity and a reduced peak sodium current. The relation between waveform amplitude and peak sodium current was therefore investigated.

During SAF, 256 electrograms were recorded in the right atrium free wall and the sodium membrane current I_{Na} was measured in the “cell” right below each electrode. The peak sodium current, defined as the maximum of the absolute value of I_{Na} (in pA/pF) during an upstroke, was extracted and plotted in Fig. 11.17 as a function of the corresponding waveform amplitude, normalized with respect to the amplitude of a waveform recorded during sinus rhythm. Fig. 11.17 shows that, in a tissue with uniform properties, variations in waveform amplitude are correlated with the peak sodium current.

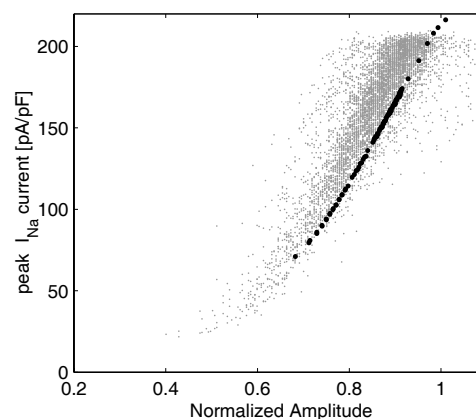


Figure 11.17 — Relation between the peak sodium current and (normalized) waveform amplitude during SAF (gray cloud of points) and during a S_1 - S_2 protocol in a unidimensional fiber (thick black dots).

In addition, to better understand the effect of front-tail interactions, several S_1 - S_2 pro-

protocols were simulated on a unidimensional fiber (2 cm long) with the same conduction properties as the atrial model. Both stimuli were applied at an extremity of the fiber so that the diastolic interval ranged from 0 to 500 ms, and 10 unipolar electrograms were recorded along the fiber. The peak sodium current is also displayed on Fig. 11.17 as a function of the waveform amplitude. In order to make possible the comparison between the fiber and the atrial model, the waveform amplitudes were normalized with respect of the amplitude of the waveform generated by the S_1 impulse propagation. The resulting curve follows the set of points measured during SAF. Notably, in both models, low amplitude signals are associated with short diastolic intervals.

Thus, in a homogeneous isotropic tissue, the effect of refractoriness due to front-tail interactions accounts for most of the variations in waveform amplitude.

11.4.2 Conduction Blocks and Long Double Potentials

Morphology of unipolar and bipolar electrograms in presence of conduction blocks has been extensively studied in the context of atrial flutter catheter ablation^{346,362–364} and lead to criteria for the detection of conduction blocks.^{343,344} In these studies, functional conduction blocks were associated with positive asymmetric waveforms (R patterns) and with the presence of double potentials. Other studies on human atrial fibrillation,^{13,181} on human ventricular tachycardia³⁶⁵ and on a rabbit model of ventricular fibrillation³⁴⁵ confirmed these findings.

Similar results were obtained during SAF. Fig. 11.18 presents an example of activation map during a functional conduction block (here, the activation pattern looks like a U-turn), with electrograms measured at eight selected locations. Along the line of block, long-double potentials were observed (e.g. electrograms 1–4 of Fig. 11.18). At a distance of more than 6 mm from the conduction block, however, no double potential was found (e.g. electrograms 6–8). In addition, positive asymmetric signals (R and Rs patterns) were frequent close to the line of block (e.g. electrogram 1–2, first peak of electrogram 4, second peak of electrogram 5). Note that the amplitude of electrograms 1–2 was significantly smaller than for electrograms

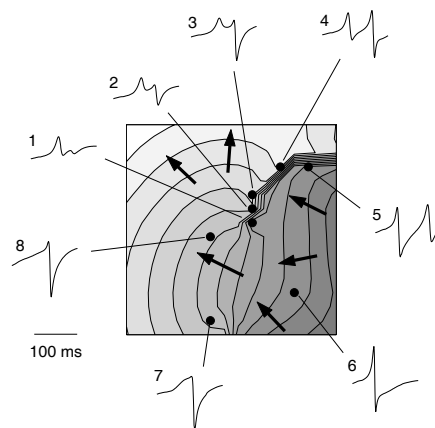


Figure 11.18 — Activation map of a functional conduction block occurring during SAF. The thick black line represents a line of block. Arrows illustrate wavefront propagation from dark gray to white. Eight selected electrograms, measured at locations displayed as black dots, are plotted around the figure.

7–8 representing a broad wavefront propagation.

In a uniform and isotropic tissue, the set of waveforms with small amplitude and positive asymmetry (see Fig.11.5B) can be consistently associated with the presence of conduction blocks or functional wavebreaks, as confirmed numerically by a direct glance at the activation maps corresponding to these waveforms, and as experimentally verified by Chorro *et al.*³⁴⁵

11.4.3 Comparison of Different Simulated AF Dynamics

We will now consider amplitude-versus-asymmetry diagrams constructed from SAF signals recorded in a uniform isotropic tissue. Four different simulated dynamics of AF were analyzed and compared in terms of waveform morphology:

- (A) SAF using the modified Luo–Rudy model ($G_{si} = 0.07 \text{ mS/cm}^2$) and a conduction velocity (CV) of 70 cm/s,
- (B) SAF using the modified Luo–Rudy model ($G_{si} = 0.05 \text{ mS/cm}^2$) and a CV of 70 cm/s,
- (C) SAF using the Courtemanche model and a CV of 40 cm/s,
- (D) SAF using a Courtemanche model incorporating inhomogeneous vagal stimulation and a CV of 90 cm/s. The *conduction properties*, however, remained uniform.

In all the cases, the tissue conductivities were uniform and isotropic in order to avoid the possible influence of fiber structure and heterogeneity. Fig. 11.19 displays amplitude-versus-asymmetry diagrams constructed from approximately 6000 waveforms (for each case) measured in the right atrium free wall. In order to facilitate further discussion, 3 qualitative regions are highlighted in each scatter plot: region 1 corresponds to QS and rS patterns, region 2 to Rs and R patterns with large amplitude (around $A = 0.5$ here), and region 3 to Rs and R patterns with small amplitude. To assist the comparison, Table 11.1 gives the fraction of QS, rS, Rs and R patterns, the average waveform asymmetry, and the standard deviation of waveform amplitude, and recalls the average number of wavelets and a measure of organization (correlation length, see subsection 10.2.2) of the corresponding dynamics. The observation of Fig. 11.19 and Table 11.1 suggests the following remarks:

	A	B	C	D
QS	1.6 %	4 %	0.5 %	1.2 %
rS	81 %	87.5 %	69.5 %	94.7 %
Rs	15.4 %	8 %	28 %	4 %
R	2 %	0.5 %	2 %	0.1 %
Mean asymmetry	-0.21	-0.26	-0.09	-0.23
Amplitude SD	0.16	0.13	0.14	0.11
# Wavelets	3.2 ± 1.6	4.0 ± 1.8	1.5 ± 0.5	4.6 ± 1.7
Correlation length	1.51 cm	1.34 cm	2.02 cm	4.22 cm

Table 11.1 — Characteristics of waveform morphology (percentage of QS, rS, Rs and R patterns, mean asymmetry and standard deviation of amplitude, following the definitions of subsection 11.1.3) and wavelet dynamics (number of wavelets and correlation length) for four different SAF. The column labels A to D correspond to the cases enumerated at the beginning of the subsection.

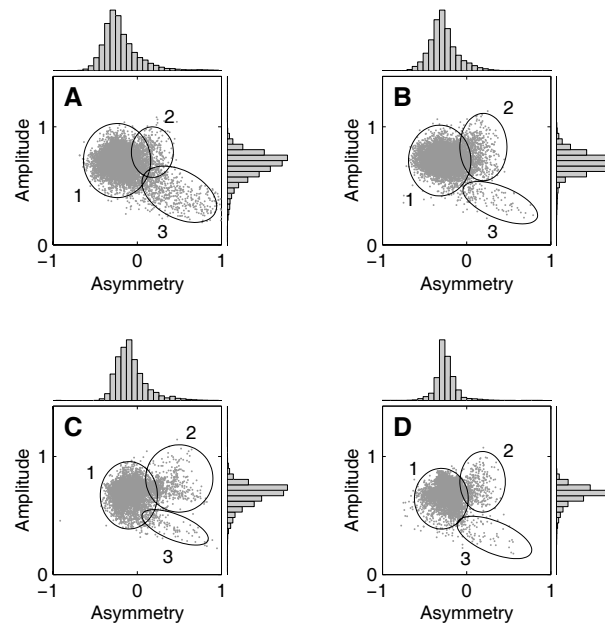


Figure 11.19 — Amplitude-versus-asymmetry diagrams combined with amplitude and asymmetry histograms for the four different SAF dynamics. Each scatter plot is divided into 3 qualitative regions: region 1 corresponds to QS and rS patterns, region 2 to Rs and R patterns with large amplitude (around $A = 0.5$ here), and region 3 to Rs and R patterns with small amplitude. The labels A to D correspond to the cases enumerated at the beginning of the subsection.

- Region 1 of Figs. 11.19A–D corresponds to curved or near-planar wavefronts and contains the majority of the signals. The average asymmetry is more negative in presence of multiple spirals (case A and B, which could be considered as AF type III) than for a more organized SAF like case C (AF type II). Although case D is statistically organized (a clear dominant frequency is observed in the signals), its dynamics consists of more than 4 wavelets with short wavelength and thus with high curvature and a larger negative asymmetry. Waveform asymmetry in region 1 is therefore more sensitive to wavelength than to spatial organization. Notice that, in case D, the asymmetry distribution is more concentrated around its mean value because most spirals have a very similar shape and curvature (the action potential duration is almost rate-independent). Moreover, when large beat-to-beat variations in action potential duration (and excitable gap) is possible, the spread of amplitude distribution is also wider (case A as compared to case D).
- According to section 11.3, large amplitude waveforms with a Rs or R pattern (region 2) can be attributed to wavefront collision. This region is less marked and less positively asymmetric in case A. Actually, when the action potential duration (APD) restitution slope is smaller (like cases B, C and D with respect to case A), spontaneous wavebreaks are less frequent and thus long lines of wavefront collision become more likely. For instance, the dynamics of case C is characterized by long lines of collision in the right atrium free wall, as confirmed by its wide and clearly positive asymmetric region 2. The large proportion of Rs (or RS) patterns in case C, however, is mainly due to near-planar wavefronts.

- Region 3 corresponds to conduction blocks and wavebreaks (see subsection 11.4.2). In these simulations, functional conduction blocks and wavebreaks mostly arose as a consequence of an unstable APD alternans. This mechanism, described by Fox *et al.*,^{267,268} requires a steep (dynamic) APD restitution (slope ≥ 1) and is illustrated by the larger size and density of region 3 in case A (steep APD restitution) as compared to case C and D (slope of *dynamic* APD restitution only slightly > 1). In contrast, conduction blocks in case D are essentially structural, due to APD heterogeneities.

Since wavelength seems to play an important role to determine wavefront curvature and waveform asymmetry, the average asymmetry was computed for a large set of simulations of SAF in a uniform tissue using the modified Luo–Rudy model with effective refractory period (ERP) ranging from 180 to 275 ms (obtained by altering the parameter G_{si}) and a CV of 70 cm/s, and using the same membrane model as case A but with a CV ranging from 50 to 100 cm/s. Fig. 11.20 shows the average asymmetry as a function of ERP (left panel) and as a function of the CV (right panel). For each set of parameters, 8 to 16 episodes of SAF were considered and statistical data were displayed. The results confirm that when the wavelength is shorter (due to a decrease in either CV or ERP), the possibly larger curvature of wavefronts (especially spirals) leads to more negative asymmetry.

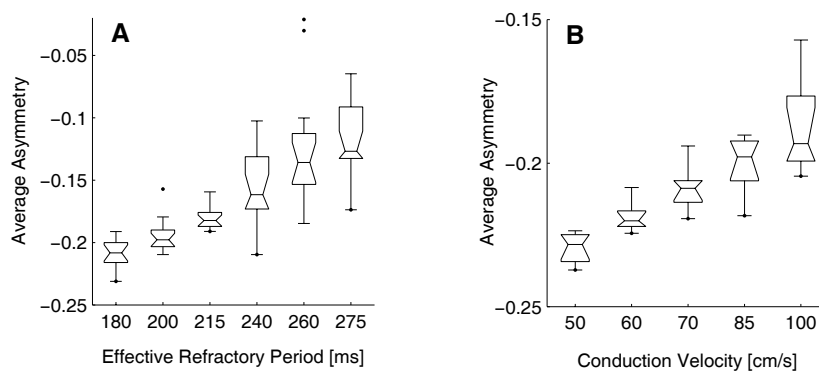


Figure 11.20 — Effect of wavelength on average waveform asymmetry in a uniform tissue. (A) Average asymmetry as a function of effective refractory period. (B) Average asymmetry as a function of conduction velocity. Waveform asymmetry is averaged over all the 256 electrograms in a time interval ranging from 2 (non-sustained SAF) to 20 s (sustained SAF). Statistics are computed over a set of 16 SAF episodes (panel A) and 8 SAF episodes (panel B). Medians, quartiles and range are displayed. Outliers are indicated by a dot. The notches represent a robust estimate of the uncertainty on the median.

Therefore, waveform morphology gives some insight into wavelet dynamics (wavelength, restitution curve, collision, wavebreaks). The comparison was made possible by the fact that the substrate was in all cases uniform. Since the substrate properties are unfortunately difficult to control in clinical or experimental studies, *variations* in electrogram morphology should be considered instead.

11.5 Baseline Modulation

All the factors discussed above concern only the details of depolarization. But the repolarization process also generates current. As a result, there is a significant baseline modulation

in single site electrograms, as shown by observing for instance the electrogram of Fig. 11.21. Some remarks about this question are mentioned in this section for completeness.

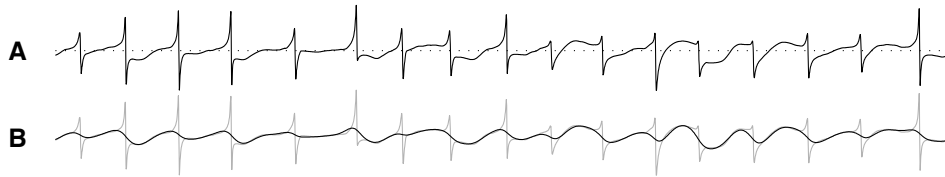


Figure 11.21 — Example of baseline modulation in a signal measured during SAF: (A) electrogram with the zero potential line (dotted line), (B) baseline extracted with the help of a low-pass filter.

These baseline modulations are associated with the propagation of the repolarization wave (waveback). Mechanisms similar to the effect of wavefront shape could be proposed for waveback (with inverse sign, because the current sources are reversed). Convex waveback (resp. concave waveback) would be expected to lead to an essentially positive (resp. negative) deflection. Unfortunately, the following factors make the situation much more complex:

- The current sources due to the repolarization process are not spatially concentrated around the waveback. They may even spread over a region several-centimeter wide. Therefore, talking about the effect of waveback shape does not really make sense.
- Unipolar electrograms can be affected by distant events.^{366,367} This is particularly the case for baseline variations.
- Repolarization wave propagation is sensitive to APD gradients established during SAF. Fig. 11.22 shows changes in the baseline for successive beats during which the activation patterns are similar but the recovery patterns are different due the presence of APD gradients. While it is difficult to account for all aspects of the variations,

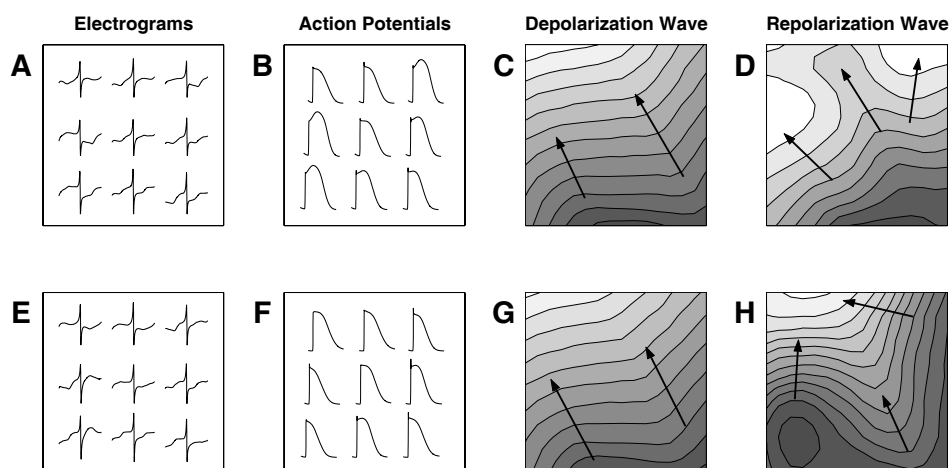


Figure 11.22 — Illustration of baseline variations in presence of APD gradients. For two consecutive beats during pacing in the pulmonary veins (initiation protocol for SAF), electrogram waveforms (A,E), corresponding action potentials (B,F), depolarization wave isochrones (C,G) and repolarization wave isochrones (E,H), measure in the right atrium free wall, are shown.

a general trend is that when long-to-short APDs are measured along propagation (Figs. 11.22A–D, on the left region of each panel), negative deflections are observed. On the other hand, in case of short-to-long APD gradient (Figs. 11.22E–H, on the left region of each panel), positive deflection are observed.

- Baseline modulation depend on the details of all ionic currents participating to or delaying the repolarization. In the case on ventricular cells, Gima and Rudy²³⁵ investigated the ionic basis of T-wave resulting from long QT syndrome, Brugada syndrome and acute ischemia, precisely by analyzing these “baseline variations”. When studying the depolarization phase only, this model-dependence was very limited since most of the cardiac cell models (both ventricular and atrial cell models) are using almost exactly the same kinetics for the fast inward sodium current which is by far the main contribution during depolarization.
- In experimental signals, some variations of the baseline are artifacts caused by the motion of the wall or by the difficulty to define the zero potential.³⁶⁸ Acquisition systems often try to smooth out these artifacts by filtering. True electrophysiological baseline variations may be affected in the same way. In summary, the validity of a direct comparison of baseline variations with experimental signals may be questionable.

Baseline modulations are caused by the repolarization current sources and are affected by APD gradients, possibly also by distant events. More information than only activation and recovery patterns would be needed to completely explain these variations.

11.6 Conclusion

This chapter addressed the question of unipolar electrogram morphology during SAF. Electrogram waveforms were characterized by their amplitude and asymmetry. In order to separate the effects of the wavefront dynamics from those of the substrate, SAF was first initiated on a uniform and isotropic model of the atria.

In this model, the vast majority of the waveforms were single potentials. In addition, results showed how amplitude-versus-asymmetry diagrams representing electrogram morphology during SAF can be segmented into four qualitative regions (see Fig. 11.23): (1) a region with negative asymmetry, (2) a region of approximately symmetric signals, (3) a region

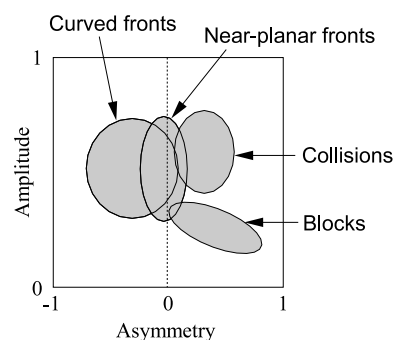


Figure 11.23 — Schematic representation of the different regions in an amplitude-versus-asymmetry diagram that can be associated with a class of activation patterns.

of positive-asymmetric large-amplitude waveforms, and (4) a region of positive-asymmetric small-amplitude waveforms. Each of these regions was associated with a class of activation patterns: region 1 corresponds to curved wavefronts, region 2 to near-planar wavefronts, region 3 to wavefront collisions or merging, and region 4 to conduction blocks and wavebreaks.

These conclusions, however, are limited to uniform isotropic tissues. The impact of substrate properties (heterogeneity, fiber structure) and mechanisms for electrogram fractionation will be investigated in the next chapter.

Electrogram Morphology: Effect of the Substrate

As compared to experimental data,^{13, 181, 345, 346} electrograms measured in a uniform isotropic model of cardiac tissue tend to be less asymmetric and less fractionated (see previous chapter). We hypothesized that the extreme simplicity of the substrate, *i.e.* of the tissue structure, in the computer model was one of the reasons for these differences.

An advantage of the use of computer models to study electrogram morphology is their ability to reliably control the substrate properties. While the previous chapter concentrated on the effect of wavefront dynamics, this one will consider the changes in waveform morphology arising when the substrate is altered. Distribution of waveform morphology during paced beats and during simulated AF (SAF) will be analyzed in anisotropic and heterogeneous tissue. Finally, the limitations of monolayer tissue models for understanding electrograms will be discussed by simulating 3D models including transmural heterogeneity.

12.1 Effect of Tissue Properties

Heterogeneities can be introduced as spatial variations in membrane or conduction properties. This section summarizes the effect of *uniform* changes of these tissue properties in a simple unidimensional model of cardiac fiber.

12.1.1 Membrane Model

The membrane model determines the current sources which generate the electrogram signals. Modification of the cell model (*e.g.* due to remodeling) may result in biased waveform morphology.²³⁵ Here, it is shown that the impact on waveform amplitude and asymmetry is small, provided that conduction properties remain unchanged. Alteration of the sodium channels will be treated in the next subsection.

The shape of electrogram waveforms computed using different membrane models were compared in a unidimensional fiber with a length of 3 cm and a resistivity of 200 Ω cm during simple propagation initiated at an extremity of the fiber. Unipolar electrograms were recorded 1 mm (in the radial direction) from the middle of the fiber with a sampling frequency of 5 kHz. The modified Luo–Rudy model, the original Courtemanche *et al.* model, the Courtemanche *et al.* model modified for simulation of AF, the Courtemanche *et al.* model

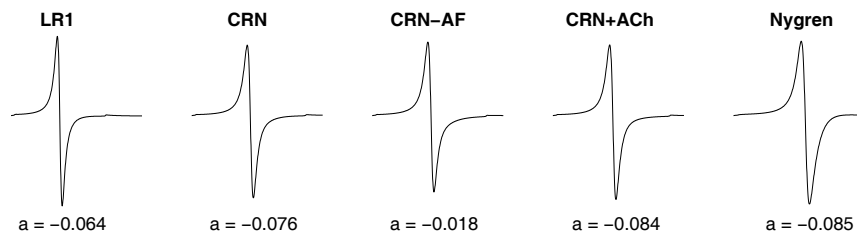


Figure 12.1 — Electrogram waveforms computed on a unidimensional fiber using different membrane models: the modified Luo–Rudy model (LR1), the original Courtemanche *et al.* model (CRN), the Courtemanche *et al.* model modified for simulation of AF (CRN–AF), the Courtemanche *et al.* model including vagal stimulation (CRN+ACh), and the Nygren *et al.* model (Nygren). Waveform asymmetry is displayed just below each electrogram.

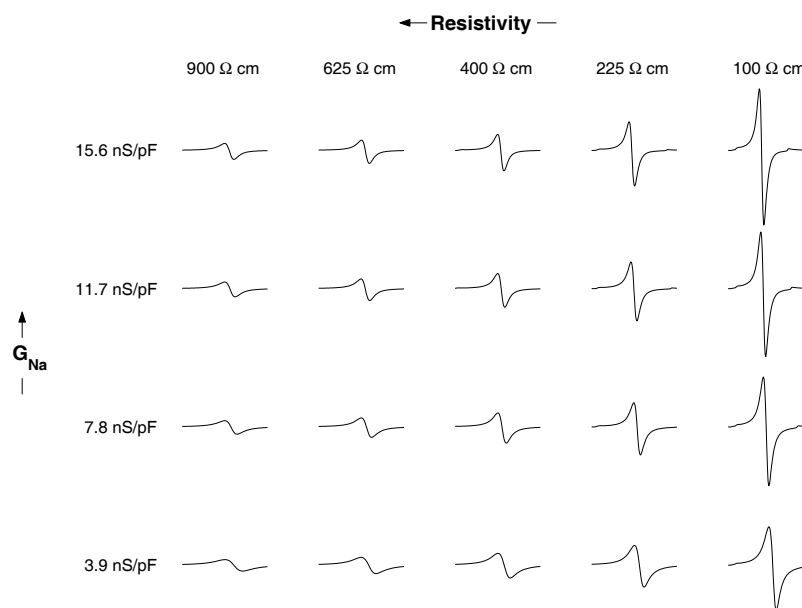


Figure 12.2 — Electrogram waveforms for different set of parameters affecting conduction velocity (in a unidimensional fiber using the Courtemanche model). The sodium channel conductance G_{Na} ranges from 3.9 to 15.6 nS/pF (the standard value in the Courtemanche model is 7.8 nS/pF), and the tissue resistivity from 100 to 900 Ω cm.

including vagal stimulation, and the Nygren *et al.* model were successively considered. The resulting waveforms, shown on Fig. 12.1, are very similar to each other because all of these models include almost the same sodium kinetics. Small negative asymmetry is systematically observed due to the asymmetric rising phase of the underlying action potential.

Thus, waveform morphology is robust with respect to changes in membrane model or ionic channel properties (sodium channels excepted). Moreover, baseline morphology is characterized by a small negative asymmetry.

12.1.2 Conduction Properties

Since electrograms mainly reflect the depolarization process, the parameters affecting wavefront propagation are expected to have an important impact on electrogram morphology.

This subsection reports the effect of sodium channel conductance and tissue resistivity.

In the same unidimensional fiber model as the previous subsection, a simple propagation was initiated using a Courtemanche membrane kinetics. The conduction velocity was modified by altering sodium channel conductance G_{Na} (between a decrease of 50% and an increase of 100%) and by setting the tissue resistivity to a value in the range 100–900 Ω cm. Fig. 12.2 displays the resulting electrogram waveforms and demonstrates that waveform amplitude increases when the sodium channel conductance increases or when the tissue resistivity is reduced. The asymmetry, however, remain unchanged.

Therefore, the faster the conduction velocity, the larger the waveform amplitude, whatever the means used to increase the conduction velocity sodium: channel conductance, cell-to-cell coupling or dynamic reduction of conduction velocity due to refractoriness (see subsection 11.4.1).

12.2 Effect of Anisotropy

Anisotropy has been shown to impact both the asymmetry and the amplitude of electrograms for paced beats.^{333,334} In order to help quantify the effect of anisotropy on waveform asymmetry, electrogram morphology was studied in an anisotropic two-dimensional sheet of tissue, and in the atrial model during sinus rhythm and SAF. In each case, the anisotropy ratio (see subsection 4.2.2) was as used a control parameter ranging from 1:1 (isotropic tissue) to 9:1. This range corresponds to physiological values.^{146,148}

12.2.1 Working Hypothesis

The theory of oblique double layer gives a theoretical framework for the description of the effect of anisotropy on electrogram morphology (see subsection 11.2.2). In this subsection, a working hypothesis is derived from this approach.

According to Eq. (11.3), the electrogram is written as a superposition of dipolar fields³¹ with the density of dipolar moment $\boldsymbol{\mu}$ equal to

$$\boldsymbol{\mu} = \boldsymbol{\sigma}_i \cdot \mathbf{n} = \sigma_{i,t} \mathbf{n} + (\sigma_{i,l} - \sigma_{i,t})(\mathbf{a}^\top \mathbf{n}) \mathbf{a} \quad (12.1)$$

and distributed along the wavefront (\mathbf{a} is the fiber orientation unit vector, $\sigma_{i,l}$ the longitudinal conductivity and $\sigma_{i,t}$ the transverse conductivity). The second equality comes from the decomposition (4.19) and shows that the dipolar moment has a component normal to the wavefront and a component along the fiber, which is nonzero only in presence of anisotropy. The factor $\mathbf{a}^\top \mathbf{n}$ is equal to the cosine of the angle between the fiber orientation and the direction of propagation.

The distribution of dipolar moments along convex and concave wavefronts is illustrated in Fig. 12.3. In the isotropic case, the dipoles are normal to the wavefront (Figs. 12.3A and D). When the tissue conduction properties are anisotropic, the dipoles tend to align along the fibers (Figs. 12.3B, C, E and F). As a results, during propagation along a fiber, the effects of wavefront curvature are partly compensated so that the difference between convex and concave wavefronts is smaller than in an isotropic tissue (Figs. 12.3B and E). In contrast, the effects of wavefront curvature are amplified during propagation across a fiber (Fig. 12.3C and F). Since the R wave (resp. S wave) is associated with the density of positive current source \oplus (resp. negative current source \ominus), we hypothesized that:

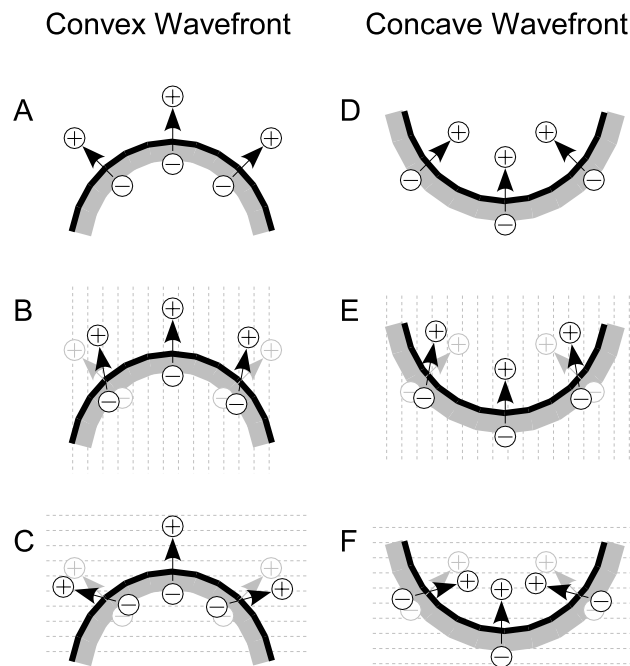


Figure 12.3 — Distribution of dipolar moments on convex (A–C) and concave (D–F) wavefronts on a plane tissue. The black half-circles are wavefronts and the gray regions indicate the zones of activated tissue. The dipoles are displayed as an arrow joining a negative (\ominus) and a positive (\oplus) current source. The substrate is isotropic in (A) and (D), and anisotropic in the other subfigures. The wavefront propagates along the fiber in (B) and (E), and across the fiber in (C) and (F), as shown by the dotted lines representing the fibers. The dipoles of (A) and (D) are superimposed in light gray for comparison.

Effect of anisotropy: When a wavefront propagates *along a fiber*, the asymmetry of the resulting waveform is reduced as compared to the isotropic case. On the other hand, when a wavefront propagates *across a fiber*, the effect of curvature on asymmetry is *amplified*.

This statement will be evaluated in two-dimensional plane sheet of tissue and in an atrial model during pacing and during SAF.

12.2.2 Anisotropy in a Two-Dimensional Tissue

A center-paced beat was simulated in a 6×6 cm, two-dimensional sheet of anisotropic tissue with a longitudinal resistivity of $150 \Omega \text{ cm}$. Anisotropy ratios of 1:1, 1.5:1, 2.25:1, 3:1, 4:1 and 5:1 were successively considered. Unipolar electrograms were recorded in a grid of 64×64 electrodes. Asymmetry and amplitude were extracted from each signal.

Fig. 12.4 shows the isochrones and the lines of equal asymmetry on the tissue (fibers are oriented horizontally). In an isotropic tissue (Fig. 12.4A), the asymmetry decreases with the distance from the stimulus site. In presence of anisotropy, wavefronts propagating along a fiber are associated with symmetric waveforms except very close to the stimulus site where the wavefront is initiated (Fig. 12.4B–F). The asymmetry becomes very sensitive to direction and curvature for propagation across fibers. Notice that, in the 64×64 electrode array, the percentage of rS patterns (waveform asymmetry $< -1/2$) globally increases with the anisotropy ratio, as shown in Table 12.1.

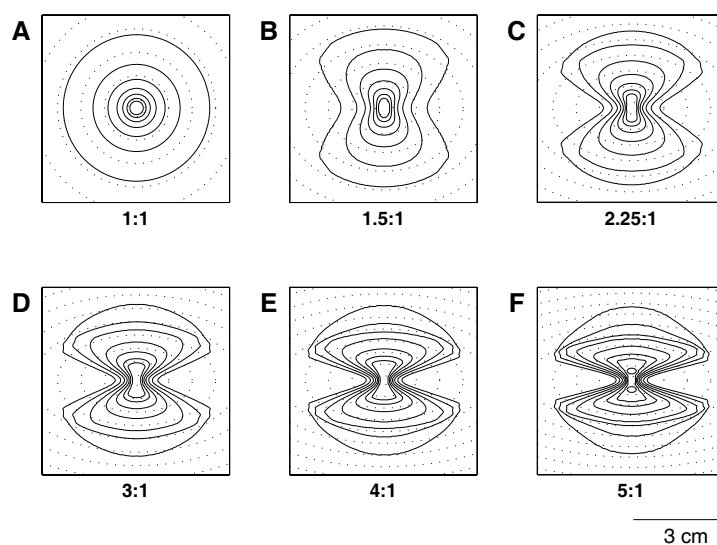


Figure 12.4 — Lines of equal waveform asymmetry in a center-paced beat initiated in a 2D sheet of tissue (6×6 cm) with an anisotropy ratio of (A) 1:1, (B) 1.5:1, (C) 2.25:1, (D) 3:1, (E) 4:1 and (F) 5:1. Contours correspond to an asymmetry of -0.7, -0.6, -0.5, -0.4, -0.3 and -0.25, from the center to the border respectively. Dotted lines are isochrones.

aniso. ratio	rS [%]
1:1	4.4
1.5:1	5.4
2.25:1	8.2
3:1	12.0
4:1	15.8
5:1	17.7

Table 12.1 — Percentage of rS patterns (waveform asymmetry $< -1/2$) in a center-paced two-dimensional model for different anisotropy ratios. This percentage is computed over the 64×64 grid of electrode equally spaced over the tissues of Fig. 12.4.

In order to better understand the transition from an isotropic to a strongly anisotropic tissue and its link with the effect of curvature, the electrograms were decomposed into an axial and a conormal component, following Colli-Franzone *et al.*^{335,352} In a tissue with fiber orientation vector \mathbf{a} and longitudinal (resp. transverse) conductivity σ_l (resp. σ_t), the current source $I_m = S_v^{-1} \nabla \cdot \boldsymbol{\sigma} \nabla V_m$ was written as the sum of an axial component $I_{m,ax}$ and a conormal component $I_{m,co}$ defined as

$$I_{m,ax} = S_v^{-1} (\sigma_l - \sigma_t) \nabla_{\mathbf{a}}^2 V_m \quad \text{and} \quad I_{m,co} = S_v^{-1} \sigma_t \nabla^2 V_m \quad (12.2)$$

where $\nabla_{\mathbf{a}} = \mathbf{a}^T \nabla$ is the directional derivative and the conductivity tensor, supposed to be constant, is given by $\boldsymbol{\sigma} = \sigma_t \mathbb{I} + (\sigma_l - \sigma_t) \mathbf{a} \mathbf{a}^T$ according to Eq. (4.19). Axial and conormal components of an electrogram were computed from the corresponding current sources $I_{m,ax}$ and $I_{m,co}$. In an isotropic tissue, the axial component vanishes ($\sigma_t = \sigma_l$). On the other hand, with increasing anisotropy ratio, the axial component begins to have an important impact.

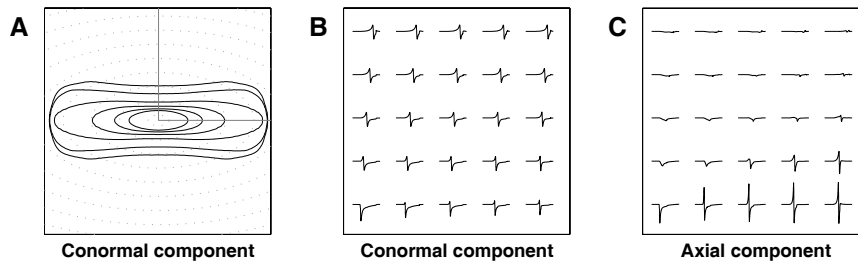


Figure 12.5 — Illustration of the decomposition of electrograms into an axial and a conormal component in a center-paced two-dimensional tissue with an anisotropy ratio of 4:1. (A) Lines of equal waveform asymmetry for the conormal component. Contours correspond to an asymmetry of -0.7 , -0.6 , -0.5 , -0.4 , -0.3 and -0.25 , from the center to the border respectively. Dotted lines are isochrones. (B–C) Conormal and axial component of the electrograms in the upper-right square drawn on panel A.

Fig. 12.5 presents such a decomposition in the tissue with an anisotropy ratio of 4:1. The conormal component behaves like in an isotropic tissue (Fig. 12.5A–B): in the axial direction (*i.e.*, in the horizontal direction from the bottom left corner toward the right), the curvature is high and the waveforms are strongly negative asymmetric, while in the transverse direction (*i.e.*, in the vertical direction from the bottom left corner toward the top), the small curvature leads to relatively symmetric signals, except close to the stimulation site. In contrast, the axial component (Fig. 12.5C) is symmetric in the axial direction, and, in the transverse direction, consists of a negative deflection. When the anisotropy ratio increases, the contribution of the axial component becomes dominant in the axial direction leading to symmetric waveforms. In the transverse direction, however, the signals tend to be more negative asymmetric, in agreement with Table 12.1.

These results are consistent with our working hypothesis based on the prediction of the oblique dipole layer theory (see subsection 11.2.3), that is, in this two-dimensional model, curvature effects are reduced in the axial direction and reinforced in the transverse direction.

12.2.3 Fiber Orientation in the Atrial Model

After having isolated the impact of anisotropy on waveform morphology in a 2D model, this effect was further investigated in an atrial model including a simplified fiber structure, whose fiber orientation was presented in subsection 4.2.2.

Sinus rhythm and four different simulated dynamics of AF in an anisotropic tissue were analyzed and compared in terms of waveform morphology for anisotropy ratios of 1:1, 2.25:1, 4:1, 6.25:1 and 9:1 :

- (A) Sinus rhythm using the Courtemanche model and a longitudinal to transverse conduction velocity (CV) ratio of 40:40, 50:33, 60:30, 67:27 and 75:25 cm/s,
- (B) SAF using the Courtemanche model and the same CV ratios as (A),
- (C) SAF using a Courtemanche model incorporating inhomogeneous vagal stimulation and longitudinal to transverse CV ratios of 90:90, 90:60, 90:45, 90:36 and 90:30 cm/s,
- (D) SAF using the modified Luo–Rudy model ($\overline{G}_{si} = 0.07$ mS/cm²) and longitudinal to transverse CV ratios of 120:120, 120:80, 120:60, 120:48 and 120:40 cm/s,

(E) SAF using the modified Luo–Rudy model ($\bar{G}_{si} = 0.055 \text{ mS/cm}^2$) and the same CV ratios as (D).

In all cases, the anisotropy ratio was constant over the whole tissue and no conduction heterogeneity was present. Unipolar electrograms were recorded at the 256 sites in the plaque region (right atrium free wall). Amplitude and asymmetry of about 8 000 waveforms (during SAF, only 256 during sinus rhythm) were extracted for analysis. Fig. 12.6 shows the variation of amplitude versus the asymmetry of the electrograms over the entire plaque for each dynamics (A) to (E) mentioned above, and for different anisotropy ratios. Observation

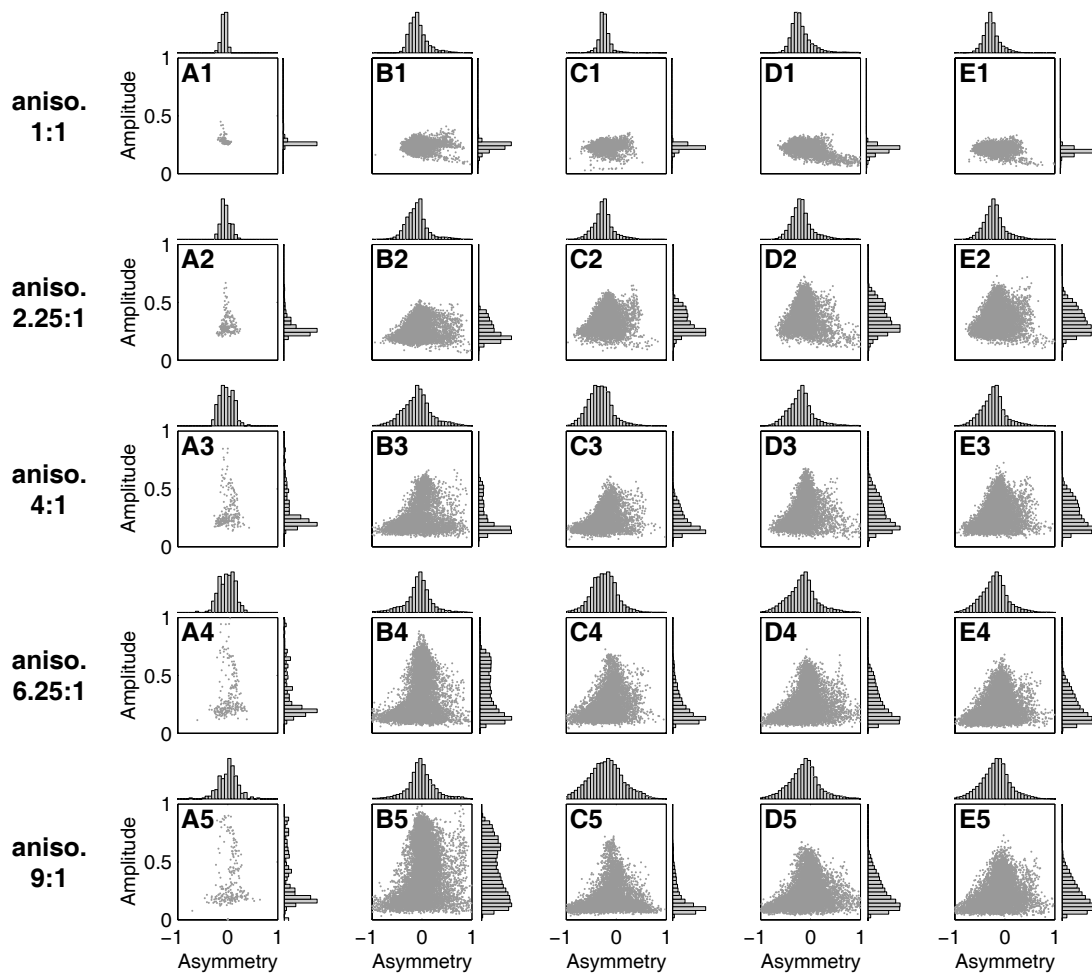


Figure 12.6 — Examples of amplitude-versus-asymmetry plots for sinus rhythm and four different dynamics of simulated AF, and for various anisotropy ratios. Rows 1 to 5 correspond to anisotropy ratios of 1:1, 2.25:1, 4:1, 6.25:1 and 9:1. Columns A to E correspond to the dynamics (A) to (E) described at the beginning of the subsection. All of those electrograms are recorded in the grid of electrodes located in the right atrium free wall.

of Fig. 12.6 suggests the following remarks:

- During sinus rhythm in the isotropic atria, the waveform morphology is similar over the whole atria (Fig. 12.6 A1) and is revealed as a tight cluster of points. Increasing the anisotropy ratio increases the spread of the waveform amplitudes (Fig. 12.6 A2–A5). Small amplitudes are generally associated with the component of propagation across

fibers while large amplitudes correspond to the component of propagation along fibers. The signals remain, however, quite symmetric during sinus rhythm with an increase in asymmetry for small amplitude electrograms associated with transverse conduction.

- During SAF in the isotropic atria (Fig. 12.6 B1–E1), a dispersion of waveform amplitude and asymmetry is observed due to wavefront curvature, collisions and wavelet dynamics (see previous chapter). Increasing the anisotropy ratio (Fig. 12.6, rows 2–5) acts to increase the variations in asymmetry and amplitude of the electrograms. Even with modest anisotropy there is a marked increase in the distribution of low amplitude signals with highly negative asymmetry. These low amplitude waveforms correspond to propagation across fibers. Large amplitude signals are associated with propagation along fibers and are rather symmetric, as suggested by the two-dimensional study of the previous subsection. Positive asymmetric waveforms are the result of wavefront collisions. Since wavefronts can collide in both the axial and the transverse direction, a larger range of amplitudes is observed for positive than for negative asymmetric signals.
- In general, the amplitude distributions are maximal at low amplitudes. The reason is that the shape of an expanding wavefront or a spiral in an anisotropic tissue is elongated in the direction of the fibers (elliptic isochrones), so that most of the wavefront length is actually propagating across fibers and contributes to the class of low amplitude signals. When the wavelength is long enough and the curvature is limited, the amplitude presents two local maxima, one for axial propagation and one for transverse propagation (Fig. 12.6 B4–B5).
- The phenomena described above do not depend on SAF dynamics and on the cell model, since the effect of anisotropy is qualitatively identical for all of the four cases of SAF presented (Fig. 12.6 columns B–E).

In order to quantify the presence of highly negative asymmetric waveforms in strongly anisotropic tissue, the fraction of rS waveforms was determined during SAF for each case and reported on Fig. 12.6. In isotropic tissue, rS patterns were quite rare (approximately 2%) despite the presence of highly curved fronts during SAF. Increasing the anisotropy ratio from 1:1 to 4:1, however, increased this fraction to nearly 12%. This fraction stayed relatively constant at 11–15% for anisotropy ratios up to 9:1. Fig. 12.6 shows that this behavior is very similar (both qualitatively and quantitatively) for the different dynamics simulated, except SAF case (B) characterized by a larger wavelength and thus less pronounced curvature.

The results suggest that an analysis of amplitude and asymmetry distributions of unipolar electrograms may be used to detect the onset of structural remodeling from isotropic to anisotropic or vice versa associated with chronic AF. Changes in electrogram morphology may reveal a dynamic change in the interaction or number of the wavefronts over time, or reveal stabilization due to some intervention.

12.3 Effect of Heterogeneity

Regardless of anisotropy, the vast majority of computed electrograms in the uniform atria were found to be single, biphasic signals. According to the classification scheme of Konings *et al.*,¹³ most of them (98%) were single potentials, between 1–2% of the signals were

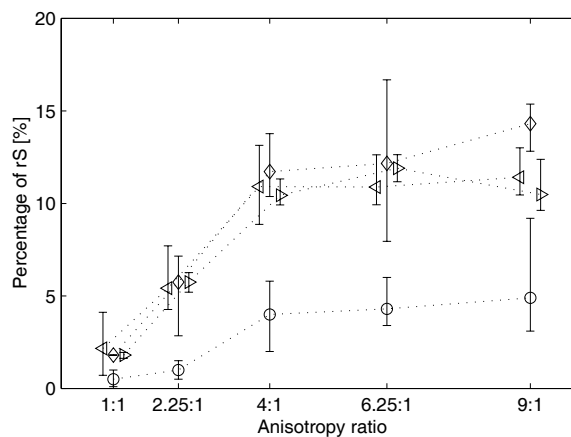


Figure 12.7 — Percentage of rS patterns during SAF with different anisotropy ratios. Circles represent SAF dynamics of case (B), diamonds case (C), right triangles case (D) and left triangles case (E). In each case, median, first and third quartile are computed from 8 different SAF episodes with exactly the same tissue properties.

doubles and only very rare examples of fragmented electrograms were found. Simulated double potentials were observed at the core of a spiral wave rotating around the measuring electrode, or close to lines of functional block (see subsection 11.4.2). Wavefront curvature and collisions alone therefore do not seem to be the basis for multiphasic signals often seen in AF.

In contrast, Konings *et al.*¹³ reported $77\pm 12\%$ of singles, $17\pm 7\%$ of short and long doubles, and $6\pm 4\%$ of fragmented potentials. These proportions depended on the type of AF, the percentage of long-doubles and fragmented potentials increasing with the complexity of AF. Comparison of simulated and experimental results suggests that other mechanisms not present in the model are necessary to account for the experimental proportion of double and fragmented potentials.

Previous experimental and simulation studies have suggested that the majority of fractionation arises from tissue heterogeneity or changes in material properties.^{138, 156, 369–374} This section investigates how a significant number of fractionated waveforms can be generated in presence of heterogeneities in tissue conductivity.

12.3.1 Discontinuity in Conductivity

To demonstrate how a change in material properties can affect the time course of the electrogram, a simulation was performed on a simplified model consisting of a one-dimensional cable (length 5 cm, space step $100\ \mu\text{m}$) with inhomogeneous resistivity.

Three cases were studied: an abrupt increase in conduction velocity (Fig. 12.8A) corresponding to a decrease in resistivity from 600 to $115\ \Omega\ \text{cm}$, an abrupt decrease in conduction velocity (Fig. 12.8B), corresponding to an increase in resistivity from 115 to $600\ \Omega\ \text{cm}$, and a propagation through a region of slowed conduction (Fig. 12.8C). Electrograms with varying asymmetry and degree of fragmentation arise in the proximity of the discontinuity in properties, and on a longer distance in the slow conduction velocity area. Figs. 12.8A–B show that this effect dependent on the direction of propagation. In addition, the amplitude of the

signal is decreased in the slow conduction regions. Further fragmentation can be obtained by increasing the number of discontinuity boundaries (Fig. 12.8C). It is important to note that secondary current sources are formed at the transition of material properties. As a result, the source produces a deflection that decrease in amplitude as function of distance from the discontinuity. Figs. 12.8D–E show this decrease and the time alignment of the deflections for points located 2 to 5 mm away from the discontinuity.

In summary, double potentials are observed close (distance < 5 mm) to a discontinuity in conductivity in the region of slower conduction. In addition, when the secondary current source is aligned with a deflection (nearly on the discontinuity point, distance < 2 mm), the resulting waveform is a single potential, but its asymmetry is strongly affected.

12.3.2 A Heterogeneous Atrial Model

Simulations on the whole atrial model were also performed to study the effect of the characteristic length scale of these heterogeneities on the occurrence of fractionated signals, and to determine whether fractionated electrograms are fixed at given sites during SAF. Isotropic conduction properties were used to avoid interferences with effects of anisotropy.

Heterogeneity patterns of conductivity were assigned randomly on the whole atrial sur-

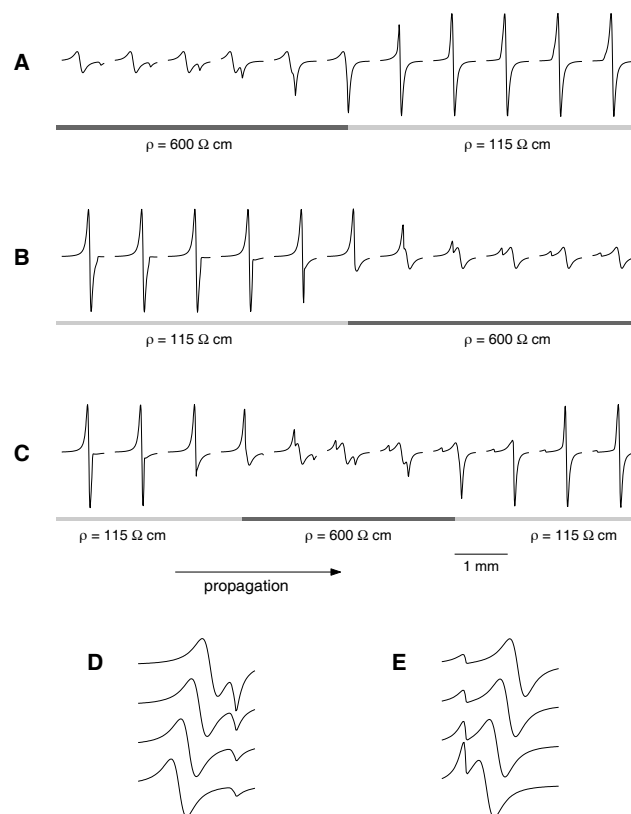


Figure 12.8 — Electrogram waveform in presence of conduction velocity (CV) heterogeneities simulated in a cable (length 5 cm, space step $100 \mu\text{m}$). Wavefronts are propagating from left to right and 11 electrograms located between $x = 2$ cm to $x = 3$ cm are recorded. (A) slow to fast CV discontinuity, (B) fast to slow CV discontinuity, (C) region (5 mm long) of decreased CV, (D) time-alignment of the four first electrograms of panel A, (E) time-alignment of the four last electrograms of panel B.

face with patches having on average a characteristic length scale of 2 cm (Fig. 12.9A) and 0.5 cm (Fig. 12.9B), using the method described in subsection 4.2.3. For SAF initiated in the heterogeneous tissue, the percentage of fractionated electrogram was computed over 55 ± 1 waveforms for each of the 256 electrodes in the right atrium free wall. Figs. 12.9A and B display these fragmentation maps. Fig. 12.9C shows examples of a variety of simulated multiphasic signals similar to those often seen in clinical recordings during AF, including doubles, long doubles, doubles near a spiral tip and triples. All types are seen for both heterogeneity patterns, although triples are more common for 5 mm patches. Globally, the proportion of fractionated electrograms was found to be 15–17%, and was independent of the length scale of the heterogeneity over the given range. These values are within physiological range ($23 \pm 12\%$ recorded in human AF by Konings *et al.*¹³). Analysis of the signals showed that the location of doubles or fractionated potentials was not fixed even in the presence of fixed heterogeneity. Fig. 12.9E presents fragmentation maps associated with the activation maps shown in Fig. 12.9D. As shown, for some beats a single is recorded at a given site while for another beat a fractionated signal was recorded. The occurrence of beat-to-beat variation in electrogram morphology depends on the direction of the activation front (and previous recovery pattern) relative to the heterogeneity, and the distance of the recording site from the discontinuity of tissue properties as the wavefront encounters the heterogeneity. It should be noted that if the heterogeneity was larger than the entire plaque regions, the signals in the recording area should resemble those in the isotropic case.

One notable difference between the two length scales is that increasing the spatial frequency of the heterogeneity tends to affect the distribution of amplitudes. Fig. 12.10 shows the distributions of waveform morphology during SAF for the different heterogeneity patterns. For homogeneous, isotropic tissue the amplitude distribution is very narrow. In tissue with patchy heterogeneity of a length scale of 5 mm, however, the distribution of amplitudes is broader due to the fact that the wavefront is slowed in the region of reduced conductivity that is randomly distributed over the entire plaque array. With heterogeneity on a larger scale (2 cm), the distribution has a double peak, one for each wave speed.

Notice that waveforms measured in regions of slow conduction are on average more positive asymmetric than those recorded in regions of faster conduction (see Fig. 12.10). When a wavefront encounters a zone of slow conduction, a locally concave wavefront is formed in the heterogeneity because activation is delayed (see the second isochrone map of Fig. 12.9D), and thus leads to a more positive asymmetry.

Multiphasic and fractionated electrograms were rarely seen in the model with uniform properties during SAF but were more common in the models with regional heterogeneity in conductivities. The studies of Spach and Dolber³³³ showed that complex waveform shapes with multiple deflections could arise from asynchronous excitation of small groups of fibers within distances of 50 to 100 μm . Fig. 12.9 showed that multiphasic electrograms are observed at a transition of regions with different conductivities. Current sources are established at these sites and are manifested as a deflection in the electrogram. If caused by an abrupt transition, the deflections should be time aligned and with varying amplitude in the signals at neighboring sites as shown in Fig. 12.8D–E. Konings observed that in some cases of AF in patients, the multiphasic electrograms were not fixed to a given site.¹³ The computer simulations presented here showed that even with fixed anatomic heterogeneity, the occurrence of the multiphasic signal depended on the direction of the wavefront and recovery conditions

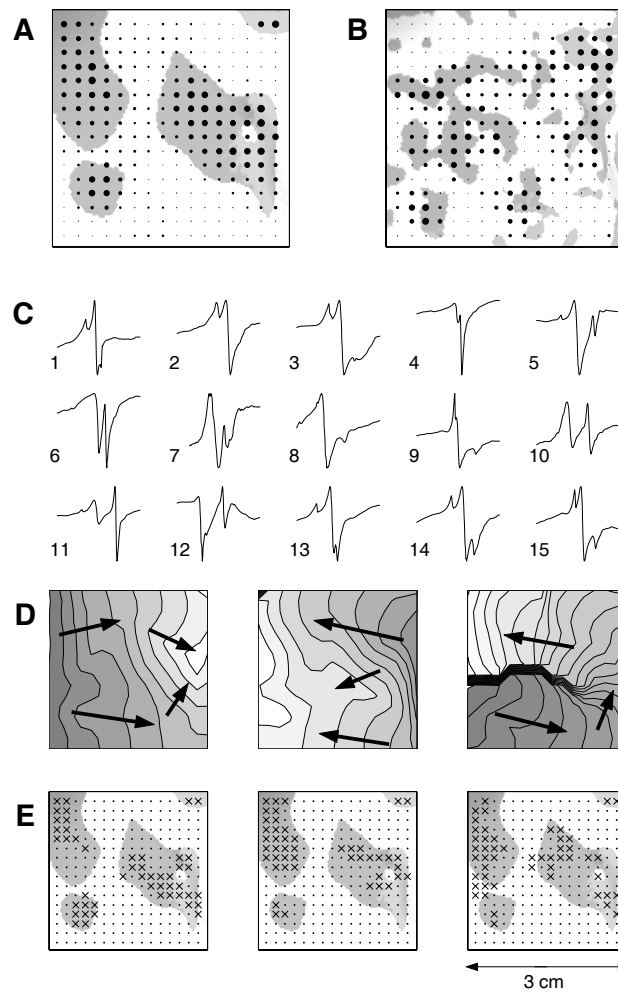


Figure 12.9 — (A) Fragmentation map indicating fraction of fragmented waveforms during SAF in the presence of heterogeneity with a length scale of 2 cm. Circles with an area proportional to the percentage of fractionated waveforms are displayed on the location of the corresponding electrode. Gray regions represent zones with decreased conductivity. (B) Fragmentation map for heterogeneity with a length scale of 2 cm. (C) Examples of simulated fractionated electrograms: short doubles (1-7), long doubles (8, 9), doubles observed at core of a spiral (10-12) and triples (13-15). (D-E) Fragmentation maps for 3 different activation patterns with heterogeneity distribution of panel (A): isochrones plotted every 10 ms (D) and fragmentation maps (E). A dot represents a single and a cross represents a fractionated potential.

preceding the front. Consequently, it is not possible to rule out fixed heterogeneity as the basis for fractionation simply because of beat-to-beat variations in signal.

The simulations suggest that the complexity of the underlying wavefront dynamics during AF is not the likely cause of these multicomponent signals in the absence of heterogeneity. In the real atria, a component of the fractionation can also arise from transmural conduction during AF. Consequently, the occurrence of fractionated signals may also depend on the degree of transmural conduction during AF. Again, time alignment of deflections should help identify the presence and possible location of the changes in properties. Since fragmentation is observed between 2 and 5 mm from the line of discontinuity, triples should be generated near patches whose size ranges from 4 to 10 mm. In addition, the occurrence of lower amplitude electrograms should increase in the presence of regional heterogeneities

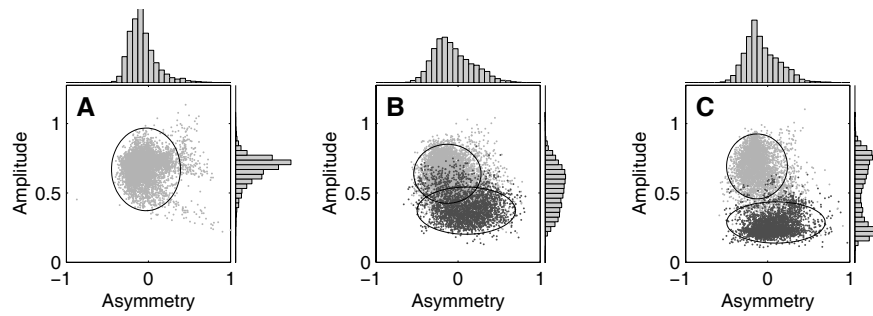


Figure 12.10 — Waveform morphology distribution during SAF in (A) homogeneous atria, (B) atria with heterogeneities with a characteristic length scale of 5 mm, (C) atria with heterogeneities with a characteristic length scale of 2 cm. In panels (B) and (C), the dark gray clouds of points correspond to electrograms measured on the heterogeneities (region of slow conduction). The ellipses emphasize the differences between the two regions with different conduction velocities.

since the amplitude decreases in the slow conducting patches.

12.4 Effect of Tissue Transmural Heterogeneity

Up to now, we considered only wavefront propagation in monolayer tissues. Although the atrial tissue is thin, three-dimensional effects like transmural heterogeneities may impact waveform morphology, even if the activation sequence seems unchanged. This section shows examples of waveform asymmetry distributions resulting from paced beats in a thick tissue, in order to discuss the limitations of monolayer tissues for explaining electrogram morphology.

12.4.1 Plane Wave Propagation in a 3D Tissue

Plane waves are the simplest 3D propagations and, for this reason, were simulated in a 1.5×1.5 cm sheet of tissue with a total thickness δ ranging from 0.75 to 3 mm (spatial discretization $150 \mu\text{m}$). A wavefront was initiated by stimulating a lateral face of the parallelepiped and a unipolar electrogram was recorded in the center of the tissue, 1 mm above the epicardial surface. Propagation in a tissue with uniform isotropic conduction properties (resistivity $200 \Omega \text{ cm}$) was used as a reference.

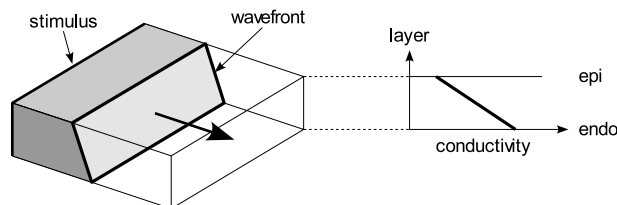


Figure 12.11 — Schematic representation of the 3D heterogeneous tissue model. The gray region shows the activated cells, and the wavefront propagation is illustrated by an arrow. The graph on the right depicts the transmural gradient of conductivity.

Transmural heterogeneity was then introduced in the tissue by assigning a different resis-

tivity to each tissue layer (200 Ω cm in the middle layer, and a ratio epicardial/endocardial resistivity ranging from 1/9 to 9). In presence of a transmural gradient of conductivity, the wavefront surface was slanted and propagated uniformly like a (nearly) plane wave (see Fig. 12.12A), so that there was a constant activation delay between the epicardium and the endocardium (see Fig. 12.11). This wavefront was characterized by its angle with respect to the homogeneous case (see Fig. 12.12A), a positive angle corresponding to an endocardium activation prior to epicardium activation. Wavefront propagation was simulated in 40 different heterogeneous tissues whose transmural conductivity gradient was adjusted so that wavefront angles varied from -45 to $+45$ degrees. All these simulations were carried out for 5 different thicknesses ranging from 0.75 to 3 mm (5 to 20 layers).

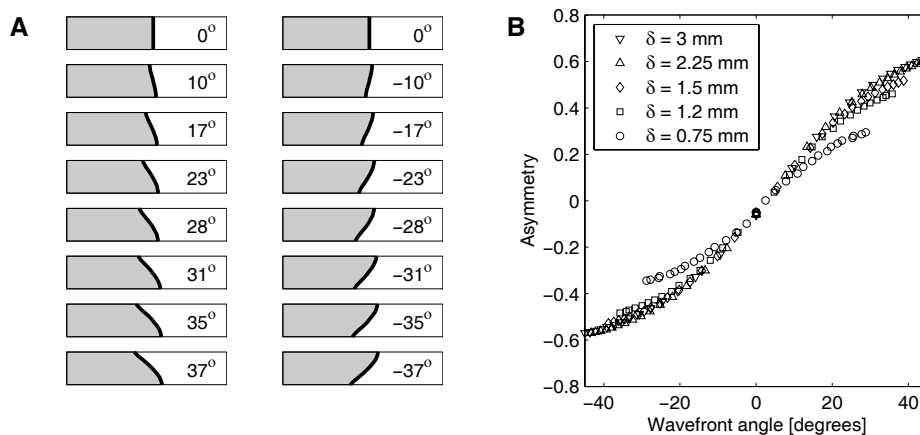


Figure 12.12 — Effect of wavefront angle on electrogram asymmetry. (A) Examples of steady-state wavefront shape. The gray regions are activated and the thick black lines represent wavefronts. The wavefront angle is given near the wavefront it corresponds to. (B) Waveform asymmetry as a function of the wavefront angle, for different tissue thicknesses δ .

Fig. 12.12B shows the waveform asymmetry as a function of the wavefront angle. When the epicardium is activated *before* the endocardium (negative wavefront angle), negative asymmetric electrograms are measured near the epicardial surface. In contrast, these waveforms become positive asymmetric if the epicardium is activated *after* the endocardium. Notice that even for moderate wavefront angle (± 20 degrees), the asymmetry can be significant (about ± 0.2) and comparable in magnitude with the effect of curvature (see subsection 11.2.5) and anisotropy (see subsection 12.2.2). In the given range of thickness, waveform asymmetry is determined mostly by the wavefront angle and is not very sensitive to tissue thickness, except for very thin tissues (thickness $\delta < 1$ mm) in which large wavefront angles are difficult to obtain.

In this subsection, the effect of an activation delay between the epicardium and the endocardium was briefly considered. This delay was created by introducing a transmural gradient of conductivity and lead to significant changes in waveform asymmetry. However, large variations in conductivity (up to a factor of 9) were necessary to reproduce those slanted wavefront with an angle > 30 degrees. Some other mechanisms (possibly dynamical instead of structural) may be involved to generate this class of wavefront geometry in a real heart.

12.4.2 Paced Beat in a Multilayer Atrial Model

In order to estimate the interplay between the effects of wavefront curvature and transmural heterogeneity, paced beats were simulated on a 3D multilayer model of the atria with uniform thickness of 1 mm (5 layers), following the approach presented in section 5.4. Unipolar electrograms were recorded in a 16×16 grid of electrodes located near the tissue surface in the right atrium free wall, and distributions of waveform asymmetry were computed. Wavefronts were initiated near the anatomical location of (A) the septum, (B) the sino-atrial node and (C) near the tricuspid valve. Three substrates were considered: a homogeneous tissue used as reference, a tissue with a transmural gradient of conductivity leading to an activation time delay between epi- and endocardium of about 2 ms, and a tissue with the same gradient of conductivity, but reversed.

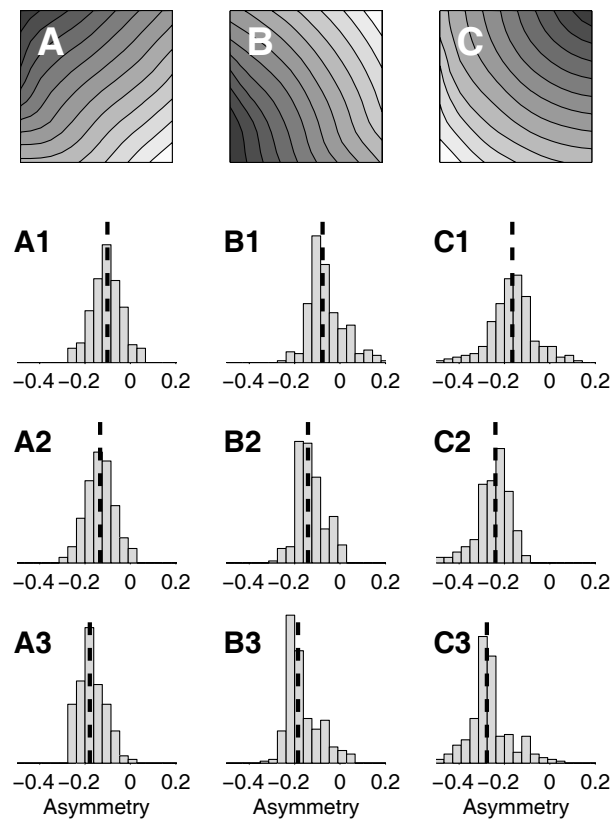


Figure 12.13 — Effect of transmural gradients of conductivity on the waveform asymmetry distribution in a multilayer model of the atria. Wavefronts are initiated near the septum (column A), the sino-atrial node (column B) and near the tricuspid valve (column C). (A)–(C) Isochrone maps. (A1)–(C1) Asymmetry distributions when the endocardium is activated 2 ms before the epicardium, (A2)–(C2) with synchronized activation of epi- and endocardium, and (A3)–(C3) when the epicardium is activated 2 ms before the endocardium. The dashed vertical lines indicates the mean of the distribution.

Fig. 12.13 A–C shows, for the homogeneous (reference) tissue, the isochrones measured in the mapping area. The activation sequences remained almost unchanged after the introduction of a transmural gradient of conductivity. The asymmetry distributions, however, were significantly altered by this modification of the conduction properties. As compared to the homogeneous case (Fig. 12.13 A2–C2), asymmetry distributions were shifted toward

more positive asymmetry when the endocardium was activated 2 ms before the epicardium (Fig. 12.13 A1–C1), and toward more negative asymmetry when the epicardium was activated first, in agreement with the results of the previous subsection. The mean asymmetry values are given in Table 12.2 to facilitate the comparison.

Mean asymmetry	A	B	C
endo. activated first	-0.10 ± 0.05	-0.07 ± 0.06	-0.17 ± 0.08
synchronized	-0.13 ± 0.04	-0.14 ± 0.05	-0.25 ± 0.05
epi. activated first	-0.17 ± 0.05	-0.18 ± 0.05	-0.28 ± 0.07

Table 12.2 — Mean wavefront asymmetry in presence of different transmural gradients of conductivity in the three activation patterns (A, B, C) of Fig. 12.13: endocardium activated 2 ms before the epicardium, synchronized activation of epi- and endocardium, and epicardium activated 2 ms before the endocardium.

Therefore, even in a thin tissue, transmural gradients of conduction properties affect wavefront asymmetry distribution. Epicardial isochrones may not be sufficient to explain electrogram morphology in a thin tissue with transmural heterogeneities.

12.5 Conclusion

In this study, a computer model was used to investigate morphology changes of SAF electrograms due to modification of the tissue properties. The results showed that:

- In the presence of anisotropy, curvature effects are reduced in the axial direction and reinforced in the transverse direction. As a consequence, wavefronts propagating along fibers are associated with large amplitude symmetric signals, and wavefronts propagating across fibers are associated with small amplitude waveforms and a large range of asymmetry (see Fig. 12.14A). A larger spread in amplitude is observed for positive asymmetric than for negative asymmetric waveforms since collisions can occur in both the longitudinal and the transverse direction.
- Heterogeneities in tissue conductivity lead to larger variations in waveform amplitude (see Fig. 12.14B). In addition, wavefront dynamics is affected. For instance, with patchy heterogeneity, wavefront curvature tends to be more convex in fast regions and more concave in slow regions. This has an impact on waveform asymmetry.
- Multiphasic signals are rarely seen in uniform isotropic tissue. Rather, multiphasic signals are commonly observed in tissue with patchy heterogeneity, that is, with discontinuities in tissue conductivity. The relative amount of fractionation is not greatly affected by the length scale of the heterogeneity but the frequency of occurrence of low amplitude signals is more broadly distributed with heterogeneity with larger length scales.
- When there is a delay in activation time between the epicardium and the endocardium, the resulting waveform asymmetry can be greatly affected even if the tissue is thin. This is the case when a transmural gradient of conductivity is present and suggests that the effects of 3D structures on electrogram morphology should be further investigated.

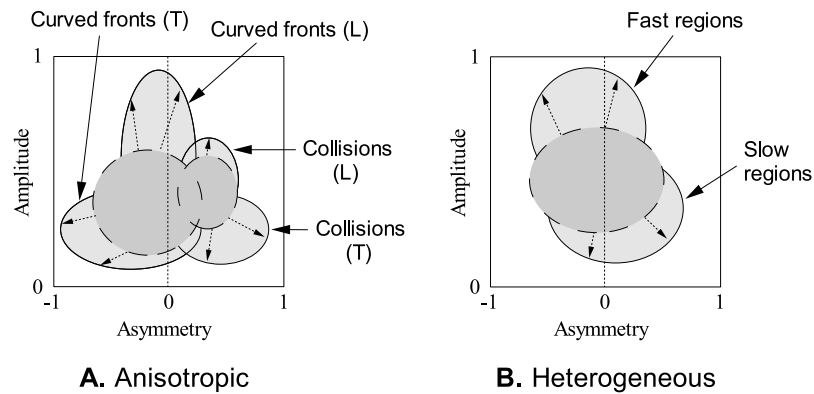


Figure 12.14 — Schematic representation of the different regions in an amplitude-versus-asymmetry diagram that can be associated with a class of activation patterns. The dark gray regions represent the uniform isotropic case. The light gray regions and the corresponding arrows illustrate the changes when anisotropy (panel A) or patchy heterogeneity (panel B) are introduced. (A) In an anisotropic tissue, the 4 regions shown are associated with transverse (T) and longitudinal (L) curved wavefronts and transverse (T) and longitudinal (L) collisions. (B) In a tissue with patchy heterogeneities, 2 regions are shown, corresponding to electrograms measured in fast conduction regions and in slow conduction regions.

The simulations demonstrate that analysis of the morphology of single site electrograms may provide insights into the substrate maintaining AF and could be useful in monitoring the time course of a given therapy.

Conclusion

The introduction of chapter 2 emphasized that computer modeling should aim at investigating specific questions. It is therefore natural to conclude this dissertation by considering the insights our atrial model has provided into relevant questions (most of them are still open) and the perspectives the model suggests. For each of the following questions, a brief summary of the observations collected *in the framework of our atrial model* is given.

Questions about Atrial Fibrillation

Can atrial fibrillation (AF) be initiated in a uniform tissue?

Even in an atrial model with perfectly uniform conduction and membrane properties, a sustained and complex activity was initiated through clinically relevant pacing protocols like S_1 – S_2 – S_3 , burst-pacing or ramp protocols (section 8.2). Initiation of this simulated AF (SAF) was the result of a dynamical instability due to an interplay between the non-planar geometry of the atria and a non-uniform action potential duration (APD) alternans. This mechanism, however, required a steep APD restitution curve (subsection 8.2.2).

What are the factors facilitating AF initiation?

One source of instability and induction of wavelet breakup is a steep restitution curve. The results showed that single site burst-pacing protocols lead to SAF when the maximal slope of the (dynamic) restitution curve was larger than 1 (subsection 8.2.2). As a complementary initiation mechanism, the presence of large gradients in APD due to heterogeneity can help breakups occur even when the restitution curve is flat (section 8.3).

What are the mechanisms underlying AF perpetuation?

Although computer models cannot determine which mechanism is actually effective during human AF, models of AF can be proposed in which the underlying mechanisms can be isolated and described in detail. In this work, three different possible “perpetuators” of AF were identified and investigated: multiple reentrant wavelets (section 9.1), meandering wavelets (section 9.2), and mother rotor (section 9.3). These models were characterized by different dynamical regimes and spatiotemporal organizations (chapter 10). The first model was associated with a dynamics of continuously interacting wavelets undergoing reentries and

wavebreaks, and with a short-range spatial organization. The model of meandering wavelets lead to a more organized dynamics because of its longer wavelength. Finally, in the model of mother rotor, SAF was perpetuated by one or a few stable sources of wavelets observed as a spiral anchored to a heterogeneity, and was characterized by a marked spatiotemporal organization.

What are the factors promoting AF maintenance?

In the model, wavelength (effective refractory period \times conduction velocity) was found to be a key factor for SAF perpetuation. Decreasing APD or conduction velocity (longitudinal or transverse, or both) acted to increase SAF duration (subsection 9.1.4). When the wavelength was shorter than a critical value, SAF was sustained (subsection 10.3.3).

What is the effect of remodeling on AF perpetuation?

Remodeling was implemented in the model as an abrupt reduction in both the APD and the rate adaptation (section 9.1.3). As a result, SAF duration was prolonged, in agreement with the concept “AF begets AF”. Interestingly, the conditions facilitating SAF initiation were different from those prolonging SAF duration. While initiation was based on an instability inducing the first wavebreak, sustained SAF was usually associated with a less unstable wavelet dynamics.

What about AF termination?

In an atrial model with normal conduction and membrane properties (baseline model) or when the wavelength was too long, electrically-induced SAF was not sustained and converted to sinus rhythm after a few seconds (subsection 9.1.1). SAF self-terminated through mutual interactions of wavefronts or interactions with boundary and refractory tissue.

Questions about Atrial Electrograms

What is the effect of wavelet dynamics on electrogram morphology?

Unipolar electrograms, computed during SAF at 256 sites in right atrium to simulate a mapping array, exhibited a wide variety of morphologies (chapter 11). Electrogram morphology was quantified by the distribution of waveform asymmetry and amplitude. Results obtained in a uniform isotropic atrial tissue showed that: (1) wavefront curvature affects waveform asymmetry, convex fronts being associated with negative asymmetries, concave fronts with positive asymmetries, and nearly planar fronts with approximately symmetric waveforms; (2) wavefront collisions generate large-amplitude positive asymmetric signals; (3) the occurrence of conduction blocks was related to small-amplitude positive asymmetric waveforms.

What is the effect of the fiber structure on electrogram morphology?

Simulations were performed in an atrial model with a gross fiber architecture based on histology (chapter 12). Increasing anisotropy ratios from 1:1 to 9:1 were considered. The results

showed that: (1) In a homogeneous and isotropic tissue the presence of highly asymmetric electrograms is rare although there is a marked variability in amplitude and symmetry; (2) The introduction of anisotropy increases this variability in symmetry and amplitude of the electrograms especially for propagation across fibers; (3) More specifically, when a wavefront propagates along a fiber, the asymmetry of the resulting waveform is reduced as compared to the isotropic case. On the other hand, when a wavefront propagates across a fiber, the effect of curvature on asymmetry is amplified.

What is the origin of electrogram fractionation?

Regardless of anisotropy, the vast majority of computed electrograms in the uniform atria were found to be single, biphasic signals, suggesting that the complexity of the underlying wavefront dynamics during AF is not the likely cause of these multicomponent signals in the absence of heterogeneity. Multiphasic and fractionated electrogram waveforms, however, were more common in models with regional heterogeneity in conductivities (section 12.3). Moreover, even with fixed anatomic heterogeneity, the occurrence of multiphasic signals depended on the direction of the wavefront and recovery conditions preceding the front.

Questions about Future Developments

What would be the next milestones in the project?

In any area of computer modeling, validation is crucial. Further comparisons with experimental data are therefore required. Electrograms were shown to be a key tool for this purpose (chapter 10). Extension to surface electrocardiograms would be an important achievement since these signals are routinely measured for non-invasive clinical diagnosis.

Future extensions should also include further developments of the atrial model. Three-dimensional structures like pectinate muscles, Bachmann's bundle and crista terminalis were found to affect atrial activation⁷ and may have an impact on the mechanisms perpetuating atrial arrhythmias. A three-dimensional tissue could also account for the breakthrough activations observed in experiments.¹⁸¹

Finally, therapeutic interventions such as radio-frequency ablations, antitachycardia pacing or drug delivery can already be tested in the model. This constitutes a natural extension to the study of AF initiation.

Finally, does it make sense to use computer models to investigate questions about AF?

Despite the unavoidable limitations of the models, we believe that this work illustrates the usefulness of computer models for research in cardiology and we hope that the combined use of anatomically and electrophysiologically realistic computer models and experimental mapping will help unlock the mechanisms underlying AF in order to eventually better treat diseases and cure patients.

Bibliography

1. R. Ruffly, "Atrial fibrillation," in *Cardiac Electrophysiology: From Cell to Bedside* (D. P. Zipes and J. Jalife, eds.), pp. 682–690, W. B. Saunders, Philadelphia, 2000.
2. E. N. Prystowsky, D. W. Benson, V. Fuster, R. G. Hart, G. N. Kay, R. J. Myerburg, G. V. Naccarelli, and D. G. Wyse, "Management of patients with atrial fibrillation," *Circulation*, vol. 93, pp. 1262–1277, 1996.
3. P. A. Wolf, T. R. Dawber, H. E. J. Thomas, and W. B. Kannel, "Epidemiologic assessment of chronic atrial fibrillation and risk of stroke: the Framingham study," *Neurology*, vol. 28, no. 10, pp. 973–977, 1978.
4. C. Ayala, W. A. Wattigney, J. B. Croft, A. Hyduk, and G. A. Mensah, "Public health and aging: Atrial fibrillation as a contributing cause of death and Medicare hospitalization – United States, 1999," *MMWR*, vol. 52, pp. 128–131, Feb. 2003.
5. L. Kappenberger, "Arrhythmia: a therapeutic dilemma," in *Computer Simulation and Experimental Assessment of Cardiac Electrophysiology* (N. Virag, O. Blanc, and L. Kappenberger, eds.), pp. 185–188, Futura Publishing, Armonk, New York, 2001.
6. C. S. Henriquez and A. A. Papazoglou, "Using computer models to understand the roles of tissue structure and membrane dynamics in arrhythmogenesis," *Proc. IEEE*, vol. 84, pp. 334–354, Mar. 1996.
7. D. M. Harrild and C. S. Henriquez, "A computer model of normal conduction in the human atria," *Circ. Res.*, vol. 87, pp. e25–e36, 2000.
8. E. J. Vigmond, R. Ruckdeschel, and N. Trayanova, "Reentry in a morphologically realistic atrial model," *J. Cardiovasc. Electrophysiol.*, vol. 12, pp. 1046–1054, Sept. 2001.
9. C. W. Zemlin, H. Herzog, S. Y. Ho, and A. Panfilov, "A realistic and efficient model of excitation propagation in the human atria," in *Computer Simulation and Experimental Assessment of Cardiac Electrophysiology* (N. Virag, O. Blanc, and L. Kappenberger, eds.), pp. 29–34, Futura Publishing, Armonk, New York, 2001.
10. R. L. Winslow, D. F. Scollan, A. Holmes, C. K. Yung, J. Zhang, and M. S. Jafri, "Electrophysiological modeling of cardiac ventricular function: from cell to organ," *Annu. Rev. Biomed. Eng.*, vol. 2, pp. 119–155, 2000.
11. A. V. Panfilov, "Modelling of re-entrant patterns in an anatomical model of the heart," in *Computational Biology of the Heart* (A. V. Panfilov and A. V. Holden, eds.), pp. 259–276, John Wiley & Sons, 1997.
12. A. Michelucci, P. Bartolini, G. Calcagnini, F. Censi, A. Colella, S. Morelli, L. Padeletti, P. Pieragnoli, and V. Barbaro, "Mapping the organization of atrial fibrillation with basket catheters. Part II: Regional patterns in chronic patients," *Pacing Clin. Electrophysiol.*, vol. 24, no. 7, pp. 1089–1096, 2001.
13. K. T. S. Konings, J. L. R. M. Smeets, O. C. Penn, H. J. J. Wellens, and M. A. Allesie, "Configuration of unipolar atrial electrograms during electrically induced atrial fibrillation in humans," *Circulation*, vol. 95, pp. 1231–1241, 1997.
14. I. Peterson, "The EKG sequence," *Science News Online*, vol. 163, no. 20, 2002.
15. O. Blanc, *A computer model of human atrial arrhythmia*. Ph.D. thesis number 2537, Ecole Polytechnique Fédérale de Lausanne, Switzerland, 2002.
16. E. M. Cherry, F. Xie, Z. Feliciano, and A. Garfinkel, "Computer modeling of atrial fibrillation," *Card. Electrophys. Rev.*, 2001.
17. K. Shivkumar and J. N. Weiss, "Atrial fibrillation: From cells to computers," *Cardiovasc. Res.*, vol. 52, pp. 171–173, 2001.
18. H. G. Othmer, *Some Mathematical Questions in Biology: The Dynamics of Excitable Media*, vol. 21 of *Lectures on Mathematics in the Life Sciences*. The American Mathematical Society, Providence, Rhode Island, 1988.
19. G. W. Beeler and H. Reuter, "Reconstruction of the action potential of ventricular myocardial fibres," *J. Physiol.*, vol. 268, pp. 177–210, 1977.
20. P. S. Landa, *Nonlinear Oscillations and Waves in Dynamical Systems*, ch. 24. Kluwer Academic Publisher, 1996.
21. A. Scott, *Nonlinear Science Emergence and Dynamics of Coherent Structures*, ch. 4. Oxford Applied and Engineering Mathematics, 1999.
22. P. J. Hunter, P. A. McNaughton, and D. Noble, "Analytical models of propagation in excitable cells," *Prog. Biophys. Molec. Biol.*, vol. 30, pp. 99–144, 1975.
23. R. A. FitzHugh, "Impulses and physiological states in theoretical models of nerve membrane," *Biophys. J.*, vol. 1, pp. 445–466, 1961.
24. J. Nagumo, S. Animoto, and S. Yoshizawa, "An active pulse transmission line simulating nerve axon," *Proc. Inst. Radio Engineers*, vol. 50, pp. 2061–2070, 1962.

25. R. R. Aliev and A. V. Panfilov, "A simple two-variable model of cardiac excitation," *Chaos, Solitons and Fractals*, vol. 7, pp. 293–301, 1996.
26. J. M. Rogers, "Modeling the cardiac action potential using B-spline surfaces," *IEEE Trans. Biomed. Eng.*, vol. 47, pp. 784–791, June 2000.
27. F. J. L. van Capelle and D. Durrer, "Computer simulation of arrhythmias in a network of coupled excitable elements," *Circ. Res.*, vol. 47, pp. 454–466, 1980.
28. F. Fenton and A. Karma, "Vortex dynamics in three-dimensional continuous myocardium with fiber rotation: Filament instability and fibrillation," *Chaos*, vol. 8, pp. 20–47, Mar. 1998.
29. Z. Qu, J. Kil, F. Xie, A. Garfinkel, and J. N. Weiss, "Scroll waves dynamics in a tree-dimensional cardiac tissue model: Roles of restitution, thickness and fiber orientation," *Biophys. J.*, vol. 78, pp. 2761–2775, June 2000.
30. E. J. Vigmond and L. J. Leon, "Restitution curves and the stability of reentry in three-dimensional simulations of cardiac tissue," *Comput. Visual Sci.*, vol. 4, pp. 237–247, 2002.
31. R. Plonsey and R. C. Barr, *Bioelectricity: A Quantitative Approach*. Kluwer Academic Plenum Publishers, second ed., 2000.
32. B. Hille, *Ionic Channels of Excitable Membranes*. Sunderland, Massachusetts, 1984.
33. L. D. DeFelice, *Electrical Properties of Cells. Patch Clamp for Biologists*. Plenum Publishing Corporation, 1997.
34. A. L. Hodgkin and A. F. Huxley, "A quantitative description of membrane current and its application to conduction and excitation in nerve," *J. Physiol.*, vol. 117, pp. 500–544, 1952.
35. L. Ebihara and E. A. Johnson, "Fast sodium current in cardiac muscle: a quantitative description," *Biophys. J.*, vol. 32, pp. 779–790, 1980.
36. J.-P. Drouhard and F. A. Roberge, "Revised formulation of the Hodgkin–Huxley representation of the sodium current in cardiac cell," *Comp. Biomed. Res.*, vol. 20, pp. 333–350, 1987.
37. K. Skouibine, N. Trayanova, and P. Moore, "A numerically efficient model for simulation of defibrillation in an active bidomain sheet of myocardium," *Math. Biosci.*, vol. 166, pp. 85–100, 2000.
38. C.-H. Luo and Y. Rudy, "A model of the ventricular cardiac action potential," *Circ. Res.*, vol. 68, pp. 1501–1526, June 1991.
39. R. E. McAllister, D. Noble, and R. W. Tsien, "Reconstruction of the electrical activity of cardiac Purkinje fibres," *J. Physiol.*, vol. 251, pp. 1–59, 1975.
40. D. Noble, "A modification of the Hodgkin–Huxley equations applicable to Purkinje fibre action and pace-maker potentials," *J. Physiol.*, vol. 160, pp. 317–352, 1962.
41. D. DiFrancesco and D. Noble, "A model of cardiac electrical activity incorporating ionic pumps and concentration changes," *Phil. Trans. Roy. Soc. London*, vol. B307, pp. 353–398, 1985.
42. C. Cabo and R. C. Barr, "Propagation model using the DiFrancesco–Noble equations. Comparison to reported experimental results," *Med. & Biol. Eng. & Comput.*, vol. 30, pp. 292–302, May 1992.
43. C.-H. Luo and Y. Rudy, "A dynamic model of the cardiac ventricular action potential: I. Simulations of ionic currents and concentration changes," *Circ. Res.*, vol. 74, pp. 1071–1096, June 1994.
44. C.-H. Luo and Y. Rudy, "A dynamic model of the cardiac ventricular action potential: II. Afterdepolarizations, triggered activity and potentiation," *Circ. Res.*, vol. 74, pp. 1097–1113, June 1994.
45. J. Zeng, K. R. Laurita, D. S. Rosenbaum, and Y. Rudy, "Two components of the delayed rectifier K^+ current in ventricular myocytes of the guinea pig type," *Circ. Res.*, vol. 77, pp. 140–152, 1995.
46. R. M. Shaw and Y. Rudy, "Electrophysiological effects of acute myocardial ischemia: a theoretical study of altered cell excitability and action potential duration," *Cardiovasc. Res.*, vol. 35, pp. 256–272, 1997.
47. P. C. Viswanathan, R. M. Shaw, and Y. Rudy, "Effects of I_{Kr} and I_{Ks} heterogeneity on action potential duration and its rate dependence: A simulation study," *Circulation*, vol. 99, pp. 2466–2474, 1999.
48. G. M. Faber and Y. Rudy, "Action potential and contractility in $[Na^+]_i$ overloaded cardiac myocytes," *Biophys. J.*, vol. 78, pp. 2392–2404, 2000.
49. C. E. Clancy and Y. Rudy, "Cellular consequences of HERG mutations in the long QT syndrome: precursors to sudden cardiac death," *Cardiovasc. Res.*, vol. 50, pp. 301–313, 2001.
50. E. Chudin, J. Goldhaber, A. Garfinkel, J. Weiss, and B. Kogan, "Intracellular Ca^{2+} dynamics and the stability of ventricular tachycardia," *Biophys. J.*, vol. 77, pp. 2930–2941, Dec. 1999.
51. J. J. Fox, J. L. McHarg, and R. F. Gilmour, "Ionic mechanism of electrical alternans," *Am. J. Physiol. (Heart. Circ. Physiol.)*, vol. 282, no. 2, pp. H516–H530, 2002.
52. R. L. Winslow, J. Rice, S. Jafri, E. Marban, and B. O'Rourke, "Mechanisms of altered excitation-contraction coupling in canine tachycardia-induced heart failure. II. Model studies," *Circ. Res.*, vol. 84, pp. 571–586, 1999.
53. M. S. Jafri, J. J. Rice, and R. L. Winslow, "Cardiac calcium dynamics: The roles of ryanodine receptor adaptation and sarcoplasmic reticulum load," *Biophys. J.*, vol. 74, pp. 1149–1168, 1998.
54. F. H. Samie, O. Berenfeld, J. Anumonwo, S. F. Mironov, S. Udassi, J. Beaumont, S. Taffet, A. M. Pertsov, and J. Jalife, "Rectification of the background potassium current. A determinant of rotor dynamics in ventricular fibrillation," *Circ. Res.*, vol. 89, pp. 1216–1223, 2001.
55. S. V. Pandit, R. B. Clark, W. R. Giles, and S. S. Demir, "A mathematical model of action potential heterogeneity in adult rat left ventricular myocytes," *Biophys. J.*, vol. 81, pp. 3029–3051, Dec. 2001.
56. L. Priebe and D. J. Beuckelmann, "Simulation study of cellular electric properties in heart failure," *Circ. Res.*, vol. 82, pp. 1206–1223, 1998.
57. S. Abramovich-Siman and S. Akselrod, "A single pacemaker cell model based on the phase response curve," *Biol. Cybern.*, vol. 79, pp. 67–76, 1998.

58. S. Abramovich-Siman and S. Akselrod, "A pacemaker cell pair model based on the phase response curve," *Biol. Cybern.*, vol. 79, pp. 77–86, 1998.
59. S. Dokos, B. Celler, and N. Lovell, "Ion currents underlying sinoatrial node pacemaker activity: A new single cell mathematical model," *J. Theor. Biol.*, vol. 181, pp. 245–272, 1996.
60. S. L. Cloherty, N. H. Lovell, B. G. Celler, and S. Dokos, "Inhomogeneity of action potential wave-shape assists frequency entrainment of cardiac pacemaker cells," *IEEE Trans. Biomed. Eng.*, vol. 48, pp. 1108–1115, Oct. 2001.
61. Y. Kurata, I. Hisatome, S. Imanishi, and T. Shiramoto, "Dynamical description of sinoatrial node pacemaking: Improved mathematical model for primary pacemaker cell," *Am. J. Physiol. (Heart. Circ. Physiol.)*, vol. 283, pp. H2074–H2101, 2002.
62. D. Noble and S. J. Noble, "A model of sino-atrial node electrical activity based on a modification of the DiFrancesco-Noble equations," *Proc. Roy. Soc. London*, vol. B222, pp. 295–304, 1984.
63. S. S. Demir, J. W. Clark, C. R. Murphey, and W. R. Giles, "A mathematical model of a rabbit sinoatrial node cell," *Am. J. Physiol.*, vol. 266, pp. C832–C852, 1994.
64. S. S. Demir, J. W. Clark, and W. R. Giles, "Parasympathetic modulation of sinoatrial node pacemaker activity in rabbit heart: a unifying model," *Am. J. Physiol.*, vol. 276, pp. H2221–H2244, 1999.
65. H. Zhang, A. V. Holden, I. Kodama, H. Honjo, M. Lei, T. Varghese, and M. R. Boyett, "Mathematical models of action potentials in the periphery and center of the rabbit sinoatrial node," *Am. J. Physiol. (Heart. Circ. Physiol.)*, vol. 279, pp. H397–H421, 2000.
66. M. R. Boyett, H. Zhang, A. Garny, and A. V. Holden, "Control of the pacemaker activity of the sinoatrial node by intracellular Ca^{2+} . Experiments and modelling," *Proc. Roy. Soc. London*, vol. A359, pp. 1091–1110, 2001.
67. R. Wilders, H. J. Jongasma, and A. C. G. van Ginneken, "Pacemaker activity of the rabbit sinoatrial node. a comparison of mathematical models," *Biophys. J.*, vol. 60, pp. 1202–1216, Nov. 1991.
68. R. L. Rasmusson, J. W. Clark, W. R. Giles, K. Robinson, R. B. Clark, E. F. Shibata, and D. L. Campbell, "A mathematical model of the single bullfrog cardiac pacemaker cell," *Am. J. Physiol. (Heart. Circ. Physiol.)*, vol. 259, pp. H352–H369, 1990.
69. A. Nygren, C. Fiset, L. Firek, J. W. Clark, D. S. Lindblad, R. B. Clark, and W. R. Giles, "Mathematical model of an adult human atrial cell. The role of K^+ currents in repolarization," *Circ. Res.*, vol. 82, pp. 63–81, 1998.
70. M. Courtemanche, R. J. Ramirez, and S. Nattel, "Ionic mechanisms underlying human atrial action potential properties: Insights from a mathematical model," *Am. J. Physiol.*, vol. 275, pp. H301–H321, 1998.
71. M. Courtemanche, R. J. Ramirez, and S. Nattel, "Ionic targets for drug therapy and atrial fibrillation-induced electrical remodeling: Insights from a mathematical model," *Card. Res.*, vol. 42, pp. 477–489, 1999.
72. R. J. Ramirez, S. Nattel, and M. Courtemanche, "Mathematical analysis of canine atrial action potentials: Rate, regional factors and electrical remodeling," *Am. J. Physiol. (Heart. Circ. Physiol.)*, vol. 279, pp. H1767–H1785, 2000.
73. J. Kneller, R. J. Ramirez, D. Chartier, M. Courtemanche, and S. Nattel, "Time-dependent transients in ionically based mathematical model of the canine atrial action potential," *Am. J. Physiol. (Heart. Circ. Physiol.)*, vol. 282, pp. H1437–H1451, 2002.
74. J. Kneller, R. Zou, E. J. Vigmond, Z. Wang, J. Leon, and S. Nattel, "Cholinergic atrial fibrillation in a computer model of two-dimensional sheet of canine atrial cells with realistic ionic properties," *Circ. Res.*, vol. 90, pp. e73–e87, 2002.
75. D. W. Hilgemann and D. Noble, "Excitation-contraction coupling and extracellular calcium transients in rabbit atrium: reconstruction of the basic cellular mechanisms," *Proc. Roy. Soc. London*, vol. B230, pp. 163–205, 1987.
76. R. L. Rasmusson, J. W. Clark, W. R. Giles, K. Robinson, R. B. Clark, E. F. Shibata, and D. L. Campbell, "A mathematical model of electrophysiological activity in a bullfrog atrial cell," *Am. J. Physiol. (Heart. Circ. Physiol.)*, vol. 259, pp. H370–H389, 1990.
77. D. S. Lindblad, C. R. Murphey, J. W. Clark, and W. R. Giles, "A model of the action potential and underlying membrane currents in a rabbit atrial cell," *Am. J. Physiol. (Heart. Circ. Physiol.)*, vol. 271, pp. H1666–H1691, 1996.
78. P. Jørgensen, C. Schäfer, P. G. Guerra, M. Talajic, S. Nattel, and L. Glass, "A mathematical model of human atrioventricular nodal function incorporating concealed conduction," *Bull. Math. Biol.*, vol. 64, pp. 1083–1099, 2002.
79. B.-S. Kim, Y.-H. Kim, G.-S. Hwang, H.-N. Pak, S. C. Lee, W. J. Shim, D. J. Oh, and Y. M. Ro, "Action potential duration restitution kinetics in human atrial fibrillation," *J. Am. Coll. Cardiol.*, vol. 39, no. 8, pp. 1329–1336, 2002.
80. H. P. Hanson, M. M. Bradley, J. E. Bossert, R. R. Linn, and L. W. Younker, "The potential and promise of physics-based wildfire simulation," *Environmental Science & Policy*, vol. 3, pp. 161–172, 2000.
81. A. T. Winfree, "Rotors, fibrillation and dimensionality," in *Computational Biology of the Heart* (A. Panfilov and A. Holden, eds.), pp. 101–135, John Wiley & Sons, 1997.
82. F. Xie, A. Garfinkel, and J. N. Weiss, "Electrical refractory period restitution and spiral wave reentry in simulated cardiac tissue," *Am. J. Physiol. (Heart. Circ. Physiol.)*, vol. 283, pp. H448–H460, 2003.
83. J. M. Pastore and D. S. Rosenbaum, "Role of structural barriers in the mechanism of alternans-induced reentry," *Circ. Res.*, vol. 87, no. 12, pp. 1157–1163, 2000.
84. H. M. Hastings, F. H. Fenton, S. J. Evans, O. Hottomaroğlu, J. Geethu, K. Gittelsohn, J. Nilson, and A. Garfinkel, "Alternans and the onset of ventricular fibrillation," *Phys. Rev. E*, vol. 62, pp. 4043–4048, Sept. 2000.

85. M. A. Murda'h, W. J. Mckenna, and A. J. Camm, "Repolarization alternans: Techniques, mechanisms, and cardiac vulnerability," *Pacing Clin. Electrophysiol.*, vol. 20, pp. 2641–2657, Oct. 1997.
86. Z. Qu, J. N. Weiss, and A. Garfinkel, "Cardiac electrical restitution properties and stability of reentrant spiral waves: a simulation study," *Am. J. Physiol. (Heart. Circ. Physiol.)*, vol. 276, pp. H269–H283, 1999.
87. Z. Qu, F. Xie, A. Garfinkel, and J. N. Weiss, "Origins of spiral wave meander and breakup in a two-dimensional cardiac tissue model," *Ann. Biomed. Eng.*, vol. 28, pp. 755–771, 2000.
88. Z. Qu, A. Garfinkel, P.-S. Chen, and J. N. Weiss, "Mechanisms of discordant alternans and induction of reentry in simulated cardiac tissue," *Circulation*, vol. 102, pp. 1664–1670, Oct. 2000.
89. M. A. Watanabe, F. H. Fenton, S. J. Evans, H. M. Hastings, and A. Karma, "Mechanisms for discordant alternans," *J. Cardiovasc. Electrophysiol.*, vol. 12, pp. 196–206, Feb. 2001.
90. J. N. Weiss, A. Garfinkel, H. S. Karagueuzian, Z. Qu, and P. S. Chen, "Chaos and the transition to ventricular fibrillation: a new approach to antiarrhythmic drug evaluation," *Circulation*, vol. 99, pp. 2819–2826, 1999.
91. A. Garfinkel, P.-S. Chen, D. O. Walter, H. S. Karagueuzian, B. Kogan, S. J. Evans, M. Karpoukhin, C. Hwang, T. Uchida, M. Gotoh, O. Nwosokawa, P. Sager, and J. N. Weiss, "Quasiperiodicity and chaos in cardiac fibrillation," *J. Clin. Invest.*, vol. 99, pp. 305–314, Jan. 1997.
92. Z. Qu, J. N. Weiss, and A. Garfinkel, "From local to global spatiotemporal chaos in a cardiac tissue model," *Phys. Rev. E*, vol. 61, pp. 727–732, Jan. 2000.
93. J. N. Weiss, P.-S. Chen, Z. Qu, H. S. Karagueuzian, and A. Garfinkel, "Ventricular fibrillation. How do we stop the waves from breaking," *Circ. Res.*, vol. 87, pp. 1103–1107, 2000.
94. A. Garfinkel, Y. H. Kim, O. Voroshilovsky, Z. Qu, J. R. Kil, M. H. Lee, H. S. Karagueuzian, J. N. Weiss, and P. S. Chen, "Preventing ventricular fibrillation by flattening cardiac restitution," *Proc. Natl. Acad. Sci. USA*, vol. 97, pp. 6061–6066, 2000.
95. R. F. J. Gilmour, "A novel approach to identifying antiarrhythmic drug targets," *Drug Discov. Today*, vol. 8, pp. 162–167, 2003.
96. M. L. Koller, M. L. Riccio, and R. F. Gilmour, "Dynamic restitution of action potential duration during electrical alternans and ventricular fibrillation," *Am. J. Physiol. (Heart. Circ. Physiol.)*, vol. 275, no. 44, pp. H1635–H1642, 1998.
97. O. Bernus, R. Wilders, C. W. Zemlin, H. Vershelde, and A. V. Panfilov, "A computationally efficient electrophysiological model of human ventricular cells," *Am. J. Physiol. (Heart. Circ. Physiol.)*, vol. 282, pp. H2296–H2308, June 2002.
98. O. Bernus, H. Vershelde, and A. V. Panfilov, "Modified ionic models of cardiac tissue for efficient large scale computations," *Phys. Med. Biol.*, vol. 47, pp. 1947–1959, June 2002.
99. O. Blanc, N. Virag, J.-M. Vesin, and L. Kappenberger, "A computer model of human atria with reasonable computation load and realistic anatomical properties," *IEEE Trans. Biomed. Eng.*, vol. 48, pp. 1229–1237, Nov. 2001.
100. R. A. Gray and J. Jalife, "Ventricular fibrillation and atrial fibrillation are two different beasts," *Chaos*, vol. 8, no. 1, pp. 65–78, 1998.
101. F. Xie, Z. Qu, and A. Garfinkel, "Dynamics of reentry around a circular obstacle in cardiac tissue," *Phys. Rev. E*, vol. 58, pp. 6355–6358, Nov. 1998.
102. O. Blanc, N. Virag, A. Nicoulin, V. Jacquemet, and L. Kappenberger, "Simulation of arrhythmias in a computer model of human atria," in *Computer Simulation and Experimental Assessment of Cardiac Electrophysiology* (N. Virag, O. Blanc, and L. Kappenberger, eds.), pp. 21–28, Futura Publishing, Armonk, New York, 2001.
103. M.-H. Lee, Z. Qu, G. A. Fishburn, S. T. Lamp, E. H. Chang, T. Ohara, O. Voroshilovsky, J. R. Kil, A. R. Hamzei, N. C. Wang, S.-F. Lin, J. N. Weiss, A. Garfinkel, H. S. Karagueuzian, and P.-S. Chen, "Patterns of wave break during ventricular fibrillation in isolated swine right ventricle," *Am. J. Physiol. (Heart. Circ. Physiol.)*, vol. 281, pp. H253–H265, 2001.
104. A. M. Pertsov, "Three-dimensional organization of reentry in fibrillating ventricular wall," in *Computer Simulation and Experimental Assessment of Cardiac Electrophysiology* (N. Virag, O. Blanc, and L. Kappenberger, eds.), pp. 63–68, Futura Publishing, Armonk, New York, 2001.
105. A. V. Panfilov, "Three-dimensional organization of electrical turbulences in the heart," *Phys. Rev. E*, vol. 59, no. 6, pp. R6251–R6254, 1999.
106. W. D. Stein, *Channels, Carriers, and Pumps. An Introduction to Membrane Transport*. Academic Press, Inc., 1990.
107. W. A. Catterall, "Structure and regulation of voltage-gated Ca^{2+} channels," *Annu. Rev. Cell Dev. Biol.*, vol. 16, pp. 521–555, 2000.
108. W. A. Catterall, "From ionic currents to molecular mechanisms: The structure and function of voltage-gated sodium channels," *Neuron*, vol. 26, pp. 13–25, Apr. 2000.
109. G. Yellen, "The voltage-gated potassium channels and their relatives," vol. 419, pp. 35–42, Sept. 2002.
110. D. M. Roden, J. R. Balsler, A. L. George Jr, and M. E. Anderson, "Cardiac ion channels," *Annu. Rev. Physiol.*, vol. 64, pp. 431–475, 2002.
111. N. H. Sabah, "Origin of the resting potential," *IEEE Eng. Med. Bio.*, vol. 18, no. 5, pp. 100–105, 1999.
112. N. H. Sabah, "Rectification in biological membranes," *IEEE Eng. Med. Bio.*, vol. 19, no. 1, pp. 106–113, 2000.
113. N. H. Sabah, "Reactance of biological membranes," *IEEE Eng. Med. Bio.*, vol. 19, no. 4, pp. 89–95, 2000.
114. N. H. Sabah, "Aspects of nerve conduction," *IEEE Eng. Med. Bio.*, vol. 19, no. 6, pp. 111–118, 2000.
115. R. J. Elliott, L. Angoun, and J. B. Moore, *Hidden Markov models*, vol. 29 of *Applications of mathematics*. Springer, 1995.
116. S. V. Vaseghi, *Advanced Digital Signal Processing and Noise Reduction*. John Wiley & Sons, Ltd, 2000.

117. C. W. Gardiner, *Handbook of Stochastic Methods for Physics, Chemistry and Natural Sciences*. Springer series in synergetics, Berlin: Springer, 2nd ed., 1997.
118. F. Reif, *Fundamentals of Statistical and Thermal Physics*. Series in fundamentals of physics, McGraw-Hill, 1985.
119. L. P. Endresen and J. S. Høye, "A possible resolution of the gating paradox," *Biophys. J.*, vol. 76, pp. 1918–1921, Apr. 1999.
120. L. S. Liebovitch and T. I. Tóth, "A model of ion channel kinetics using deterministic chaotic rather than stochastic processes," *J. Theor. Biol.*, vol. 148, pp. 243–267, 1991.
121. L. S. Liebovitch and T. I. Tóth, "Using fractals to understand the opening and closing of ion channels," *Ann. Biomed. Eng.*, vol. 18, pp. 177–194, 1990.
122. J. B. Bassingthwaite, L. S. Liebovitch, and B. J. West, *Fractal Physiology*. Oxford Univ. Press, 1994.
123. L. A. Irvine, M. S. Jafri, and R. L. Winslow, "Cardiac sodium channel Markov model with temperature dependence and recovery from inactivation," *Biophys. J.*, vol. 76, pp. 1868–1885, Apr. 1999.
124. C. E. Clancy and Y. Rudy, "Linking a genetic defect to its cellular phenotype in a cardiac arrhythmia," *Nature*, vol. 400, pp. 566–569, Aug. 1999.
125. S. Glasstone, K. J. Laidler, and H. Eyring, *The theory of rate processes: the kinetics of chemical reactions, viscosity, diffusion and electrochemical phenomena*. New York & London: McGraw Hill, 1941.
126. J. W. Moore and R. G. Pearson, *Kinetics and Mechanism*. John Wiley, New York, 1981.
127. K. J. Laidler, *Chemical Kinetics*. Harper-Collins Publishers, 3rd ed., 1987.
128. H. Ashida, "Stochastic description of the three-state model of the Na channel," *J. Theor. Biol.*, vol. 121, pp. 45–57, 1986.
129. H. Callen, *Thermodynamics and an Introduction to Thermostatistics*. New York: Wiley, 2nd ed., 1985.
130. N. F. Mott, "The theory of crystal rectifiers," *Proc. R. Soc. Lond. B*, vol. 171, pp. 27–38, 1939.
131. M. B. Jackson, "Allosteric mechanisms in the activation of ligand-gated channels," in *Channels, Receptors and Transporters* (L. J. DeFelice, ed.), Biophysics Textbooks Online www.biophysics.org, 2002.
132. H. J. Jongsma and M. B. Rook, "Morphology and electrophysiology of cardiac gap junction channels," in *Cardiac Electrophysiology: From Cell to Bedside* (D. P. Zipes and J. Jalife, eds.), pp. 115–126, W.B. Saunders Company, 1995.
133. R. D. Veenstra, "Physiology of cardiac gap junction channels," in *Cardiac Electrophysiology: From Cell to Bedside* (D. P. Zipes and J. Jalife, eds.), pp. 62–69, W.B. Saunders Company, 1990.
134. S. Baigent, J. Stark, and A. Warner, "Modelling the effect of gap junction nonlinearities in systems of coupled cells," *J. Theor. Biol.*, vol. 186, pp. 223–239, 1997.
135. A. P. Henriquez, R. Vogel, B. J. Muller-Borer, C. S. Henriquez, R. Weingart, and W. E. Cascio, "Influence of dynamic gap junction resistance on impulse propagation in ventricular myocardium: A computer simulation study," *Biophys. J.*, vol. 81, pp. 2112–2121, Oct. 2001.
136. H. J. Jongsma and R. Wilders, "Gap junctions in cardiovascular disease," *Circ. Res.*, vol. 86, no. 12, pp. 1193–1197, 2000.
137. M. B. Wagner, T. Namiki, R. Wilders, R. W. Joyner, H. J. Jongsma, E. E. Verheijck, R. Kumar, D. A. Golod, W. N. Goolsby, and A. C. G. van Ginneken, "Electrical interactions among real cardiac cells and cell models in a linear strand," *Am. J. Physiol. (Heart. Circ. Physiol.)*, vol. 276, pp. H391–H400, 1999.
138. M. deCastro, E. Hofer, A. P. Munuzuri, Gómez-Gesteira, G. Plank, J. Schaffenhofer, Pérez-Munuzuri, and V. Pérez-Villar, "Comparison between the role of discontinuities in cardiac conduction and in a one-dimensional hardware model," *Phys. Rev. E*, vol. 59, no. 5, pp. 5962–5969, 1999.
139. V. A. Holden and V. A. Panfilov, "Modelling propagation in excitable media," in *Computational Biology of the Heart* (A. Panfilov and A. Holden, eds.), pp. 217–233, John Wiley & Son, 1997.
140. U. Hornung, ed., *Homogenization and Porous Media*, vol. 6 of *Interdisciplinary Applied Mathematics*. New York: Springer, 1997.
141. A. V. Holden, M. J. Poole, and J. V. Tucker, "An algorithmic model of the mammalian heart: Propagation, vulnerability, re-entry and fibrillation," *Int. J. Bifurc. Chaos*, vol. 6, no. 9, pp. 1623–1635, 1996.
142. E. Braunwald, "Valvular heart disease," in *Heart disease, a textbook of cardiovascular medicine* (E. Braunwald, ed.), pp. 1007–1077, W.B. Saunders Company, Philadelphia, 1992.
143. J. W. Kirklin and B. G. Barret-Boyes, "Anatomy, dimensions, and terminology," in *Cardiac Surgery*, pp. 3–60, Churchill Livingstone, New-York, 1990.
144. S. Y. Ho, Sanchez-Quintana, J. A. Cabrera, and R. H. Anderson, "Anatomy of the left atrium: Implications for radiofrequency ablation of atrial fibrillation," *J. Cardiovasc. Electrophysiol.*, vol. 10, pp. 1525–1533, 1999.
145. K. Shinagawa, H. Mitamura, A. Takeshita, T. Sato, H. Kanki, S. Takatsuki, and S. Ogawa, "Determination of refractory periods and conduction velocity during atrial fibrillation using atrial capture in dogs: Direct assessment of the wavelength and its modulation by a sodium channel blocker, pilsicainide," *J. Am. Coll. Cardiol.*, vol. 35, no. 1, pp. 246–253, 2000.
146. T. Koura, M. Hara, S. Takeuchi, K. Ota, Y. Okada, S. Miyoshi, A. Watanabe, K. Shiraiwa, H. Mitamura, I. Kodama, and S. Ogawa, "Anisotropic conduction properties in canine atria analyzed by high-resolution optical mapping. Preferential direction of conduction block changes from longitudinal to transverse with increasing age," *Circulation*, vol. 105, pp. 2092–2098, 2002.
147. R. J. Schilling, N. S. Peters, J. Goldberger, A. H. Kadish, and D. W. Davies, "Characterization of the anatomy and conduction velocities of the human right atrial flutter circuit determined by noncontact mapping," *J. Am. Coll. Cardiol.*, vol. 38, no. 2, pp. 385–393, 2001.

148. A. Hansson, M. Holm, P. Blomstrom, R. Johansson, C. Luhrs, J. Brandt, and S. B. Olsson, "Right atrial free wall conduction velocity and degree of anisotropy in patients with stable sinus rhythm studied during heart surgery," *Eur. Heart J.*, vol. 19, no. 2, pp. 293–300, 1998.
149. D. Wei, O. Okazaki, K. Harumi, E. Harasawa, and H. Hosaka, "Comparative simulation of excitation and body surface electrocardiogram with isotropic and anisotropic computer heart model," *IEEE Trans. Biomed. Eng.*, vol. 42, no. 4, pp. 343–357, 1995.
150. S. Y. Ho, J. A. Cabrera, V. H. Tram, J. Farré, R. H. Anderson, and D. Sánchez-Quintana, "Architecture of the pulmonary veins: Relevance to radiofrequency ablation," *Heart*, vol. 86, pp. 265–270, 2001.
151. S. Y. Ho, R. H. Anderson, and D. Sánchez-Quintana, "Atrial structure and fibres: Morphologic bases of atrial conduction," *Card. Res.*, vol. 54, pp. 325–336, 2002.
152. S. Y. Ho, "Understanding atrial anatomy: implications for atrial fibrillation ablation," *Cardiology International*, pp. 17–20, Special Issue, Summer 2002.
153. T. Oostendorp, A. van Oosterom, and G. Huiskamp, "Interpolation on a triangulated 3D surface," *J. Comp. Phys.*, vol. 80, pp. 331–343, 1989.
154. M. N. Obreztkhikova, E. A. Sosunov, E. P. Anyukhovskiy, N. S. Moise, R. B. Robinson, and M. R. Rosen, "Heterogeneous ventricular repolarization provides a substrate for arrhythmias in a German shepherd model of spontaneous arrhythmic death," *Circulation*, vol. 108, pp. 1389–1394, 2003.
155. R. Arora, S. Verheule, L. Scott, A. Navarrete, V. Katari, E. Wilson, D. Vaz, and J. E. Olgin, "Arrhythmogenic substrate of the pulmonary veins assessed by high-resolution optical mapping," *Circulation*, vol. 107, pp. 1816–1821, 2003.
156. W. S. Ellis, D. M. Auslander, and M. D. Lesh, "Fractionated electrograms from a computer model of heterogeneously uncoupled anisotropic ventricular myocardium," *Circulation*, vol. 92, pp. 1619–1626, 1995.
157. G. Bub, A. Shrier, and L. Glass, "Spiral wave generation in heterogeneous excitable media," *Phys. Rev. Lett.*, vol. 88, pp. 058101–1, Feb. 2002.
158. F. Xie, Z. Qu, J. N. Weiss, and A. Garfinkel, "Interactions between stable spiral waves with different frequencies in cardiac tissue," *Phys. Rev. E*, vol. 59, pp. 2203–2205, Feb. 1999.
159. H. Zhang, R. W. Winslow, and A. V. Holden, "Reentrant excitation initiated in models of inhomogeneous atrial tissue," *J. Theor. Biol.*, 1998.
160. M. Vinson, "Interaction of spiral waves in inhomogeneous excitable media," *Physica D*, vol. 116, pp. 313–324, 1998.
161. F. Xie, Z. Qu, J. N. Weiss, and A. Garfinkel, "Coexistence of multiple spiral waves with independent frequencies in a heterogeneous excitable medium," *Phys. Rev. E*, vol. 63, pp. 1–4, Feb. 2001.
162. S. Bouzat and H. S. Wio, "Pattern dynamics in inhomogeneous active media," *Physica A*, vol. 293, pp. 405–420, 2001.
163. I. M. Elfadel and R. W. Picard, "Gibbs random fields, cooccurrences, and texture modeling," *IEEE Trans. Pattern Anal. Machine Intell.*, vol. PAMI-16, pp. 24–37, Jan. 1994.
164. G. R. Cross and A. K. Jain, "Markov random field texture models," *IEEE Trans. Pattern Anal. Machine Intell.*, vol. PAMI-5, pp. 25–39, Jan. 1983.
165. H. Derin and H. Elliott, "Modeling and segmentation of noisy and textured images using Gibbs random fields," *IEEE Trans. Pattern Anal. Machine Intell.*, vol. PAMI-9, pp. 39–55, Jan. 1987.
166. S. Lakshmanan and H. Derin, "Simultaneous parameter estimation and segmentation of Gibbs fields using simulated annealing," *IEEE Trans. Pattern Anal. Machine Intell.*, vol. PAMI-11, pp. 799–813, Aug. 1989.
167. S. Geman and D. Geman, "Stochastic relaxation, Gibbs distributions, and the Bayesian restoration of images," *IEEE Trans. Pattern Anal. Machine Intell.*, vol. PAMI-6, no. 6, pp. 721–741, 1984.
168. A. J. Koch and H. Meinhardt, "Biological pattern formation: From basic mechanisms to complex structures," *Rev. Mod. Phys.*, no. 66, pp. 1481–1507, 1994.
169. S. D. Girouard, J. M. Pastore, K. R. Laurita, K. W. Gregory, and D. S. Rosenbaum, "Optical mapping in a new guinea pig model of ventricular tachycardia reveals mechanisms for multiple wavelengths in a single reentrant circuit," *Circulation*, vol. 93, pp. 603–613, 1996.
170. N. M. S. de Groot and M. A. Allesie, "Ten years of mapping of human atrial fibrillation," in *Computer Simulation and Experimental Assessment of Cardiac Electrophysiology* (N. Virag, O. Blanc, and L. Kappenberger, eds.), pp. 3–11, Futura Publishing, Armonk, New York, 2001.
171. S. B. Knisley and M. R. Neuman, "Simultaneous electrical and optical mapping in rabbit hearts," *Ann. Biomed. Eng.*, vol. 31, pp. 32–41, 2003.
172. A. N. Iyer and R. A. Gray, "An experimentalist's approach to accurate localization of phase singularities during reentry," *Ann. Biomed. Eng.*, vol. 29, pp. 47–59, 2001.
173. W. M. Smith, R. E. Ideker, and P. D. Wolf *et al.*, "Intraoperative cardiac mapping," in *Proc. 8th Ann. Conf. IEEE Eng. Med. Biol. Soc.*, pp. 1283–1285, 1986.
174. G. Bonneau, G. Tremblay, P. Savard, R. Guardo, A. R. LeBlanc, R. Cardinal, P. L. Page, and R. A. Nadeau, "An integrated system for intraoperative cardiac activation mapping," *IEEE Trans. Biomed. Eng.*, vol. 34, no. 6, pp. 415–423, 1987.
175. F. X. Witkowski and P. B. Corr, "An automated simultaneous transmural cardiac mapping system," *Am. J. Physiol.*, vol. 247, pp. H661–H668, 1984.
176. J. M. T. de Bakker, M. J. Janse, and F. J. L. van Capelle *et al.*, "An interactive computer system for guiding the surgical treatment of life-threatening ventricular tachycardias," *IEEE Trans. Biomed. Eng.*, vol. 31, pp. 362–368, 1984.
177. A. P. G. Hoeks, G. M. L. Schmitz, M. A. Allesie, H. Jas, S. J. Hollen, and R. S. Reneman, "Multi-channel storage and display system to record the electrical activity of the heart," *Med. & Biol. Eng. & Comput.*, vol. 26, no. 4, pp. 434–438, 1988.

178. P. R. Ershler, R. L. Lux, and B. W. Steadman *et al.*, "A 128 lead online intraoperative mapping system," in *Proc. 8th Ann. Conf. IEEE Eng. Med. Biol. Soc.*, pp. 1289–1291, 1986.
179. K. Laurita, C. W. Thpmas, and M. Kavuru *et al.*, "Data acquisition system for cardiac mapping," in *Proc. 10th Ann. Conf. IEEE Eng. Med. Biol. Soc.*, pp. 104–105, 1988.
180. E. Macchi, P. R. Ershler, and R. L. Lux *et al.*, "Online mapping of three-dimensional time varying bioelectric fields," in *Proc. 10th Ann. Conf. IEEE Eng. Med. Biol. Soc.*, pp. 1289–1291, 1988.
181. K. T. S. Konings, *Mapping of Electrically Induced Atrial Fibrillation in Humans*. PhD thesis, University of Maastricht, Maastricht, The Netherlands, 1999.
182. J. C. Strikwerda, *Finite Difference Schemes and Partial Differential Equations*. Wadsworth and Brooks/Cole Mathematics Series, 1989.
183. G. D. Smith, *Numerical Solution of Partial Differential Equations. Finite Difference Methods*. Oxford Univ. Press, third ed., 1985.
184. H. I. Saleheen, P. D. Claessen, and K. T. Ng, "Three-dimensional finite-difference bidomain modeling of homogeneous cardiac tissue on a data-parallel computer," *IEEE Trans. Biomed. Eng.*, vol. 44, pp. 200–204, Feb. 1997.
185. H. I. Saleheen and K. T. Ng, "New finite difference formulations for general inhomogeneous anisotropic bioelectric problems," *IEEE Trans. Biomed. Eng.*, vol. 44, pp. 800–809, Sept. 1997.
186. C. K. Yung, "Application of a stiff, operator splitting scheme to the computational modeling of electrical propagation in cardiac ventricles," Master's thesis, John Hopkins Univ., Baltimore, MD, 2000.
187. G. Huiskamp, "Simulation of depolarization in a membrane-equations-based model of the anisotropic ventricle," *IEEE Trans. Biomed. Eng.*, vol. 45, pp. 847–855, Sept. 1998.
188. H. K. Versteeg and W. Malalasekera, *An Introduction to Computational Fluid Dynamics. The Finite Volume Method*. Longman, 1995.
189. D. M. Harrild and C. S. Henriquez, "A finite volume model of cardiac propagation," *Ann. Biomed. Eng.*, vol. 28, pp. 315–334, 1997.
190. D. M. Harrild, R. C. Penland, and C. S. Henriquez, "A flexible method for simulating cardiac conduction in three-dimensional complex geometries," *J. Electrocardiol.*, vol. 33, pp. 241–251, 2000.
191. A. Quarteroni and A. Valli, *Numerical Approximation of Partial Differential Equations*, vol. 23 of *Springer Series in Computational Mathematics*. Springer, 1997.
192. I. Ohnaka and T. Fukusako, "Finite element method and a matrix method in transient heat-conduction problems," in *Sixth International Heart Transfer Conference, Toronto, Canada*, vol. 3, p. 251, 1988.
193. J. Rogers, M. Courtemanche, and A. McCulloch, "Finite elements methods for modelling impulse propagation in the heart," in *Computational Biology of the Heart* (A. Panfilov and A. Holden, eds.), pp. 217–233, John Wiley & Son, 1997.
194. P. J. Hunter, M. P. Nash, and G. B. Sands, "Computational electromechanics of the heart," in *Computational Biology of the Heart* (A. V. Panfilov and A. V. Holden, eds.), pp. 345–407, John Wiley & Sons, 1997.
195. J. Oniboni, "Modeling and numerical simulation of electrical wave propagation in heart," Tech. Rep. RR-4245 (in french), INRIA Sophia Antipolis, France, Aug. 2001.
196. W. Quan, S. J. Evans, and H. M. Hastings, "Efficient integration of a realistic two-dimensional cardiac tissue model by domain decomposition," *IEEE Trans. Biomed. Eng.*, vol. 45, pp. 372–385, Mar. 1998.
197. E. M. Cherry, H. S. Greenside, and C. S. Henriquez, "A space-time adaptive method for simulating complex cardiac dynamics," *Phys. Rev. Lett.*, vol. 84, pp. 1343–1348, 2000.
198. D. J. Rose, H. Shao, and C. S. Henriquez, "Discretization of anisotropic convection-diffusion equations, convective M-matrices and their iterative solution," *VLSI Design*, vol. 10, no. 4, pp. 485–529, 2000.
199. S. Zozor, O. Blanc, V. Jacquemet, N. Virag, J.-M. Vesin, E. Pruvot, L. Kappenberger, and C. S. Henriquez, "A numerical scheme for modeling wavefront propagation on a monolayer of arbitrary geometry," *IEEE Trans. Biomed. Eng.*, vol. 50, no. 4, pp. 412–420, 2003.
200. E. J. Vigmond, F. Aguel, and N. A. Trayanova, "Computational techniques for solving the bidomain equations in three dimension," *IEEE Trans. Biomed. Eng.*, vol. 49, no. 11, pp. 1260–1269, 2002.
201. L. J. Leon and F. A. Roberge, "Structural complexity effects on transverse propagation in a two-dimensional model of myocardium," *IEEE Trans. Biomed. Eng.*, vol. 38, pp. 997–1009, Oct. 1991.
202. E. J. Vigmond and L. J. Leon, "Computationally efficient model for simulating electrical activity in cardiac tissue with fiber rotation," *Ann. Biomed. Eng.*, vol. 27, pp. 160–170, 1999.
203. G. Teschl, *Ordinary Differential Equations and Dynamical Systems*. (Lecture Notes), Institut für Mathematik, Universität Wien, Wien, Austria, 2003.
204. G. H. Golub and C. F. Van Loan, *Matrix computations*. Johns Hopkins studies in the mathematical sciences, Johns Hopkins University Press, 1996.
205. H. Shao, *Numerical Analysis of Meshing and Discretization for Anisotropic Convection-Diffusion Equations with Applications*. PhD thesis, Department of Computer Science, Duke University, Durham, NC, 1999.
206. C. Giacovazzo, *Fundamentals of crystallography*. IUCr texts on crystallography, Oxford University Press, 2nd ed., 2002.
207. N. W. Ashcroft and N. D. Mermin, *Solid state physics*. Philadelphia Saunders College, 1976.
208. S. Mallat, *A wavelet tour of signal processing*. Academic Press, 1998.
209. D. Lanser and J. G. Verwer, "Analysis of operator splitting for advection-diffusion-reaction problems from air pollution modeling," Tech. Rep. MAS-R9805, Centrum voor Wiskunde en Informatica, P.O. Box 94079, 1090 GB Amsterdam, The Netherlands, May 1998.

210. O. M. Knio, H. N. Najm, and P. S. Wyckoff, "A semi-implicit numerical scheme for reacting flow. I. Stiff chemistry," *J. Comp. Phys.*, vol. 143, pp. 381–402, 1998.
211. O. M. Knio, H. N. Najm, and P. S. Wyckoff, "A semi-implicit numerical scheme for reacting flow. II. Stiff, operator-split formulation," *J. Comp. Phys.*, vol. 154, pp. 428–467, 1999.
212. X.-L. Luo, "Operator splitting algorithm for viscoelastic flow and numerical analysis for the flow around a sphere in a tube," *J. Non-Newtonian Fluid Mech.*, vol. 63, no. 2–3, pp. 121–140, 1996.
213. Z. Qu and A. Garfinkel, "An advanced algorithm for solving partial differential equation in cardiac conduction," *IEEE Trans. Biomed. Eng.*, vol. 46, pp. 1166–1168, Sept. 1999.
214. C. J. Budd and M. D. Piggott, "Geometric integration and its applications," short course at scicade'01, Dept. of Math. Sciences, Univ. of Bath, Claverton Down, Bath, BA2 7AY, UK, 2001.
215. E. Hairer, S. P. Nørrett, and G. Wanner, *Solving Ordinary Differential Equations. I. Nonstiff Problems*, vol. 8 of *Springer Series in Computational Mathematics*. Springer, 1993.
216. S. Strang, "On the construction and comparison of difference schemes," *SIAM J. Numer. Anal.*, pp. 506–517, 1968.
217. V. S. Varadarajan, *Lie Groups, Lie Algebra, and Their Representations*. Springer, 1984.
218. E. Hairer and G. Wanner, *Solving Ordinary Differential Equations. II. Stiff and Differential-Algebraic Problems*, vol. 14 of *Springer Series in Computational Mathematics*. Springer, 1996.
219. R. S. Varga, *Matrix Iterative Analysis*. Springer, 2nd ed., 2000.
220. M. V. Mascagni, "Numerical methods for neuronal modeling," in *Methods in Neuronal Modeling* (C. Koch and I. Segev, eds.), chap. 13, *Computational Neuroscience*, pp. 439–481, MIT Press, 1989.
221. D. W. Peaceman and H. H. Rachford Jr, "The numerical solution of parabolic and elliptic differential equations," *J. Soc. Industr. Appl. Math.*, vol. 3, pp. 28–41, 1955.
222. J. W. Cooley and F. A. Dodge Jr, "Digital computer solutions for excitation and propagation of the nerve impulse," *Biophys. J.*, vol. 6, pp. 583–599, 1966.
223. C. F. Gerald and P. O. Wheatley, *Applied Numerical Analysis*. Addison-Wesley Publishing Company, 1989.
224. W. H. Press, S. A. Teukolsky, W. T. Vetterling, and B. P. Flannery, *Numerical Recipes in C: The Art of Scientific Computing*. New York: Cambridge Univ. Press, second ed., 1994.
225. J. Sundnes, G. T. Lines, and A. Tveito, "Efficient solution of ordinary differential equations modeling electrical activity in cardiac cells," *Math. Biosci.*, vol. 172, pp. 55–72, 2001.
226. J. W. Moore and F. Ramon, "On numerical integration of the Hodgkin and Huxley equations for a membrane action potential," *J. Theor. Biol.*, vol. 45, pp. 249–273, 1974.
227. S. Rush and H. Larsen, "A practical algorithm for solving dynamic membrane equations," *IEEE Trans. Biomed. Eng.*, vol. 25, pp. 389–392, July 1978.
228. R. A. Gray, K. Takkellapati, and J. Jalife, "Dynamics of anatomical correlates of atrial flutter and fibrillation," in *Cardiac Electrophysiology: From Cell to Bedside* (D. P. Zipes and J. Jalife, eds.), pp. 356–363, W.B. Saunders Company, 2000.
229. M. A. Allesie and M. J. Janse, "Mechanisms of atrial arrhythmias," in *Electropharmacological Control of Atrial Arrhythmias* (B. Singh and H. J. J. Wellens, eds.), pp. 115–133, Futura Publishing Comp., 1994.
230. D. Porras, J. M. Rogers, W. M. Smith, and A. E. Pollard, "Distributed computing for membrane-based modeling of action potential propagation," *IEEE Trans. Biomed. Eng.*, vol. 47, pp. 1051–1057, Aug. 2000.
231. H. I. Saleheen, P. D. Claessen, and K. T. Ng, "Three-dimensional finite-difference bidomain modelling of homogeneous cardiac tissue on a data-parallel computer," *IEEE Trans. Biomed. Eng.*, vol. 44, no. 2, pp. 200–204, 1997.
232. J. L. Cox, T. E. Canavan, R. B. Schuessler, M. E. Cain, B. D. Lindsay, C. Stone, P. K. Smith, P. B. Corr, and J. P. Boineau, "The surgical treatment of atrial fibrillation. II. intraoperative electrophysiologic mapping and description of the electrophysiologic basis of atrial flutter and atrial fibrillation," *J. Thorac. Cardiovasc. Surg.*, vol. 101, pp. 406–426, 1991.
233. A. van Oosterom, "Forward and inverse problems in electrocardiography," in *Computational Biology of the Heart* (A. V. Panfilov and A. V. Holden, eds.), pp. 295–343, John Wiley & Sons, 1997.
234. M. S. Spach and J. M. Kootsey, "Relating the sodium current and conductance to the shape of transmembrane and extracellular potentials by simulation: Effect of propagation boundaries," *IEEE Trans. Biomed. Eng.*, vol. 32, pp. 743–755, Oct. 1985.
235. K. Gima and Y. Rudy, "Ionic current basis of electrocardiographic waveforms: A model study," *Circ. Res.*, vol. 90, pp. 889–896, 2002.
236. R. P. Feynman, R. B. Leighton, and M. Sands, *Electromagnetism and matter*, vol. 2 of *The Feynman lectures on physics*. Addison-Wesley, 1989.
237. R. M. Shaw and Y. Rudy, "Ionic mechanisms of propagation in cardiac tissue. Roles of the sodium and L-type calcium currents during reduced excitability and decreased gap junction coupling," *Circ. Res.*, vol. 81, pp. 727–741, 1997.
238. Y. Wang and Y. Rudy, "Action potential propagation in inhomogeneous cardiac tissue: Safety factor considerations and ionic mechanisms," *Am. J. Physiol. (Heart. Circ. Physiol.)*, vol. 278, pp. H1019–H1029, 2000.
239. M. Courtemanche, "Complex spiral wave dynamics in a spatially distributed ionic model of cardiac electrical activity," *Chaos*, vol. 6, no. 4, pp. 579–600, 1996.
240. J. Wu and D. P. Zipes, "Effects of spatial segmentation in the continuous model of excitation," *J. Cardiovasc. Electrophysiol.*, vol. 10, pp. 965–72, 1999.
241. M. A. Allesie, W. J. E. P. Lammers, F. I. M. Bonke, and J. Hollen, "Experimental evaluation of Moe's multiple wavelet hypothesis of atrial fibrillation," in *Cardiac Arrhythmias* (D. P. Zipes and J. Jalife, eds.), pp. 265–276, Grune & Stratton, 1985.

242. M. A. Allesie, P. L. Rensma, J. Brugada, J. L. R. M. Smeets, O. Penn, and C. J. H. Kirchhof, "Pathophysiology of atrial fibrillation," in *Cardiac Electrophysiology: From Cell to Bedside* (D. P. Zipes and J. Jalife, eds.), pp. 548–559, W.B. Saunders Company, 1990.
243. H. J. Sih, D. P. Zipes, E. J. Berbari, and J. E. Olgin, "A high-temporal resolution algorithm for quantifying organisation during atrial fibrillation," *IEEE Trans. Biomed. Eng.*, vol. 46, Apr. 1999.
244. M. Mansour, R. Mandapati, O. Berenfeld, J. Chen, F. H. Samie, and J. Jalife, "Left-to-right gradient of atrial frequencies during acute atrial fibrillation in the isolated sheep heart," *Circulation*, vol. 103, pp. 2631–2636, 2001.
245. M. A. Allesie, P. L. Rensma, and J. Brugada, "Pathophysiology of atrial fibrillation," in *Cardiac Electrophysiology: From Cell to Bedside* (D. P. Zipes and J. Jalife, eds.), pp. 548–559, W. B. Saunders, Philadelphia, 1995.
246. J. Chen, R. Mandapati, O. Berenfeld, A. C. S. nes, R. A. Gray, and J. Jalife, "Dynamics of wavelets and their role in atrial fibrillation in the isolated sheep heart," *Cardiovasc. Res.*, vol. 48, pp. 220–232, 2000.
247. D. Li, L. Zhang, J. Kneller, and S. Nattel, "Potential ionic mechanism for repolarization differences between canine right and left atrium," *Circ. Res.*, vol. 88, pp. 1168–1175, 2001.
248. E. Cherry, F. Fenton, H. M. Hastings, F. Xie, A. Garfinkel, J. N. Weiss, and S. J. Evans, "The role of decreased conduction velocity in the initiation and maintenance of atrial fibrillation in a computer model of human atria," *Pacing Clin. Electrophysiol.*, vol. 25, no. 4 (Part II, Abstract Suppl.), p. 538, 2002.
249. T. Ikeda, T. Uchida, D. Hough, J. J. Lee, M. C. Fishbein, W. J. Mandel, P. S. Chen, and H. S. Karagueuzian, "Mechanism of spontaneous termination of functional reentry in isolated canine right atrium: evidence for the presence of an excitable but nonexcited core," vol. 94, pp. 1962–1973, 1996.
250. J. Wang, L. Liu, J. Feng, and S. Nattel, "Regional and functional factors determining induction and maintenance of atrial fibrillation in dogs," *Am. J. Physiol.*, vol. 271, pp. H148–H158, 1996.
251. R. J. Schilling, A. H. Kadish, N. S. Peters, J. Goldberger, and D. Wyn Davies, "Endocardial mapping of atrial fibrillation in the human right atrium using a non-contact catheter," *Eur. Heart J.*, vol. 21, pp. 550–564, 2000.
252. R. B. Krol, S. Saksena, A. Prakash, I. Giorgberidze, and P. Mathew, "Prospective clinical evaluation of a programmed atrial stimulation protocol for induction of sustained atrial fibrillation and flutter," *J. Interv. Card. Electrophysiol.*, vol. 3, pp. 19–25, 1999.
253. A. S. Manolis, J. Cameron, T. Deering, E. H. Han, and N. A. Estes 3rd, "Sensitivity and specificity of programmed atrial stimulation for induction of supraventricular tachycardias," *Clin. Cardiol.*, vol. 11, pp. 307–310, 1988.
254. H. Akira, C.-M. Chang, S. Zhou, C.-C. Chou, J. Yi, Y. Miyauchi, Y. Okuyama, M. C. Fishbein, H. S. Karagueuzian, L. S. Chen, and P.-S. Chen, "Induction of atrial fibrillation and nerve sprouting by prolonged left atrial pacing in dogs," *Pacing Clin. Electrophysiol.*, vol. 26, pp. 2247–2252, 2003.
255. A. Elvan, K. Wylie, and D. P. Zipes, "Pacing-induced chronic atrial fibrillation impairs sinus node function in dogs. Electrophysiological remodeling," *Circulation*, vol. 94, pp. 2953–2960, 1996.
256. B. J. Scherlag, W. S. Yamanashi, P. Schauerte, M. Scherlag, Y.-X. Sun, Y. Hou, W. M. Jackman, and R. Lazzara, "Endovascular stimulation within the left pulmonary artery to induce slowing of heart rate and paroxysmal atrial fibrillation," *Cardiovasc. Res.*, vol. 54, pp. 470–475, 2002.
257. P. S. Fischbach, T. D. Barrett, R. Goyal, B. C. Tran, Z. A. Syed, J. K. Hennan, and B. R. Lucchesi, "Conversion of atrial fibrillation by the experimental antiarrhythmic drug tedisamil in two canine models," *J. Cardiovasc. Electrophysiol.*, vol. 12, pp. 1138–1144, 2001.
258. S. P. Thomas and D. L. Ross, "Induction of atrial fibrillation and flutter in dogs using methacholine," *J. Interv. Card. Electrophysiol.*, vol. 3, pp. 301–305, 1999.
259. M. Brignole, C. Menozzi, B. Sartore, M. Barra, and I. Monducci, "The use of atrial pacing to induce atrial fibrillation and flutter," *Int. J. Cardiol.*, vol. 12, pp. 45–54, 1986.
260. M. A. Bray and J. P. Wikswo, "Use of topological charge to determine filament location and dynamics in a numerical model of scroll wave activity," *IEEE Trans. Biomed. Eng.*, vol. 49, no. 10, pp. 1086–1093, 2002.
261. A. Vinet, D. R. Chialvo, D. C. Michaels, and J. Jalife, "Nonlinear dynamics of rate-dependent activation in models of single cardiac cells," *Circ. Res.*, vol. 67, no. 6, pp. 1510–1524, 1990.
262. H. S. Karagueuzian and B. Y. Kogan, "Action potential duration restitution dynamics and its relation to spiral wave formation: an experimental and computer simulation study," in *Cardiac Mapping* (M. Shenasa, M. Borggreffe, and G. Breithardt, eds.), pp. 627–645, Futura Publishing, Mt. Kisco, New York, 1993.
263. R. F. Gilmour, M. A. Watanabe, and N. F. Otani, "Restitution properties and dynamics of reentry," in *Cardiac Electrophysiology: From Cell to Bedside* (D. P. Zipes and J. Jalife, eds.), pp. 378–385, W. B. Saunders, Philadelphia, 2000.
264. T. Ohara, K. Ohara, J.-M. Cao, M.-H. Lee, M. C. Fishbein, W. J. Mandel, P.-S. Chen, and H. S. Karagueuzian, "Increased wave break during ventricular fibrillation in the epicardial border zone of hearts with healed myocardial infarction," *Circulation*, vol. 103, pp. 1465–1472, 2001.
265. S. Nattel and D. Li, "Ionic remodeling in the heart: Pathophysiological significance and new therapeutic opportunities for atrial fibrillation," *Circ. Res.*, vol. 87, pp. 440–447, 2000.
266. N. El-Sherif, "Reentrant mechanisms in ventricular arrhythmias," in *Cardiac Electrophysiology: From Cell to Bedside, 2nd edition* (D. P. Zipes and J. Jalife, eds.), pp. 567–582, W.B. Saunders Company, 1995.
267. J. J. Fox, R. F. Gilmour, and E. Bodenschatz, "Conduction block in one-dimensional heart fibers," *Phys. Rev. Lett.*, vol. 89, no. 19, p. 198101, 2002.

268. J. J. Fox, M. L. Riccio, F. Hua, E. Bodenschatz, and R. F. Gilmour Jr, "Spatiotemporal transition to conduction block in canine ventricle," *Circ. Res.*, vol. 90, pp. 289–296, 2002.
269. C. Cabo, A. M. Pertsov, J. M. Davidenko, W. T. Baxter, R. A. Gray, and J. Jalife, "Vortex shedding as a precursor of turbulent electrical activity in cardiac muscle," *Biophys. J.*, vol. 70, pp. 1105–1111, 1996.
270. P. M. van Dam and A. van Oosterom, "Atrial excitation assuming uniform propagation," *J. Cardiovasc. Electrophysiol.*, vol. 14, pp. S166–S171, 2003.
271. M. A. Watanabe and M. L. Koller, "Mathematical analysis of dynamics of cardiac memory and accommodation: Theory and experiment," *Am. J. Physiol. (Heart. Circ. Physiol.)*, vol. 282, pp. H1534–H1547, 2002.
272. A. C. Skanes, R. Mandapati, O. Berenfeld, J. M. Davidenko, and J. Jalife, "Spatiotemporal periodicity during atrial fibrillation in the isolated sheep heart," *Circulation*, vol. 98, pp. 1236–1248, 1998.
273. R. Mandapati, A. Skanes, J. Chen, O. Berenfeld, and J. Jalife, "Stable micro-reentrant sources as a mechanism of atrial fibrillation in the isolated sheep heart," *Circulation*, vol. 101, pp. 194–199, 2000.
274. L. Liu and S. Nattel, "Differing sympathetic and vagal effects on atrial fibrillation in dogs: role of refractoriness heterogeneity," *Am. J. Physiol.*, vol. 273, no. 2 Pt 2, pp. H805–H816, 1997.
275. L. J. Leon, F. A. Roberge, and A. Vinet, "Simulation of two-dimensional anisotropic cardiac reentry: effects of the wavelength on the reentry characteristics," *Ann. Biomed. Eng.*, vol. 22, pp. 592–609, 1994.
276. G. K. Moe, "On the multiple wavelet hypothesis of atrial fibrillation," *Arch. Int. Pharmacodyn. Ther.*, vol. 140, pp. 183–188, 1962.
277. G. K. Moe, W. C. Rheinboldt, and J. A. Abildskov, "A computer model of atrial fibrillation," *Am. Heart J.*, vol. 67, pp. 200–220, 1964.
278. M. A. Allesie, K. Konings, C. J. H. J. Kirchhof, and M. Wijffels, "Electrophysiologic mechanisms of perpetuation of atrial fibrillation," *Am. J. Cardiol.*, vol. 77, pp. 10A–23A, 1996.
279. K. T. S. Konings, C. J. H. J. Kirchhof, J. R. L. M. Smeets, H. J. J. Wellens, O. C. Penn, and M. A. Allesie, "High density mapping of electrically induced atrial fibrillation in man," *Circulation*, vol. 89, pp. 1665–1680, 1994.
280. Z. Wang, P. Pagé, and S. Nattel, "Mechanism of flecainide's antiarrhythmic action in experimental atrial fibrillation," *Circ. Res.*, vol. 71, pp. 271–287, 1992.
281. J. Wang, G. W. Bourne, Z. Wang, C. Villemaire, M. Talajic, and S. Nattel, "Comparative mechanism of antiarrhythmic drug action in experimental atrial fibrillation. Importance of use dependent effects on refractoriness," *Circulation*, vol. 88, pp. 1030–1044, 1993.
282. T. Lewis, *The Mechanism and Graphic Registration of the Heart Beat*. Show & Sons, London, 3rd ed., 1925.
283. J. Jalife, "Rotors and spiral waves in atrial fibrillation," *J. Cardiovasc. Electrophysiol.*, vol. 14, pp. 776–780, 2003.
284. M. Haissaguerre, P. Jais, D. C. Shah, A. Takahashi, M. Hocini, G. Quiniou, S. Garrigue, A. Le Mouroux, P. Le Metayer, and J. Clementy, "Spontaneous initiation of atrial fibrillation by ectopic beats originating in the pulmonary veins," *N. Eng. J. Med.*, vol. 339, pp. 659–666, 1998.
285. J. Jalife, O. Berenfeld, A. Skanes, and R. Mandapati, "Mechanisms of atrial fibrillation: Mother rotors or multiple daughter wavelets, of both?," *J. Cardiovasc. Electrophysiol.*, vol. 9, pp. S2–12, 1998.
286. M. C. E. F. Wijffels, C. J. H. J. Kirchhof, R. Dorland, and M. A. Allesie, "Atrial fibrillation begets atrial fibrillation: A study in awake chronically instrumented goats," *Circulation*, vol. 92, pp. 1954–1968, 1995.
287. V. Ducry, "Localization and tracking of phase singularities in a computer model of human atria," Master's thesis, Signal Processing Institute, EPFL, Lausanne, Switzerland, 2004.
288. P. L. Rensma, M. A. Allesie, W. J. Lammers, F. I. Bonke, and M. J. Schalij, "Length of excitation wave and susceptibility to reentrant atrial arrhythmias in normal conscious dogs," *Circ. Res.*, vol. 62, no. 2, pp. 395–410, 1988.
289. Y. Asano, J. Saito, K. Matsumoto, K. Kaneko, T. Yamamoto, and M. Uchida, "On the mechanism of termination and perpetuation of atrial fibrillation," *Am. J. Cardiol.*, vol. 69, no. 12, pp. 1033–1038, 1992.
290. G. W. Botteron and J. M. Smith, "Quantitative assessment of the spatial organization of atrial fibrillation in the intact human heart," *Circulation*, vol. 93, pp. 513–518, 1996.
291. J. Sekiya, Y. Ohnishi, T. Inoue, and M. Yokoyama, "Monophasic action potentials of the right atrium in patients with paroxysmal atrial fibrillation," *Jpn Circ. J.*, vol. 65, pp. 893–896, 2001.
292. O. Berenfeld, R. Mandapati, S. Dixit, A. C. Skanes, J. Chen, M. Mansour, and J. Jalife, "Spatially distributed dominant excitation frequencies reveal hidden organization in atrial fibrillation in the Langendorff-perfused sheep heart," *J. Cardiovasc. Electrophysiol.*, vol. 11, pp. 869–879, 2000.
293. V. Barbaro, P. Bartolini, G. Calcagnini, and F. Censi, "Extraction of physiological and clinical information from intra-atrial electrograms during atrial fibrillation: Review of methods," *Ann. Ist. Super. Sanità*, vol. 37, no. 3, pp. 319–324, 2001.
294. T. H. Everett, J. R. Moorman, L.-C. Kok, J. G. Akar, and D. E. Haines, "Assessment of global atrial fibrillation organization to optimize timing of atrial defibrillation," *Circulation*, vol. 103, pp. 2857–2861, 2001.
295. T. H. Everett IV, J. G. Akar, L.-C. Kok, J. R. Moorman, and D. E. Haines, "Use of global atrial fibrillation organization to optimize the success of burst pace termination," *J. Am. Coll. Cardiol.*, vol. 40, no. 10, pp. 1831–1840, 2002.
296. S. A. C. Schuckers, "Approximate entropy as a measure of morphologic variability for ventricular tachycardia and fibrillation," *Comp. in Cardiol.*, vol. 25, pp. 265–268, 1998.
297. L. G. Gamero, A. Plastino, and M. E. Torres, "Wavelet analysis and nonlinear dynamics in a nonextensive setting," *Physica A*, vol. 246, pp. 487–509, 1997.

298. M. T. Martin, J. Perez, and A. Plastino, "Fisher information and nonlinear dynamics," *Physica A*, vol. 291, pp. 523–532, 2001.
299. M. T. Martin, A. R. Plastino, and A. Plastino, "Tsallis-like information measures and the analysis of complex signals," *Physica A*, vol. 275, pp. 262–271, 2000.
300. M. E. Torres and L. G. Gamero, "Relative complexity changes in time series using information measures," *Physica A*, vol. 286, pp. 457–473, 2000.
301. X.-S. Zhang, Y.-S. Zhu, N. V. Thakor, and Z.-Z. Wang, "Detecting ventricular tachycardia and fibrillation by complexity measure," *IEEE Trans. Biomed. Eng.*, vol. 46, pp. 548–555, May 1999.
302. F. Kaspar and H. G. Schuster, "Easily calculable measure for the complexity of spatiotemporal patterns," *Phys. Rev. A*, vol. 36, pp. 842–848, July 1987.
303. B. P. T. Hoekstra, C. G. H. Diks, M. A. Allesie, and J. DeGoede, "Nonlinear analysis of the pharmacological conversion of sustained atrial fibrillation in conscious goats by the class Ic drug cibenzoline," *Chaos*, vol. 7, no. 3, pp. 430–446, 1997.
304. A. Casaleggio and G. Bortolan, "Automatic estimation of the correlation dimension for the analysis of electrocardiograms," *Biol. Cybern.*, vol. 81, pp. 279–290, 1999.
305. L. T. Mainardi, G. Calcagnini, A. Porta, F. Censi, P. Bartolini, and S. Cerutti, "Linear and non-linear parameters for the classification of atrial fibrillation episodes from intra-atrial signals," *Comp. in Cardiol.*, vol. 26, pp. 691–694, 1999.
306. A. Porta, G. Baselli, F. Lombardi, N. Montano, A. Malliani, and S. Cerutti, "Conditional entropy approach for the evaluation of the coupling strength," *Biol. Cybern.*, vol. 81, pp. 119–129, 1999.
307. F. Censi, V. Barbano, P. Bartolini, G. Calcagnini, A. Michelucci, and S. Cerutti, "Non-linear coupling of atrial activation processes during atrial fibrillation in humans," *Biol. Cybern.*, vol. 85, pp. 195–201, 2001.
308. B. P. T. Hoekstra, C. G. H. Diks, M. A. Allesie, and J. DeGoede, "Nonlinear analysis of epicardial atrial electrograms of electrically induced atrial fibrillation in man," *J. Cardiovasc. Electrophysiol.*, vol. 6, no. 6, pp. 419–440, 1995.
309. C. D. Wagner and P. B. Persson, "Chaos in the cardiovascular system: an update," *Cardiovasc. Res.*, vol. 40, pp. 257–264, 1998.
310. H. F. Pitschner, A. Berkovic, S. Grumbrecht, and J. Neuzner, "Multielectrode basket catheter mapping for human atrial fibrillation," *J. Cardiovasc. Electrophysiol.*, vol. 9, pp. S48–56, 1998.
311. L. Faes, G. Nollo, R. Antolini, F. Gaita, and F. Ravelli, "A method for quantifying atrial fibrillation organization based on wave-morphology similarity," *IEEE Trans. Biomed. Eng.*, vol. 49, no. 12, pp. 1504–1513, 2002.
312. S. Guan, C.-H. Lai, and G. W. Wei, "A wavelet method for the characterization of spatiotemporal patterns," *Physica D*, vol. 163, pp. 49–79, 2002.
313. E. Stone and A. Cutler, "Introduction to archetypal analysis of spatio-temporal dynamics," *Physica D*, vol. 96, pp. 110–131, 1996.
314. A. Cutler and L. Breiman, "Archetypal analysis," *Technometrics*, vol. 36, no. 4, pp. 338–374, 1994.
315. J. M. Rogers, P. V. Bayly, R. E. Ideker, and W. M. Smith, "Quantitative techniques for analysing high-resolution cardiac-mapping data," *IEEE Eng. Med. Bio.*, pp. 62–72, Jan./Feb. 1998.
316. G. W. Botteron and J. M. Smith, "A technique for measurement of the extent of spatial organization of atrial activation during atrial fibrillation in the intact human heart," *IEEE Trans. Biomed. Eng.*, vol. 42, pp. 579–586, June 1995.
317. H. J. Sih, A. V. Sahakian, C. E. Arentzen, and S. Swiryn, "A frequency domain analysis of spatial organization of epicardial maps," *IEEE Trans. Biomed. Eng.*, vol. 42, pp. 718–727, July 1995.
318. B.-R. Choi, T. Liu, M. Lavasani, and G. Salama, "Fiber orientation and cell-cell coupling influence ventricular fibrillation dynamics," *J. Cardiovasc. Electrophysiol.*, vol. 14, pp. 851–860, 2003.
319. N. H. March and M. P. Tosi, *Introduction to Liquid State Physics*. World Scientific, New Jersey, 2002.
320. N. Goldenfeld, *Lectures on Phase Transitions and the Renormalization Group*, vol. 85 of *Frontiers in physics*. Addison-Wesley, 1992.
321. P. V. Bayly, E. E. Johnson, P. D. Wolf, W. M. Smith, and R. E. Ideker, "Measuring changing spatial complexity in ventricular fibrillation using the Karhunen–Loève decomposition of 506-channel epicardial data," *Comp. in Cardiol.*, pp. 53–56, 1993.
322. P. V. Bayly, E. E. Johnson, P. D. Wolf, W. M. Smith, and R. E. Ideker, "Predicting patterns of epicardial potentials during ventricular fibrillation," *IEEE Trans. Biomed. Eng.*, vol. 42, pp. 898–907, Sept. 1995.
323. J. M. Smith and G. W. Botteron, "Estimation of the correlation length of activation processes during atrial fibrillation," *Comp. in Cardiol.*, pp. 41–44, 1993.
324. H. J. Sih, E. J. Berbari, D. P. Zipes, and J. E. Olgin, "A new algorithm for measuring atrial fibrillation organization," *Comp. in Cardiol.*, vol. 25, pp. 273–276, 1998.
325. M. Kirchner, L. Faes, F. Olivetti, R. Riccardi, M. Scaglione, F. Gaita, and R. Antolini, "Local electrical characterization of human atrial fibrillation," *Comp. in Cardiol.*, 2000.
326. L. Faes, G. Nollo, M. Kirchner, E. Olivetti, F. Gaita, R. Riccardi, and R. Antolini, "Principal component analysis and cluster analysis for measuring the local organisation of human atrial fibrillation," *Med. Biol. Eng. Comput.*, vol. 39, no. 6, pp. 656–663, 2001.
327. J. García, P. Lander, L. Sörnmo, S. Olmos, G. Wagner, and P. Laguna, "Comparative study of local and Karhunen–Loève-based ST-T indexes in recordings from human subjects with induced myocardial ischemia," *Comp. Biomed. Res.*, vol. 31, pp. 271–292, 1998.
328. M. Meixner, S. M. Zoldi, S. Bose, and E. Schöll, "Karhunen–Loève local characterization of spatiotemporal chaos in a reaction-diffusion system," *Phys. Rev. E*, vol. 61, pp. 1382–1385, Feb. 2000.
329. S. M. Zoldi and H. S. Greenside, "Karhunen–Loève decomposition of extensive chaos," *Phys. Rev. Lett.*, vol. 78, p. 16871690, Mar. 1997.

330. M. A. Allesie, F. I. M. Bonke, and F. J. G. Shopman, "Circus movement in rabbit atrial muscle as a mechanism of tachycardia. III. The leading circle concept: a new model of circus movement in cardiac tissue without the involvement of an anatomic obstacle," *Circ. Res.*, vol. 41, pp. 9–18, 1977.
331. N. Maglaveras, J. M. De Bakker, F. J. Van Capelle, C. Pappas, and M. J. Janse, "Activation delay in healed myocardial infarction: A comparison between model and experiment," *Am. J. Physiol.*, vol. 269, no. 4 Pt 2, pp. H1441–H1449, 1995.
332. M. S. Spach, W. T. Miller 3rd, E. Miller-Jones, R. B. Warren, and R. C. Barr, "Extracellular potentials related to intracellular action potentials during impulse conduction in anisotropic canine cardiac muscle," *Circ. Res.*, vol. 45, pp. 188–204, 1979.
333. M. S. Spach and P. C. Dolber, "Relating extracellular potentials and their derivatives to anisotropic propagation at a macroscopic level in human cardiac muscle. evidence for electrical uncoupling of side-by-side fiber connections with increasing age," *Circ. Res.*, vol. 58, pp. 356–371, 1986.
334. P. Colli Franzone, L. Guerri, C. Viganotti, E. Macchi, S. Baruffi, S. Spaggiari, and B. Taccardi, "Potential fields generated by oblique dipole layers modeling excitation wavefronts in the anisotropic myocardium. comparison with potential fields elicited by paced dog hearts in a volume conductor," *Circ. Res.*, vol. 51, pp. 330–346, 1982.
335. P. Colli Franzone, L. Guerri, M. Pennacchio, and B. Taccardi, "Anisotropic mechanisms for multiphasic unipolar electrograms: Simulation studies and experimental recordings," *Ann. Biomed. Eng.*, vol. 28, pp. 1326–1342, 2000.
336. B.-U. Köhler, C. Hennig, and R. Orglmeister, "The principles of software QRS detection," *IEEE Eng. Med. Bio.*, pp. 42–57, Jan./Feb. 2002.
337. D. S. Benitez, P. A. Gaydecki, A. Zaidi, and A. P. Fitzpatrick, "A new QRS detection algorithm based on the hilbert transform," *Comp. in Cardiol.*, vol. 27, pp. 379–382, 2000.
338. G. Thonet, *New Aspects of Time-Frequency Analysis for Biomedical Signal Processing*. PhD thesis, Swiss Federal Institute of Technology, Lausanne (EPFL), Thesis no. 1913, 1999.
339. B. Boashash, "Estimating and interpreting the instantaneous frequency of a signal," *Proc. IEEE*, vol. 80, no. 4, pp. 520–568, 1992.
340. A. Pikovsky, M. Rosenblum, and J. Kurths, *Synchronization, a universal concept in nonlinear sciences*. Cambridge Univ. Press, 2001.
341. S. K. Mitra, *McGraw-Hill International Editions*. Digital Signal Processing: a Computer-based Approach, 1998.
342. M. H. Hayes, *Statistical Digital Processing*. McGraw-Hill International Editions, Singapore, 1996.
343. F. G. Evans, J. M. Rogers, W. M. Smith, and R. E. Ideker, "Automatic detection of conduction block based on time-frequency analysis of unipolar electrograms," *IEEE Trans. Biomed. Eng.*, vol. 46, no. 9, pp. 1090–1097, 1999.
344. J. Villacastin, J. Almendral, A. Arenal, N. P. Castellano, S. Gonzalez, M. Ortiz, García, B. Vallbona, J. Moreno, J. F. Portales, and E. G. Torrecilla, "Usefulness of unipolar electrograms to detect isthmus block after radiofrequency ablation of typical atrial flutter," *Circulation*, vol. 102, pp. 3080–3085, 2000.
345. F. J. Chorro, A. Ferrero, J. Canoves, L. Mainar, J. C. Porres, A. Navarro, J. Sanchis, J. Millet, V. Bodi, V. Lopez-Merino, and L. Such, "Significance of the morphological patterns of electrograms recorded during ventricular fibrillation," *Pacing Clin. Electrophysiol.*, vol. 26, pp. 1262–1269, 2003.
346. G. Fenelon and P. Brugada, "Unipolar waveforms and monophasic action potentials in the characterization of slow conduction in human atrial flutter," *Pacing Clin. Electrophysiol.*, vol. 21, pp. 2580–2587, 1998.
347. J. M. T. de Bakker, R. N. W. Hauer, and T. A. Simmers, "Activation mapping: Unipolar versus bipolar recording," in *Cardiac Electrophysiology: From Cell to Bedside, 2nd edition* (D. P. Zipes and J. Jalife, eds.), pp. 849–858, W.B. Saunders Company, 1994.
348. T. A. Simmers, "Unipolar mapping of the pulmonary veins," *J. Cardiovasc. Electrophysiol.*, vol. 13, pp. 857–858, 2002.
349. P. Colli Franzone, L. Guerri, M. Pennacchio, and B. Taccardi, "Spreading of excitation in 3-D models of the anisotropic cardiac tissue. I. validation of the eikonal model," *Math. Biosci.*, vol. 113, pp. 145–209, 1993.
350. P. Colli Franzone, L. Guerri, M. Pennacchio, and B. Taccardi, "Spread of excitation in 3-D models of the anisotropic cardiac tissue. II. Effects of fiber architecture and ventricular geometry," *Math. Biosci.*, vol. 147, pp. 131–171, 1998.
351. P. Colli Franzone, L. Guerri, M. Pennacchio, and B. Taccardi, "Spread of excitation in 3-D models of the anisotropic cardiac tissue. III. Effects of ventricular geometry and fiber structure on the potential distribution," *Math. Biosci.*, vol. 151, pp. 51–98, 1998.
352. P. Colli-Franzone, "Ventricular excitation: wavefronts, electrograms and potential patterns," in *Computer Simulation and Experimental Assessment of Cardiac Electrophysiology* (N. Virag, O. Blanc, and L. Kappenberger, eds.), pp. 55–61, Futura Publishing, Armonk, New York, 2001.
353. L. D. Landau and E. M. Lifshitz, *The classical theory of fields*, vol. 2 of *Course of theoretical physics*. Pergamon Press, 1975.
354. A. Messiah, *Quantum mechanics*. Series in physics, North-Holland, 1976.
355. P. Colli Franzone, L. Guerri, and S. Tentoni, "Mathematical modeling of the excitation process in myocardial tissue: influence of fiber rotation on wavefront propagation and potential field," *Math. Biosci.*, vol. 101, no. 2, pp. 155–235, 1990.
356. E. Kreyszig, *Advanced engineering mathematics*. Wiley, 8th ed., 1999.
357. J. Beaumont, N. Davidenko, J. M. Davidenko, and J. Jalife, "Spiral waves in two-dimensional models of ventricular muscle: Formation of a stationary core," *Biophys. J.*, vol. 75, pp. 1–14, July 1998.
358. R. Houben, "Activation wavefront curvature," tech. rep., Bakken Research Institute, Maastricht, The Netherlands, 2002.

359. P. V. Bayly, B. H. KenKnight, J. M. Rogers, R. E. Hillsley, R. E. Ideker, and W. M. Smith, "Estimation of conduction velocity vector fields from epicardial mapping data," *IEEE Trans. Biomed. Eng.*, vol. 45, no. 5, pp. 563–571, 1998.
360. A. R. Barnette, P. V. Bayly, S. Zhang, G. O. Walcott, R. E. Ideker, and W. M. Smith, "Estimation of 3-D conduction velocity vector fields from cardiac mapping data," *IEEE Biomed. Eng.*, vol. 47, no. 8, pp. 1027–1035, 2000.
361. V. G. Fast and A. G. Kléber, "Block of impulse propagation at an abrupt tissue expansion. Evaluation of the critical strand diameter in 2- and 3-dimensional computer models," *Cardiovasc. Res.*, vol. 30, pp. 449–459, 1995.
362. B. Olshansky, K. Okumura, R. W. Henthorn, and A. L. Waldo, "Characterization of double potentials in human atrial flutter studies during transient entrainment," *J. Am. Coll. Cardiol.*, vol. 15, no. 4, pp. 833–841, 1990.
363. J. M. Morgan, G. Haywood, A. Schirdewan, P. Brugada, P. Geelen, U. Meyerfeldt, P. Roberts, and C. Gibbson, "Double potentials define linear lesion conduction block using a novel mapping/linear lesion ablation catheter," *J. Cardiovasc. Electrophysiol.*, vol. 14, pp. 236–242, 2003.
364. M. Andronache, C. de Chillou, H. Miljoen, I. Magnin-Poull, M. Messier, P. Dotto, D. Beurrier, T. Doan, P. Houriez, A. Bineau-Jorisse, B. Thiel, B. Brembilla-Perrot, J.-L. Massing, N. Sadoul, and E. Aliot, "Correlation between electrogram morphology and standard criteria to validate bidirectional cavotricuspid block in common atrial flutter ablation," *Europace*, vol. 5, pp. 335–341, 2003.
365. B. Olshansky, D. Moreira, and A. L. Waldo, "Characterization of double potentials during ventricular tachycardia. Studies during transient entrainment," *Circulation*, vol. 87, no. 2, pp. 373–381, 1993.
366. S. M. Blanchard, R. J. Damiano Jr, T. Asano, W. M. Smith, R. E. Ideker, and J. E. Lowe, "The effects of distant cardiac electrical events on local activation in unipolar epicardial electrograms," *IEEE Trans. Biomed. Eng.*, vol. 34, pp. 539–546, 1987.
367. R. J. Damiano Jr, S. M. Blanchard, T. Asano, J. L. Cox, and J. E. Lowe, "Effects of distant potentials on unipolar electrograms in an animal model utilizing the right ventricular isolation procedure," *J. Am. Coll. Cardiol.*, vol. 11, no. 5, pp. 1100–1109, 1988.
368. D. B. Geselowitz, "The zero of potential," *IEEE Eng. Med. Bio.*, pp. 128–132, Jan./Feb. 1998.
369. W. S. Ellis, D. M. Auslander, and M. D. Lesh, "Effects of coupling heterogeneity on fractionated electrograms in a model of nonuniformly anisotropic ventricular myocardium," vol. 27 (Suppl.), pp. 171–178, 1994.
370. P. I. Gardner, P. C. Ursell, J. J. Fenoglio, and A. L. Wit, "Electrophysiologic and anatomic basis for fractionated electrograms recorded from healed myocardial infarcts," *Circulation*, vol. 72, pp. 596–611, 1985.
371. M. A. McGuire, J. M. de Bakker, J. T. Vermeulen, T. Opthof, A. E. Becker, and M. J. Jansen, "Origin and significance of double potentials near the atrioventricular node. correlation of extracellular potentials, intracellular potentials, and histology," *Circulation*, vol. 89, pp. 2351–2360, 1994.
372. A. Kadish and J. Spear, "Identification of conduction block in cardiac muscle: in vitro observations in canine epicardium," *Cardiovasc. Res.*, vol. 28, no. 2, pp. 259–269, 1994.
373. J. M. de Bakker, F. J. van Capelle, M. J. Janse, S. Tasseroni, J. T. Vermeulen, N. de Jonge, and J. R. Lahpor, "Fractionated electrograms in dilated cardiomyopathy: origin and relation to abnormal conduction," *J. Am. Coll. Cardiol.*, vol. 27, pp. 1071–1078, 1996.
374. I. Chouvarda, N. Maglaveras, J. M. de Bakker, F. J. van Capelle, and C. Pappas, "Deconvolution and wavelet-based methods for membrane current estimation from simulated fractionated electrograms," *IEEE Trans. Biomed. Eng.*, vol. 48, pp. 294–301, 2001.

Curriculum Vitae

Vincent JACQUEMET
Rue du golf 76
CH-1971 Grimisuat / VS
Switzerland

vincent.jacquemet@epfl.ch
lausanneheart.epfl.ch
born on April 8, 1976
Swiss nationality, single

Research interests:

Complex dynamical systems, Biophysical modeling,
Numerical simulation and Signal processing.

Education —>>

- | | |
|-----------|--|
| 2000-2004 | Swiss Federal Institute of Technology, Lausanne (EPFL)
Ph.D. student in biomedical engineering at Signal Processing Institute in collaboration with Division of Cardiology, Vaud University Hospital (CHUV) under the direction of Profs. M. Kunt and L. Kappenberger. |
| 1995-2000 | Swiss Federal Institute of Technology, Lausanne (EPFL)
Master of Science in physics — theoretical physics
▷ <i>Alumni association's award: second best grade of the school</i> |
| 1990-1995 | Lycée-collège des Creusets, Sion
Federal Diploma of Maturity — scientific section |

Research Experience —>>

- | | |
|-----------|--|
| 2000-2004 | Research assistant at Signal Processing Institute, EPFL
▷ <i>Computer simulation of the electrical activity of the heart.</i> |
| 2000 | Master thesis at Institute of Theoretical Physics, EPFL
▷ <i>Study of a statistical model of mass aggregation.</i> |
| 1998 | Internship (1 month) at Station aérologique , Payerne (MeteoSwiss)
▷ <i>Development of visualization and statistical tools for atmospheric data.</i> |
| 1998-1999 | Student projects at EPFL:
▷ Study of irreversible statistical models (spin dynamics, sandpile models, turbulence models).
▷ Numerical simulation of a chip prehensor based on aerodynamic effects.
▷ Analysis of shock waves generated by high speed trains entering a tunnel. |

Teaching Experience —>>>

2000-2003	Teaching assistant: <i>exercises and laboratory sessions (signal processing, biomedical signal processing)</i> Supervision of student projects.
1998-1999	Teaching assistant (while student): <i>Numerical analysis</i>

Communication Skills —>>>

French	native language
English	fluent
German	basic knowledge

Computer Skills —>>>

Environment	Linux/Unix, Windows
Programming	C/C++, Matlab: <i>wide experience</i> Unix shell, Fortran, Pascal: <i>good knowledge</i> OpenGL (visualization), CVS, Perl: <i>basic notions</i>

Publications

Journal Papers

- L. Frachebourg, V. Jacquemet, and P.A. Martin, “Inhomogeneous Ballistic Aggregation,” *J. Stat. Phys.*, vol. 105, pp. 745–769, Dec. 2001.
- N. Virag, V. Jacquemet, C.S. Henriquez, S. Zozor, O. Blanc, J.-M. Vesin, E. Pruvot, and L. Kappenberger, “Study of Atrial Arrhythmias in a Computer Model Based on MR Images of Human Atria,” *Chaos*, vol. 12, pp. 754–763, Sept. 2002.
- S. Zozor, O. Blanc, V. Jacquemet, N. Virag, J.-M. Vesin, E. Pruvot, L. Kappenberger, C.S. Henriquez, “A Numerical Scheme for Modeling Wavefront Propagation on a Monolayer of Arbitrary Geometry,” *IEEE Trans. Biomed. Eng.*, vol. 50, no. 4, Apr. 2003.
- V. Jacquemet, N. Virag, Z. Ihara, L. Dang, O. Blanc, S. Zozor, J. Vesin, L. Kappenberger and C.S. Henriquez, “Study of Unipolar Electrogram Morphology in a Computer Model of Atrial Fibrillation,” *J. Cardiovasc. Electrophysiol.*, vol. 14, pp. S172–S179, Oct. 2003.

Book Chapters

- O. Blanc, N. Virag, A. Nicoulin, V. Jacquemet, and L. Kappenberger, “Simulation of Arrhythmias in a Computer Model of Human Atria”, in *Computer Simulation and Experimental Assessment of Cardiac Electrophysiology* (N. Virag, O. Blanc, L. Kappenberger, eds.), ch. 3, pp. 21–28, Futura Publishing, Armonk, New York, 2001.
- E. Pruvot, V. Jacquemet, J.-M. Vesin, N. Virag, J. Koerfer, M. Fromer, and L. Kappenberger, “Action Potential Duration Alternans in a Mono-Cellular Model Based on the Beeler–Reuter Kinetics,” in *Computer Simulation and Experimental Assessment of Cardiac Electrophysiology* (N. Virag, O. Blanc, L. Kappenberger, eds.), ch. 9, pp. 69–77, Futura Publishing, Armonk, New York, 2001.

Conference Papers and Abstracts

North American Society of Pacing and Electrophysiology (NASPE)

- E. Pruvot, V. Jacquemet, J.-M. Vesin, O. Blanc, N. Virag, J. Koerfer, M. Fromer, and L. Kappenberger, “Periods of Prolonged Transient Alternans in APD Revealed by Delivery of an Extrastimulus near Period-Doubling Bifurcation,” in *PACE*, vol. 24 (Part II), p. 670, Apr. 2001.
- V. Jacquemet, C. S. Henriquez, S. Zozor, N. Virag, E. Pruvot, O. Blanc, J.-M. Vesin, and L. Kappenberger, “Simulation of Atrial Electrograms During Atrial Fibrillation,” in *PACE*, vol. 24 (Part II), p. 605, Apr. 2002.
- V. Jacquemet, Z. Ihara, L. Dang, O. Blanc, N. Virag, J.-M. Vesin, L. Kappenberger, C.S. Henriquez, “Analysis of Electrogram Morphology to Detect Gross Structural Remodeling During Chronic AF: A Model Study.” in *PACE*, vol. 26 (Part II), p. 1025, Apr. 2003.
- L. Dang, Z. Ihara, V. Jacquemet, N. Virag, O. Blanc, J.-M. Vesin, L. Kappenberger, “Optimization of Antitachycardia Pacing Using a Computer Model of Atrial Arrhythmias.” in *PACE*, vol. 26 (Part II), p. 1026, Apr. 2003.

European Society of Cardiology (ESC)

- E. Pruvot, V. Jacquemet, J.-M. Vesin, N. Virag, O. Blanc, M. Fromer, and L. Kappenberger, "Periods of Prolonged Transient Alternans in APD Revealed by Delivery of an Extrastimulus near Period-Doubling Bifurcation," vol. 22, p. 221, *Eur. Heart J.*, ESC 2001, Stockholm, Sweden, 2001.
- V. Jacquemet, N. Virag, C. S. Henriquez, O. Blanc, J.-M. Vesin, E. Pruvot, and L. Kappenberger, "Study of Initiation and Perpetuation of Atrial Fibrillation in a Computer Model of Human Atria Based on Magnetic Resonance Images," vol. 23, p. 46, *Eur. Heart J.*, ESC 2002, Berlin, Germany, Sept. 2002.
- N. Virag, O. Blanc, L. Dang, V. Jacquemet, Z. Ihara, J.-M. Vesin, C.S. Henriquez, and L. Kappenberger, "Characterizing Anti-Tachy Pacing Efficiency in a Numerical Model of Human Atrial Arrhythmias," *Eur. Heart J.*, 24 (Abstr. Suppl.), p. 603, ESC 2003, Vienna, Austria, Sept. 2003.

International Congress on Electrocardiology (ICE)

- V. Jacquemet, N. Virag, Z. Ihara, L. Dang, O. Blanc, J.-M. Vesin, C.S. Henriquez, L. Kappenberger, "A Computer Model of Sustained Atrial Fibrillation to Study Atrial Electrograms." *International Journal of Bioelectromagnetism*, Vol. 5, No.1 pp. 181–182, ICE 2003, Helsinki, Finland, June 2003.

Digital Signal Processing (DSP)

- V. Jacquemet, S. Zozor, N. Virag, O. Blanc, J.-M. Vesin, C. S. Henriquez, E. Pruvot, and L. Kappenberger, "Simulated Atrial Fibrillation in a Computer Model of Human Atria," vol. I, pp. 1 393–398, DSP, Santorini, Greece, July 2002.

Engineering in Medicine and Biology Society (EMBS)

- L. Dang, N. Virag, Z. Ihara, V. Jacquemet, O. Blanc, J. Vesin and L. Kappenberger, "Evaluation of Ablation Patterns by Means of a Computer Model of Human Atria," in *Proc. EMBS 2003*, Cancun, Mexico, Sept. 2003.

International Meeting on Atrial Fibrillation

- L. Kappenberger, N. Virag, L. Dang, V. Jacquemet, A. Forclaz, J. Schlaepfer, and P. Ruchat, "How to Study Atrial Fibrillation: A Computer Model," in *Proc. V International Meeting on Atrial Fibrillation 2003*, pp. 15-21, Bologna, Italy, Sept. 2003.

Invited Talks

- V. Jacquemet, "A Computer Model of Human Atria", *First International Workshop on Cardiac Modeling in Arrhythmogenic Right Ventricular Dysplasia*, French Atomic Commission (CEA), Paris, France, Nov. 2001.
- V. Jacquemet, "AF Initiation and Perpetuation: What Can Computer Models Tell Us About Animal Models?," *Third International Workshop on Computer Simulation and Experimental Assessment of Electrical Cardiac Function*, Lausanne, Switzerland, Dec. 2002.
- V. Jacquemet (on behalf of L. Kappenberger), "How to Study Atrial Fibrillation: A Computer Model," *V International Meeting on Atrial Fibrillation 2003*, Bologna, Italy, Sept. 2003.